UNIVERSITAT
POLITÈCNICA
DE VALÈNCIA

EXPERIMENTAL AND MODELLING STUDY OF INTERFACIAL PHENOMENA IN ANNULAR FLOW WITH UNCERTAINTY QUANTIFICATION

DOCTORAL THESIS

Author:
Yago Rivera Durán

Supervisors:
Dr. José Luis Muñoz-Cobo González
Dr. César Berna Escriche

Valencia, March 2023

AKNOWLEDGEMENTS

I would like to take this opportunity to express my sincere gratitude to the individuals who have provided unwavering support and guidance throughout my research journey. First and foremost, I am grateful to my doctoral thesis supervisors, Professor emeritus Dr. José Luis Muñoz-Cobo González and Dr. César Berna Escriche, for their exceptional support throughout this endeavor. They have been integral pillars in both the development of this thesis and shaping my academic and research career. I would also like to extend my gratitude to Professor Alberto Escrivá Castells, who has always been willing to lend a helping hand, and whose invaluable feedback has been of immeasurable assistance.

My research has been reviewed by three members of the scientific community, Dr Pierre Ruyer, Dr César Queral, and Dr Valentina Valori, to whom I would like to express my appreciation for their time and comments, which have helped to enrich and strengthen the arguments presented in this thesis. I would also like to acknowledge the members of the final defense committee Dr Luis E. Herranz, Prof. Dr Rafa Miró and Dr Valentina Valori for their feedback during the defense. Their thoughtful questions and comments helped me to better articulate my research and demonstrate its significance.

I would like to take this opportunity to express my heartfelt gratitude towards my family and friends for their unwavering support throughout my academic journey. Their love, encouragement, and understanding have been a source of inspiration and motivation for me during the ups and downs of this journey. I am grateful to have had their unwavering support, which has made this journey less daunting and more fulfilling. I would also like to acknowledge their patience and sacrifice as they have often put their own needs aside to support me in my academic pursuits. Thank you for believing in me and cheering me on.

I would also like to acknowledge the support provided by the Ministerio de Economía, Industria y Competitividad and the Agencia Nacional de Investigación under the FPI grant BES-2017-080031, which provided funding for my research. This financial support has allowed me to conduct the necessary research to complete this thesis. Their support is a testament to their commitment to supporting and advancing academic research. Thank you for investing in my research and supporting my academic pursuits.

Finally, I want to express my deep appreciation to all the people who have played a significant role in my academic journey. Without their support and encouragement, completing this thesis would not have been possible.

ABSTRACT

Annular flow is one of the most important two-phase flow regimes and is characterized by a very small liquid fraction known as a liquid film travelling close to the wall and a gas core. Annular flow can be observed during the operation of nuclear plants, in different transient scenarios, and many other industrial applications. The liquid film is decisive in many of them as it has a high mass, momentum and energy transfer capacity. Many of these properties are due to the film exhibiting nonlinear interfacial behavior with the generation of interfacial waves. In addition, in certain facilities where the liquid film acts as a coolant, it is essential to know its behavior both for optimization and safety reasons.

In order to study the fundamentals of the liquid film, a series of experiments have been carried out in a facility designed to generate air-water annular flow in a vertical circular pipe. In this facility, the time evolution of the liquid film thickness has been measured under different conditions and sub-regimes, such as free-fall flow or upward and downward cocurrent flow. The measurement system used has been designed and built for this application and consists of 3-electrode conductance probes mounted flush to the wall and arranged at different distances from the entrance of the test section. Both the electronics and the calibration device were specifically designed to work with these conductance probes. The facility has two different diameters to compare the effect of the pipe diameter and increase the range of measurements available in databases.

One of the main characteristics of the liquid film is its interfacial waves. The two primary types of waves that can be distinguished are the disturbance waves, which are large coherent waves, and the ripple waves, small, non-coherent waves that are constantly generated before disappearing when absorbed by other waves. The main variables of the liquid film analyzed in the experimental setup are the mean film thickness, the height and frequency of the disturbance waves, the height of the ripple waves and the height of the unperturbed liquid. Different experimental studies have been carried out to add additional value to the measurements. For downward annular flow, the development of the film through different measuring zones has been studied, and the different test section diameters have been compared. In addition, multiple correlations have been proposed, and the results have been compared with similar studies by other authors. To analyze the upward annular flow, a study of the effect of surface tension on the liquid film variables by adding small amounts of 1-butanol has been added.

The modelling of annular flow by numerical analysis is also the subject of this thesis. Computational Fluid Dynamics (CFD) codes are computational tools that allow the analysis of fluid behavior. They have undergone a strong evolution

over the last few years thanks to technological advances, and the results obtained from their correct use are very promising. However, multiphase flow remains challenging to model, and it is necessary to contrast the predictions of CFD codes with experimental measurements. Therefore, the developed annular flow phenomenology has also been studied using the ANSYS CFX code.

There is a significant knowledge gap in the uncertainty quantification of CFD codes. Some methodologies are available, although many are in the early stages or have not been explored by researchers. All applications of CFD codes in nuclear safety require extensive knowledge of the uncertainty of the predictions, so developing these methodologies is crucial. This thesis shows the fundamentals of Polynomial Chaos Expansion (PCE) as a method to calculate the uncertainty of simulation results by propagation. The PCE by Gauss-Hermite quadrature has also been applied to the simulations of two experiments. On the one hand, in the experimental setup of this thesis, and on the other hand to an international benchmark related to nuclear safety. This method has proved to be very efficient when the number of uncertain variables is very small.

SINOPSIS

El flujo anular es uno de los regímenes de flujo bifásico más importantes y se caracteriza por que una fracción de líquido muy pequeña conocida como película de líquido que viaja cerca de la pared y un núcleo gaseoso. El flujo anular se puede observar durante la operación de plantas nucleares y en diferentes escenarios transitorios, aunque también en muchas otras aplicaciones industriales. La película de líquido es determinante en muchas de ellas ya que posee una alta capacidad de transferencia de masa, momento y energía. Parte de estas propiedades se deben a que la película presenta un comportamiento interfacial no linear con desarrollo de ondas interfaciales. Además, en determinadas instalaciones donde se la película de líquido actúa como refrigerante, es esencial conocer su comportamiento tanto por motivos de optimización como por razones de seguridad.

Para estudiar los fundamentos del comportamiento de la película de líquido se han llevado a cabo una serie de experimentos en una instalación diseñada para generar flujo anular aire-agua en tubería circular vertical. En esta instalación se ha medido la evolución temporal del espesor de la película de líquido bajo diferentes condiciones y subregímenes, como flujo en caída libre o flujo en cocorriente ascendente y descendente. El sistema de medida empleado se ha diseñado y construido para esta aplicación y consiste en sondas de conductancia de 3 electrodos rasantes a la pared y dispuestas en diferentes partes de la sección de test. Tanto el sistema electrónico como el dispositivo de calibración se diseñaron específicamente para trabajar con estas sondas de conductancia. La instalación cuenta con dos diámetros diferentes para poder comparar también el efecto del diámetro de la tubería así como aumentar el rango de medidas disponibles en bases de datos.

Una de las características más particulares de la película de líquido son sus ondas interfaciales. Las principales ondas que se pueden diferenciar son las *disturbance waves*, ondas coherentes de gran calibre; y las *ripple waves*, ondas de pequeño tamaño, no coherentes que se generan constantemente antes de desaparecer al ser absorbidas por otras ondas. Las variables principales de la película de líquido que se han analizado en la instalación experimental son el espesor medio, la altura y frecuencia de las *disturbance waves*, la altura de las *ripple waves* y la altura de líquido no perturbado. Se han llevado a cabo diferentes estudios experimentales con objeto de añadir un valor adicional a las medidas. Para flujo anular descendente se ha estudiado el desarrollo de la película a través de diferentes zonas de medida y se han comparado las secciones de test de diferente diámetro. Además, múltiples correlaciones se han propuesto y los resultados se han comparado con estudios similares de otros autores. Para el análisis del flujo anular ascendente, se ha añadido un estudio del efecto de la

tensión superficial en las variables de la película de líquido mediante la adición de pequeñas cantidades de 1-butanol.

Es objeto de esta tesis también la modelación del flujo anular mediante análisis numérico. Los códigos de fluidodinámica computacional (CFD) son herramientas computacionales que permiten analizar el comportamiento de los fluidos. Han experimentado una fuerte evolución a lo largo de los últimos años gracias a los avances tecnológicos y los resultados que se obtienen de su correcta utilización son muy prometedores. No obstante, el flujo multifásico sigue siendo difícil de modelar y es necesario contrastar las predicciones de los códigos CFD con medidas experimentales. Por lo tanto, la fenomenología de flujo anular desarrollado se ha estudiado también mediante el código ANSYS CFX. Existe un importante vacío de conocimiento en la cuantificación de la incertidumbre de dichos códigos CFD. Si bien existen algunas metodologías para ello, muchas se encuentran en etapas tempranas o no hay sido exploradas por los investigadores. Todas las aplicaciones de los códigos CFD en el área de seguridad nuclear requieren de un extensivo conocimiento de la incertidumbre de las predicciones por lo que el desarrollo de estas metodologías es muy importante. En esta tesis se muestran los fundamentos del Polynomial Chaos Expansion (PCE) como método para calcular la incertidumbre de los resultados de simulación mediante propagación. El PCE por cuadratura de Gauss-Hermite se ha aplicado a las simulaciones de dos experimentos. Por un lado en la instalación experimental de esta tesis y por otro lado a un benchmark internacional relacionado con seguridad nuclear. Este método ha resultado ser muy eficiente cuando el número de variables inciertas es muy reducido.

SINOPSI

El flux anular és un dels règims de flux bifàsic més importants i es caracteritza perquè la fracció de líquid és molt xicoteta coneguda com a pel·lícula de líquid. El flux anul·lar es pot observar durant l'operació de plantes nuclears i en diferents escenaris transitoris, encara que també en moltes altres aplicacions industrials. La pel·lícula de líquid és determinant en moltes d'elles ja que posseeix una alta capacitat de transferència de massa, moment i energia. Part d'aquestes propietats es deuen al fet que la pel·lícula presenta un comportament interfacial no linear amb desenvolupament d'ones interfacials. A més, en determinades instal·lacions on li la pel·lícula de líquid actua com a refrigerant, és essencial conéixer el seu comportament tant per motius d'optimització com per raons de seguretat.

Per a estudiar els fonaments del comportament de la pel·lícula de líquid s'han dut a terme una sèrie d'experiments en una instal·lació dissenyada per a generar flux anular aïre-aigua en canonada circular vertical. En aquesta instal·lació s'ha mesurat l'evolució temporal de la grossària de la pel·lícula de líquid sota diferents condicions i subrégimenes, com a flux en caiguda lliure o flux en cocorriente ascendent i descendent. El sistema de mesura emprat s'ha dissenyat i construït per a aquesta aplicació i consisteix en sondes de conductància de 3 elèctrodes i disposades en diferents parts de la secció de test. Tant el sistema electrònic com el dispositiu de calibratge es van dissenyar específicament per a treballar amb aquestes sondes de conductància. La instal·lació compta amb dos diàmetres diferents per a poder comparar també l'efecte del diàmetre de la canonada així com augmentar el rang de mesures disponibles en bases de dades.

Una de les característiques més particulars de la pel·lícula de líquid són les seues ones interfacials. Les principals ones que es poden diferenciar són les *disturbance waves*, ones coherents de gran calibre; i les *ripple waves*, ones de xicoteta grandària, no coherents que es generen constantment abans de desaparéixer en ser absorbides per altres ones. Les variables principals de la pel·lícula de líquid que s'han analitzat en la instal·lació experimental són la grossària mitjana, l'altura i freqüència de les *disturbance waves*, l'altura de les *ripple waves* i l'altura de líquid no pertorbat. S'han dut a terme diferents estudis experimentals a fi d'afegir un valor addicional a les mesures. Per a flux anul·lar descendent s'ha estudiat el desenvolupament de la pel·lícula a través de diferents zones de mesura i s'han comparat els diferents diàmetres. A més, múltiples correlacions s'han proposat i els resultats s'han comparat amb estudis similars d'altres autors. Per a l'anàlisi del flux anul·lar ascendent, s'ha afegit un estudi de l'efecte de la tensió superficial en les variables de la pel·lícula de líquid mitjançant l'addició de xicotetes quantitats de 1-butanol.

És objecte d'aquesta tesi també el modelatge del flux anul·lar mitjançant anàlisi numèrica. Els codis de fluidodinámica computacional (CFD) són eines computacionals que permeten analitzar el comportament dels fluids. Han experimentat una forta evolució al llarg dels últims anys gràcies als avanços tecnològics i els resultats que s'obtenen de la seua correcta utilització són molt prometedors. No obstant això, el flux multifásico continua sent difícil de modelar i és necessari contrastar les prediccions dels codis CFD amb mesures experimentals. Per tant, la fenomenologia de flux anular desenvolupat s'ha estudiat també mitjançant el codi ANSYS CFX. Existeix un important buit de coneixement en la quantificació de la incertesa d'aquests codis CFD. Si bé, existeixen algunes metodologies per a això moltes es troben en etapes primerenques o no hi ha sigut explorades pels investigadors. Totes les aplicacions dels codis CFD en l'àrea de seguretat nuclear requereixen d'un extensiu coneixement de la incertesa de les prediccions pel que el desenvolupament d'aquestes metodologies és molt important. En aquesta tesi es mostren els fonaments del *Polynomial Chaos Expansion* (PCE) com a mètode per a calcular la incertesa dels resultats de simulació mitjançant propagació. El PCE per quadratura de Gauss-Hermite s'ha aplicat a les simulacions de dos experiments. D'una banda en la instal·lació experimental d'aquesta tesi i d'altra banda a un benchmark internacional relacionat amb seguretat nuclear. Aquest mètode ha resultat ser molt eficient quan el nombre de variables incertes és molt reduït.

NOMENCLATURE

ACRONIMS

CFD	Computational Fluid Dynamics
BWR	Boiling Water Reactor
PWR	Pressurized Water Reactor
LOCA	Loss of Coolant Accident
SBLOCA	Small-Break Loss Of Coolant Accident
LOHS	Loss of Heat Sink Accident
ECCS	Emergency Core Coolant Systems
DW	Disturbance Wave
RW	Ripple Wave
CECM	Constant Electric Current Method
WMS	Wire Mesh sensor
LIF	Laser Induced Fluorescence
PCB	Printed Circuit Board
PIV	Particle Image Velocimetry
RANS	Reynolds-Averaged Navier-Stokes
DNS	Direct Numerical Simulation
VOF	Volume of Fluid Method
FEM	Finite Element Method
FVM	Finite Volume Method
FDM	Finite Difference Method
MC	Monte Carlo Method
LHS	Latin Hypercube Sampling
DS	Deterministic Sampling
PCE	Polynomial Chaos Expansion
POD	Proper Orthogonal Decomposition
MVEM	Mean-Variance Estimation Method
NN	Neural Network
LRA	Low-Rank Approximation
EV	Expected Value

DPS	Density Preserving Sampling
UMAE	Uncertainty meth. For Accuracy Extrapolation
GEPELON	Ondulatory Film Generation
DAQ	Data Acquisition
ABS	Acrylonitrile Butadiene Styrene
SST	Shear Stress Transport
LES	Large Eddy Simulation
DES	Detached Eddy simulation
OECD	Organization for Economic Co-operation and Development
NEA	Nuclear Energy Agency

VARIABLES

ν_{fluid}	Kinematic viscosity
D	Diameter
W	Channel Width
Q_{fluid}	Fluid Flow Rate
j_{fluid}	Fluid Superficial Velocity
Re	Superficial Reynolds Number
Re_{film}	Film Reynolds Number
$Re_{G\ maxhDW}$	Gas Re for maximum DW height
Ka	Kapitza Number
St	Strouhal Number
Fr	Froude Number
X	Lockhart-Martinelli Parameter
σ	Surface Tension
u_{film}	Film Velocity
l_0	Integral Length Scale
λ	Taylor Microscale
k	Turbulent Kinetic Energy
ε	Turbulent Energy Dissipation
$d_{min,DW}$	Minimum distance between disturbance waves
h_{mean} or h_m	Mean Film Thickness
h_{DW}	Disturbance Wave Peak Height
υ_{DW}	Disturbance Wave Frequency

c_{DW}	Disturbance Wave Celerity
h_{bun}	Base Unperturbed Film Thickness
h_{bun+RW}	Unperturbed Film Thickness + Ripple Wave Height
$h_{i,fit}$	Film Height of the fit curve
R^2	Determination Coefficient
ε_{DAQ}	Data Acquisition Error
ε_{acc}	Random/accidental Error
ε_{syst}	Systematical Error
$\varepsilon_{fit,cal}$	Fit Calibration Error
ε_{poa}	Positioning Error
$Re_{G\ maxhDW}$	Gas Re for maximum DW height
L_m	Viscous-gravity length

LIST OF CONTENTS

LIST OF FIGURES

LIST OF TABLES

Chapter 1
Introduction

1.1. TWO-PHASE ANNULAR FLOW REGIME

Over the last 50 years, the annular flow has been the subject of study by researchers worldwide as it is one of the most important two-phase flow regimes. It can be observed in different industry applications, including civil, chemical or nuclear equipment. Knowing the different two-phase flow regimes is very important as it allows us to understand how fluids behave and to design and optimize the facilities in which they appear. In addition, studying each regime in detail is very useful for developing, validating and verifying mathematical models that allow us to simulate the behavior of the fluids in the installations (Andreani et al., 2008).

Annular flow is characterized by having a small amount of liquid moving through the wall and a gaseous core. Generally, the liquid contains small bubbles of gas, while the gas contains small droplets that separate from the liquid film.

One of the most common scenarios in which two-phase flow appears is during the phase change of water due to heating inside a vertical pipe (Wolf, 1995). Figure 1.1 shows a schematic of the most important two-phase flow regimes. As we begin to heat, small bubbles of water vapor separate from the wall zone and begin to travel in a dispersed pattern along with the liquid stream. The bubbles tend to adopt a spherical shape as this is the lowest energy at the surface. This first regime is known as bubbly flow. As the amount of vapor increases, the bubbles begin to collapse forming larger structures such as "cap" bubbles or "bullet" bubbles (because of their shape). These regimes are known as cap-bubbly flow and slug flow respectively. If we continue heating, there will come a time when the vapor fraction (known as the void fraction) is much higher than the liquid water fraction and the gas concentrates in the central part of the pipe. After a transition regime known as churn flow, the liquid settles in the wall zone while the gas concentrates in the center of the pipe leading to annular flow. It is common to observe the liquid film with small gas bubbles and the gaseous core with small liquid droplets (Azzopardi, 1997).

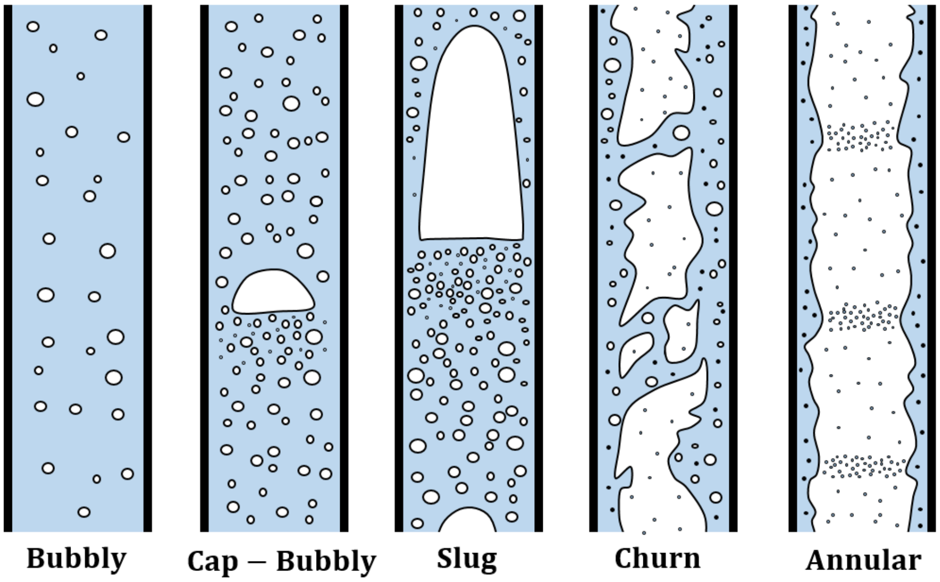

Source: Author's design

Figure 1.1. Most important two-phase upward gas-liquid flow regimes.

The liquid film observed in annular flow plays a fundamental role in the heating process. This is because liquid water has a much higher heat transfer coefficient than vapor and gases in general. As the liquid film is in the wall zone, heat transfer from the wall to the liquid is significantly enhanced. In addition, the interface between the liquid and gas is wave-like and exhibits very turbulent behavior with large and small waves and eddies. Annular flow has one of the highest convective heat transfer capacities (Sawant et al., 2009) due to the behavior of the liquid film. This further promotes heat exchange but may result in the wall drying out in certain scenarios. If the wall runs out of liquid film in an area where there is heating, the liquid will not absorb the heat and the wall will do so by increasing the temperature. This can lead to the phenomenon known as thermal fatigue, where the material is subjected to strong temperature changes that end up degrading the material or even causing its failure.

In vertical annular flow, the direction of movement of each of the fluids is an important parameter since the behavior of the film will be slightly different in each of them. A schematic of the different types of annular flow is shown in Figure 1.2:

- If the liquid film moves in an ascent direction, the upward annular flow can be observed. It occurs when the gas stream, which is moving upward, is large enough to entrain the liquid film. In this case there is only one option which is gas and liquid moving in the same direction or cocurrent. For this regime to occur, the gas velocity must be considerably large so that, generally the entrainment value (fraction of liquid dispersed as droplets in the gas) will be high. Consequently, the liquid film is usually very narrow, with many ripple waves.
- If the liquid film moves in a descending direction (known as downward annular flow), different variants are observed since, due to the effect of gravity alone, the liquid film tends to move in a descending direction.
    - Free fall annular flow. In this regime, there is no gas movement and the film would simply move by the action of gravity. Since there are no drag forces, droplet entrainment is very small or non-existent. In addition, both the film and the interfacial waves reach greater thicknesses.
    - Cocurrent downward annular flow. If the gas flow direction is the same as that of the liquid film, it will interact with it, increasing its velocity as a consequence of drag forces. In this regime, there is no critical gas velocity as in the upward flow since the film will also tend to fall due to the action of gravity. However, a critical point may occur when the gas and liquid interface velocities are equal. Below this point, the gas, with almost no velocity, would tend to slow the film slightly. On the contrary, above this value, it would produce the opposite effect and accelerate the film.
    - Counter-current downward annular flow. This flow occurs only if the gas moves in an upward direction but its velocity is lower than the critical velocity above which the drag forces exceed the gravity forces, which would produce the upward movement of the liquid film. It would be possible to observe this regime if there is a reduction of the gas velocity in a cocurrent upward annular flow regime. Below the critical velocity, the film would stop ascending and begin to fall down the wall.

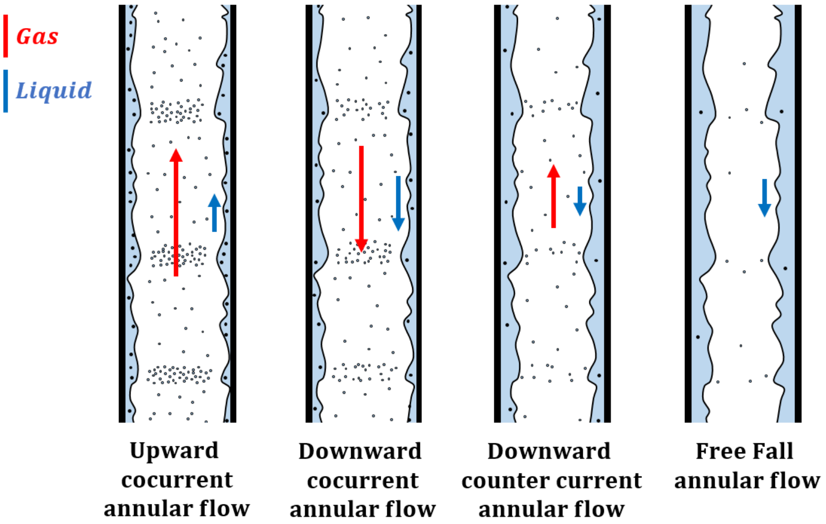

Source: Author's design

Figure 1.2. Types of annular flow according to the direction of phase movement.

Both the annular flow regime and the other two-phase flow regimes are common in energy systems such as steam generators, heat exchangers, nuclear reactors, etc. In the case of nuclear power plants, the annular flow occurs in different components depending on the type of nuclear reactor (Kolev, 2015). In the case of the Boiling Water Reactor or BWR, it is possible to observe the upward cocurrent annular flow in the reactor core itself as a consequence of the evaporation of the water as it moves between the fuel elements. In this type of reactor, the dryout phenomenon is well known, which occurs when, under certain operating conditions, the liquid film disappears resulting in the wall drying. The increase in wall temperature can rapidly deteriorate the materials, leading to a potential safety failure. In addition, the liquid film in BWR reactors during operation is very thin and moves at high velocities. This results in an increase in droplet breakout and a high value of liquid concentration in the gas phase (*entrainment*), which further contributes to the reduction of the liquid film on the wall. This is why a considerable effort has been and continues to be invested in studying this flow regime.

In the Pressurized Water Reactor or PWR type reactors, the water is in a liquid state during operation. However, in steam generators, the hot water coming from the core exchanges heat with a secondary circuit in charge of supplying steam to the turbines. In this process of steam generation in the secondary circuit, the cocurrent upward annular flow may occur during the operation of the nuclear power plant. In addition, during LOCA (*Loss of Coolant Accident*) or LOHS (*Loss of Heat Sink Accident*) accidents, both PWR and BWR face scenarios where both upward and downward annular flow play a major role, being the liquid film indispensable for heat removal. For example, in BWRs during ECCS (*Emergency Core Coolant Systems*) injection, cooling water enters the core forming the liquid film in the downward direction. During a LOCA in a PWR the liquid inventory in the reactor may decrease to a water level in the primary circuit below the level of the steam generator. In this case, steam will be produced which may condense inside the U-tubes of the steam generator. This is known as reflux condensation and is one of the most important phenomena (Jeong et al., 1998) during the evolution of SBLOCA (*Small-Break Loss Of Coolant Accident*).

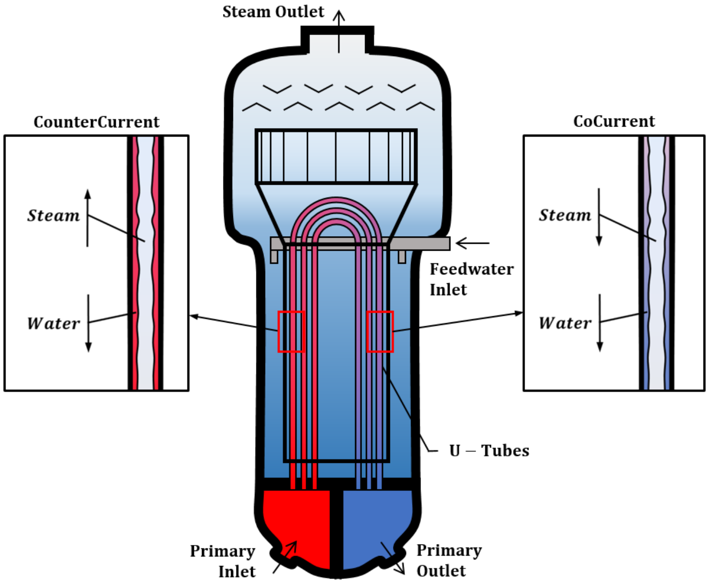

Source: Author's design

Figure 1.3. Steam generator schematic and reflux condensation behavior.

Although annular flow with upward movement is usually studied, different variants are observed in reflux condensation processes inside steam generators (Figure 1.3). In the inlet or ascending part of the tubes, the liquid-vapor flow is countercurrent, with the liquid descending by gravity and the vapor ascending and condensing on the walls. However, in the downstream section of the generator tubes, the film falls by gravity and does so in cocurrent motion with the vapor.

In order to be able to optimize the design and operation of these systems, reducing costs, increasing their efficiency and improving their safety, it is necessary to research the physical processes related to the liquid film in annular flow. Furthermore, modelling these processes using thermal-hydraulic codes such as RELAP and TRACE or computational dynamics (CFD) codes such as ANSYS

Fluent and CFX is an extremely complicated task (Andreani et al., 2008). According to (Woods et al., 2009), the experimental database needs to be extended in order to accomplish this task. This has become evident in recent years as researchers worldwide have shown interest in liquid films and interfacial waves and how they can enhance the exchange of heat, mass and energy.

1.2. WAVY LIQUID FILM

As mentioned in the previous section, in the annular liquid-gas flow, we find a small fraction of liquid that is located on the wall forming what is known as a liquid film. This film has an enormous effect on heat transfer with the wall, as well as mass, momentum and energy transfer between phases. One of the phenomena that most influences these processes is the wavy behavior of the liquid-gas interphase.

Interfacial waves have been studied over the years using different methodologies, which will be discussed below. In general terms, most authors divide the types of waves that may appear into three classes shown in Figure 1.4 and discussed below (S. V. Alekseenko et al., 2008; Dasgupta et al., 2017; Schubring, Shedd, et al., 2010; Setyawan et al., 2016). However, it is important to mention that the precise definition and characterization of these waves remain unresolved, and it is difficult to establish a fixed system to differentiate between the different types.

- *Disturbance Waves* or DW are waves of large amplitude with an order of magnitude up to five times the average thickness of the liquid film. They are established as coherent waves, i.e. they cover the entire perimeter of the annular ring they form as they move through the film.
- *Ripple Waves* or RW are small waves that can be located in the area between two consecutive DWs or even above them. The lifetime of these waves is much shorter and they usually contribute to the growth of the DW waves by disappearing in the process. RWs are considered non-coherent in the complete annular ring, although they are coherent over small distances.
- *Ephemeral Waves* or EW are waves that present an amplitude between the RW and DW and an intermediate lifetime that allows them to remain and grow longer than the RW. They form on the backside of the DW and travel until the next DW absorbs them.

Some authors also add *ring waves* and *huge waves* to the list. The first ones correspond to coherent waves similar to the EW that appear in the zone where the entrainment starts, generally in vertical ascending annular flow. The huge waves correspond to waves of large size and amplitude that appear for low gas and liquid velocities. These waves are associated with a transition regime between annular flow and churn or slug flow.

The presence of large waves such as DW is one of the main causes of entrainment (S. V. Alekseenko et al., 2014; Azzopardi, 1997). This phenomenon refers to the number of droplets that are carried by the gas stream in the annular flow. For this reason, a distinction is often made between two types of annular flow, with and without droplet detachment. Between these two regions there is a transition zone in which a critical gas velocity is observed that leads to the onset of the start-up. This critical gas velocity depends, among other things, on the liquid velocity itself, which is generally much lower. For droplet breakout to occur, the drag force of the gas has to exceed the surface tension forces that retain the liquid at the DW crest (Ishii & Grolmes, 1975). Therefore, the critical gas velocity required to initiate droplet entrainment is lower the higher the liquid film velocity.

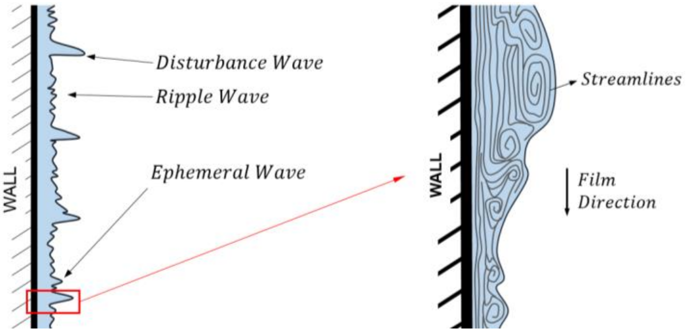

Source: Author's design

Figure 1.4. Diagram of the most important types of waves appearing in the annular flow and the detail of the streamlines of a wave.

During the last few years, with the advancement of optical methods, the analysis of liquid film vortices has become more popular (Ivan Zadrazil & Markides, 2014). This is because by means of film photography it is possible to track the particles and thus obtain the flow streamlines. This technique is explained in detail in the next section. Knowing the behavior of these vortices allows to understand one of the most important mechanisms of heat transfer of the liquid film. Figure 1.4 shows an example scheme where the flow lines in a disturbance wave have been represented and the generation of vortices and recirculation zones within the waves can be observed.

Before concluding the section, it is convenient to define some of the most important variables of the liquid film. These variables will allow for characterizing the flow from a quantitative point of view and establishing relationships between flow rates, dimensions and expected results. Figure 1.5 shows schematically the most important ones: mean film thickness, mean DW height, mean DW frequency, mean DW celerity and mean unperturbed film thickness.

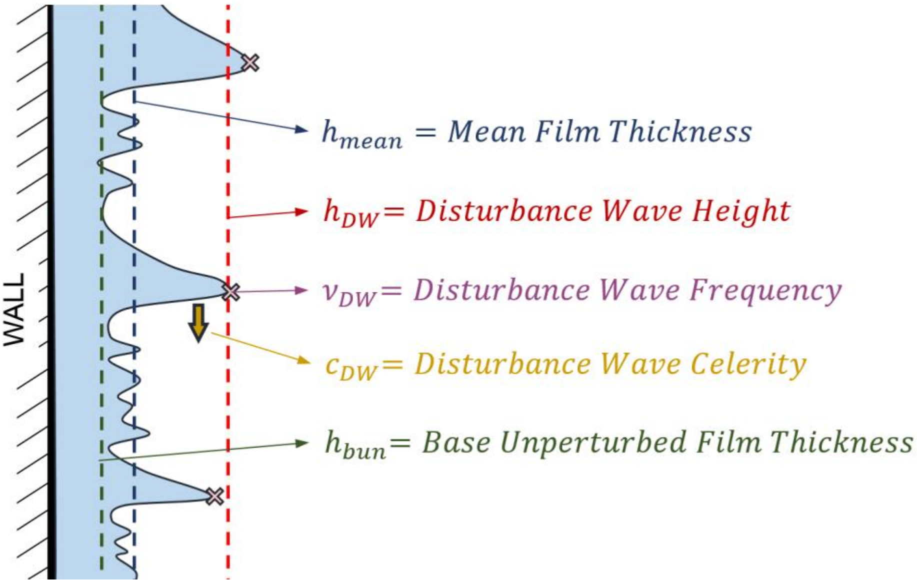

Source: Author's design

Figure 1.5. Most important variables of the liquid film.

The mean film thickness refers to the time average of the height of the liquid at a given point. This variable indicates how high the fluid film would be if there were no waves at the interface. It gives an idea of the average thickness that allows us, in turn, to calculate the average speed at which it moves.

On the other hand, Figure 1.5 also shows the variables related to the disturbance waves. Specifically, the most important are the waves' height, frequency, and celerity. Generally, wave counting is used to obtain the values of height and frequency. The height is obtained by averaging the height of the wave peaks, while the frequency can be obtained by dividing the number of peaks by the sampling time. The celerity of the waves corresponds to their speed, which will be different from the speed of the film. In general, the waves travel at higher velocities than the film as they are less exposed to the wall effect and interact more with the gas. Only in certain cases of downward countercurrent flow could the opposite happen.

The last variable shown in Figure 1.5 is the mean undisturbed base thickness. As its name indicates, it refers to the minimum film thickness where the liquid will always be found. It is complex to analyze since the layer is often very thin. However, it is important because it allows us to analyze if the wall runs out of liquid at some point.

1.3. LIQUID FILM MEASUREMENT TECHNIQUES

Since annular flow began to be studied, the liquid film has been investigated from different points of view. Techniques have evolved over time and have become more accurate and specific. However, each technique has its advantages and none is free of drawbacks. This section shows all the methodologies reported in the literature and how different authors have carried out liquid film measurements. The industrial needs for the calculation of this film have also favored the evolution of different techniques depending on the objective pursued. The most common classification is made according to the type of film evolution to be obtained, i.e., whether the measurements are made on an average, point in time or spatial basis (Figure 1.6).

- <u>Localised: Time average</u>. Averaging measurements are generally point measurements, allowing the average film thickness to be obtained over extended times, but only in one region. Averaging systems have practically become obsolete in research, although they still have some industrial applications. This is because they only provide averages of the entire film in a given section, without information on specific interface and wave phenomenology.
- <u>Localised: Time evolution</u>. Point time evolution measurements are the most common since they provide information on interfacial phenomena over significant time scales. Their great popularity is mainly due to the ease of implementation and use in a wide range of applications. These techniques make it possible to obtain reasonably localized measurements, with spatial resolutions generally in the order of millimeters. Sometimes this position can be moved, or the measurement system can be replicated at different positions.
- <u>Global: Spatial evolution</u>. Spatial evolution measurements make it possible to obtain the evolution of the film in space for a specific moment in time. Nowadays it is possible to obtain the time evolution of the spatial region of interest so it is possible to study the liquid film globally. Some of these techniques even allow observing the motion of the liquid, thus being able to obtain the patterns of vortex motion. However, in general, spatial evolution measurement techniques do not allow data to be obtained over long periods of time. It is therefore necessary to ensure that the averages include sufficient representative data to be considered as such.

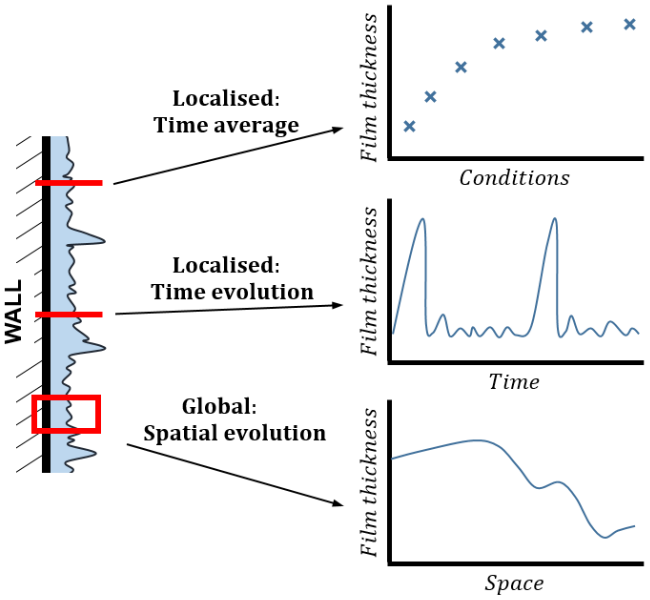

Source: Author's design

Figure1.6. Outline of the most important types of liquid film measurements.

1.3.1. TIME AVERAGE THICKNESS MEASUREMENT METHODS

By means of these methods, the annular flow liquid film began to be studied. One of the first papers that laid the foundations dates back to before the 1950s (Grimley, 1945) where the current flowing between two electrodes several centimeters apart was calculated by feeding the liquid with the necessary electrolytes. The methods of measuring the mean thickness are mainly divided into three groups: hold-up measurements, film conductance methods and weighing methods (Figure 1.7).

Hold-up methods were introduced in (Collier & Hewitt, 1961) and consist of measuring the mean thickness using a known volume of liquid that is isolated at an instant of time in the test section. The liquid inlet and outlet valves are synchronized so that it is possible to operate them at the same instant of time. The isolated liquid is then extracted and used to determine the average liquid thickness. These methods have many limitations and are not valid for any type of flow with droplet entrainment or detachment. Some examples of the use of this technique can be found in (Collier & Hewitt, 1961), (Ueda & Tanaka, 1974) or (Yih & Hsu, 1985).

Mean film conductance methods were quite widely used and consisted of calculating the current of an alternating current bridge between two electrodes placed at a certain distance from each other inside the pipe. Details of the measurement system can be found in (Collier & Hewitt, 1964).

Finally, the weighing method, as the name suggests, was carried out by collecting a measurement of the weight of the water in the test section during the experiment. It is very similar to the hold-up methods and is only valid for measurements in laminar regime. This method was applied among others by (Aragaki et al., 1987).

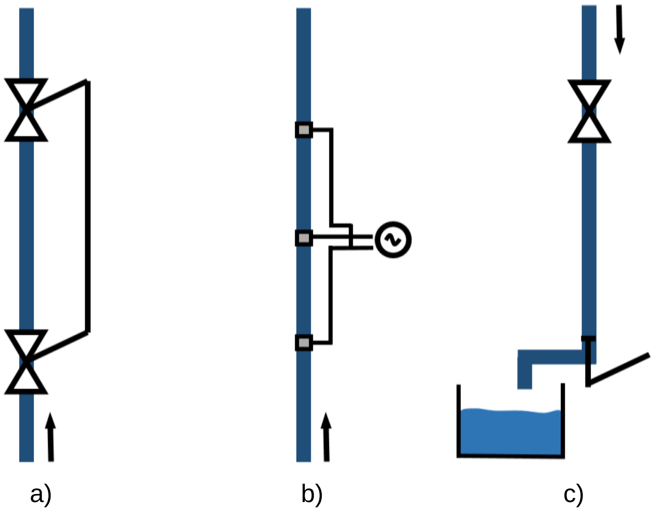

Source: Author's design

Figure 1.7. Time average thickness measurement methods, a) Hold-up methods, b) Mean film conductance methods and c) Weighing methods..

These techniques are now obsolete and have been progressively replaced by methods that allow much more information to be obtained from the liquid film.

1.3.2. LOCALIZED TIME EVOLUTION MEASUREMENT METHODS

This category includes techniques designed to observe how the thickness of the liquid film varies at a point. Although authors generally speak of point measurements, in reality it is a small region of the order of millimeters, so it would be more accurate to speak of localized measurements. If the area is small enough that there are no variations in film thickness, it is understood that the spatial resolution is good. This group includes: electrical methods, such as conductance and capacitance probes or parallel wires; radioactive methods, such as absorption or radioactive emission; acoustic methods, such as the ultrasonic pulse technique; and light methods, such as light absorption or laser scattering techniques.

ELECTRICAL METHODS

The most important group of localized measurement methods is the electrical techniques. These take advantage of the electrical properties of the water or liquid to calculate the film thickness and obtain information on its behavior. In general terms, we can differentiate between capacitance sensors and conductance sensors depending on the electrical property on which they are based.

Capacitance probes are one of the most popular options and are usually used when the fluid does not conduct electricity. This technique is based on the difference between the dielectric constant of the liquid and the gas, so the value obtained by placing two electrodes will be higher or lower depending on the thickness of the liquid film. There are already quotes from the 80's and 90's where this type of probes were already used for downward annular flow measurements in free fall (Ambrosini et al., 1998; Aragaki et al., 1987; Fujita et al., 1986; Heishichiro Takahama & Kato, 1980). More recently this technique has been replaced by other techniques although we still find applications such as (Strazza et al., 2011) which use these sensors to estimate the difference in electrical permittivity in a liquid-liquid system. In (Voulgaropoulos et al., 2021) they carry out an interesting work comparing film thickness measurements in vertical free-fall and cocurrent flow using optical methods and capacitance probes. The authors conclude that the measurements obtained by capacitance probes agree very well with those obtained by other methods. The maximum discrepancies are between 10 and 20% depending on the mean film thickness.

The twins of the capacitance probes are the conductance probes. Their use is even more widespread and their operation is very similar, although in this case they are based on the electrical conductance property of the liquid. As with capacitance probes, it is necessary to calibrate the devices according to the configuration of their electrodes to obtain the relationship between water conductivity and film thickness. The most typical format is to place the electrodes *flush-mounted* with the wall and there are many possible configurations in which they can be distributed (Figure 1.8). Note that the Figure probes are designed as connection ports between two pipes for liquid film measurements inside. In this way, the sensor would be fitted in the area of the test section where it is desired to measure and the electrode area would be flush with the inside diameter of the pipe (Figure 1.9).

There are multiple citations using each configuration, e.g., the work of (Cuadros et al., 2019; Rivera et al., 2019; H Takahama et al., 1983; Vijayan et al., 2002; Webb & Hewitt, 1975) explore 2- and 3-circular electrode conductance probes for upward, downward cocurrent and counter-current annular flow. The parallel strip configuration was rarely used because of its low spatial resolution. We highlight the work of (Chu & Dukler, 1974, 1975) where they measured the thickness for tubes of various diameters. On the other hand, concentric electrodes have the advantage of being very compact, which allows high spatial resolution to be obtained. For this reason, they are the electrodes of choice for more advanced spatial measurement methods (see section 1.3.3.). This technique has been employed by (Fukano, 1998) combined with the CECM (*Constant Electric Current Method*) technique, by (Zhao et al., 2013b) in vertical upward annular flow for diameters as small as $13\ mm$, or by (Almabrok et al., 2016) combining the results obtained with WMS (*Wire Mesh Sensor*) type sensors. Ring electrodes are very useful for providing consistent film averaging results, although at the cost of losing much of the interface information. This technique was used by (Asali et al., 1985; S Ghosh et al., 2013; Kulov et al., 1979) for multiple diameters and comparing the measurements with other methods. More recently (Setyawan et al., 2016) uses ring electrodes in conjunction with the CECM technique to calculate the liquid film in horizontal annular flow and combine the results with LED illuminated photographs.

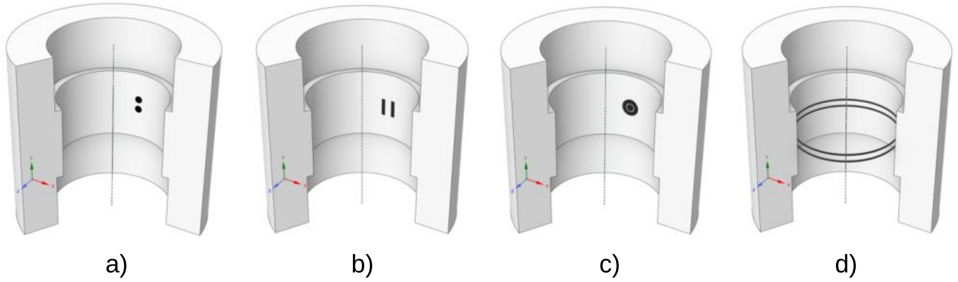
a) b) c) d)

Source: Author's design

Figure 1.8 . Different configurations of electrodes mounted flush to the wall; a) two circular electrodes, b) parallel strips, c) concentric electrodes and d) ring electrodes.

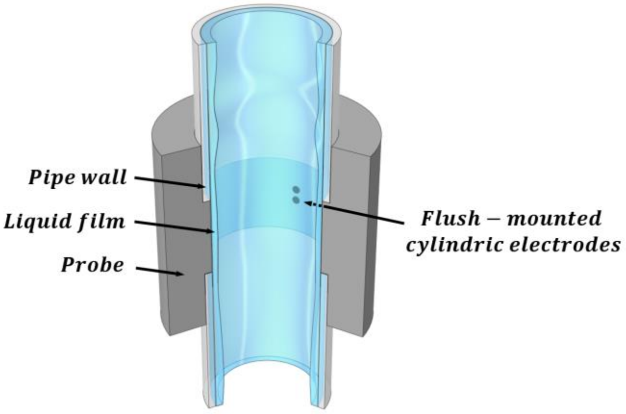

Source: Author's design

Figure 1.9 . sensor connection system in the test section.

Additionally, within the group of electrical methods, we find sensors with a different configuration than *flush-mounted* sensors, such as parallel *wire* probes. These specific conductance probes consist of two parallel and very thin wires (of the order of tenths of a millimeter or less) that are attached perpendicularly to the wall through which the liquid flows (see Figure 1.10a). The two wires are separated by a certain distance. This method is intrusive and the wires disrupt the passage of the film, however, being so thin they hardly disturb it.

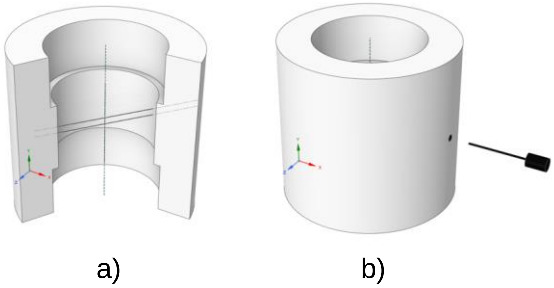

Source: Author's design

Figure 1.10 . Typical configuration: a) parallel wire electrodes and b) tip contact sensors.

The parallel wires method was widespread before the beginning of the 21st century in citations such as (Karapantsios & Karabelas, 1995; Koskie et al., 1989; Mudawar & Houpt, 1993b, 1993a; Nencini & Andreussi, 1982). More recently we find the work of (de Jong & Gabriel, 2003) which uses this type of sensors to measure upflow film thickness in microgravity. On the other hand, (S Ghosh et al., 2013) makes a comparison between parallel wire conductance probes and ring electrode conductance probes. It is also worth mentioning the interesting work of (Ju et al., 2018) who uses this type of sensors in an 8x8 *rod-bundle* and compares the measurements with *flush-mounted* conductance probes with two circular electrodes. In four of the rods they also use ring electrode probes and, in this way, they analyze the liquid film in upward annular flow obtaining the radial and axial distribution and the effect of the spacers. In (G. Wang et al., 2021) an investigation is carried out using parallel wire probes to measure film thickness and DW velocity. The velocity is measured by placing two consecutive probes a certain distance apart, so that by measuring simultaneously with both they can calculate the time it takes for a wave to travel from one probe to another. Their study aims to extend the field of knowledge to the specific regime of *wispy annular flow* (or annular flow "in hair") that occurs under certain conditions.

Finally, within the category of electrical film thickness measurement systems we can also include *needle contact probes*. This type of sensors is not able to measure exactly the film thickness and is only used in annular flow on the outside of the pipe. These sensors (see schematic in Figure 1.10b) use a movable tip which is placed at a known distance from the wall acting as an electrode. The second electrode is placed flush with the wall so that when the liquid film is large enough and touches the tip, the circuit is closed and a signal is sent to the data acquisition board. This particular operation makes them very useful devices for detecting pulses, waves and distance between wave peaks. Currently they are hardly used for annular flow measurements, although they are still employed for the calculation of the gap fraction in other types of two-phase flow regimes, such as bubble flow. Of particular note is the work of (Mascarenhas & Mudawar, 2013) where they measure the characteristics of the liquid film in an installation with downward annular flow water heating. For this purpose, they use a tip equipped with a total of 12 thermocouples in only $5\ mm$. By applying a constant current to the tip they calculate the thickness by means of the voltage drop that occurs. This voltage drop will in turn be a function of the percentage of tip immersed in liquid. This technique is known as *hot wire needle probe*. Additionally, they have another tip placed at a certain distance that allows them to obtain the speed of movement of the waves.

In addition to electrical methods, there are other methods that take advantage of other properties of the liquid such as the speed of sound in the liquid, energy absorption or refraction of light. Some of these techniques are briefly outlined below, although due to their complexity compared to other methods their use is more limited.

RADIOACTIVE METHODS

Among the radioactive methods, the most important are radioactive absorption and radioactive emission. These techniques are very expensive and represent a certain risk for this specific use. The absorption method consists of detecting the loss of radiation in the film by means of an emitter and a receiver. Different types of radiation have been analyzed, for example the *X-ray absorption* technique in an inclined plane, the operation scheme of which can be seen in the diagram below (Solesio, 1978) in the Figure 1.11. Previously, the *beta-ray attenuation* method had been explored (Cravarolo et al., 1961), and later on, *microwave techniques* were analyzed (El-Sayed et al., 1983; Roy et al., 1986). On the other hand, the radioactive emission technique consists of doping water with a radioactive substance and measuring it by using a detector. This method was employed by (Jackson, 1955) doping the water with Itrium-91. Currently, these methods have been replaced by simpler and more effective methods that do not require the use of radioactive substances.

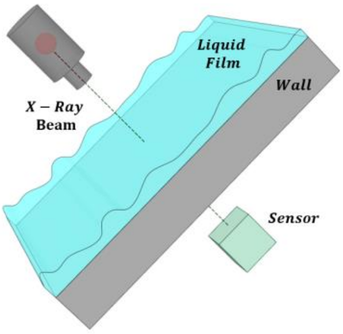

Source: Author's design, based on (Solesio, 1978)

Figure 1.11 . Schematic diagram of the operation of the radioactive X-ray absorption method.

ACOUSTIC METHODS

Within the non-electrical methods we find in second place the acoustic methods, whose use is much less dangerous. Their operation, like the previous group, also requires a transmitter and a receiver. The most common technique is the ultrasonic *pulse-echo method* where the emitter and receiver are located next to each other. The emitter sends out a pulse which, after a certain time, bounces off the liquid-gas interface and returns until it is picked up by the receiver (see Figure 1.12). It is necessary to discriminate noise and bounces originating from other parts of the system such as the liquid-wall interface. This technique is still in use today, finding both classical papers (Chun et al., 1984; Serizawa et al., 1994) as well as recent ones (Liang et al., 2021; M. Wang, Zheng, & Wu, 2019; M. Wang, Zheng, & Xu, 2019). It is worth mentioning the work of Liang et al., 2021 where they compare the measurements made by this technique in an experimental facility and the simulation results. Additionally, they propose a pattern identification method based on neural networks.

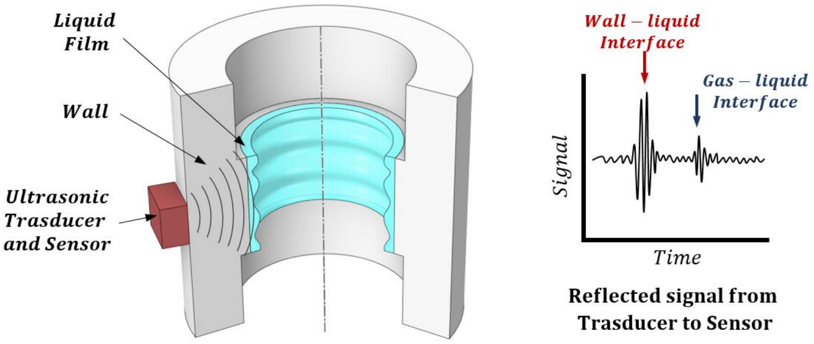

Source: Author's design

Figure 1.12 . Schematic of the operation of the ultrasonic pulse method.

LIGHTING METHODS

Finally, the methods of *light absorption* (Lilleleht & Hanratty, 1961), *light shading* (S. V. Alekseenko et al., 1985) and *fiber optics* (Yu & Tso, 1995) were used, although they have been discontinued for this application due to their complicated calibration and limited use. They are mainly based on the Lambert-Beer Law describing the intensity passing through the liquid film, i.e., the ratio of energy entering to energy leaving the film. The main problems stemmed from the refraction and scattering of light which introduced large errors and made measurements difficult. These methods evolved into the *laser scattering method*, where the relationship between the film thickness and the length of scattered light passing through the liquid is calculated (C. Li et al., 2021), thus reducing some of the drawbacks of the original techniques.

Another evolution of the absorption techniques was the *fluorescent* technique (Azzopardi, 1978; Schmitt et al., 1982). They consisted of doping the liquid with a fluorescent dye, such as the sodium salt of fluorescein or the different variants of Rhodamina. In this way it was possible to measure the intensity emitted by these particles, which depended on the thickness of the liquid film. Like all other light methods, they suffer from scattering and refraction problems that must be taken into account for the calculation of the thickness. Additionally, the properties of the dye can have an effect on the interface, for example by producing a variation of the surface tension, whose influence on the behavior of the interface is decisive.

Mention should also be made in this section of interferometric methods, which are based on the way in which the reflectivity of light changes with the angle of incidence at the interface (Coney et al., 1989; Karimi & Kawaji, 1998, 1996), although their use is also very limited at present.

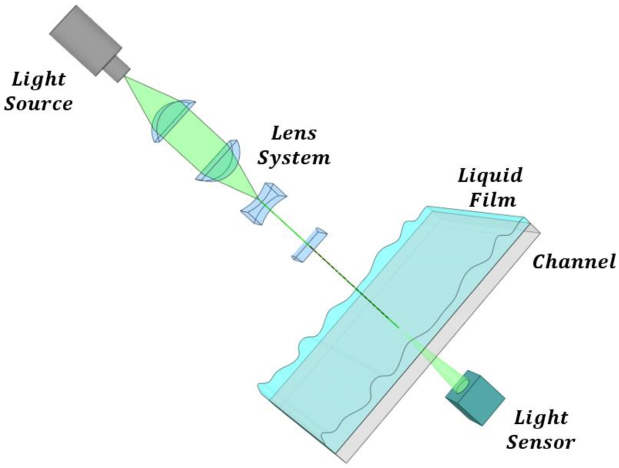

Source: Author's design

Figure 1.13. Schematic of the main components of the light absorption measurement system.

1.3.3. SPATIAL EVOLUTION FILM MEASUREMENT METHODS

Within the group of methods to measure the spatial evolution of the film are those techniques capable of obtaining information on the thickness of the film in a region of space. Some of them allow measuring the average thickness in a given time while others allow observing the behavior for a specific time instant and even its temporal evolution. In this section we will show the most important characteristics of electrical methods such as the *conductivity multiprobe* and image-assisted methods such as the *laser induced fluorescence* (LIF) technique.

ELECTRICAL METHODS

To observe the evolution of the liquid film in space, variants of the conductance probe and tip-contact sensor methods were developed. Although there are different configurations, the most important one is known as *multi-conductance probe*. This device consists of a set of small conductivity probes, usually arranged in the *flush-mounted* format of concentric electrodes. These electrodes are mounted on a flexible PCB (*printed circuit board*) capable of adopting the shape through which the liquid film slides. Each pair of electrodes is capable of providing a spatial resolution of measurement in the order of millimeters. To obtain a good measurement of the spatial evolution of the film, the number of measurement points must be very high and their spatial resolution as small as possible. For this purpose multiplexers are generally used which switch the signal to groups of electrodes multiple times per second thus reducing noise and the demands on the signal device.

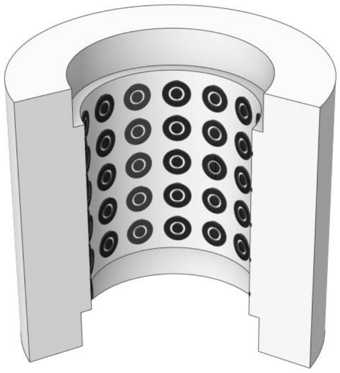

Source: Author's design

Figure 1.14. Schematic of the layout of a conductivity multiprobe.

Conductivity multiprobes have been studied in detail in recent years along with *wire mesh sensors*, whose principle of operation is identical, but they are responsible for obtaining information in a transverse plane of the pipe. At (Damsohn & Prasser, 2009) a high-speed sensor of this type is presented and its calibration is analyzed taking into account the possible configurations of the electrodes (shape, intrusion, spacing, etc.). In addition, the authors report that they are able to detect by algorithms the deposition patterns and the impact of droplets on the film.

At (Lee et al., 2016) the performance of a sensor printed on PCB using three electrodes per position is analyzed. By using one emitter electrode and two receiver electrodes, it is possible to calculate the liquid film as a function of the ratio of intensities between the emitter and each of the receivers.

More recently, (A. Liu et al., 2021) use a conductivity multiprobe to measure the liquid film in annular upward flow. The measurement device is equipped with a total of 160 measurement points and mounted on PCB. In this study the authors make an interesting comparison with all available empirical correlations of liquid film thickness, base thickness (not influenced by waves) and interfacial friction factor with very satisfactory results.

OPTICAL METHODS

The last group of methods to be discussed in this thesis is the optical methods. This category groups all those methods that use photon detection (generally by means of high-speed cameras) to obtain the thickness of the liquid film in annular flow. These methods emerged as an evolution of localized techniques and are currently highly developed. Optical methods are the most widely used at present due to their relative simplicity compared to other methods and the large amount of information provided by their measurements. The most important techniques to be discussed are *light absorption by photography*, *light intersection*, *laser-induced fluorescence* (LIF) and some variants of the latter such as *angle LIF* or *luminance-based LIF*. There are other less widespread techniques such as *pigment luminance method* (PLM) which are based on capturing the light scattered by TiO_2 particles in water (Hagiwara et al., 1984; Ohba et al., 1996). However, the limitations and errors of these methods, such as the assumption of uniformity in particle distribution or the intrusion of aerosols in the fluids, led to their discontinuation.

The method of *light absorption by photography* consists of calculating the amount of light from a light source that is absorbed by the liquid film (see schematic diagram of Figure 1.15). This is done by using, as mentioned before, the Lambert-Beer law, which relates these two variables. It is necessary to obtain the light attenuation coefficient of the corresponding liquid by calibration, as well as the reference intensity of the light source.

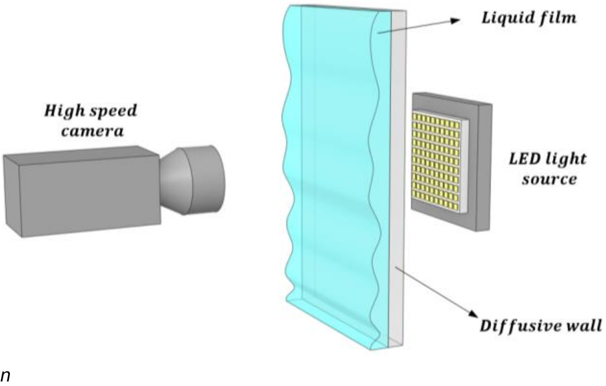

Source: Author's design

Figure 1.15 . Schematic of the main elements of the photo-assisted light absorption method.

The paper by (Schubring, Shedd, et al., 2010) describes the process of measuring film thickness using this technique. In addition, they introduce a variable, which they call *Score*, that allows them to establish correlations to predict the velocity or frequency of the waves. At (Mendez et al., 2017) an even more detailed explanation of the method is given, including the calibration of the devices. Once measurements are obtained, the authors propose a series of correlations to obtain the maximum height of the waves, speed, wavelength and even a classification of wave profiles.

On the other hand, the evolution of interferometric methods has given rise to methods of film spatial evolution by light intersection. The principle of operation is the same, but in this case a scanner is responsible for sending a laser beam to the film, which returns a portion as scattered light back to the film (Figure 1.16). The scanner measures the angle of reflection in a dot matrix and determines the film thickness by the difference between the measurements during operation and the calibration measurements (without liquid film). This technique is used to measure the liquid film in external flow as it is impossible to place the system inside a pipe.

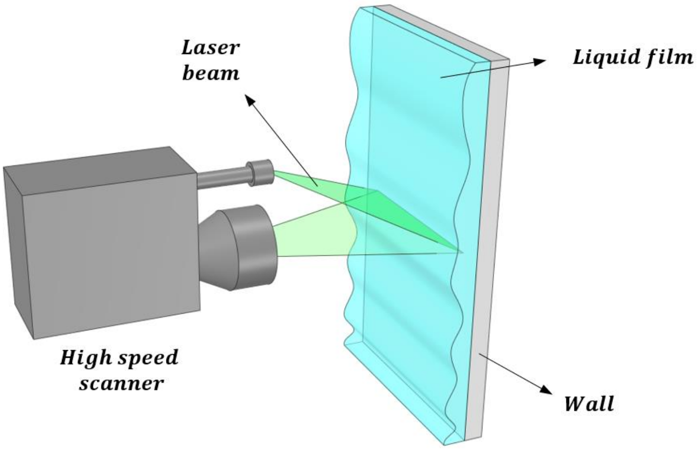

Source: Author's design

Figure 1.16 . Schematic of the main elements of the light intersection method.

An example of the use of this technology is shown in (Åkesjö et al., 2015) where the authors explain the operation of the scanner and how they perform liquid film thickness measurements. In this case they add a product to the liquid in order to analyze a larger number of regimes by increasing the viscosity and density. A series of studies by the same group continue the research and compare the experimental and (Åkesjö et al., 2017, 2018) and comparing experimental measurements and simulation results.

The next category of techniques is known as *Laser Induced Fluorescence* (LIF). This technique and its different variants are very widespread nowadays due to its ease of implementation and the large amount of information obtained from its measurements. To carry out the measurements it is necessary to dope the liquid with a fluorescent material, commonly Rhodamine B or 6G, which is illuminated by a laser plane in the measurement section. A high-speed camera is then used to take images of the liquid film, which will be visible by the fluorescence of the particles it contains. The key to this technique is the difference between the wavelength between the laser light ($532\ nm$) and the light emitted by the fluorescent particles ($610\ nm$). By using a filter in the high-speed camera it is possible to discard the laser light, thus obtaining very clean images of the liquid film. Generally, the fluorescent particles are excited by a laser plane (PLIF or *planar-laser induced fluorescence*) that has been previously filtered through a lens system. In a typical lens arrange, the first lens is responsible for limiting the height while the second must reduce the thickness of the beam to concentrate the energy in a very thin plane. In the Figure 1.17 diagram shows the main elements of the LIF measurement system. To avoid refraction of the light emitted by the film, the pipe wall must have the same refractive index as the liquid. In addition, it is usual to place a liquid box around the pipe which is filled with the same liquid that circulates inside to avoid refraction between the outer wall and the environment.

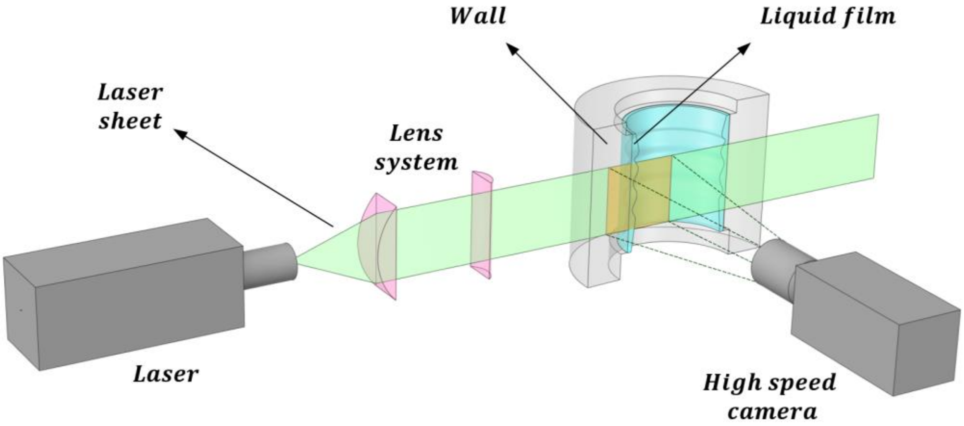

Source: Author's design

Figure 1.17 . Schematic of the main elements of the laser-induced fluorescence technique method.

LIF is a non-intrusive technique and allows obtaining measurements with very high spatial and temporal resolution, which makes possible to observe small and large interfacial waves. In addition, it allows to study the liquid phase that detaches from the interface, as well as the gas bubbles that travel with the liquid phase. This is why it has been used in many papers in the last decade. In (Schubring, Ashwood, et al., 2010) describes this system and shows details of the image processing necessary to accurately determine the interface as well as to detect gas bubbles in the film. At (Farias et al., 2012) they carry out PLIF measurements and develop a method to measure the cross section using a dual chamber system. The authors of the papers (I. Zadrazil et al., 2012; Ivan Zadrazil & Markides, 2014) perform an important work where they use the PLIF system to elaborate a map of annular flow regimes taking into account the characteristics of the interfacial waves. In addition, they include a multitude of measurements such as film thickness, roughness, frequency, wave height, bubble frequency, etc. Recently, a research has been published where PLIF measurements in a liquid-liquid regime such as water-oil are described (Ibarra et al., 2018, 2021). The authors perform the measurements using a double laser-camera system, in addition to measuring the velocity by PIV (*Particle Image Velocimetry*).

Like all the methods discussed above, LIF has also drawbacks. The main drawback that accompanies all optical methods is the error that occurs as a consequence of the refraction of light as it passes from one medium to another. The annular flow is characterized precisely by having two phases and being contained generally inside a curved pipe. The main errors that occur as a consequence of this phenomenon are described in (Alexandros Charogiannis et al., 2019) and are shown in Figure 1.18. The first error occurs when the liquid film is not fully coherent along its circumference. In this case, the light emitted by the interface particles could impact with another part of the interface resulting in a lower film thickness than the real one. The second error is due to the difference in the refractive index of the pipe material, which may result in displaced interface observations. This error usually results in an increase in film thickness that does not correspond to the actual film thickness.

To these errors must be added any other refraction of the light both from the laser light before exciting the liquid and from the photons emitted by the activated particles. Although the pipe is designed with a material with a refractive index similar to that of the liquid, it should be noted that the light must pass through a curved material which, however small the difference in index, can produce deviations in the beam.

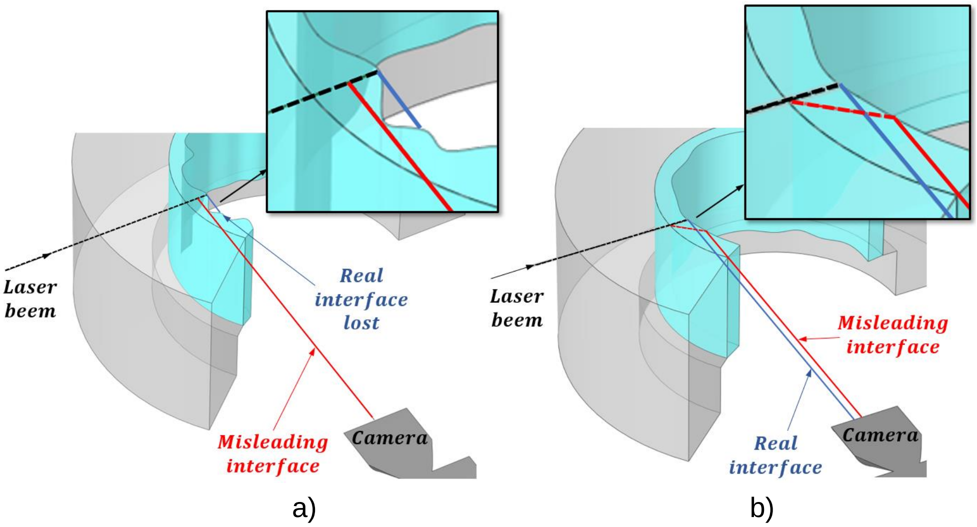

Source: Author's design

Figure 1.18 . Main errors in measurements using LIF, a) non-coherent interface error and b) wall-liquid refraction error.

To avoid making these mistakes, the LIF technique has undergone some variations in recent years giving rise to alternative approaches to it. The first one we observed is the *brightness-based laser induced fluorescence* (BBLIF) technique which is based on capturing the brightness of the fluorescent light emitted by the dye in the liquid. For this purpose, they use the equation (1.1), which is taken from (S. V. Alekseenko et al., 2012) where there is a relation between luminosity J with the local film thickness h.

$$J(x) = C(x) \cdot \left[1 - e^{-a \cdot h(x)}\right] \cdot \left[1 + K \cdot e^{-a \cdot h(x)}\right] + D(x) \tag{1.1}$$

The remaining variables must be calculated in calibration tests, a is the fluorescence light absorption coefficient, K is the interfacial refractive index (between the ring flux phases), $C(x)$ is the compensation matrix, which corrects for possible uniformities in the excitation light, and $D(x)$ is the dark level of the chamber. This technique has been applied by some authors with very good results such as (S. V. Alekseenko et al., 2012). The results of the study of the coherence of the *disturbance waves* in the interior of a pipe are confirmed by this technique (Isaenkov et al., 2017). The differences in film thickness for circular ducts and rectangular ducts are studied by this technique. A comparison between the differences in film thickness for circular and rectangular ducts is made at (Vasques et al., 2018). They also show a comparison between the differences in the behavior of the film depending on the direction of the annular flow (ascending and descending) finding differences between the base thickness and the *disturbance waves* between $10 - 30\%$ higher for the ascending flow. In (Cherdantsev et al., 2019) the results of the comparison between measurements using PLIF and BBLIF in cocurrent downward annular flow are published. Based on the measurements, the authors concluded that BBLIF was a very good technique for measuring film thickness in flat regions but that its sensitivity was reduced for thicker regions. In addition, it had some vulnerability to light reflections in complex or agitated flows. (Fan et al., 2020) studied the film thickness in downward annular flow using BBLIF and by CFD simulation, obtaining very promising results in the simulations. Finally, it is worth mentioning the work of (An et al., 2020) who implemented a device to move the BBLIF measurement system in height along the pipe and thus physically move the region *of interest* or *region of interest* (ROI). Among their results, they show that the DW velocity increases with distance, in addition to the liquid and gas velocities.

Finally, another novel technique currently being studied is *structural planar-laser induced fluorescence* (S-PLIF). This technique consists of using a structured light plane, usually by means of a *Ronchi ruling plate,* which is nothing more than a constant interval spacing optical device developed with high precision, definition and contrast. The Ronchi ruling plate is placed between the uniform laser light plane and the pipe so that the light arrives in parallel and alternating bright and dark streaks. By analyzing the gradient of these lines in the liquid film it is possible to determine the true gas-liquid interface (see Figure 1.19).

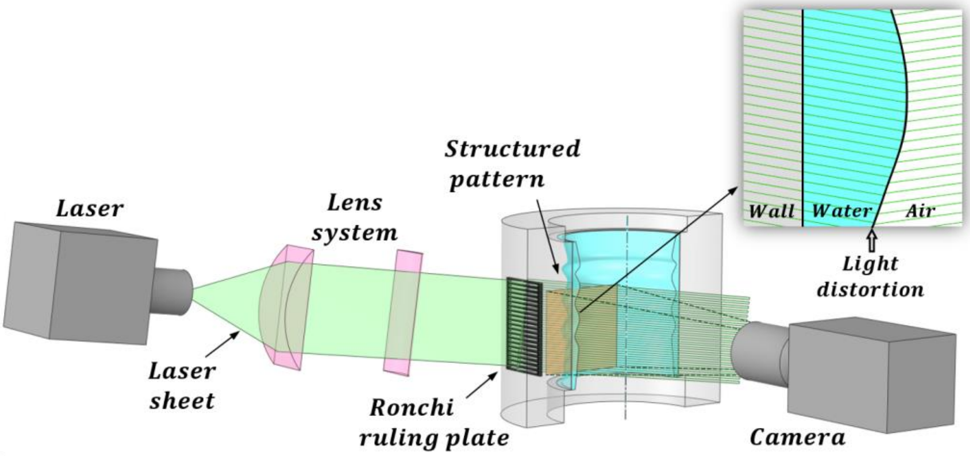

Source: Author's design

Figure 1.19 . Advanced S-PLIF technique incorporating a structured light pattern.

This technique was first introduced at the *13th International Conference on Heat Transfer, Fluid Mechanics and Thermodynamics* (A. Charogiannis et al., 2017). A more complete development of this technique can be found in the paper (Alexandros Charogiannis et al., 2019) where the authors show the main errors of the different techniques and how the S-PLIF and the angle of inclination of the measurements help to reduce them. As already discussed in the section on electrical methods and capacitance probes, in (Voulgaropoulos et al., 2021) a comparison is made between experimental measurements of film thickness in annular downward flow between the S-PLIF technique and the capacitance probe. The results obtained are very similar in both cases, with slight differences of no more than 20% in film thickness.

1.4. EXPERIMENTAL FACILITIES

This section lists the most important characteristics of the experimental facilities that have been designed over the last few years for annular flow film thickness measurement. In the Table 1.1 references of some of the most relevant facilities of the 21st century are included. Additionally, it shows information about the annular flow regime, the range of experimental measurements and the measurement system used.

Table 1.1 . Summary table of the most important experimental facilities since 2000 indicating the type of two-phase flow regime, the range of input parameters and the measurement system.

Reference	Type of regime	Range	System of measure
(Wolf et al., 2001)	Cocurrent upward	D = 31.8mm Re_L 300 - 3800 Re_g 125k - 275k	Concentric conductance probe
(Ambrosini et al., 2002).	Flat free fall inclined and vertical	W = 600mm Re_L 600 - 6000 Inclination 0º - 45º. Temp. 25ºC, 50ºC, 75ºC	Capacitance probe
(S. V. Alekseenko et al., 2008)., (S. V. Alekseenko et al., 2012).	Cocurrent downward	D = 15 mm Re_L 560-1400 Re_g 22000 - 58000	PLIF and BBLIF
(Damsohn & Prasser, 2009)	Cocurrent horizontal	W = 50mm Re_L 57 - 230 Re_g 31250 - 62500	Conductance multi-probe
(Sawant et al., 2009)	Cocurrent upward	D = 9.4mm P 1.2 - 6 bar Re_L 786 - 3929 Re_g 3525 - 14100	Extraction and weighing
(Gross et al., 2009)	Downward counter-current	D = 28.2 mm Re_L 40 - 360	Light absorption
(Schubring, Ashwood, et al., 2010).	Cocurrent upward	D = 23.4 mm Re_L 1467 - 7335 Re_g 51188 - 119925	PLIF
(Strazza et al., 2011).	Water-oil cocurrent horizontal	D = 21 mm Inclination (-10º) - (+15º) Re_{agua} 9875 - 44765 Reaceite 45 - 980	Capacitance probe
(Camassa et al., 2012).	Air-oil cocurrent	D = 10 mm Re-oil 0.010 - 0.024	Video camera recording

	upward	Re_g 2626 - 9310	
(Farias et al., 2012)	Cocurrent horizontal	D = 15 mm Re_L 878-1755 Re_g 18750 - 31875	PLIF
(Mascarenhas & Mudawar, 2013)	Free fall external vertical	D = 25.4 mm Re_L 5700 and 10800	Needle contact probe
(Zhao et al., 2013a)	Cocurrent upward	D = 34.5 mm Re_L 844-2412 Re_g 43540 - 93300	Concentric conductance probe
(I. Zadrazil et al., 2014).	Cocurrent downward	D = 32.4 mm Re_L 1224-6128 Re_g 0 - 84600	PLIF
(Pan et al., 2015)	Cocurrent upward	D = 25.4 mm Re_L 798 - 5308 Re_g 16796 - 47657	Video camera recording
(Pham et al., 2015)	3x3 rod-bundle cocurrent upward	D = 12mm Re_L 251 - 401 Re_g 17025 - 46650	Video camera recording
(Musa Aliyu, 2015), (Almabrok et al., 2016)	Free fall and cocurrent downward	D = 101.6 mm Free fall: Re_L 4000 - 20200 Cocurrent: Re_L 5277 - 105538 Re_g 9469 - 188113	Concentric conductance probe and capacitance WMS
(Åkesjö et al., 2015), (Åkesjö et al., 2017), (Åkesjö et al., 2018)	Free fall external vertical	D = 60 mm Re_L 3200 - 11600	Video camera recording by light intersection
(Lee et al., 2016)	Free fall vertical plane	W = 400mm Re in nozzle: Re_L 10533 - 19091	Conductivity multi-probe
(G. Wang et al., 2017)	Cocurrent downward	D = 25.4 mm Re_L 29195 Re_g 12000 - 18000	Conductivity probe
(Qiao et al., 2017)	Cocurrent downward	D = 50.8 mm Re_L 10600 - 106000 Re_g 32 - 6350	Concentric conductance probe and video camera recording
(Van Nimwegen et al., 2017)	Cocurrent upward	D = 34, 50 and 80 mm Re_L 11 - 19641 Re_g 0 - 156528	Video camera recording
(A. Charogiannis et al., 2017)	Free fall vertical	D = 32.4 mm Re_L 588 - 5700	S-PLIF
(Isaenkov et al., 2017)	Cocurrent downward in piping and plan	D = 11.7 mm W = 50 mm Re_L 560 - 1600 Re_g 16088 - 41681	BBLIF
(Guzanov et al., 2017)	Free fall vertical plane	W = 50 mm Re_L 23 - 91	Video camera recording by light intersection
(Mendez et al., 2017)	Free fall vertical plane	W = 100 mm Re_L 1 - 6 Ka = 3.7	Video camera recording by light absorption
(Ibarra et al., 2018), (Ibarra et al., 2021)	Water-oil cocurrent horizontal	D = 32 mm Re_{agua} 5820 - 11650 Re_{aceite} 1850 - 3350	PLIF-PIV
(Vasques et al., 2018), (Fan et al., 2020)	Cocurrent ascending and downward	D = 11.7 mm Re_L 560 - 1600 Re_g 16088 - 41681	BBLIF

(Xue & Zhang, 2018)	Free fall vertical	D = 25 mm Re_L 2500 - 9600	PLIF
(C. Wang et al., 2018)	Cocurrent horizontal	D = 50 mm Re_L 1045 - 3135 Re_g 96875 - 187500	Conductance probe parallel wires
(Cherdantsev et al., 2019), (Alexandros Charogiannis et al., 2019), (Cherdantsev et al., 2019)	Cocurrent downward	D = 32.4 mm Re_L 560 - 5320 Re_g 0 - 85100	PLIF, BBLIF and S-PLIF
(M. Wang, Zheng, & Xu, 2019), (M. Wang, Zheng, & Wu, 2019)	Cocurrent horizontal	D = 50 mm Re_L 313 - 5225 Re_g 31250 - 93750	Ultrasonic pulses
(Cuadros et al., 2019)	Cocurrent upward	D = 44 mm Re_L 2023 - 5057 Re_g 60225 - 105600	Conductance probe circular electrodes flush to the wall
(Czernek & Witczak, 2020)	Cocurrent downward	D = 12.5, 16, 22 and 54 mm Re_{aceite} 0 - 154 Re_{aire} 0 - 100000	Light absorption
(An et al., 2020)	Cocurrent downward	D = 32.4 mm Re_L 1104 - 5284 Re_g 39500 - 79000	BBLIF with test section movement
(Liang et al., 2021).	Cocurrent horizontal	D = 30 mm Re_L 627 - 7837 Re_g 1125 - 56250	Ultrasonic pulses
(Rivera, Muñoz-Cobo, Cuadros, et al., 2021).	Cocurrent upward	D = 44 mm Re_L 2023 - 5057 Re_g 60225 - 105600 $\sigma = 45 \cdot 10^{-3} - 72 \cdot 10^{-3}$ N/m	Conductance probe circular electrodes flush to the wall
(G. Wang et al., 2021).	Cocurrent upward	D = 25.4 mm Re_L 1700 - 60000 Re_g 15000 - 50000	Conductance probe parallel wires
(L. song Wang et al., 2022)	Cocurrent upward	D = 50 mm Re_L 731 - 3710 Re_g 26531 - 70750	Video camera recording

Important information:

Reynolds numbers have been extracted from the corresponding articles or calculated using data from the articles by means of one of the following formulas: $Re = {}^{j \cdot D}/_{\nu}$ (if the surface velocity is known j) o $Re = {}^{4 \cdot Q}/_{\pi \cdot D \cdot \nu}$ (if the flow rate is Q is given).

In some cases it has been necessary to make the conversion between film Reynolds and surface Reynolds of the liquid by means of the following relation $Re_{superficial} = 4 \cdot Re_{film}$(eq. (1.8)).

In case the viscosity of the fluids is not indicated in the paper, the following kinematic viscosity values have been used: $\nu_{agua} = 9.57 \cdot 10^{-7}\, m^2/s$, $\nu_{aire} = 1.6 \cdot 10^{-5}\, m^2/s$ y $\nu_{aceite} = 8.9 \cdot 10^{-5}\, m^2/s$.

Depending on the type of two-phase flow regime under study, the different facilities vary slightly from each other, but all of them maintain a similar structure. They generally consist of three main parts which are the liquid circuit, the gas circuit and the test section. For free-fall analysis systems, the gas circuit is normally omitted since this fluid acts simply by being stagnant in the test section. In the case of facilities for liquid-liquid measurements, the gas circuit is replaced by a supply line of the other liquid to be studied. The components of both circuits for the liquid-gas regime are explained below.

The main liquid circuit is usually structured as a *loop* or closed circuit. The liquid that is introduced into the circuit is pre-treated to avoid problems in the facility and is usually accumulated in a tank to ensure a constant supply during operation. The liquid line has different devices to carry out control and supervision. The minimum essential devices seen in all installations are the pump, flow meter, control valves and thermocouple or resistance thermometer. Additionally, it is common to find a by-pass system, particle filters and even temperature control units to ensure that this parameter does not alter the results. The latter device is especially useful when the measurement system is based on electrical methods as they are very sensitive to temperature changes.

The gas circuit consists of elements very similar to the liquid circuit, replacing the pump with a compressor. The system usually consists of an open circuit when dealing with air, reserving the closed circuit for more expensive or harmful substances. Both the gas and liquid lines are connected to the test section by means of some kind of injection system that adapts the fluid inlet in the most appropriate way for the type of regime to be studied. In air-water annular regime measurement facilities it is convenient to use injectors that implement a sintered porous pipe. These devices have a stainless steel tube with micropores of known size. By applying a pressure difference it is possible to pass the water through the porous pipe and into the test section in the form of a film on the wall (see Figure 1.20). This facilitates the positioning of the liquid on the wall in a state close to the one it will eventually adopt when fully developed.

Finally, the test section must be designed in such a way as to allow the correct development of the flow introduced. In other words, it is necessary to dimension our test section with a sufficient length so that in the measurement zone the flow is fully developed. It is considered fully developed when the average properties of the flow do not vary with time. While the instantaneous behavior in this zone will vary constantly, the average of the most important flow characteristics will not. For example, the film thickness is influenced by interface disturbance waves, but the mean film thickness over a significant time will remain constant.

The problem is that it is not simple to determine at what distance from the inlet the flow is considered fully developed. In fact, this distance has been the subject of study by different researchers offering very interesting information for the optimal design of experimental facilities. (Heishichiro Takahama & Kato, 1980) carried out this study determining that the mean film thickness of the downward annular flow is found to be developed after a length equivalent to 32 diameters in the liquid Reynolds number range from 1600 to 4000. The previous study of (Webb & Hewitt, 1975) claimed that at least a distance equivalent to 160 and 470 diameters were necessary to fully develop the wave thickness and its frequency respectively. However, it was indicated that from 150 diameters onwards the differences were between 1 and 10% depending on the gas flow rates. In one of the studies carried out by the author of the thesis (Rivera et al., 2020) the evolution of the average film thickness and the height of the *disturbance waves along* a pipeline was analyzed, obtaining a development distance of 83 diameters.

The materials and final format of the test section will depend on the measurement system selected. For example, to measure air-water annular flow using a PLIF system it is necessary to have a pipe of a material whose refractive index is as close as possible to that of water (I. Zadrazil et al., 2014). The pipe material is not as demanding if an electrical measuring port is to be used (Cuadros et al., 2019).

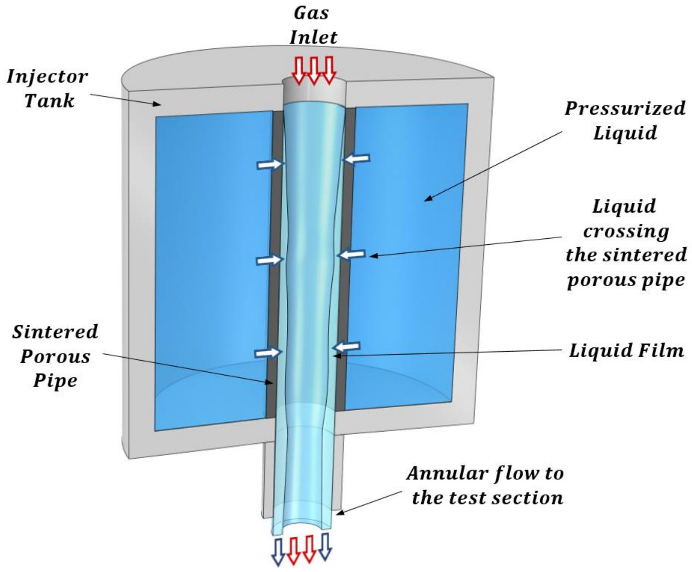

Source: Author's design

Figure 1.20 . Operation of the injector for cocurrent downward annular flow generation by means of a sintered porous pipe.

The characteristics and dimensioning of the facility determine the range of the input parameters. It should be taken into account that the final measurements will be valid only within the established range, being very limited the possibilities to extrapolate the data outside it. However, as installations can be of very different sizes, it is necessary to establish the input variables in a way that is comparable between them. Fluid flow rate does not represent an ideal format as it will be very different between a small facility and a larger one. Generally the fluid surface velocity or Reynolds number is used. In two-phase flow regimes, the surface velocity, or j is defined as the velocity value at which the fluid would move if it were to occupy the entire cross-section of the pipe. In other words, the surface velocity results from the division between the fluid flow rate and the pipe diameter (or hydraulic diameter for other sections). Using the surface velocity value, it is also easy to obtain the surface Reynolds number ($Re_{superficial}$) following the relation of equation (1.2) between the surface velocity j, the diameter or hydraulic diameter D and the kinematic viscosity ν.

$$Re_{superficial} = \frac{j \cdot D}{\nu} \tag{1.2}$$

Knowing the relationship between liquid flow rate and surface velocity Q and the surface velocity j, the surface Reynolds number can also be calculated as indicated in equation (1.3).

$$Re_{superficial} = \frac{4 \cdot Q}{\pi \cdot D \cdot \nu} \tag{1.3}$$

Although using this relation to compare between installations seems reasonable, both the velocity and the Reynolds number obtained are not real. This is precisely because the liquid or gas does not occupy the entire section. Although for gas the value is usually quite close to the real value (in annular flow the void fractions are very large), in the case of liquid it makes no physical sense. To address this problem, many authors choose to use the film Reynolds number, which uses the film velocity instead of the surface velocity u_{film} instead of the surface velocity and the film thickness h_m as the characteristic length (Equation (1.4)).

$$Re_{film} = \frac{u_{film} \cdot h_m}{\nu} \tag{1.4}$$

Since a priori we know neither the value of the film velocity nor its thickness, we use the relationship between the inlet flow rate and the film velocity, eq. (1.5), assuming that the liquid moves through a circular crown of thickness h_m.

$$\begin{aligned} \boldsymbol{u_{film}} &= \frac{Q}{A_{corona}} = \frac{Q}{\pi \cdot \left(\left(\frac{D}{2}\right)^2 - \left(\frac{D}{2} - h_m\right)^2\right)} \\ &= \frac{Q}{\pi \cdot \left(\left(\frac{D}{2}\right)^2 - \left(\left(\frac{D}{2}\right)^2 + {h_m}^2 - 2\frac{D}{2}h_m\right)\right)} \\ &= \frac{Q}{\pi \cdot \left(\frac{D^2}{2} - \frac{D^2}{2} - {h_m}^2 + Dh_m\right)} = \frac{\boldsymbol{Q}}{\boldsymbol{\pi \cdot \left(Dh_m - {h_m}^2\right)}} \end{aligned} \tag{1.5}$$

We can see that the area of the film corresponds to $\pi \cdot \left(Dh_m - {h_m}^2\right)$. However, a simplification can be applied to this expression, which consists in assuming that $h_m \ll D$. This is valid for annular flow since we know that the average film thickness is about two orders of magnitude below the pipe diameter. Under this assumption we can consider that in the subtraction inside the parenthesis $Dh_m \gg {h_m}^2$. Therefore, the film area can be written simply as shown in Eq. (1.6).

$$A_{corona} = \pi \cdot \left(Dh_m - {h_m}^2\right) \xrightarrow{h_m \ll D} A_{corona} = \pi D h_m \tag{1.6}$$

Finally, if we substitute the film velocity u_{film} we have calculated in equation (1.4) we obtain Eq. (1.7) of the film Reynolds number.

$$\boldsymbol{Re_{film}} = \frac{u_{film} \cdot h_m}{\nu} = \frac{\frac{Q}{\pi D h_m} \cdot h_m}{\nu} = \frac{\boldsymbol{Q}}{\boldsymbol{\pi \cdot D \cdot \nu}} \tag{1.7}$$

Using this expression it is possible to calculate the film Reynolds using design variables. In fact, the film Reynolds and the surface Reynolds are obtained from very similar expressions which, by comparing them, can quickly deduce the expression (1.8).

$$Re_{superficial} = 4 \cdot Re_{film} \tag{1.8}$$

Taking into account the simplification previously justified, the surface Reynolds number is four times the film Reynolds number. Although there is no universal consensus on the use of one or the other Reynolds number, the relationship is very simple so going from one to the other is very fast.

As far as this doctoral thesis is concerned, all Reynolds numbers used correspond to the surface Reynolds number unless specifically stated. In addition, in order to avoid the use of unnecessary subscripts, the following will be used directly Re as indicated by the expression (1.9).

$$Re = Re_{superficial} \tag{1.9}$$

Returning to the description of the test section, another aspect that requires a detailed explanation is the length of the pipe. Generally, when studying a given flow, one first wants to show how it behaves under steady-state conditions. On the one hand, stationary conditions refer to the constancy of the parameters that influence the behavior so that, when these variables are known, it is possible to determine how the flow moves. On the other hand, the conditions must be developed, i.e., the flow must be moving long enough to have completed the formation of all the characteristic structures of the flow. In the case of annular flow, after introducing the liquid and gas into the pipe it is necessary for the velocity profiles of both to develop and for the formation of interfacial waves, among other things, to be completed. Therefore, the length of the pipe plays an important role and should be considered before conducting experiments. However, there is no universal law that allows us to know what exactly this distance is since it is dependent on multiple factors such as geometry or inlet conditions. Usually, the length of the pipe is indicated by its relation to the equivalent number of diameters. For example, if a 50 mm diameter pipe measures 50 diameters (50D), its length will be $L_{50mm} = 50 \cdot 0.05\ [m] = 2.5\ [m]$, i.e. 50 multiplied by the diameter of the pipe. In this way, it is possible to establish criteria for different geometry of the installation. If you want to design a 12 mm diameter installation to compare with the previous one, the equivalent length following this criterion would be $L_{12mm} = 50 \cdot 0.015\ [m] = 0.75\ [m]$. This criterion is the most widespread among annular flow researchers to establish comparisons between facilities of different diameters.

Regarding the most important flow variables, the mean film thickness is the first to develop. This means that it is the one that needs the least equivalent diameters of length for stability to be observed in its value. In the investigation of (Heishichiro Takahama & Kato, 1980) it is concluded that for low liquid flow rates (liquid Reynolds numbers less than 400) at least 32D are necessary for the average film thickness to be developed. On the other hand, for higher flow rates stability is reached earlier with at least 12D. At (Karapantsios & Karabelas, 1995) it is indicated that this distance may not be sufficient. These researchers observed that while the mean thickness remained constant in many cases, a decrease in minimum film thickness and an increase in wave height could be distinguished. Although it will be discussed in greater detail in the following chapters, in (Rivera et al., 2020) it was observed that in free-falling annular flow 83D were necessary to observe a consistent degree of development in the mean film thickness.

If we consider the disturbance wave type interfacial wave variables, the distance necessary for the values to be developed and constant is greater. In (Webb & Hewitt, 1975) it is indicated that 160D and 470D are necessary for the wave height and frequency respectively. However, in practice, from 150D onwards, they reported small variations of the values with respect to greater distances. At (Rivera et al., 2020) it was observed that for 83D the wave height was very close to that obtained with a sensor at 117D, the error of the measurements being almost equivalent to the separation between the two.

1.5. CFD SIMULATIONS

Computational Fluid Dynamics (CFD) codes are tools that allow numerical analysis to be performed to solve fluid mechanics problems. These codes are implemented in computers because they are capable of carrying out the large amount of calculations necessary to simulate the motion of fluids, as well as associated processes such as mass and energy transfer. The advance of technologies in the last decades has favored the development of CFD codes allowing to solve more and more complex problems.

To study the behavior of fluids, it is necessary to solve the governing equations by using mathematical techniques and algorithms. The phenomena associated with fluid motion are governed by nonlinear partial differential equations. For most of the problems to be solved by CFD, their analytical solution is impossible to solve. That is why numerical solutions are used by means of discretization methods that approximate the differential equations using a system of algebraic equations. These equations can be solved by computer using iterative calculations.

CFD codes must be validated using experiments or real values of the problems to be solved. In this way, we ensure that the result obtained from the simulations is very close to the real one and always within the uncertainty band derived from the uncertain variables that influence the process. When a CFD code is validated for a certain application it is possible to carry out similar simulations without additional experiments. The information offered by CFD codes is currently very complete with access to all kinds of direct and indirect variables. Compared to performing experiments, simulations are much more economical and generally less energy consuming.

1.5.1. NAVIER-STOKES FUNDAMENTAL EQUATIONS

The fundamental equations governing the motion of single-phase incompressible fluids are the Navier-Stokes equations. These can be written in different ways, although all of them are equivalent and come from Newton's second law. The following equations development has been done as simple a as possible to understand the origin of these equations.

Since we are dealing with fluids, the equations must be described by fluid volumes instead of particles. Starting from Newton's equation, but describing it as volumes we would obtain:

$$m\bar{a} = \sum \bar{f} \;\rightarrow\; \rho\bar{a} = \sum \frac{\bar{f}}{V} \;\rightarrow\; \rho\frac{d\bar{u}}{dt} = \sum \bar{F} \tag{1.10}$$

It should be noted that $\bar{u}$ is a vector field that depends on (x, y, z, t). Therefore, the derivative of the velocity with respect to time could be expressed by partial derivatives as follows:

$$\begin{aligned}\frac{d\bar{u}}{dt} &= \frac{\partial\bar{u}}{\partial t}\frac{dt}{dt} + \frac{\partial\bar{u}}{\partial x}\frac{dx}{dt} + \frac{\partial\bar{u}}{\partial y}\frac{dy}{dt} + \frac{\partial\bar{u}}{\partial z}\frac{dz}{dt} = \frac{\partial\bar{u}}{\partial t} + \frac{\partial\bar{u}}{\partial x}u_x + \frac{\partial\bar{u}}{\partial y}u_y + \frac{\partial\bar{u}}{\partial z}u_z \\ &= \frac{\partial\bar{u}}{\partial t} + \bar{u}\cdot(\nabla\bar{u})\end{aligned} \tag{1.11}$$

So far, our momentum equation would look as follows:

$$\frac{\partial\bar{u}}{\partial t} + \bar{u}\cdot(\nabla\bar{u}) = \sum \bar{F} \tag{1.12}$$

The right hand side of the equation corresponds to the forces acting on the fluid. This summation must include all the representative forces which, in this case, are the pressure force, the gravity force and the viscosity force. The pressure forces are due to changes in the pressure and are therefore represented by the pressure gradient $-\nabla P$. The force of gravity in volumetric terms corresponds to $\rho\bar{g}$. Viscous forces arise due to the resistance to deformation that each fluid possesses. Although the reasoning behind this formula is more complex, this force can be calculated by means of $\mu\nabla^2\bar{u}$ for a Newtonian fluid (constant viscosity).

A simplified way of writing it by substituting all the terms and dividing by the density would be the following equation (1.13):

$$\frac{\partial\bar{u}}{\partial t} + \bar{u}\cdot(\nabla\bar{u}) = -\frac{1}{\rho}\nabla P + \nu\nabla^2\bar{u} + \bar{g} \pm \bar{F} \tag{1.13}$$

The variables present in this equation are:

- $\bar{u}$ represents a vector so it has components in x, y, z. In other words, the components of the $\bar{u}$ are (u_x, u_y, u_z).
- The operator · we see in $\bar{u}\cdot(\nabla\bar{u})$ divides the simplified equation into three equations, one for the velocity component.
- ρ is the density of the incompressible fluid
- P is a pressure scalar, not a vector. However, the operator ∇ represents the spatial partial derivatives in x, y, z. Although the pressure is a scalar, the pressure gradient term is a vector.

$$\nabla = \left[\frac{\partial}{\partial x}, \frac{\partial}{\partial y}, \frac{\partial}{\partial z}\right] \tag{1.14}$$

- ν is the viscosity or resistance to movement.
- g is the acceleration of gravity. It is a vector that always points in one direction.
- F corresponds to external forces affecting the fluid.

If we look at the equation we can identify different terms. First, the terms to the left of the equal are those related to acceleration. On the contrary, those on the right are associated with the forces or stresses. The individual terms are:

- $\frac{\partial\bar{u}}{\partial t}$ is the time term of the velocity.
- $\bar{u}\cdot(\nabla\bar{u})$ is the *convective term* (also called *advective*) of the velocity.
- ∇P is the pressure gradient term.
- $\nu\nabla^2\bar{u}$ is the viscous term.
- $\bar{g}$ is the gravity term.
- $\bar{F}$ is the term for external forces.

If we expand the equation (ignoring the external forces term) in each of the components we would obtain:

$$\frac{\partial u_x}{\partial t} + \left(u_x\frac{\partial u_x}{\partial x} + u_y\frac{\partial u_x}{\partial y} + u_z\frac{\partial u_x}{\partial z}\right) = -\frac{1}{\rho}\frac{\partial P}{\partial x} + \nu\left(\frac{\partial^2 u_x}{\partial x^2} + \frac{\partial^2 u_x}{\partial y^2} + \frac{\partial^2 u_x}{\partial z^2}\right) + g_x \tag{1.15}$$

$$\frac{\partial u_y}{\partial t}+\left(u_x\frac{\partial u_y}{\partial x}+u_y\frac{\partial u_y}{\partial y}+u_z\frac{\partial u_y}{\partial z}\right)=-\frac{1}{\rho}\frac{\partial P}{\partial y}+\nu\left(\frac{\partial^2 u_y}{\partial x^2}+\frac{\partial^2 u_y}{\partial y^2}+\frac{\partial^2 u_y}{\partial z^2}\right)+g_y$$

$$\frac{\partial u_z}{\partial t}+\left(u_x\frac{\partial u_z}{\partial x}+u_y\frac{\partial u_z}{\partial y}+u_z\frac{\partial u_z}{\partial z}\right)=-\frac{1}{\rho}\frac{\partial P}{\partial z}+\nu\left(\frac{\partial^2 u_z}{\partial x^2}+\frac{\partial^2 u_z}{\partial y^2}+\frac{\partial^2 u_z}{\partial z^2}\right)+g_z$$

In addition to the partial differential equations of momentum, we know that the law of conservation of mass must be satisfied so that, for incompressible fluids, we can add the equation (1.16). In other words, for incompressible fluids the fluid entering a volume must be equal to the fluid leaving.

$$\boxed{\frac{\partial \rho}{\partial t}+\frac{\partial \rho u_x}{\partial x}+\frac{\partial \rho u_y}{\partial y}+\frac{\partial \rho u_z}{\partial z}=\frac{\partial \rho}{\partial t}+\nabla\bar{u}=0} \tag{1.16}$$

For incompressible fluids, the viscous stress tensor τ can be defined as follows. This conversion is usually performed to simplify the equation.

$$\tau=\mu\,\nabla^2\bar{u} \tag{1.17}$$

If we further multiply by the density, the Navier-Stokes momentum equation would look like this:

$$\boxed{\frac{\partial \rho\bar{u}}{\partial t}+\rho\bar{u}\cdot(\nabla\bar{u})=-\nabla P+\nabla\tau+\rho\bar{g}\pm\bar{F}} \tag{1.18}$$

For the energy equation, it is convenient to start with the standard form of the scalar transport equation for the internal energy, eq. (1.19).

$$\frac{\partial(\rho e)}{\partial t}+\nabla\cdot(\rho e\bar{u})=-\nabla\cdot q+S_e \tag{1.19}$$

If we look to the left of the equal, the first term is known as the unsteady term or temperature change flow and then there is the convection term of the internal energy in the velocity field. On the right hand side of the equation we have $(-\nabla\cdot \mathrm{q})$ which corresponds to the diffusion term and, finally, the rest of the internal or thermal energies that could affect the domain in each particular case known as the energy source term.

The temperature, which is generally the variable of interest in the internal energy equation, is found in the variable $e=c_pT$. Substituting we obtain:

$$\frac{\partial(\rho c_p T)}{\partial t}+\nabla\cdot\left(\rho\bar{u}c_pT\right)=-\nabla\cdot q+S_e \tag{1.20}$$

To continue working on the energy equation we must remember Fourier's Law for heat flow, eq. (1.21). The heat flow q is proportional to the negative gradient of temperatures and depends on the variable λ which represents the thermal conductivity of the material.

$$q=-\lambda\nabla T \tag{1.21}$$

Again, substituting in equation (1.20) we obtain the following equation. The diffusion term in this case would refer only to the conductivity.

$$\frac{\partial(\rho c_p T)}{\partial t} + \nabla \cdot \left(\rho \bar{u} c_p T\right) = \nabla \cdot (\lambda \nabla T) + S_e \tag{1.22}$$

This equation is not valid for compressible fluids, particularly when the study problem has a high velocity of motion, much of the internal energy is converted into kinetic or mechanical energy. The kinetic energy per unit mass is defined as follows.

$$K = \frac{1}{2}(\bar{u} \cdot \bar{u}) = \frac{1}{2}(|\bar{u}|)^2 \tag{1.23}$$

Using the product rule, we can develop the time derivative of the product of the velocity by obtaining the following equation (1.24).

$$\frac{\partial\left({}^1\!/_2\, u^2\right)}{\partial t} = \bar{u}\frac{\partial \bar{u}}{\partial t} \tag{1.24}$$

On the right-hand side we observe the term ${}^{\partial \bar{u}}\!/_{\partial t}$ which indicates the rate of change of the velocity field with time. This variable has been studied previously in the Navier-Stokes momentum equation, eq. (1.13) or eq (1.18). Omitting the external forces term, we would obtain the following equation.

$$\frac{\partial\left({}^1\!/_2\, \rho u^2\right)}{\partial t} = -\rho \bar{u}\, [\bar{u} \cdot (\nabla \bar{u})] - \nabla(P\bar{u}) + \nabla(\tau \cdot \bar{u}) + \rho g \bar{u} \tag{1.25}$$

Performing some mathematical operations and introducing the expression of the kinetic energy per unit of mass K of the equation (1.23) we obtain the equation of conservation of kinetic energy:

$$\frac{\partial(\rho K)}{\partial t} + \nabla \cdot (\rho K \bar{u}) = -\nabla(P\bar{u}) + \nabla(\tau \cdot \bar{u}) + \rho g \bar{u} \tag{1.26}$$

This equation is presented with the first term being the unstable term that indicates the rate of variation of the kinetic energy, followed by the convection term of the kinetic energy in the velocity field. On the right hand side of the equation we observe firstly the energy of the pressure gradient; secondly, the strain energy; and finally, the potential energy.

The internal energy equation has been obtained, as well as the kinetic energy conservation equation. Therefore, the next step is to obtain the total energy equation E which will result from the sum of the internal and kinetic energy.

$$E = e + K \tag{1.27}$$

Adding therefore the equations of internal energy (1.19) and kinetic energy equations (1.26) we obtain:

$$\frac{\partial(\rho e)}{\partial t}+\frac{\partial(\rho K)}{\partial t}+\nabla\cdot(\rho e\bar{u})+\nabla\cdot(\rho K\bar{u}) = -\nabla\cdot q+S_e-\nabla(P\cdot\bar{u})+\nabla(\tau\cdot\bar{u})+\rho g\bar{u} \tag{1.28}$$

Substituting $E = e + K$ we obtain the equation of conservation of total energy in the flow field.

$$\boxed{\frac{\partial(\rho E)}{\partial t}+\nabla\cdot(\rho E\bar{u}) = -\nabla\cdot q-\nabla(P\cdot\bar{u})+\nabla(\tau\cdot\bar{u})+\rho g\bar{u}+S_e} \tag{1.29}$$

The direct *numerical simulation* (DNS) of the equations is possible by means of a very high-cost computation for low Reynolds numbers. However, even for really small domains and simple geometries the cost is so high that in practice other solutions such as averaging of the equations (*Reynolds-Averaged Navier Stokes* or RANS) are chosen. For this purpose, the Navier-Stokes equations are time-averaged and a closure model is used to calculate the viscous term defining the turbulence in these equations.

It should not be forgotten that the Navier-Stokes equations themselves describe both laminar and turbulent behavior without the need for models. However, we are still far from being able to solve them in a practical way even with clusters or supercomputers. Therefore, to predict turbulent behavior, researchers have developed methods known as turbulence models. The Table 1.2 shows a summary of the most important turbulence models as well as the citation where the necessary information to understand and apply them is included.

Table 1.2. Summary table of the most important turbulence models indicating the reference citation where the most important information for their implementation can be observed.

METHOD	MOST IMPORTANT MODELS
(U)RANS	Zero-equation models (algebraic turbulence models): • Baldwin-Lomax (Baldwin & Lomax, 1978) • Cebeci-Smith (Smith & Cebeci, 1967). One-equation models: • Spalart-Almaras (SA) (Spalart & Allmaras, 1992) • Baldwin-Barth (Baldwin & Barth, 1990), • Rahman-Agarwal-Siikonen (RAS) (Rahman et al., 2011), • Wray-Agarwal (WA) (X. Han & Agarwal, 2017), • Shuai-Agarwal (Shuai & Agarwal, 2020) Two-equation models: • k-ε: o Standart (Jones & Launder, 1972) o Realisable k- ε (Shih et al., 1995) o RNG (Yakhot et al., 1992)

	• k-ω: ○ Wilcox k-ω (Wilcox, 1988) ○ Wilcox's modified k- ω model (David C. Wilcox, 1993) ○ Shear Stress Transport (SST) (Menter, 1993) ○ Menter Baseline model (BSL) (Menter, 1994) Reynolds Stress Models: • Lauder-Reece-Rodi model (LLR) (Launder et al., 1975) • Speziale-Sarkar-Gatski model (SSG) (Speziale et al., 1991) • Omega-based Reynolds Stress Models (Wilcox, 2006) Non-linear eddy viscosity Models: • Cubic k- ε Model (Craft et al., 1996) • Explicit Algebraic Reynolds Stress Model (EARSM) (Wallin & Johansson, 2000)
LES	Large Eddy Simulation Models: • Smagorinsky-Lilly SGS Model (Smagorinsky, 1963) • Dynamic SGS Model (Germano et al., 1991) • Wall-Adapted Local Eddy-viscosity Model (WALE Model) (Nicoud & Ducros, 1999)
DNS	Direct Numerical Simulation (Orszag, 1970)

Important information:

For each model, the citation where the author of the thesis has reviewed the most important information has been included. However, some models have been studied in multiple papers and it may be necessary to search for additional information to understand the actual implementation of the models in the codes.

REYNOLDS-AVERAGE NAVIER-STOKES (RANS)

The Table 1.2 is divided into 3 main groups of methods. The RANS methods (known as URANS in transient *Unsteady Reynolds-Averaged Navier Stokes* simulations) come as already mentioned from the averaging of the Navier-Stokes equations. Models based on this method assume that the turbulent fluctuations of fluids at large scales exhibit an average behavior to which a fluctuation component is added. For example, the velocity, which we have so far defined as a vector $\bar{u}(x,t)$ which depends on position and time, could be defined by its average component $\bar{U}(x)$, and its fluctuation component in time $u'(x,t)$. This is known as *Reynolds decomposition*.

$$\bar{u}(x,t) = \bar{U}(x) + u'(x,t) \tag{1.30}$$

It is important to note that the $\bar{U}(x)$ component should be calculated over a period of time that is relatively long relative to the velocity fluctuations. For incompressible flows, the average component would be calculated according to the following equation.

$$\overline{U}(x) = \frac{1}{\Delta t}\int_{t}^{t+\Delta t} \bar{u}(x,t)\, dt \tag{1.31}$$

Simulations using the RANS equations massively reduce the computational cost relative to direct numerical simulation. In return, unknown fluctuation terms are introduced into the equations that must be calculated by turbulence models at all scales of the turbulent field. These terms are known as *Reynolds Stresses* and act on the flow as additional stresses. To model them, a sufficiently large number of closure equations is added so that it is possible to calculate all unknown variables. Thus, the turbulence model used depends on the equations used to "close" the system.

Continuing with the development of our average Navier-Stokes equations, it is important to mention, first of all, that the average of our new fluctuation component u' is equal to zero. This is so by definition, since u' is everything that is not found in the average of the variable $\overline{U}$. Secondly, in order to perform the development it is necessary to know several mathematical properties among which the following stand out: $\bar{\bar{a}} = \bar{a}$, $\overline{{}^{\partial a}/_{\partial b}} = {}^{\partial \bar{a}}/_{\partial b}$ y $\overline{a \cdot b} \neq \bar{a} \cdot \bar{b}$. Therefore, although the average of u' is 0, this is not the case with its square u'^2.

$$\overline{u'} = 0 \;\; ; \quad \overline{u'^2} = \overline{u' \cdot u'} \neq 0 \tag{1.32}$$

This mean square variance will be very important for our Navier-Stokes equations, as they form the well-known *Reynolds Stresses*. Starting from the conservation of mass equation (1.16) and introducing the vector $\bar{u}$ as average and fluctuation we would obtain:

$$\frac{\partial \overline{U_x}}{\partial x} + \frac{\partial \overline{U_y}}{\partial y} + \frac{\partial \overline{U_z}}{\partial z} + \frac{\partial u'_x}{\partial x} + \frac{\partial u'_y}{\partial y} + \frac{\partial u'_z}{\partial z} = 0 \tag{1.33}$$

If we average over time this equation, we know that the velocity fluctuation terms are equal to zero (eq. (1.32). Therefore, the first three terms must sum to zero as well.

$$\overline{\frac{\partial u'_x}{\partial x} + \frac{\partial u'_y}{\partial y} + \frac{\partial u'_z}{\partial z}} = 0 \quad \rightarrow \quad \overline{\frac{\partial \overline{U_x}}{\partial x} + \frac{\partial \overline{U_y}}{\partial y} + \frac{\partial \overline{U_z}}{\partial z}} = \frac{\partial \overline{U_x}}{\partial x} + \frac{\partial \overline{U_y}}{\partial y} + \frac{\partial \overline{U_z}}{\partial z} = 0 \tag{1.34}$$

Since we know that $\nabla\overline{U}$ is equal to 0, we can return to eq. (1.33) and confirm that the fluctuation terms are equal to 0. In this way we would have our RANS equations of mass conservation.

$$\boxed{\nabla\overline{U} = 0 \quad \rightarrow \quad \nabla\overline{u'} = 0} \tag{1.35}$$

To develop the momentum equation, the process is a little more complex. The process for obtaining the RANS moment equation for one of the components (in this case it will be the x-component) is shown below, although the process is similar for the rest. We start from the equation (1.15).

$$\frac{\partial u_x}{\partial t} + \left(u_x \frac{\partial u_x}{\partial x} + u_y \frac{\partial u_x}{\partial y} + u_z \frac{\partial u_x}{\partial z}\right) = -\frac{1}{\rho}\frac{\partial P}{\partial x} + \nu\left(\frac{\partial^2 u_x}{\partial x^2} + \frac{\partial^2 u_x}{\partial y^2} + \frac{\partial^2 u_x}{\partial z^2}\right) + g_x \tag{1.36}$$

Following the same process as for the mass conservation equation, we introduce into the equation our velocity variable as average velocity and fluctuation. The resulting equation is quite long so each term has been introduced within square brackets to facilitate its interpretation.

$$\begin{aligned}
&\left[\frac{\partial \overline{U_x}}{\partial t} + \frac{\partial u'_x}{\partial t}\right] + \left[\left(\overline{U_x}\frac{\partial \overline{U_x}}{\partial x} + \overline{U_x}\frac{\partial u'_x}{\partial x} + u'_x \frac{\partial \overline{U_x}}{\partial x} + u'_x \frac{\partial u'_x}{\partial x}\right)\right.\\
&\quad + \left(\overline{U_y}\frac{\partial \overline{U_x}}{\partial y} + \overline{U_y}\frac{\partial u'_x}{\partial y} + u'_y \frac{\partial \overline{U_x}}{\partial y} + u'_y \frac{\partial u'_x}{\partial y}\right)\\
&\quad + \left.\left(\overline{U_z}\frac{\partial \overline{U_x}}{\partial z} + \overline{U_z}\frac{\partial u'_x}{\partial z} + u'_z \frac{\partial \overline{U_x}}{\partial z} + u'_z \frac{\partial u'_x}{\partial z}\right)\right] =\\
&\quad = \left[-\frac{1}{\rho}\frac{\partial \overline{P}}{\partial x} - \frac{\partial p'}{\partial x}\right]\\
&\quad + \left[\nu\left(\frac{\partial^2 \overline{U_x}}{\partial x^2} + \frac{\partial^2 \overline{U_x}}{\partial y^2} + \frac{\partial^2 \overline{U_x}}{\partial z^2}\right) + \nu\left(\frac{\partial^2 u'_x}{\partial x^2} + \frac{\partial^2 u'_x}{\partial y^2} + \frac{\partial^2 u'_x}{\partial z^2}\right)\right]\\
&\quad + g_x
\end{aligned} \tag{1.37}$$

Similar to the procedure followed for the conservation of mass equation, we are going to perform time averaging of this equation and eliminate the terms that we know are equal to zero. In this step we are going to apply all the rules that we have seen previously to each term of the equation, and cross out those that are zero.

$$\begin{aligned}
&\left[\cancel{\frac{\partial \overline{U_x}}{\partial t}} + \cancel{\overline{\frac{\partial u'_x}{\partial t}}}\right] + \left[\left(\overline{U_x}\frac{\partial \overline{U_x}}{\partial x} + \cancel{\overline{U_x}\frac{\partial \overline{u'_x}}{\partial x}} + \cancel{\overline{u'_x}\frac{\partial \overline{U_x}}{\partial x}} + \overline{u'_x \frac{\partial u'_x}{\partial x}}\right)\right.\\
&\quad + \left(\overline{U_y}\frac{\partial \overline{U_x}}{\partial y} + \cancel{\overline{U_y}\frac{\partial \overline{u'_x}}{\partial y}} + \cancel{\overline{u'_y}\frac{\partial \overline{U_x}}{\partial y}} + \overline{u'_y \frac{\partial u'_x}{\partial y}}\right)\\
&\quad + \left.\left(\overline{U_z}\frac{\partial \overline{U_x}}{\partial z} + \cancel{\overline{U_z}\frac{\partial \overline{u'_x}}{\partial z}} + \cancel{\overline{u'_z}\frac{\partial \overline{U_x}}{\partial z}} + \overline{u'_z \frac{\partial u'_x}{\partial z}}\right)\right] =\\
&\quad = \left[-\frac{1}{\rho}\frac{\partial \overline{P}}{\partial x} - \cancel{\frac{\partial \overline{p'}}{\partial x}}\right]\\
&\quad + \left[\nu\left(\frac{\partial^2 \overline{U_x}}{\partial x^2} + \frac{\partial^2 \overline{U_x}}{\partial y^2} + \frac{\partial^2 \overline{U_x}}{\partial z^2}\right) + \cancel{\overline{\nu\left(\frac{\partial^2 u'_x}{\partial x^2} + \frac{\partial^2 u'_x}{\partial y^2} + \frac{\partial^2 u'_x}{\partial z^2}\right)}}\right]\\
&\quad + g_x
\end{aligned} \tag{1.38}$$

Simplifying the equation we would obtain.

$$\begin{aligned}
&\overline{U_x}\frac{\partial \overline{U_x}}{\partial x} + \overline{U_y}\frac{\partial \overline{U_x}}{\partial y} + \overline{U_z}\frac{\partial \overline{U_x}}{\partial z} + \overline{u'_x \frac{\partial u'_x}{\partial x}} + \overline{u'_y \frac{\partial u'_x}{\partial y}} + \overline{u'_z \frac{\partial u'_x}{\partial z}}\\
&\quad = -\frac{1}{\rho}\frac{\partial \overline{P}}{\partial x} + \nu\left(\frac{\partial^2 \overline{U_x}}{\partial x^2} + \frac{\partial^2 \overline{U_x}}{\partial y^2} + \frac{\partial^2 \overline{U_x}}{\partial z^2}\right) + g_x
\end{aligned} \tag{1.39}$$

Previously the *Reynolds stress* term was already introduced, but it is not until now that we identify them for the first time. The *Reynolds stresses* correspond to the terms marked in red in the equation (1.39). This name is due to the fact that when they are calculated they have units of force per unit volume, exactly the same as the other stresses. By applying the *chain rule identity* to these terms, it is possible to reconvert these terms to the final format of the RANS moment equation.

$$\begin{aligned}\overline{U_x}\frac{\partial \overline{U_x}}{\partial x} + \overline{U_y}\frac{\partial \overline{U_x}}{\partial y} + \overline{U_z}\frac{\partial \overline{U_x}}{\partial z} + \frac{\partial \overline{u'_x u'_x}}{\partial x} + \frac{\partial \overline{u'_x u'_y}}{\partial y} + \frac{\partial \overline{u'_x u'_z}}{\partial z} \\ = -\frac{1}{\rho}\frac{\partial \overline{P}}{\partial x} + \nu\nabla^2\overline{U} + g_x\end{aligned} \tag{1.40}$$

If we want to obtain the URANS equations to calculate the evolution of the average variables, i.e. to simulate a transient scenario, we must recover the first term of the equation (1.38) thus obtaining:

$$\begin{aligned}\frac{\partial \overline{U_x}}{\partial t} + \overline{U_x}\frac{\partial \overline{U_x}}{\partial x} + \overline{U_y}\frac{\partial \overline{U_x}}{\partial y} + \overline{U_z}\frac{\partial \overline{U_x}}{\partial z} + \frac{\partial \overline{u'_x u'_x}}{\partial x} + \frac{\partial \overline{u'_x u'_y}}{\partial y} + \frac{\partial \overline{u'_x u'_z}}{\partial z} \\ = -\frac{1}{\rho}\frac{\partial \overline{P}}{\partial x} + \nu\nabla^2\overline{U} + g_x\end{aligned} \tag{1.41}$$

Generalizing, we obtain the final equation:

$$\boxed{\frac{\partial \overline{U}}{\partial t} + \overline{U}\cdot\nabla\overline{U} = -\frac{1}{\rho}\nabla\overline{P} + \nu\nabla^2\overline{U} - \nabla\overline{u'\cdot u'} + g_x} \tag{1.42}$$

The technique used to solve the Reynolds stresses defines the different RANS turbulence models. The Table 1.2 shows a compendium of the most important models, being grouped by the number of additional equations needed to solve these stresses. *Zero-equation* models do not require additional equations to solve the system. Therefore, these models are not able to adequately account for the effect of turbulence. However, they can be useful to perform initialization of variables (initial conditions along the domain) in simulations where other more advanced models may have difficulties to converge.

Two-equation models are the most common within the set of RANS models as they are suitable for a wide range of applications and achieve a good balance between computational speed and accuracy. This has made them the standard models so far for the industry.

More advanced RANS models, such as *Reynolds Stress Equation Models* (RSM) are based on the direct calculation of Reynolds stresses. Therefore, they are able to detect more complex interactions in different turbulent flows. These techniques are generally referred to as *Second Order Closure Models*. However, in practice, these models are not always superior to two-equation models.

LARGE EDDY SIMULATIONS (LES)

The *Large Eddy Simulations* (LES) technique is based on the calculation of the Navier-Stokes equations for turbulent eddy scales above a certain threshold. For lower scales, *sub-grid* techniques are used to model the turbulent behavior. The threshold where the filtering of the equations occurs is generally defined by the mesh size. Therefore, the mesh plays an even more important role in this type of simulations.

The most common filtering of equations is known as *band-pass filtering*. This method consists of defining a function to decompose the variables (let's suppose any variable φ) into two components: filtered $\tilde{\varphi}$ and residual φ'. For ease of writing, the filtered component will be represented by a wavy top bar and the residual by an apostrophe. However, it should be noted that they are not related to the average variable and its fluctuation as in the RANS case. We start from the Navier-Stokes momentum equation (1.13), without gravity or external forces to facilitate tracking, applying a spatial filter to the variables.

$$\frac{\partial \tilde{u}}{\partial t} + (\nabla \widetilde{uu}) = -\frac{1}{\rho}\nabla \tilde{P} + \nu \nabla^2 \tilde{u} \tag{1.43}$$

If we add the condition of conservation of mass, we can observe that the system cannot be solved for both variables $\tilde{u}$ y $\widetilde{uu}$. Therefore, some mathematical techniques must be employed to manipulate the equation. Unlike in the RANS case, the rules for filtered variables are practically the opposite since $\tilde{\tilde{u}} \neq \tilde{u}$ in addition to the fact that $u' \neq 0$ and that $\tilde{u}\tilde{u} \neq \widetilde{uu}$. However, for the case of the sum of filtered variables, we can equal $\widetilde{u+u} = \tilde{u} + \tilde{u}$. Working with these rules we can modify the above equation following the "Leonard decomposition".

$$\frac{\partial \tilde{u}}{\partial t} + \nabla(\widetilde{uu} + \tilde{u}\tilde{u} - \tilde{u}\tilde{u}) += -\frac{1}{\rho}\nabla \tilde{P} + \nu \nabla^2 \tilde{u} \tag{1.44}$$

Continuing with the development, we modify the position of the terms of the equation as follows.

$$\frac{\partial \tilde{u}}{\partial t} + \nabla(\tilde{u}\tilde{u}) += -\frac{1}{\rho}\nabla \tilde{P} + \nu \nabla^2 \tilde{u} + \nabla(\tilde{u}\tilde{u} - \widetilde{uu}) \tag{1.45}$$

The main part of the term that we have moved to the right-hand side is called subgrid or *subgrid-scale stress* and is usually expressed by τ^{SGS}.

$$\tau^{SGS} = (\tilde{u}\tilde{u} - \widetilde{uu}) \tag{1.46}$$

This tensor τ^{SGS} represents the effect of small eddy scales that have not passed spatial filtering. The filter is generally given by the spatial discretization in finite control volumes so the mesh used has a direct impact on the calculation of the turbulence. To solve the system it is therefore necessary to establish a *subgrid-scale stress model,* commonly known as SGS model. There are multiple models available to solve this tensor, although the most common ones are based on the Boussinesq hypothesis (Boussinesq, 1877), which postulates that the variable *Eddy Viscosity* μ^{SGS} (o ν^{SGS} if we have divided by the density ρ in the equations) can be used to model eddy turbulence. This variable describes the energy transfer as a consequence of eddy motion and is related to the tensor τ^{SGS} according to the following equation. This equation arises from the decomposition of the tensor into its *anisotropic* (or *deviatoric*) part and its *isotropic* (or *spherical*) part.

$$\tau^{SGS} = dev(\tau^{SGS}) + sph(\tau^{SGS}) = -2\,\nu^{SGS}\bar{S} + \frac{1}{3}tr(\tau^{SGS})\mathrm{I} \tag{1.47}$$

It is important to mention that the viscosity ν^{SGS} only represents the small vortex scales unlike the *Eddy Viscosity* of the RANS models which represents all turbulent scales. Usually the isotropic (spherical) part is not modeled together with the subgrid stress and is included in the filtered static pressure where it can be resolved, modeled or neglected. The matrix I represents the identity matrix and the tensor $\bar{S}$ corresponds to the large-scale stress which can be calculated according to the following equation.

$$\bar{S} = \frac{1}{2}(\nabla\tilde{u} + \nabla\tilde{u}^{T}) \tag{1.48}$$

Rearranging the terms and simplifying, the final moment equation for the calculation using LES would look as follows.

$$\frac{\partial\tilde{u}}{\partial t} + \nabla(\tilde{u}\tilde{u}) += -\frac{1}{\rho}\nabla\tilde{P} + \nabla\cdot\left[\left(\nu + \nu^{SGS}\right)\nabla\tilde{u}\right] \tag{1.49}$$

There are multiple models to solve for viscosity ν^{SGS} although the most commonly used are shown in Table 1.2.

It is commonly considered that a good LES model should solve at least 80% of the turbulent kinetic energy, leaving a maximum of 20% for *sub-grid* modeling. Therefore, it is important to know the problem to be solved in order to adjust the mesh size in each zone of the domain. In this way, one would proceed to reduce the cell size where small vortices are most important.

Integral Length Scale corresponds to the representative size of the eddies in each zone of our domain. The exact definition of this variable is the size of a vortex of *mean turbulent kinetic energy* and provides a good reference for adjusting the mesh size.

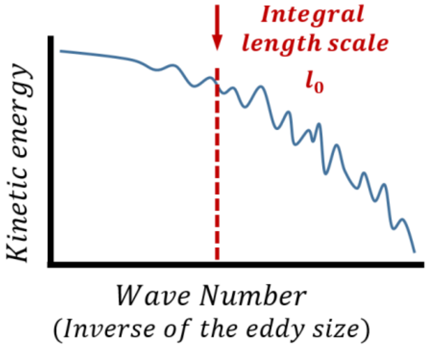

Source: Author's design

Figure 1.21. Evolution of the kinetic energy contained in the different vortex size scales.

It is possible to carry out a RANS simulation beforehand to know the *Integral Length Scale*. This variable will take a different value at each node and will help us to create a map with the areas where our meshing should be finer. In practice, it is considered that the mesh spacing should be around one fifth of this variable. It is possible to use $l_0 = {k^{3/2}}/{\varepsilon}$ ó $l_0 = {k^{1/2}}/{C_\mu \omega}$ can be used to calculate the *Integral Length Scale* depending on the RANS turbulence model used in the simulation. Approximately one fifth of this length represents a cell size small enough to resolve 80% of the turbulent kinetic energy.

After performing the LES simulation it is possible to observe the turbulent kinetic energy that our code is solving (not modeling) by calculating it using equation (1.23). Recall that the velocity fluctuation u' has three components $\left(u'_x\, u'_y\, u'_z\right)$. Therefore, to calculate the resolved turbulent kinetic energy it will be necessary to perform the calculation using the sum of the diagonal components of the *Reynolds Stress Tensor* diagonal that are $\left(\overline{u'_x u'_x} + \overline{u'_y u'_y} + \overline{u'_z u'_z}\right)$. The modeled turbulent kinetic energy is obtained directly from the SGS model used. The comparison between these two variables allows us to check the proportion of the turbulent kinetic energy that is resolved by the mesh and which is being modeled in order to know the quality of the LES simulation.

Another way to meet the challenge of LES simulations is to use the Taylor *Microscale* as it also gives us information about the deformation of the field of velocity fluctuations. This scale lies roughly between what is considered small and large eddies, and gives us a reference about the scale where the viscosity substantially affects the motion of the eddies. The Taylor microscale (λ) can be approximated using the turbulent kinetic energy (k) and the turbulent energy dissipation (ε).

$$\lambda \approx \sqrt{10\nu\frac{k}{\varepsilon}} \tag{1.50}$$

The value (distance) obtained from this equation can be used as a reference to design the spacing of our meshing and thus obtain the areas that require a more refined meshing or that, on the contrary, can be kept with a less fine meshing and speed up the calculation process.

1.5.2. CFD AND ANNULAR FLOW SIMULATIONS

Over the last 30 years there have been great advances in the simulation of fluid behavior. Initially, simulations were performed at each research center using proprietary software. Over time, the first commercial codes began to appear that included graphical interfaces and expanded the range of applications that could be simulated. Nowadays, there are different open-source and commercial programs capable of simulating complex problems with very different characteristics. For example, with the same software it is possible to solve both the motion of a viscous oil in micro-channels and the motion of a fluid at supersonic velocities.

It is important to mention the great evolution in terms of computations that humanity has experienced during the last years. The development of faster and more efficient computational units has made it possible to solve really complicated problems. However, two-phase flow such as annular flow, due to its complex and nonlinear behavior, is still a major challenge for researchers and code developers.

In the previous sections the fundamental equations governing fluid behavior have been described. However, for multiphase flow the equations are more complex and undergo variations depending on the technique used. In the case of annular flow, there are two liquid-gas phases interacting with each other at the interface. In case both phases are of the same substance (vapor and liquid water), energy exchange and mass exchange will occur between them. On the other hand, for phases of different substances, the exchange will be only of energy. The theory behind this behavior involves complex mathematical calculations that are beyond the scope of this thesis. Therefore, to learn about the development of the multiphase flow equations the reader can refer to the following books: "*Fundamentals of Multiphase Flow*" (Brennen, 2013) and "*Computational Techniques for Multiphase Flows*" (Yeoh & Tu, 2010)..

If solving the equations by direct numerical simulation for a single phase is practically impossible with current computational power, for two-phase flow it is even more difficult. The power and speed required is far from the current capabilities for the multiphase flows that appear in nature. If we also include the turbulent behavior experienced by both phases in most situations, the cost escalates to unbearable levels.

Therefore, different approaches have been proposed to generate the models that are currently used to deal with this problem. First, the *Eulerian specification* approach is based on the spatial location through which the fluid passes with time. This means that the approach is from the point of view of the meshing (see Figure 1.22). In contrast, the Lagrangian *specification* approach consists of tracking a portion of the fluid as it moves through space and time. This implies that the particles are followed by solving the equations of motion for each particle. It is therefore a much more computationally expensive method, but more accurate in tracking the particles.

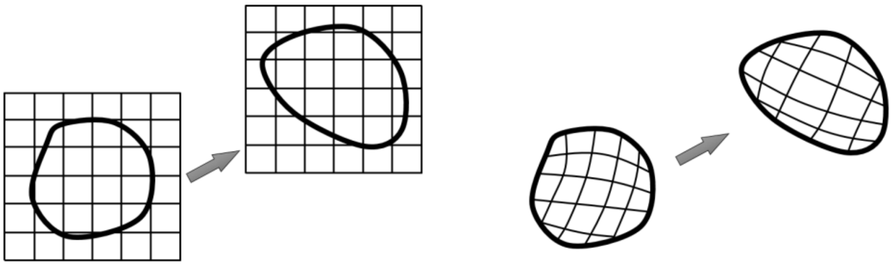

Eulerian specification ***Lagrangian specification***

Source: Author's design

Figure 1.22. Comparative between Eulerian and Lagrangian specifications.

From these two approaches arise most of the methodologies for macroscopic multiphase computation. The *Euler-Euler* methods will treat the different phases using the Eulerian approach in both cases. Therefore, the phases will be considered continuous even when we have relatively dispersed fluids. Euler-Euler methods can also be used for these cases, but the overall motion of the particles will be modeled instead of tracking individual particles. Euler-Euler models need to solve an additional equation for the void fraction of each phase. The coupling between phases is done by the pressure and phase exchange coefficients to be modeled depending on the type of problem to be solved.

In contrast, *Euler-Lagrangian* methods will treat the continuous phase as Eulerian while the dispersed phase will be modeled following the Lagrangian approach. The particles of the dispersed phase can be solved individually, although they are usually modeled in the form of *clusters* to reduce the high computational cost. The dispersed phase equations allow the inclusion of a wide variety of forces to model the motion accurately, such as *drag forces*, *lift forces*, *virtual mass forces*, *history forces*, etc. The coupling between phases is realized by means of *source terms* of mass, momentum and energy exchange.

In addition, the *Volume of Fluid (*VOF) model is often included as a third group. Actually, this method is based on the Euler-Euler approach, but does not allow phase mixing to occur. Under this premise, the VOF method tracks the interface using an indicator function based on the void fraction. The void fraction will be 0 or 1 in the continuous fluid zone while at the interface we will obtain a band with void fractions between 0 and 1.

To model annular flow, both phases are generally treated as continuous fluids. While it is true that for high velocities water droplets are incorporated into the gas phase and air bubbles into the liquid phase, these are very difficult to model with the degree of accuracy observed in a real scenario. Simply, one could consider the annular flow as either separate flows or as mixed flows (dispersed and separated) known as transition flows (Ishii & Hibiki, 2006).

In the literature, it is possible to find multiple cases where the VOF model is used to simulate annular flow (Dai et al., 2013; Sumana Ghosh et al., 2010; Y. Liu et al., 2011). A large majority of the most important works of annular flow simulation is related to the chemical field, where this behavior usually appears between oil and water instead of air and water. This is the case for example of (Babakhani Dehkordi et al., 2017) who use the VOF model in a scenario where oil and water move through a *venturi* and a *nozzle* flowmeter. The results obtained are very similar to the experimental measurements, thus showing the capability of the VOF model in the simulation of this type of flow.

However, research related to air-water annular flow is much more limited. Air is a very low viscous fluid which increases the instability of the interface and increases the computational complexity. In addition, some of these focus on the development of interfacial waves, but in downward flow scenarios in an inclined plane. For example, (Gu et al., 2004) they perform an interesting study where they analyze the impact of the surface where the fluid descends, on the pattern of fluid motion, demonstrating its influence for free-fall cases.

The research carried out in (Adaze et al., 2019) is very interesting for this thesis as it details the models and parameters used to successfully simulate annular upward flow. The authors use the Euler-Euler VOF model that includes the commercial software ANSYS Fluent to carry out the simulations and focus on predicting the conditions in which the reverse flow occurs. This phenomenon appears in upward flow when the drag forces of the gas are not large enough to maintain the upward motion of the liquid. Despite the high quality of the work, the domain has been simplified to axisymmetric-2D. As the authors state in the conclusions, a 3D domain would be recommended to increase the scope of the work.

Although most studies have been conducted using VOF models, investigations using Euler-Lagrangian models are also observed in the literature. For example, multiple works by Li, H. and Anglart H. (H. Li & Anglart, 2015, 2017, 2019) where they employ this method in a steam-water annular flow system. In the work (H. Li & Anglart, 2019) they use this approach to predict the *dryout* phenomenon that can occur in pipes subjected to heating. This phenomenon is of special interest in the nuclear field where it can appear in an undesired way. For example, in the upper part of the fuel elements of a BWR reactor, the liquid film may disappear producing *dryout* and exposing the reactor to potential overheating problems (Figure 1.23). The results obtained by Li and Anglart are very satisfactory and similar to those obtained experimentally.

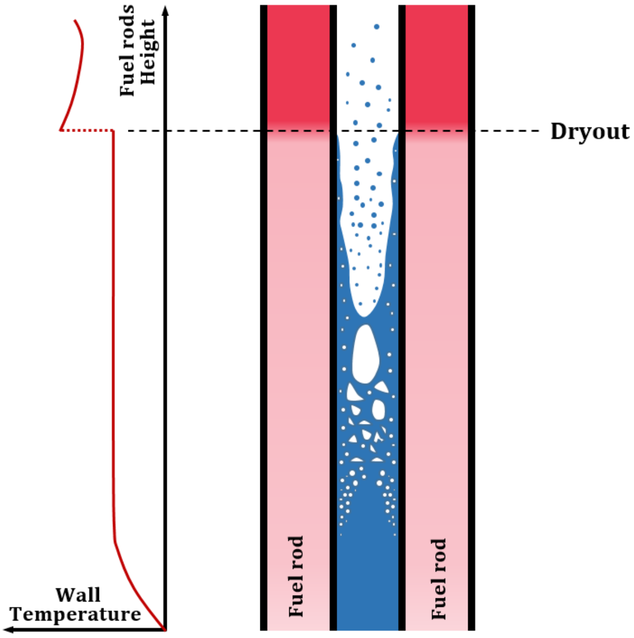

Source: Author's design

Figure 1.23. Schematic of *dryout* phenomenon and graph associated with wall temperature.

CFD simulations have been employed to also predict annular flow behavior in pipe erosion. In the work (Zahedi et al., 2017) they look at the impact of this flow on an elbow, similar to what would be encountered in an industrial facility. They develop a VOF model and observe how the erosion in the bend varies depending on the annular flow conditions.

In short, it is possible to simulate the behavior of the annular flow, although it is a challenge given the complexity of its structure. The biggest problems usually arise as a consequence of the small thickness of the liquid phase and the high velocity of the gas. The *Volume of Fluid* (VOF) multiphase model is the most commonly used as the interface is well defined, although *Euler-Lagrangian* models can be used for specific cases.

1.6. UNCERTAINTY QUANTIFICATION IN CFD

Although CFD codes offer better results every day, it is important to be aware of the uncertainty of their predictions. On the one hand, researchers know the limitations of the models used and in many cases they are highly dependent on empirical constants. The value of these constants is usually unknown, although it is possible to know the approximate range in which they could be thanks to experimental studies that support it.

On the other hand, in addition to the errors introduced as a consequence of the models, the boundary conditions may contain uncertainty. When trying to compare simulation results with experimental measurements, it must be kept in mind that the input data also contain uncertainty. For example, assuming that the inlet flow rate is 5 liters per minute is inaccurate. All measurement systems are subject to some uncertainty that must also be propagated when trying to simulate a particular scenario.

1.6.1. SOURCES OF UNCERTAINTY

Before analyzing the available techniques to calculate the uncertainty of CFD simulations, it is necessary to know what are the sources that introduce uncertainty in the simulation results. According to (Fokken et al., 2019a) the sources of uncertainty taken into account in CFD codes are divided into three main groups: uncertainty in the physical properties, uncertainty in the models and uncertainty in the initial and boundary conditions. This report also indicates that, in general terms, uncertainties related to the singularities of the Navier-Stokes equations can be disregarded, thus being able to focus the effort on physical properties, turbulence models, initial conditions and boundary conditions. The Figure 1.24 shows a classification of the types of uncertainty sources indicating the most representative of each group. Numerical errors, which are not in themselves a source of uncertainty, but affect the accuracy of the simulation, have been included in this classification.

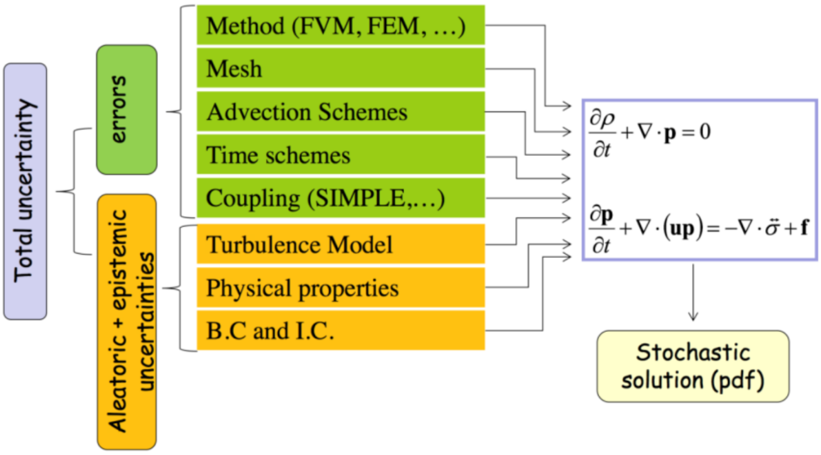

Source: (Fokken et al., 2019b) Page 19.

Figure 1.24. Schematic of the sources of uncertainty in the CFD simulations.

Although the above summary allows observing the main sources of uncertainty, it is possible to carry out a more precise listing. In the report *Review of Uncertainty Methods for Computational Fluid Dynamics Application to Nuclear Reactor Thermal Hydraulics* (OECD/NEA, 2016) a comprehensive analysis of the potential sources of uncertainty in CFD codes applied to nuclear reactors is performed. The Figure 1.25 has been elaborated following the classification made in this report and some considerations to be made within each type of uncertainty source are shown. It should be noted that not only continuous uncertain variables are taken into account, but also categorical variables such as the user's choice of the numerical models to be used in his simulation. In blue color it has been included some sources of uncertainty that are not usually taken into account but that can have a great influence on the outcome of the simulations. Nevertheless, their influence is difficult to estimate, as well as their propagation through the system. Among them we highlight for example geometry simplifications, which are very common in CFD calculations because they facilitate the meshing of the domain, increase the mesh quality and reduce the convergence time. However, complex geometries can lead to interactions that may not be taken into account in the simulations.

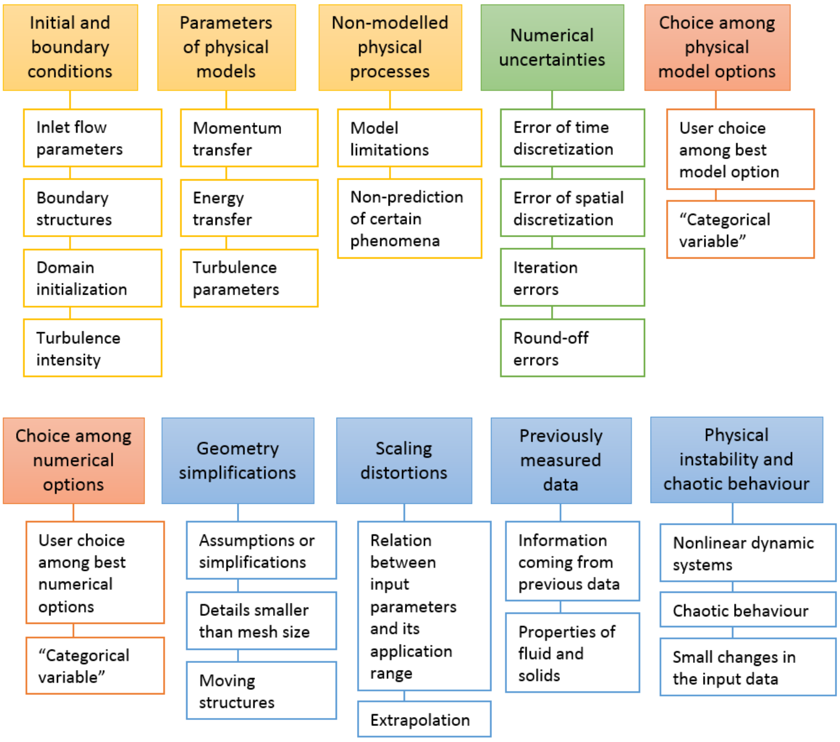

Source: Author's design based on Review of Uncertainty Methods for Computational Fluid Dynamics Application to Nuclear Reactor Thermal Hydraulics. (OECD/NEA, 2016) Pages 26-27

Figure 1.25. Detailed diagram of the types of uncertainty sources for CFD simulations as well as some aspects to be taken into account in each of them.

For ease of understanding, a list of sources of uncertainty that could be taken into account in a CFD simulation of an annular flow is shown below:

- Uncertainty in initial and boundary conditions:
  - Velocity, temperature, turbulent parameters such as k y ε, etc.
  - Physical properties of fluids and calculation models: thermal conductivity, viscosity, density, thermal expansion, etc.
- Uncertainty in the parameters of the physical models:
  - Turbulence model:
    - Model *k-ε:* $C_{\varepsilon 1}$, $C_{\varepsilon 2}$, $C_{\varepsilon 3}$, C_{μ}, Pr_k, Pr_ε, Pr_T.
    - LES *Smagorinsky* model: C_S, Pr_T, Sc_T.
    - If another model is used, its corresponding parameters.
  - Treatment of fluid density: *Boussinesq's hypothesis* or density-temperature-pressure dependence.
  - Wall laws:

        - Model selection: TBLE, Standard, Scalable...
        - Damping functions for turbulent viscosity: f_μ (constant, *van-driest*, *Piomelli*).
        - *Von-Kárman* constant.
- Uncertainty in parameters related to numerical schemes:
    - *Advection scheme*
    - Factor α if a *blend* between *second order scheme* and *upward first order scheme* is used.
    - Time scheme (implicit, explicit)
- Uncertainty in mesh parameters:
    - Type of mesh: FEM (*Finite Element Method*), FVM (*Finite Volume method*), FDM (*Finite Difference Method*), etc.
    - Number of cell layers near the wall.

As can be seen, the treatment of uncertainty in CFD simulations is a complex and time-consuming task. While it is true that there are multiple possible sources of uncertainty that can affect the simulation results, it is also true that it is necessary to evaluate the final influence that they really have. In many occasions it is possible to analyze the system to identify the uncertain variables that have more weight. Uncertainty in CFD codes is a topic that is being investigated in recent years and will continue to evolve in the future.

1.6.2. METHODS OF UNCERTAINTY QUANTIFICATION

Currently, different methods have been developed to quantify the uncertainty of CFD codes. In the field of nuclear thermal-hydraulics, different techniques have been developed for uncertainty analysis in *system codes* where the thermal-hydraulic behavior is simulated at plant level.

The different methods that have been applied to CFD simulations are very limited and present a low degree of maturity (OECD/NEA, 2016). The nuclear sector has a special interest in the development and use of the different uncertainty quantification methods since the results of the simulations, even after carrying out the propagation of the possible errors and uncertainties in the parameters, are within the safety margins.

Uncertainty quantification methods for CFD codes are generally grouped into two types, uncertainty propagation methods and extrapolation methods (see Table 1.3). Propagation methods are based on observing how the uncertainty of the input parameters is transmitted to the output. To do this, it is necessary to estimate the uncertainty of the uncertain input variables from probability functions and to sample the values it may take. The most widespread are traditionally based on a Monte Carlo random sampling that allows simultaneous variation of all uncertain variables at the same time, although the use of surrogate models to propagate the uncertainty to the output is currently being studied.

In contrast, extrapolation methods, also known as inverse problems, are based on the estimation of uncertainty from the differences between certain experimental measurements and simulation results. This process allows to adjust the uncertain parameter values of the models which is interesting to optimize and update the models themselves. Moreover, unlike propagation methods, extrapolation methods allow to take into account the impact of phenomena that have not been modeled in the simulations since they are based on the comparison of experimental measurements and simulation results. However, a large experimental database of multiple phenomena and at different scales is necessary for these methods to be accurate.

Table 1.3. Summary table of different uncertainty quantification methods including information on their advantages, disadvantages and most important features.

TYPE OF METHOD	APPROACH	METHOD	NOTES
Propagation	Based on simulations	Monte Carlo (MC) (Metropolis & Ulam, 1949)	Well known for other (non-CFD) applications. Independent of the number of uncertain variables. High number of simulations.
		Latin Hypercube Sampling (LHS) (Rakhimov et al., 2018)	Similar to the Monte Carlo method, but uses a stratified sampling scheme. Better coverage of the probability function. Optimizes the number of simulations.
		Deterministic Sampling (DS) (Hessling, 2013)	Similar to the Monte Carlo method, but the number of simulations is reduced. Simulations on samples of uncertain variables of equal "statistical moment". Highly dependent on correct selection of sampling points.
	Surrogate models	Polynomial Chaos Expansion (PCE) (Rivera, Muñoz-Cobo, Berna, et al., 2021).	Metamodel that projects the system response on an orthogonal basis of polynomials. Efficient (low number of simulations) for a low number of uncertain variables.
		Low-Rank Tensor Representations (Konakli & Sudret, 2016)	Metamodel that projects the answer in a system of multivariate polynomials obtained as tensor products of univariate polynomials. Reduced number of simulations with respect to the PCE.
		Kriging and variants (gradient enhanced, POD-kriging, etc.) (Mastrippolito et al., 2021).	The answer is obtained from a Gaussian random process defined as the sum of a deterministic and a stochastic part. It increases the stability and robustness of the metamodel as it takes into account small scale variations in the data.
		Neural-Networks (delta model, NN-Bayesian method,	Extremely poorly investigated neural network models in CFD.

		MVEM, etc.) and others. (Kabir et al., 2018)	Other surrogate models such as wavelet expansions, Neumann expansion, perturbation methods also need to be evaluated in CFD simulations.
Extrapolation	Based on system codes	UMAE Method (D'Auria et al., 1995).	Uncertainty is extrapolated from code or node information that has passed a qualification process through comprehensive experiments. It must pass a strict evaluation process. Its CFD application has not been sufficiently studied.
	Based on experiments	ASME Method	The uncertainty is extrapolated from the difference between experimental measurements and simulation results in a validation process. It does not represent the real uncertainty of the code taking into account the uncertainties of the variables, but the error made by the model. It only represents the error committed at the experimental scale.

Important information:

For each methodology an article is included where you can find more information on each of the techniques.

PROPAGATION MODELS BASED ON SIMULATIONS

Propagation models are mainly divided into two types: simulation-based models and surrogate models. In simulation-based models it is necessary to design a series of simulations where the uncertain input variables are varied according to their probability function. For this purpose, a sampling of these variables is carried out and, from the result of the different simulations, the output uncertainty is obtained. The main difference between the methods in this category is the technique used to generate the sampling of the uncertain input variables.

The main category is occupied by the Monte Carlo (MC) or random sampling method where points are analyzed randomly by attending to their probability function (Metropolis & Ulam, 1949). Latin hypercube sampling (LHS) is a method that distributes the different points so that the entire range is covered without repeating points in the same positions, thus optimizing the number of simulations to be performed. Latin hypercube sampling is well known in the scientific community and has been applied on multiple occasions in CFD simulations such as in (Rakhimov et al., 2018).

There are other methods of which we highlight deterministic sampling (DS) which reduces the number of simulations by selecting sampling points of equal statistical momentum (Fedon et al., 2021). There are different techniques to apply the deterministic sampling such as the use of excitation matrices (Hessling, 2013) such as STD (standard ensemble), SPX (minimal simplex), BIN (binary ensemble), Hadamard ensemble (Cutrono Rakhimov et al., 2019); or the use of the DPS (Density Preserving Sampling) method (Budka & Gabrys, 2013).

PROPAGATION MODELS BASED ON SURROGATE MODELS

Surrogate models or metamodels are those that represent the expected output (of a code or experiment in our case) from a model. They are especially useful when the output cannot be obtained in a simple way such as in the case of computationally demanding simulations or expensive experiments. In terms of uncertainty quantification, surrogate models provide not only the *expected value* (known as EV) but also the standard deviation, allowing to know the uncertainty of the output.

The most widespread subrogated model is the Polynomial Chaos Expansion (PCE) which is based on the projection of the output on a basis of orthogonal polynomials. To obtain the coefficients of the different polynomials there are different techniques such as the resolution of a system in collocation points, or the resolution of the integral by means of Gauss quadrature. This model using Hermite-Gauss quadrature will be studied in detail in this doctoral thesis (Rivera, Muñoz-Cobo, Berna, et al., 2021). As will be seen later, the PCE allows to reduce extensively the number of simulations for scenarios where the number of uncertain variables is small.

Multiple variants based on PCE have been developed in recent years such as Low-Rank Tensor Representation (LRA or *Low-Rank Approximation*). This technique has been studied in (Konakli & Sudret, 2016) and proposes to obtain the model response by means of a system of multivariate polynomials obtained as a tensor product of a set of univariate polynomials. According to the authors, this technique improves the response prediction for extreme situations. Moreover, this technique optimizes the number of simulations to be performed, the growth of these simulations being linear with the number of uncertain variables (Wikle, 2017).

Kriging models obtain the expected response by means of a Gaussian random process consisting of a deterministic and a stochastic component. The fact that they add a stochastic part increases the stability and robustness of the method (Mastrippolito et al., 2021). Although Kriging metamodels are well known, their applications in uncertainty quantification of CFD simulations are very limited.

The growing rise of neural networks in recent years has led to the development of these methods for uncertainty quantification. In (Kabir et al., 2018) a review of the different techniques available to quantify uncertainty is made, although the purpose of the paper is its use in other fields such as the food industry or the prediction of the percentage of renewables in the electricity mix. A large number of methods exist, such as the Delta Method, Bayesian Method, MVEM (Mean-Variance Estimation Method), etc. However, very limited work has been published on these uncertainty quantification methods. For example, (Yang Liu et al., 2021) propose a surrogate model based on neural networks to quantify the uncertainty of simulations of a *bubbly* multiphase flow.

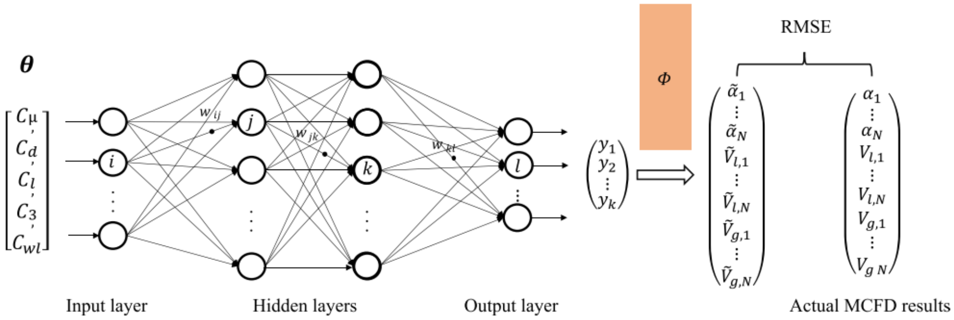

Source: (Yang Liu et al., 2021)

Figure 1.26. Surrogate model based on Neural Networks.

EXTRAPOLATION MODELS

Within the extrapolation methods it is possible to select the two most important ones: UMAE and ASME. The UMAE method is based on the extrapolation of the accuracy obtained in integral experiments performed in full-size nuclear plants. This method, developed in detail in (D'Auria et al., 1995) is mainly intended for uncertainty extrapolation in system codes such as TRACE or TRAC-B. However, the design of an extension applicable to CFD is being studied in recent years (OECD/NEA, 2016), although it is still far from being real.

On the other hand, the ASME method is the validation and verification (V&V) standard for all types of engineering applications (ASME V&V 20, 2009). This method allows determining how accurate our model is with respect to the accurate representation of the real system. Therefore, this system relies primarily on experimental data to extrapolate errors to simulation results. By applying this methodology, it is possible to end up knowing the uncertainty of the model, the numerical uncertainty, the uncertainty of the input conditions and the experimental uncertainty. From these, the uncertainty is obtained for given conditions where the experimental result is known. The uncertainty is then extrapolated to the new conditions. This method is relatively simple to apply, but very effective. However, it is strongly dependent on experimental data and represents the error made by the code rather than the actual uncertainty of the simulations.

Finally, it is possible to combine propagation and extrapolation methods, thus obtaining the benefits of each one. This is possible by using metamodels to obtain the uncertainty produced by the propagation of uncertain variables. Other uncertainties that are more complicated to study in this way are added a posteriori in an extrapolation exercise by validation of the phenomenology in experiments.

1.7. OUTLINE OF THE THESIS

As explained along the whole introduction, the main topic of the thesis is the study of the air-water annular flow and the analysis of uncertainties in the CFD simulations. The experimental part of the thesis has been developed in the thermo-hydraulics laboratory of the Institute for Energy Engineering, while the simulations have been carried out mainly in the offices of the same Institute. The specific objectives that were initially proposed are summarized as follows:

- The study of surface waves in air-water annular flow regime experimentally and by means of CFD simulation. Generation of a film thickness database for the following types of annular flow:
    - Downward free-fall.
    - Cocurrent with vertical drag.
    - Downward cocurrent.
- Development of conductivity sensors for precise measurement of liquid film thicknesses. Study of the size and separation of the electrodes to obtain an optimum sensitivity between 1 and $3\,mm$ thickness. Design and construction of the electronic circuit to amplify and rectify the sensor signal in the range $1-10\,V$. Calibration of the probes to work with the conductivity of the treated water in the laboratory.
- Uncertainty quantification and new development methods for the determination of uncertainties in calculations with CFD codes. Study of the Polynomial Chaos Expansion method by means of different techniques such as Gauss Quadrature or Collocation Points.

The following chapters of the thesis correspond to the different papers that have been published in relation to the previously introduced topic. This means that each chapter can be read individually since it is written in such a way that the study is introduced, the methodology is explained and the results are shown. However, in the introduction to the thesis, an overview of the topic as a whole has been given and the state of the art has been analyzed in much more detail. A summary of each chapter is shown below, as well as information related to the impact of each of the publications:

Chapter 1 corresponds to the introduction of the doctoral thesis. First, an overview of the most important features of the annular flow is shown, including its interest for the industry in general and for the nuclear sector in particular. Then, the particular behavior of the liquid in this flow regime is characterized and the most important variables of study are indicated. Next, an extensive literature review of the different techniques available for the measurement of the liquid film in annular flow is carried out and the experiences of other authors using them are detailed. The introduction also includes a listing of the most important experimental annular flow measurement facilities that have published measurements since 2000. Next, the state of the art of annular flow CFD simulations is detailed including the most important calculation equations. Finally, a review of the sources of uncertainty in CFD simulations and quantification methods is given.

The scientific articles that have been published as a result of the studies carried out in this thesis are included next. The first two publications correspond to the experimental part where laboratory measurements of different air-water annular flow regimes are shown. The next two are related to CFD simulation and uncertainty techniques.

Chapter 2 contains the first publication *Experiments in free falling and downward cocurrent annular flows - Characterization of liquid films and interfacial waves* (Rivera et al., 2022). This paper presents data collected in the GEPELON downward cocurrent air-water annular flow facility and proposes several correlations to calculate the most important liquid film variables. This paper includes several innovative features by presenting measurements and correlations of the liquid film at different heights and studying the sub-regime change that occurs with increasing air flow rate. This article has been published in the journal *Nuclear Engineering and Design* of the Elsevier group. Its impact factor in the 2021 *Journal Citation Reports* (JCR) of the *Web of Science* is 1.900, ranking 12/34 in the *Nuclear Science and Technology category* (Q2). According to the *Scimago Journal Rank* (SJR) of 2021, the journal is ranked 12/70 in the *Nuclear Energy and Engineering* (Q1) category.

The second publication included in **Chapter 3** of the thesis is *Experimental study of the effects produced by the changes of the liquid and gas surface velocities and the surface tension on the interfacial waves and the film thickness in annular concurrent upward vertical flows* (Rivera, Muñoz-Cobo, Cuadros, et al., 2021). In this paper, the study of the annular flow in upward cocurrent regime with vertical drag is proposed. In addition to collecting a large number of experimental measurements and correlations, this paper analyzes the effect of surface tension on the behavior of the liquid film by adding small amounts of 1-butanol. This article has been published in the journal *Experimental Thermal and Fluid Science* of the Elsevier group. Its impact factor in the *Journal Citation Reports* (JCR) of 2020 of the *Web of Science* is 3.232, ranking 7/34 in the category *Physics Fluids & Plasmas* (Q1). According to the *Scimago Journal Rank* (SJR) of 2021, the journal is ranked 8/70 in the *Nuclear Energy and Engineering* (Q1) category.

The third publication corresponding to **Chapter 4** is *CFD simulation plus uncertainty quantification of the mixing of two fluid with different density for the Cold-Leg mixing benchmark* (Rivera, Muñoz-Cobo, Berna, et al., 2021). This paper focuses on the development of the Polynomial Chaos Expansion methodology for the calculation of uncertainties by propagation in CFD simulations. The resolution of the expansion is solved by Gauss quadrature using orthogonal Hermite polynomials. In addition, the results obtained in the simulations of an international benchmark organized by the OECD/NEA (*Organization for Economic Cooperation and Development* in collaboration with the *Nuclear Energy Agency*) with open and blind phase are shown. This article has been published in the journal *Nuclear Engineering and Design* of the Elsevier Group. Its impact factor in the 2021 *Journal Citation Reports* (JCR) of the *Web of Science* is 1.900, ranking 12/34 in the *Nuclear Science and Technology category* (Q2). According to the *Scimago Journal Rank* (SJR) of 2021, the journal is ranked 12/70 in the *Nuclear Energy and Engineering* (Q1) category.

Chapter 5 corresponds to an adaptation and extension of the paper *Experimental Measurements and CFD Results of Liquid Film Thickness in Vertical Downward Air - Water Annular Flow* (Rivera, Muñoz-Cobo, Escrivá, et al., 2021). This publication has been published after having been presented at a conference with outstanding comments from the reviewers and coordinators. Although this paper presents the most important data and some results of the simulations carried out in relation to the GEPELON experimental setup, it was decided to greatly expand the contents. This chapter also includes an unpublished study on the application of the PCE methodology (developed in Chapter 4) to the simulations of the experimental facility. Therefore, the information collected in section 5.3 has been published in a short article in the *International Journal of Computational Methods and Experimental Measurement*s where the best papers of the *International Conference on Advances in Fluid Dynamics with emphasis on Multiphase and Complex Flow* (AFM/MPF 2021, 6-8 July Online) are included. This journal is not indexed in the Web of Science database. In the *Scimago Journal Rank* (SJR) of 2021 the journal is ranked 143/150 in the *Computational Mathematics category* (Q4).

Chapter 6 includes a discussion of the publications as a whole and shows the most important results of the thesis. It has been written in such a way that it is easy to concatenate the ideas of the different publications. In addition, this section contains the most important conclusions that can be drawn from the dissertation. It includes a section with the analysis of the achievement of the proposed objectives, as well as new lines of research arising from the research done.

Chapter 7 closes this document by including the complete bibliography that has been reviewed throughout the development of the thesis.

Chapter 2
FIRST PUBLICATION:
Experiments in free falling and downward cocurrent annular flows – characterization of liquid films and interfacial waves

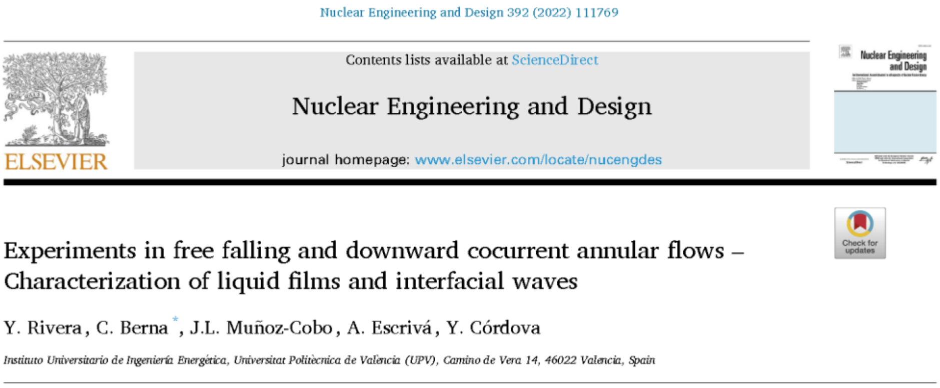

Nuclear Engineering and Design 392 (2022) 111769

Contents lists available at ScienceDirect

Nuclear Engineering and Design

journal homepage: www.elsevier.com/locate/nucengdes

Experiments in free falling and downward cocurrent annular flows – Characterization of liquid films and interfacial waves

Y. Rivera, C. Berna*, J.L. Muñoz-Cobo, A. Escrivá, Y. Córdova

Instituto Universitario de Ingeniería Energética, Universitat Politècnica de València (UPV), Camino de Vera 14, 46022 Valencia, Spain

https://doi.org/10.1016/j.nucengdes.2022.111769

Experiments in Free Falling and Downward Cocurrent Annular Flows – Characterization of Liquid Films and Interfacial Waves

Y. Rivera, C. Berna, J.L. Muñoz-Cobo, A. Escrivá, Y. Córdova
Instituto Universitario de Ingeniería Energética
Universitat Politècnica de València (UPV)
Camino de Vera 14, 46022 Valencia (Spain)
Tel: +34 963879245
Emails: yaridu@upv.es; ceberes@iie.upv.es; jlcobos@iqn.upv.es; aescriva@iqn.upv.es; yaicorc1@upv.es

Abstract

Falling liquid films and downward cocurrent flows in rounded shape pipes have been experimentally studied during the last decades, estimating the evolution of its major characteristics. The most important variables during the formation and growth of surface waves in falling downward flows have been measured using conductance probes.

The main objective of the current research paper is to study the dependency of the characteristics of the thin liquid layer for downward cocurrent annular flows. The GEPELON experimental facility consists of a vertical pipe with 3.8 m of useful test length. Two pipe diameters have been analyzed in this experimental study, 42 and $30\ mm$, in which the range covered by the liquid Reynolds number varies between $570 - 8500$ and $800 - 7900$ respectively, while the gas Reynolds numbers vary from 0 to $7.9 \cdot 10^4$ and from 0 to $1.1 \cdot 10^5$ respectively for the mentioned pipe diameters. Up to five conductance probes have been placed along the pipes test sections to capture the liquid film thickness fluctuations along time at different distances of the pipe entrance for both developing and fully developed regions.

After the study and analysis of the experimental data, the central point of this paper has been the development of new correlations for the liquid film thicknesses and the two major properties of the interfacial waves. Their adjustment procedure has been carried out in terms of dimensionless numbers, aiming to provide more general relationships. In particular, the magnitudes that characterize the interface behavior have been measured, particularly, film thicknesses, average disturbance wave amplitudes and disturbance wave frequencies for each boundary condition.

An additional part of the document contains an extensive comparison between the results obtained in this study and the data and expressions of other authors. It has been confirmed the significant dispersion existing among different researchers, especially when analyzing variables related to the interfacial waves. This highlights the lack of knowledge in some aspects even today. The different correlations proposed have been calculated based on the best fit of the data from all the series of experiments carried out in this study. Comparisons of the behaviour of these correlations with data from other researchers have also been included.

Keywords: Gas-Liquid Interface; Interfacial Waves; Disturbance Waves; Annular Downward Cocurrent Flow; Conductance Probe.

2.1. INTRODUCTION

The hydrodynamic behaviour of downward cocurrent gas-liquid annular flows has been vastly investigated over the past decades due to its huge importance in a broad range of industrial and natural processes. Specifically, a wide variety of phenomena involving free falling films is found in nature. In addition, thin liquid films freely falling or helped by a gas current appear in many industrial applications. Examples of industrial applications in which cocurrent flows occur are nuclear reactors, evaporators, condensers, and distillation columns. In particular, downward flows are observed in the nuclear industry under accidental scenarios for BWR and PWR (boiling and pressurised water reactors, respectively). In PWRs, downward flows appear in LOCAs (Loss of Coolant Accidents) and LOHS (Loss of Heat Sink Accidents) scenarios. While for BWRs, this kind of flow can be shown above the core after the injection of the ECCS (Emergency Core Coolant Systems). The characteristics of the liquid film sliding on the wall determine the heat transfer coefficient. The development of surface waves at the gas-liquid interface favours eddies' appearance, increasing the heat and mass exchange. Consequently, in order to be able to enhance the design and operation of all these systems, reducing costs and increasing efficiency, a better understanding of all physical processes involved in falling films is of great importance. Because of all these research studies, a considerable number of experimental investigations have shown that interfacial waves on a thin liquid film can substantially enhance the heat, momentum, and mass transfer rates.

In the early 20th century, Nusselt's research was one of the first to study the hydrodynamic characteristics of a thin laminar liquid film freely falling under the gravity effects (Nusselt, 1916a-b). Nusselt's model is the trivial solution of the conservation equations for a liquid film falling in a semi-infinite flat plate. Instead of the multiple simplifications of Nusselt's model, the calculations correctly estimate the liquid thickness under laminar conditions. In 1955, Kapitza proposed a modification of Nusselt's theoretical expression applicable for smooth wavy laminar flows (Aliyu, 2015). Many researchers have tried to obtain analytical solutions or empirical correlations to determine the major liquid layer characteristics under turbulent regime conditions. For instance, Musdawwar and El-Masri's (1986) proposed a semi-empirical correlation, which has shown a good accuracy against many experimental data series, but many other empirical expressions are also available (Takahama and Kato, 1980; Brauner, 1987; Pagmanaban, 2006; Aliyu, 2015).

Falling films, as they evolve downward, become turbulent and generate complex interfacial waves, which seemingly behaves randomly. This situation is favoured when cocurrent airflows are present. The wave generation and growth are dependent on the gravity force, the shear stress and the surface tension on the free gas-liquid interface. The way the surface waves emerge and grow and the hydrodynamic characteristics of the solitary waves play an essential role in the heat transfer enhancement. The initial basis which tried to understand and characterise downwards concurrent annular flows started in the 60s and 70s (Fulford, 1964; Telles and Dukler, 1970; Chu and Dukler, 1974 and 1975).

In addition, first attempts to understand the importance of the behaviour of the huge number of tridimensional interfacial waves, which are always present in any situation in which a gas-liquid interface exists, also comes from the 60s (Hanratty and Hersman, 1961; Hall-Taylor et al., 1963; Wallis 1969; Hewitt and Hall-Taylor, 1970). Two major types of interfacial waves are usually recognised that coexists on the interface between the liquid and the gas, the disturbance waves (DW) and the ripple waves (RW). It is important to emphasise that a precise nomenclature and definition of these types of waves continues up to now unsettled, even though some characteristics differencing both types of waves can be given. DWs are larger than RWs and also have significantly higher lifetimes. In addition, it is widely recognised that DWs cover the entire annulus of the tube. While RWs cover the surface between DWs, along the base film region and even over the DWs. The DWs' amplitude is much higher than those of RW, being several times larger than the mean thickness of the liquid layer. RWs are considered to be not coherent. Sekoguchi speaks about a third type of interfacial waves, the ephemeral waves, described in detail in Wolf's PhD (Wolf, 1995). These waves have amplitudes and lifetimes between RWs and DWs, being not circumferentially coherent and travelling at lower velocities than DWs. Ephemeral waves appear at the rear part of DWs, travelling between two adjacent DWs, until being reached and swallowed by the next DW. A possible cause of their appearance could be droplet deposition at high liquid flow rates. A fourth type of wave was observed by Alekseenko et al., Ohba and Nagae, the so-called "ring waves" (Alekseenko et al. 2009 and 2015). This type of wave was located in a narrow region near the onset of the entrainment region of upward annular flow, having characteristics quite similar to that of the ephemeral waves. Another type of wave is also mentioned by Sekoguchi (Alekseeenko et al., 2015), the "huge waves". They are observed at low gas and high liquid flow rates and are associated with the transition regime between slug/churn to annular flow. Huge waves are of higher amplitude, size and velocity than the DWs.

Not only the research mentioned above have been carried out related to the characterisation of the liquid and interfacial properties of annular flows. Many other research articles over the last years (Schubring and Shedd, 2008; Alekseenko et al., 2008, 2009 and 2014; Belt et al., 2010; Berna et al., 2014 and 2015; Setyawan et al., 2016; Dasgupta et al., 2017) concentrate on the wavy gas-liquid interface. Some of these studies were carried out for upward flow conditions, while others were under downward flows conditions. However, all of them provide additional details and/or consolidate the ones described above.

For instance, Berna's studies displayed a review of the most widely used expressions for annular flow characterisation along with several new correlations (Berna et al., 2014 and 2015). Alekseenko et al. (2014), under cocurrent downward flow conditions, explain that DWs and RWs are usually considered independently, while the authors consider that RWs' properties depend on the distance to the DWs. Three different zones are considered: the crest of DWs, the back slope of DWs and the base film zone. Fast RWs are shown in the first zone, while slow RWs exists in the base film region. The RWs are formed in the back slope of the DWs, and they gradually develop and stabilise as they move away from their creation point. The slow RWs run down the DW back slope, reaching the base film and travelling there until the next DW reaches it. Suppose they are formed beyond the separation or stagnation point (only exist when eddy motion is under the DWs hump, which means high enough turbulence). In that case, they accelerate towards the DWs front, where it disappears. The extinction is presumably caused by the gas shear stress, which leads them to disrupt into droplets or absorbed into the front part of the DW. Focusing on the fast and slow RWs, the authors explain that their velocities, when normalised by DWs' velocity, are almost constant for all the studied conditions. The number of fast RWs created by each DW was also constant at far distances from the entrance. Average lengths of DWs crests and back slopes decreased as gas velocity increased.

Whereas, under upward flow conditions, Dasgupta at al. (2017) goes a step further than 2014 Alekseenko's study in the relationship between DWs and RWs. The authors hypothesise that the presence of RWs is needed for a sustained DWs presence, giving a picture of the fully developed flow formed by a substrate of DWs above where large DWs move. In addition, the authors hypothesise that DWs propagate by catching downstream RWs and releasing new RWs into their upstream rear end. Even though Zhao's group showed that in the vicinity of the entrance, previously to the generation of DWs, the gas-liquid interface was plenty of waves with small amplitude and high frequency (Zhao et al., 2013). While Alekseenko's group found that, near the entrance, DWs are formed by multiple coalescence processes among these small high-frequency waves (Alekseenko et al., 2015). The authors also indicate that the most probably cause of these high frequency waves is the Kelvin-Helmholtz instability near the contact point between the gas stream and the liquid film. The authors, downstream the entrance, observed a similar phenomenon to that of the DWs formation, in this case for ephemeral waves formation, slow RWs behind the rear slope of the DWs coalesce to form these new waves.

The downward co-current annular regime characteristics, mainly those of the substrate and interfacial waves, allow distinguishing several different "sub-regimes" within it. Already in pioneering studies of annular flows, in particular those carried out by Webb and Hewitt (1975), four flow subregimes were identified, "ripple", "regular", "dual-wave" and "thick ripple" regimes, while recently, on Zadrazil's research a new regime has been proposed, the "disturbance wave" regime (Zadrazil et al., 2014). In the ripple regime, the completely gas-liquid interface is covered of RWs. The regular wave regime, flow regime in which the base film is covered by RWs, being crossed by DWs. The third type, the dual-wave regime, is characterised by the coexistence of DWs with two different shapes. The last regime identified by Webb and Hewitt, the thick ripple regime, in which the wave presence strongly diminishes, only sporadically large waves appear. The new regime identified by Zadrazil et al. (2014), the disturbance wave regime, which is characterised by more frequent waves of large amplitude than in the rest of regimes, and also with high rates of entrainment between both phases, from gas to liquid and from liquid to gas phases.

Another important aspect that has been extensively treated over the last decades are the lengths needed to reach fully developed flow. There is a conflict to determine the length needed to reach fully developed flow. Different researchers predict different development lengths depending on the analysed parameter. Usually, mean film thickness is the first variable to be fully developed, followed by wave amplitudes and finally wave frequencies. For the mean film thickness in annular flow, several researchers found that the necessary length for the flow to be fully developed depends on ReL. Specifically, for relatively low liquid Reynolds numbers, ReL = 400, the development length was found to be 32 D from the inlet. In contrast, for high liquid Reynolds numbers, Rel = 1000, this length is 12D (Takahama and Kato, 1980). Other researchers explain that the wavy flow probably would not be fully developed at these distances from the flow entrance. However, changes are not as large as those for smaller distances (Karapantsios and Karabelas, 1995). For wave amplitude and frequency, distances of at least 160 and 470 D from the inlet respectively are found to be necessary to be under fully developed flow conditions (Webb and Hewitt, 1975). Even though Webb and Hewitt also report that at about 150D from the inlet, the mean wave frequency approaches its fully developed value within approximately 10% for falling films, a value that depends on the liquid Reynolds number.

Concerning the measurement techniques used to characterise the liquid film thickness, four large groups could be established (Clark, 2001), i.e., film average (hold-up measurements, weighing methods, etc.), localised (capacitance and conductance probes, etc.), point (laser scattering methods, interferometric methods, etc.) and spatial (fluorescent imaging methods, ultrasonic transmission methods, etc.). Even though electrical methods based on conductance or capacitance have been the most widely used (Wolf et al., 2001; Belt et al., 2010; Dasgupta et al., 2017; Cuadros et al., 2019). During the last years, visualisation techniques, mainly Laser-Induce Fluorescence (LIF), are also widely used (Liu et al., 2006; Schubring et al., 2010; Zadrazil et al. 2014; Alekseenko et al., 2014; Charogiannis et al., 2019). The current study is based on the variation of water conductance with film thickness, i.e., a localised method implemented using conductance probes. Specifically, five of them have been placed at different positions from the flow entrance in the current study to characterise fully developed downward flows and under development flows.

2.2. EXPERIMENTAL FACILITY LAYOUT

2.2.1. THE GEPELON EXPERIMENTAL FACILITY

The GEPELON (GEneración de PELícula ONdulatoria or translated to english Ondulatory Film Generation) experimental flow facility, at this first stage, has been designed to generate a film of liquid stuck to the wall while having the air mass in the central part, either quiescent or in co-current, i.e. downward annular air-liquid flow descending a vertical pipe. The expected phenomena will be similar to the behavior of passive cooling systems in third-generation reactors, but only in their hydraulic behavior. The installation does not use heated fluids; therefore, it does not take into account heat transfers between the fluids or the wall in this first stage.

The facility configurations are displayed in Figure 2.1 and have been previously summarized by Rivera et al., (2020). The useful height of the experimental test section is 3.8 m approximately, and there are two different test sections, consisting of two pipes with 30 mm and 42 mm internal diameter respectively. Two main circuits constitute the facility, so that both air and water properties can be checked separately before being introduced into the test section. Therefore, the following main groups of components constitute the installation: the air pumping system, the water pumping system, the injection/mixing system, the test section and the water collection/recirculation system. This set of components is equipped with various devices and sensors, thus being able to measure and/or control the main variables necessary to know/modify the experimental conditions and to be able to perform the subsequent analysis.

The water used in all experimental data sets is thoroughly handled before being fed into the loop. Its properties are adequately controlled, in order to have an appropriate conductivity with no pollutants or impurities. Along the way from the tank to the injector, the water goes through several devices for both control and measurement. In particular, the conductivity calibration sensor, shown in Figure 2.1, records any possible change in the water conductivity before the measurements are made. These measurements are sent to the data acquisition program (DAQ) to adjust the calibration curve of the different probes. However, due to the low variability of the temperature achieved by the temperature control unit, the conductivity hardly changes once such stable conditions are attained. In addition, the pump power is maintained at the correct duty point by an inverter that monitors the water flow rate and modifies the pump frequency using a PID regulator. The water temperature is also maintained in the circuit at 21℃ through a temperature control station, which changes the water temperature if necessary to keep it constant. Several regulation and safety valves, filters and other devices, as displayed in Figure 2.1, are installed along the circuit for different complementary purposes.

In the free-fall configuration, the water flow is impelled into the system by a water pump (maximum pumping pressure of approximately $4.2\ bar$). The pump drives the water to the top of the standpipe through a self-designed pressurized water injection system. The injector's operation principle is based on the pressure difference between both sides of the device. Due to this pressure difference, the water passes through a sintered stainless steel tube due to this pressure differences (Cuadros et al., 2019). The pore size of this component is $19 \cdot 10^{-6}\ m$ and the coefficient of viscous permeability, y_S, is $0.8 \cdot 10^{-12}$. The injection system, the test section and the separation tank (Figure 2.1) are duplicated, so that there are two test sections of $42\ mm$ and $30\ mm$ inner diameter, both with a length of $3.8\ m$.

By gravity, the water descends sticking to the inner surface of the methacrylate tube and flows down through the test section, finally the water is collected in a storage tank. This water reservoir is a large capacity plastic tank, from which the water recirculation pump sucks the fluid and pushes it back into the injector system, so that the water starts a new loop.

The arrangement of the experimental installation for the second configuration, cocurrent experiments, is the same as the free falling with the only difference of the existence of an air injection system. The air stream is filtered, dedusted and demisted prior to its injection into the upper part of the facility, Figure 2.1. A compressor, a stabilization tank, a flowmeter, and several safety and control valves compose the air circuit. The compressor has maximum working pressure of 8 bars and a maximum volumetric flow rate of $3750\ l/min$ approximately. Even though, only air flows up to $2500\ l/min$ have been reached for the current experimental conditions.

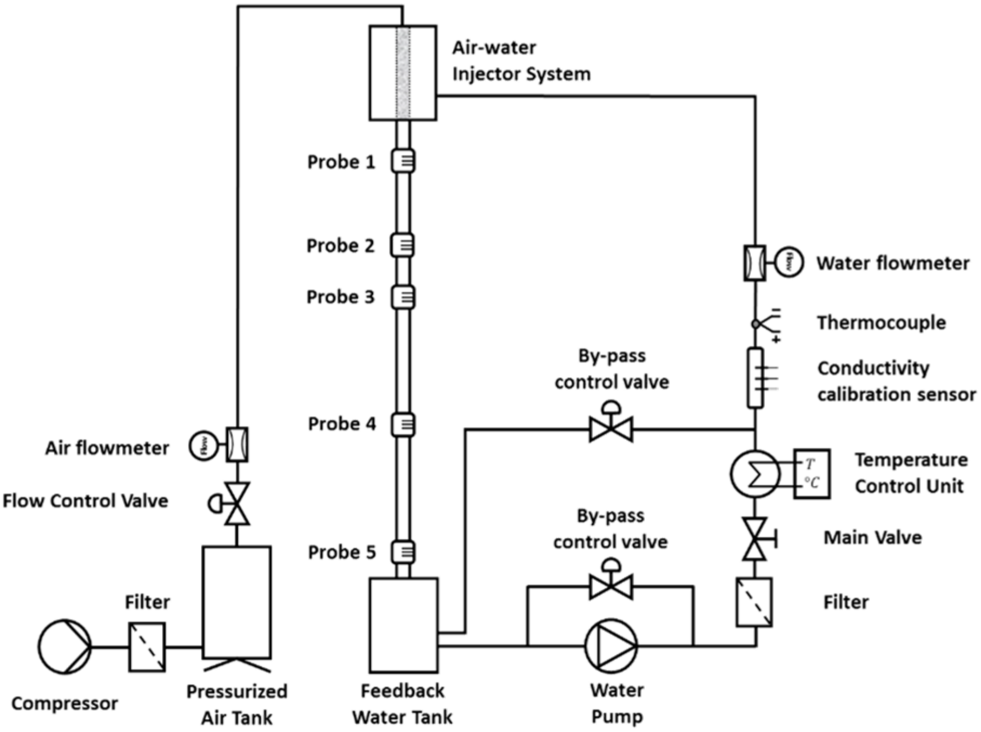

Figure 2.1. Schematic view of the GEPELON flow diagram showing the five conductance probes (Rivera et al., 2020).

As mentioned above, test section consists of two vertical methacrylate tube of almost 4 meters long. In the current experimental study two different tubes have been used, one with an inner diameter of $42\ mm$ and the other with $30\ mm$. The facility, between the water injection and extraction systems, has a height of approximately 5 meters. The experimental conditions are measured along this test section. At five distances from the water flow entrance, interfacial wave measurement ports have been installed (labelled as Probes in Figure 2.1) in order to capture the major film and wave properties.

2.2.2. CONDUCTANCE PROBE

Conductance probes are based on the difference in the conductivity of the device with the thickness of the liquid film (Clark, 2001; Tiwari et al., 2014; Muñoz-Cobo et al., 2017). This technique is probably the most widely used when trying to measure temporal variations of film thicknesses. The performance of conductance probes follows the potential field theory, in such a way that the behavior of the liquid layer between electrodes subjected to an alternating current is basically resistive when the frequency of the excitation signal is sufficiently high

(Muñoz-Cobo et al., 2020). In summary, there is a proportionality between the liquid layer between electrodes and the current transmitted between them. The conductance probe consists of three electrodes, which are embedded in the wall and aligned parallel to the flow direction. The transmitting electrode is located at one end of the device, emits a sinusoidal signal of $100\ kHz$ and $5\ Vpp$. The conductance probe has a ground connection, which is placed in the central section. At the other end of the device, the receiver electrode is positioned. This electrode is responsible for the reception of the signal. The way the device works is as follows: the electrical signal is emitted by the first electrode, this signal is transmitted through the thin layer of water, and collected by the receiver so that there is a proportionality between the received signal and the liquid layer thickness.

ARCHITECTURE OF THE CONDUCTANCE PROBE

All conductance probes have been built in Acrylonitrile Butadiene Styrene (ABS), this choice is justified by its excellent mechanical properties. The port design has an inside diameter equal to that of the test pipe cross-section, and an overall length of approximately $170\ mm$. Each conductance probe has three $1.5\ mm$ ID electrodes, each spaced $1.5\ mm$ and aligned with the flow direction. The selection of the electrode diameter and their distance is the result of a compromise solution between the desired measurement range and the desired achievable precision of the measurements. Larger and more separated electrodes make possible to measure larger thicknesses, but in return, leads to measurements of lower spatial resolution, since they are obtained by averaging over longer lengths (Rivera et al., 2021). The stainless steel electrodes are placed in the middle section of the device. (Figure 2.2A). The conductance probes are positioned near the lower part of the test section, specifically at 83 and 117 diameters of the test entrance for the 42 and 30 mm pipes respectively, as displayed in Figure 2.2B.

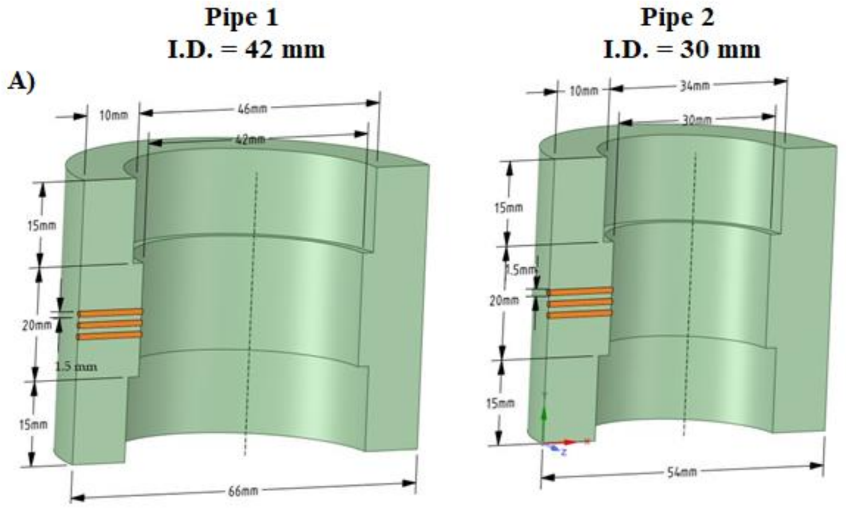

Pipe 1
I.D. = 42 mm

Pipe 2
I.D. = 30 mm

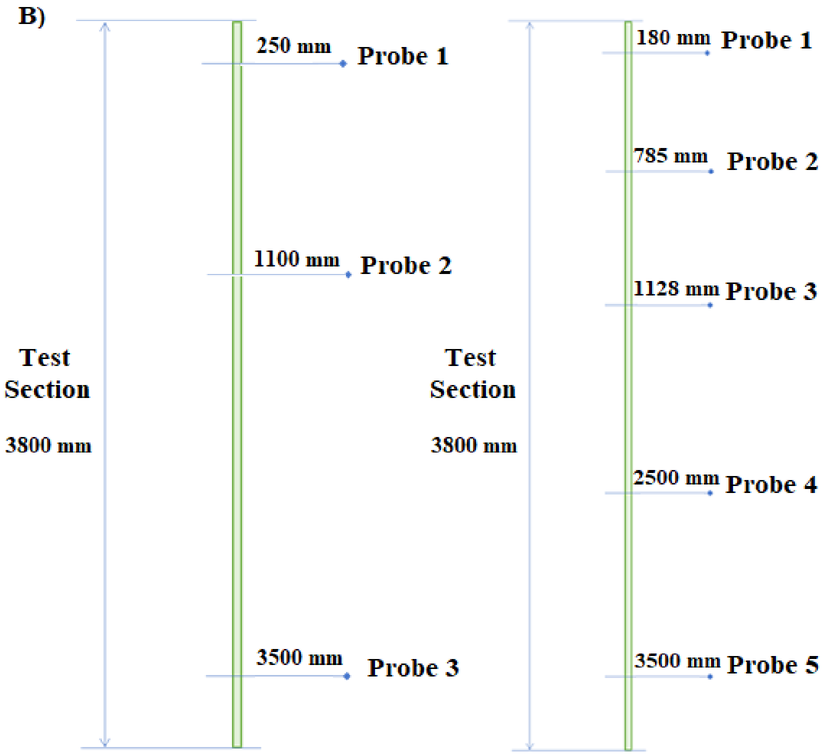

Probes	Position (mm)	Diameters
1	250	6 D
2	1100	26 D
3	3500	83 D

Probes	Position (mm)	Diameters
1	180	6 D
2	785	26 D
3	1128	38 D
4	2500	83 D
5	3500	117 D

Figure 2.2. Schematic view of the conductance probes: A) Probe Geometry; B) Facility Positioning.

ELECTRONICS OF THE CONDUCTANCE PROBE

A schematic view of the electronic circuit connected to the conductance probes is displayed in Figure 2.3. This device has been designed to emit, receive, amplify and filter an electric signal. It consists of four high-frequency amplifiers, a couple of precision resistors (0.1% tolerance) and 1N4148 diodes. High precision and low tolerance components have been used in order to have the device as most accurate as possible. The electronic second-order low-pass filter is designed to cut-off frequencies above $149\ Hz$ using the Sallen-Key architecture (Leven, 2007). Butterworth filter was selected so the attenuation above the cut-off is $-20\ dB/decade$.

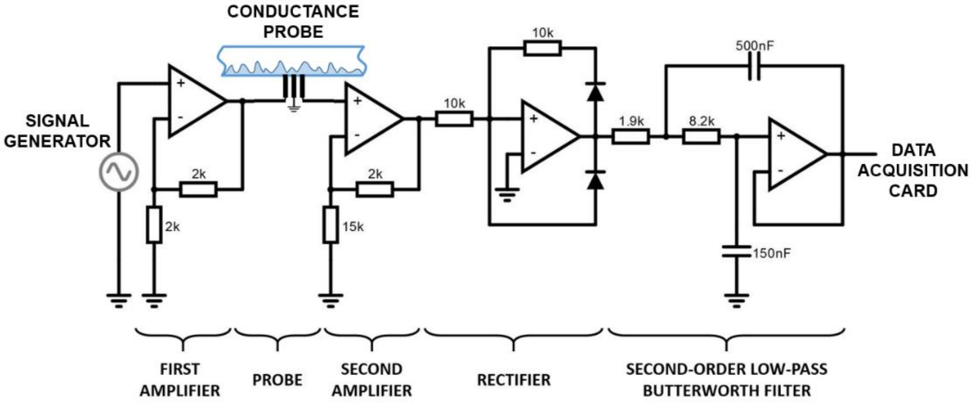

Figure 2.3. Detail view of the Electronic circuit designed for the use of the conductance probe.

The electronic circuit consists of two distinct parts, the transmitter and the receiver. One part of the electronic circuit is responsible for generating and transmitting a sine wave signal, the signal is produced by a signal generator and is directed to the electrode through the circuit that excites the transmitting electrode. While another part of the electronics picks up the signal returning from the receiving electrode, this signal will depend on the thickness of the water film between the two electrodes. Finally, the wave passes through a rectifier circuit and a filter to obtain a DC signal. This value is collected through a data acquisition card and stored in the computer for further post-processing.

The units of the initial registered raw signal are volts, values that do not directly provide any useful information, thus it is necessary to calibrate the probes beforehand to transform this raw signal (in volts) to a processed signal (in millimeters) to determine film thickness, wave amplitudes, etc. To perform the calibration, a new gadget has been designed, the probe calibration device.

CONDUCTANCE PROBES CALIBRATION PROCEDURE

The calibration procedure of each conductance probe must be carried out previously to their installation in the GEPELON facility. The objective of the calibration procedure is to be able to accurately correlate the voltage signal measured with the probes to the thicknesses of the water layer.

To achieve higher accuracy than in former surveys (Rivera et al., 2019; Cuadros et al., 2019) an improved device has been used, in line with the calibration gadget shown for a vertical upward facility (Rivera et al., 2021). The major components of the conductance probe calibration device are displayed in Figure 2.4. The water used in the experiments has been treated in order to have a fluid with a controlled value of the conductivity, in our case it has been set to $50\ \mu S$.

Multiple measurements were conducted in order to determine the optimum excitation values of the conductance probes, both for frequency and voltage. As presented above, the final excitation signal selected was a sinusoidal signal of $100\ kHz$ and $5\ Vpp$.

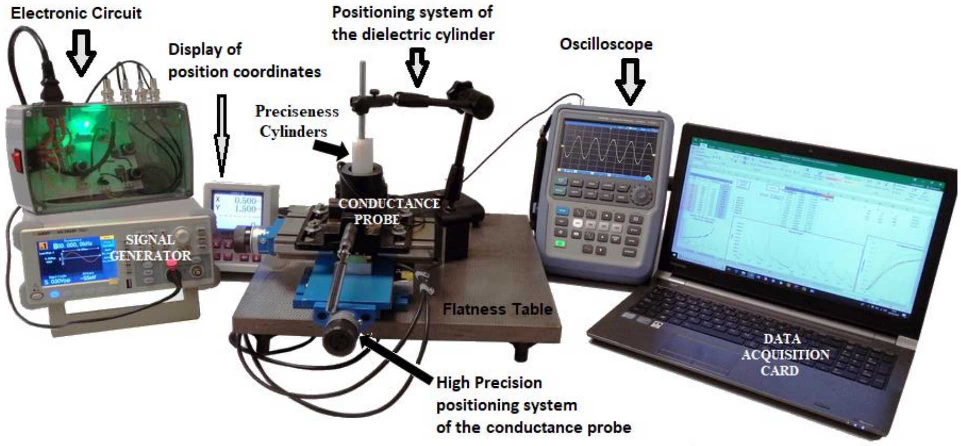

Figure 2.4. Devices of the Conductance Probe Calibration Procedure.

The calibration procedure is performed on the calibration device for all conductance probes employed in the experimental sets. This gadget consists essentially of the following main parts: an electronic precision positioning system; a flatness table; and several cylinders. Each dielectric cylinder, of known diameter, is located through the positioning system at the central position of the interior side of the conductance probe port. A high precision positioning system allows for knowing the exact placement of the cylinders, so that the exterior side of the cylinder and the interior side of the probe are at a constant known distance in their entire circumference. The existing gap between the conductance probe and the dielectric cylinder is filled with the treated water.

The major steps of the calibration procedure are as follows:

- Signal generator sends the sinusoidal signal
- Probe-emitting electrode is excited by this signal
- Electric signal goes through the know liquid layer
- Attenuated signal is received by probe-receiver electrode
- Signal is collected by the data acquisition card
- Relation between liquid layer thickness and the electric signal can be determined, as the liquid layer is known, and the signal has been measured.

The procedure has been repeated using all dielectric cylinders, in order to have enough adjustment points between electric signal and liquid layer thickness, and for each conductance probe. More than 20 calibration points have been measured for each of the 8 probes to determine any of the calibration curves.

Because of the high sensitivity to the physical properties of the environment of this type of sensors, not only the conductivity of the water but also its temperature might be of extreme importance to accurately relate the measured voltage signal to the thicknesses of the water film. Although, the shape of the calibration curve would not change appreciably due to narrow variation ranges of fluid properties affecting conductivity. Figure 2.5 shows the calibration points measured with the calibration device and the fitted calibration curves for one of the probes mounted in each of the two pipes used in the experimental facility.

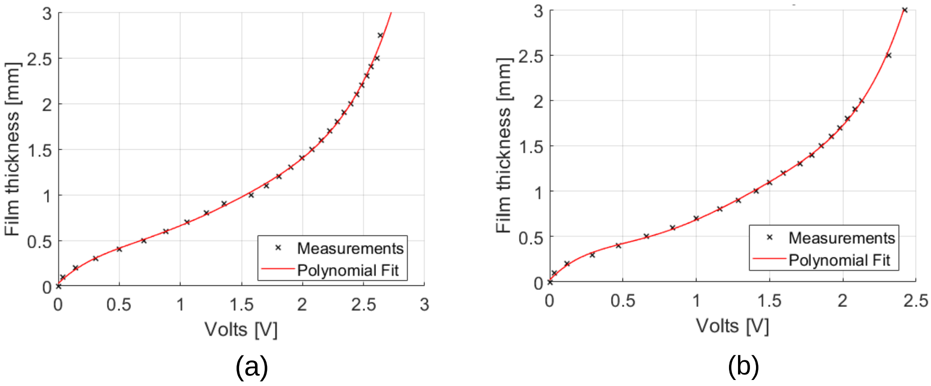

(a) (b)

Figure 2.5. Fitting Curve and Calibration Points of the Conductance Probes up to its saturation point: a) 30 mm I.D.; b) 42 mm I.D.

Additionally, in order to adjust these possible conductivity changes, a conductivity calibration sensor has been placed in the GEPELON facility, also shown in Figure 2.1. This device measures the water saturation voltage and sends the value to the DAQ program to adjust the calibration curve of the different probes. The conductivity calibration sensor, before performing the probe measurements, will register any change in the water conductivity. However, due to the high temperature stability achieved with the temperature control unit, the conductivity does not change once stable conditions are attained.

The values for both the signal amplitudes (Volts) and their conversion in film thicknesses (mm) were smaller than $3\,V$ and $3\,mm$ respectively, as shown in Figure 2.5. With this data, the calibration curves for both conductance probes, the ones for the 30 and $42\,mm$ of inner diameter, are displayed:

$$h = 0.111\,V^5 - 0.6598\,V^4 + 1.5582\,V^3 - 1.6682\,V^2 + 1.291\,V + 0.027 \qquad (2.1)$$

$$h = 0.299\,V^5 - 1.6616\,V^4 + 3.5121\,V^3 - 3.203\,V^2 + 1.718\,V + 0.020 \qquad (2.2)$$

in which V is given in Volts and thicknesses of the liquid layer are given in mm. The determination coefficients of all polynomial fits were $R^2 = 0.9993$ and 0.9995 respectively, being the RMS errors of 0.026 and $0.0018\,mm$.

The expression used to calculate the fitting errors $\varepsilon_{fit,cal}$ of Eqs. (2.1) and (2.2) is found in chapter 7 of the book of Bevington and Robinson (2003) and is given by:

$$\boldsymbol{\varepsilon_{fit,cal}} = \sqrt{\frac{\sum_{j=1}^{n}\left(\boldsymbol{h_i} - \boldsymbol{h_{i,fit}}\right)^2}{\boldsymbol{n - m}}} \tag{2.3}$$

in which h_i are the experimental data, $h_{i,fit}$ are the values obtained using the calibration curves, n is the number of the calibration data points and m the degrees of freedom (in this case 5, polynomial degree). Carrying out the calculations for both pipes, the final values of the calibration errors are 0.026 and $0.018\,mm$ for the 30 and 42 inner pipe diameters, respectively.

2.3. EXPERIMENTAL CONDITIONS, FILTERING PROCEDURE AND ERROR ANALYSIS OF THE CONDUCTANCE PROBE MEASUREMENTS

2.3.1. EXPERIMENTAL CONDITIONS TEST MATRIX

The test matrix consisted of two groups of test runs, one for each pipe diameter, changing the water and gas flows. The water flow ranges approximately from 1 to 15 and 1 to $10\,l/min$ for the 42 and $30\,mm$ of inner pipe diameters respectively, increasing the liquid flow rate liter by liter from the minimum value up to the maximum. While the air flow rate varies from stagnant conditions up to approximately $2500\,l/min$. The combinations of these two flows, both liquid and gas, have been carried out during the experimental measurement procedure. The test conditions in terms of volumetric mass flow rate, superficial velocities and superficial Reynolds numbers for the gas and liquid phases for both pipe diameters are summarized in Table 2.1. These dimensionless numbers have been defined in the usual way, the gas and liquid Reynolds numbers at the fluid entrance conditions have been defined in terms of superficial velocities:

$$Re_L = \frac{\rho_l J_L D}{\mu_l} = \frac{4\,\rho_l\,Q}{\pi D\,\mu_l} \tag{2.4}$$

$$Re_G = \frac{\rho_g\,J_g\,D}{\mu_g} \tag{2.5}$$

In short, the theoretical ranges covered by the gas Reynolds (Re_G) are from $0 - 78946$ and from $0\ -\ 110524$ for the 42 and $30\,mm$ of inner diameter pipes. While the ranges covered by the liquid Reynolds (Re_L) are from 570 to 8500 and from 800 to 7900 approximately for the 42 and $30\,mm$ of inner diameter pipes. In practice, the experimental points are not precisely those of Table 2.1 but those obtained from the averaged flow values for the six experimental data series for each condition.

In each test, the experimental conditions were monitored and stored in real-time, the variables acquired include volumetric water flow rates, temperatures and pressures, along with measurements from all conductance probes. The data acquisition system has been programmed in LabView software. Two forms of data acquisition are clearly differentiated according to their relevance. The main focus of the present research study is the measurements of the conductance probes. For this purpose, a PCI 6255 card from National Instruments (with 80 analog channels and a maximum storage capacity of $1.25\ MS/s$) was used, this data acquisition card is capable of recording up to 10^5 samples per second. While the rest of the measurements, those of lesser importance, are collected with an acquisition system that is capable of recording 100 samples per second (National Instruments cDAQ-9174 chassis compactDAQ with a NI 9207 module with 16 analog channels and a maximum rate of 500 S/s).

Table 2.1. Experimental test matrix performed in the GEPELON facility.

WATER SETUP RANGE				
Q_L [l/min]	J_{L_42} [m/s]	Re_{L_42}	J_{L_30} [m/s]	Re_{L_30}
1	0.01	566	0.02	800
2	0.02	1132	0.05	1600
3	0.04	1697	0.07	2400
4	0.05	2263	0.09	3200
5	0.06	2829	0.12	4000
6	0.07	3395	0.14	4800
7	0.08	3961	0.17	5600
8	0.10	4526	0.19	6300
9	0.11	5092	0.21	7100
10	0.12	5658	0.24	8000
11	0.13	6224		
12	0.14	6790		
13	0.16	7355		
14	0.17	7921		
15	0.18	8487		

AIR SETUP RANGE				
Q_g [l/min]	J_{g_42} [m/s]	Re_{G_42}	J_{g_30} [m/s]	Re_{G_30}
0	0	0	0	0
250	3.0	7895	5.9	11000
375	4.5	11842	8.8	17000
500	6.0	15789	11.8	22000
625	7.5	19736	14.7	28000
750	9.0	23684	17.7	33000
875	10.5	27631	20.6	39000
1000	12.0	31578	23.6	44000
1500	18.0	47368	35.4	66000
2000	24.1	63157	47.2	88000
2500	30.1	78946	58.9	111000

The procedure carried out for each test is as follows:

- Adjustment of the liquid flow rate to the target value.
- Verification of the stability of the main experimental parameters (temperatures, pressures, liquid flow rate), carried out by monitoring the signals in real time using the LabView program.

- Data collection, recording of two data files for ten seconds (a file with $5{\cdot}10^4$ points for the conductance probe and another file for the rest of the data with 10^3 points for each variable).

Six runs of ten seconds for each water flow rate have been carried out. Consequently, six series of $5{\cdot}10^4$ points of raw data for the conductance probe in each experimental condition have been recorded.

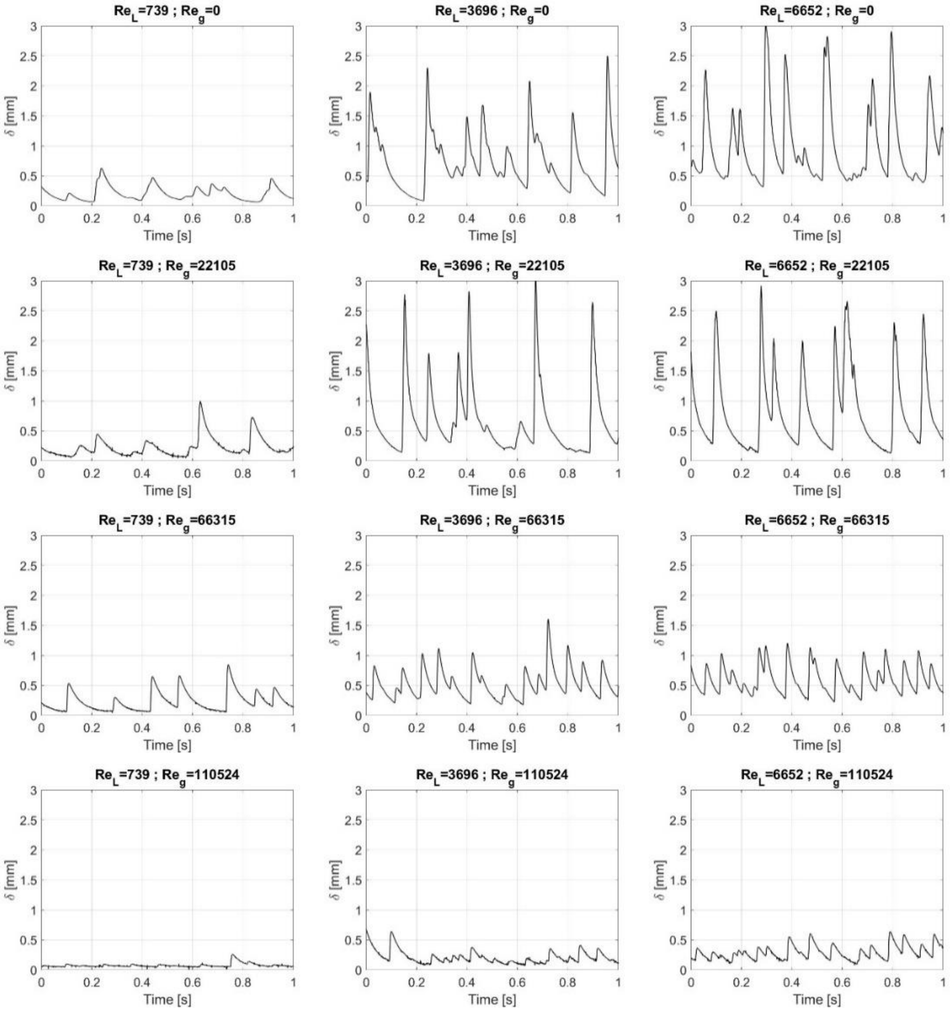

Figure 2.6. One second zoom of the film thickness variation for several air-water conditions in the fully developed region for the 30 mm inner diameter pipe.

2.3.2. MEASUREMENTS AND ERRORS OF CONDUCTANCE PROBES

After collecting the raw data of the probe signal, the next step was to use the calibration functions. In this way the volts versus time collected signal was converted in millimeters vs time. These signals give the liquid layer thickness evolution over time on the measurement region.

The next stage was to filter the converted raw data using a Savitzky-Golay moving average filter. The use of this type of filter is motivated by the fact it maintains the height and width of the peaks and, in addition, causes very low distortion in the signal (Rivera et al., 2021). The Savitzky-Golay filter was applied using a polynomial of order $p = 8$ and a frame length of $m = 101$. The comparison of the film thickness signal before and after the filtering procedure using the Savitzky-Golay moving average filter shows no appreciable differences, the height and widths of the peaks remain practically unchanged after performing the Savitzky-Golay filtering procedure. However, a noticeable reduction in the electronic noise has been achieved.

As a first contact to the experimental measurements, a zoom of one second for several representative gas and liquid experimental conditions for the fully developed flow (lower probe) are shown in Figure 2.6. As displayed in the figure, the height of the DWs presents an appreciable decrease with the gas Reynolds number, while, at a first glance, a less significant increase with the liquid Reynolds number is revealed.

The total error can be calculated by adding up the systematic and random errors in a quadratic form:

$$\boldsymbol{\varepsilon_{total}} = \sqrt{\boldsymbol{\varepsilon_{syst}}^2 + \boldsymbol{\varepsilon_{acc}}^2} \tag{2.6}$$

The systematical error has the following contributions: the error of the data acquisition system, i.e., the error of the voltage measurement equipment, ε_{DAQ}; the fitting error, $\varepsilon_{fit,cal}$, given by Eq. (2.7); and the position error during the calibration process, ε_{pos}.Then, the total value of all three terms of the systematic error can also be obtained by adding them up in a quadratic form:

$$\boldsymbol{\varepsilon_{syst}} = \sqrt{\boldsymbol{\varepsilon_{DAQ}^2} + \boldsymbol{\varepsilon_{fit,cal}^2} + \boldsymbol{\varepsilon_{pos}^2}} \tag{2.7}$$

To calculate the error caused by the data acquisition system, a propagation of the voltage error should be done in the polynomial calibration functions, given by Eqs. (1) and (2):

$$h = c_1 \cdot V^5 + c_2 \cdot V^4 + c_3 \cdot V^3 + c_4 \cdot V^2 + c_5 \cdot V + c_6 \tag{2.8}$$

then, propagating the voltage errors in the previous expression:

$$\begin{aligned}\varepsilon_{DAQ} = \left\{\frac{\partial f(V)}{\partial V}\right\}\varepsilon_V = \\ &= |c_1 \cdot V^5| \cdot \left(5 \cdot \frac{\varepsilon_V}{V}\right) + |c_2 \cdot V^4| \cdot \left(4 \cdot \frac{\varepsilon_V}{V}\right) + |c_3 \cdot V^3| \cdot \left(3 \cdot \frac{\varepsilon_V}{V}\right) \\ &+ |c_4 \cdot V^2| \cdot \left(2 \cdot \frac{\varepsilon_V}{V}\right) + |c_5 \cdot V| \cdot \sqrt{\left(\frac{\varepsilon_V}{V}\right)^2}\end{aligned} \tag{2.9}$$

Being the final values of the data acquisition system errors 0.0099 and $0.0155\, mm$ for the 30 and 42 inner pipe diameters respectively. The calibration probe positional system has a resolution of 0.002 mm, so this value has been taken as the positioning error, $\varepsilon_{pos} = 0.002\, mm$.

The accidental or random error (ε_{acc}) is evaluated from 6 sets ($N = 6$) of 10-second measurements ($5000\, samples/second$) by means of the *Standard Error of the Mean* (½ of the confidence interval). A Matlab script processes measurement data and the random error is calculated for each test. Then, the accidental error is given by:

$$\varepsilon_{acc} = t_{n-1}^{\alpha/2} \frac{s_n}{\sqrt{n}} \tag{2.10}$$

being $t_{n-1}^{\alpha/2}$ the t-Student of $1 - \alpha/2$ quantile for $n - 1$ degrees of freedom, n the number of measurements performed, and s the quasi-variance $s_n = \sqrt{\frac{\sum(x_i - \bar{x})^2}{(N-1)}}$. The quantile value of the t-Student depends on the degrees of freedom and confidence level, having a value of 2.571 for five degrees of freedom and the widely used 95% confidence level ($\alpha = 0.05$).

Finally, a summary table of the total errors for the variables estimated along this research, using Eq. (2.6), is displayed in Table 2.2.

Comment that another possible source of errors, not directly attributable to the measurement procedure, could be the extent of DWs incoherence along the circumferential section of the pipe (Cuadros et al., 2019). Summary conclusions could be that pipes of larger diameters conduct to higher DWs incoherence, while high gas flow rates lead to lower incoherence of the DWs, with no appreciable effect of the liquid mass flow rate. Anyway, as the current experimental measurements were registered during long-term intervals, then a significant mean value of the evolution of the different variables is obtained under fully developed flow conditions. Therefore, all these circumferential effects are not considered a major cause of errors.

Table 2.2. Average error and maximum error obtained for the set of all the measurements made for this study.

Variable	Acronym	Average Error	Maximum Error
Mean film thickness (mm)	h_{mean}	0.020	0.025
Disturbance waves height (mm)	h_{DW}	0.059	0.155
Disturbance waves frequency (Hz)	ν_{DW}	0.418	2.85

Another source of error attributable to conductivity probes, and intrinsically unavoidable to them by their nature, is the averaging of measurements over a small region of space. As previously mentioned, to reduce this error, a compromise must be reached in the design of the probes (number and arrangement of the electrodes, as well as the distance between them and their thickness). So that the probe does not saturate before the maximum value of liquid layer to be measured but, at the same time, it is as accurate as possible. Consequently, with an appropriate design specific to the experimental conditions, it is considered that this method has acceptable precision. Different researchers (Clark, 2001; Setyawan et al., 2016; Dasgupta 2017; Muñoz-Cobo et al. 2020) share this opinion. In the current case, a study of different probe configurations of probe has been carried out considering the arrangement, distance and thickness of electrodes. So that different arrangements have been analysed, for example, once the optimal thickness and distance is selected, several tests have been made with three electrode arrangements, parallel to the flow, perpendicular to the flow and forming an equilateral triangle. Although they all provide very similar measurements, probes with a flow-parallel arrangement have been used in this study. To obtain global information from a wider region and to go into more details of waveform analysis, especially of ripple waves, optical methods would probably be more suitable. Although, these methods also have drawbacks, mainly due to errors caused by total internal reflection (TIR) by refraction or TIR of fluorescence emission at the gas-liquid interface. Nevertheless, research is currently in progress to reduce these errors with very promising results (Cherdansev et al., 2019; Charogiannis et al., 2019).

2.4. MAGNITUDE ESTIMATION FROM THE CONDUCTANCE PROBE MEASUREMENTS

This section displays a summary of the treated measurements of the conductance probe signals, already converted into length units. Specifically, the test matrix displayed in Table 2.1 has been studied. Six series of 10 seconds for each experimental condition have been collected, from which, the principal variables concerning film thickness and interfacial waves have already been analyzed and estimated.

The magnitudes that have been analyzed in the experiments (Figure 2.7), along with their definition are:

- Mean Film Thickness, h_{mean}, averaged value of the liquid layer thickness;
- Disturbance Wave Peak Height, h_{DW}, which is measured from pipe wall to wave crest;
- Disturbance wave frequency, υ_{DW}, averaged value of the number of peaks per second.

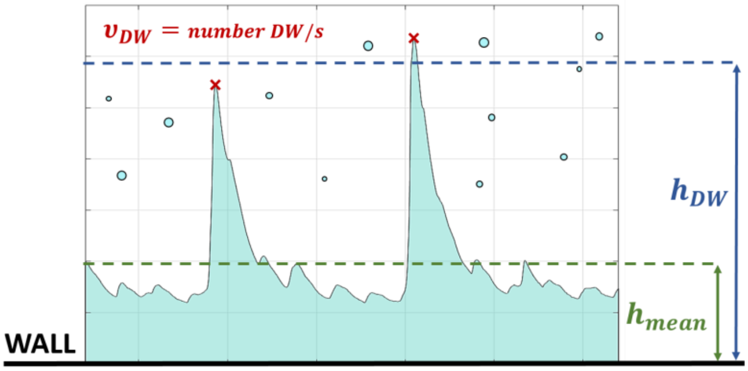

Figure 2.7. Schematic representation of the major variables that determine interfacial waves properties in vertical downward concurrent flows.

2.4.1. ANALYSIS OF FLOW DEVELOPMENT WITH DISTANCE

Several conductance probes have been placed along the facility to study the film thickness for developed conditions and for developing flow (Figure 2.1). The study of this evolution can be important because similar conditions of current research take place in different industrial processes under accidental or working conditions. For instance, both free and forced downward cocurrent flows can occur under accidental conditions on the U-tubes of steam generators in PWRs.

Figures 9a and 9b show several examples of the mean film thickness variation as a function of the distance to the $30\ mm$ inner diameter pipe entrance. As clearly shown in the figure, there is an asymptotical increase with the distance to the entrance towards a maximum value of film thickness. The value of this maximum depends on both fluid flow rates. This maximum for developed flow conditions increases with the increase of the liquid flow and decreases with the increase of the gas flow.

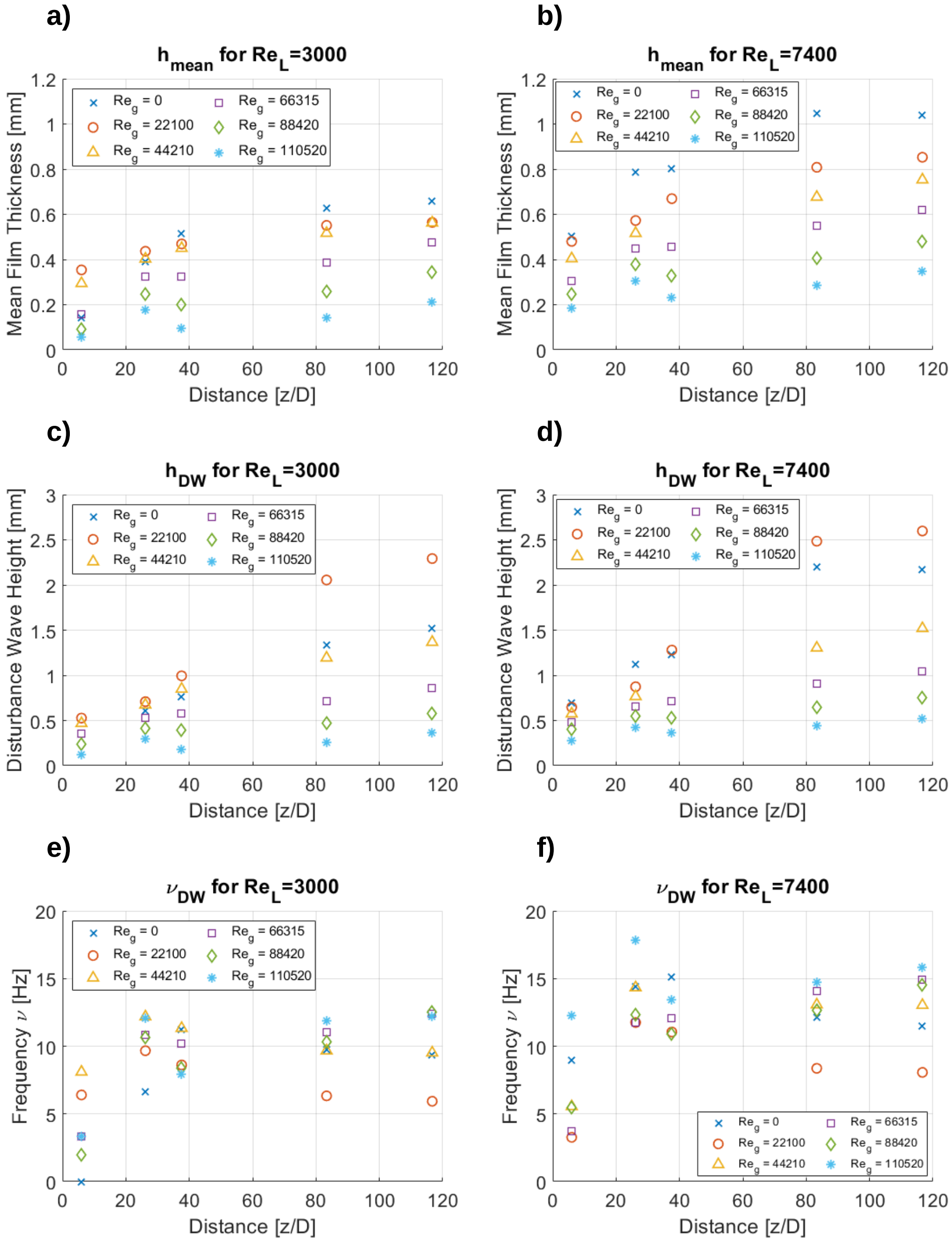

Figure 2.8. Mean Film Thickness (h_m) and disturbance waves height and frequency (h_{DW} and ν_{DW}) versus entrance distance for several gas Reynolds numbers at constant liquid Reynolds number: a), c), e) $Re_L = 3000$; b), d), f) $Re_L = 7400$.

The evolution of the disturbance wave height with distance from the inlet follows a similar but more pronounced behavior than the mean films thickness (Figure 2.8c and 2.8d). For gas Reynolds numbers lower than 44000, we observe that the height grows to probe 4, located at $83D$ and stabilises. The growth is much less noticeable for higher Reynolds numbers, and the variation from 26D onwards tends to stabilise. For larger gas Reynolds numbers, the thickness is minimal. The thickness of the film and its waves adopt values closer to the error, which stays around the same order of magnitude. This results in a reduction of stabilisation observed at large airflow rates.

The frequency of the disturbance waves follows a different behaviour from the other variables. Figures 8e and 8f show a non-constant growth until the asymptotic zone is reached. The frequency in the first probe located at 6D from the input is very low but grows suddenly until the second probe at 26D. This may be produced by the appearance of the first interfacial waves, where the differentiation between large and small waves has not yet occurred. The wave peak calculation algorithm detects a high density of relatively small-height waves. Only a part of these waves grows, and many of them end up as part of the large waves. From this point, the frequency decreases for low gas Reynolds numbers until the last probe. For higher gas Reynolds numbers, the frequency decreases and progressively starts to increase again. In this case, the influence of the gas stream is stronger, and it is maybe the cause of the slight increase in frequency downstream.

The trend followed by the measurements is asymptotic and within what is expected to be observed. Although there are still slight differences between the measurements at $83D$ and $117D$, it should be noted that these measurement zones are not particularly close to each other but differ by $34D$. Although the flow approximates to developed conditions, it should be noted that the values obtained in an even longer pipeline might differ slightly.

2.4.2. LIQUID FILM THICKNESS MEASUREMENTS

Along this section, several samples of the measurements of the liquid film thicknesses through the conductance probes of both pipe diameters will be shown. In particular, the mean liquid film thickness for developed flow conditions have been estimated (h_{mean}). This variable is usually defined as the averaged distance between the pipe wall and the gas-liquid interface. The different inlet conditions, displayed in Table 2.1, will be compared to demonstrate its effect on the variation of this variable over time.

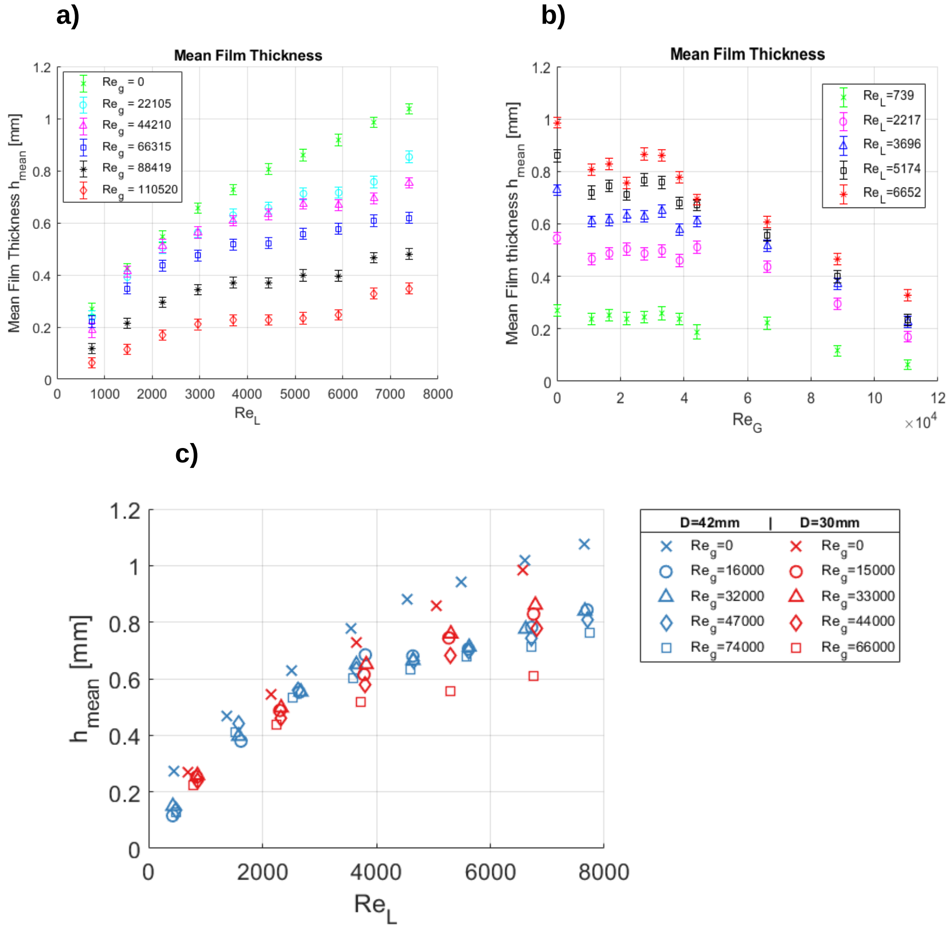

Figure 2.9. Mean Film Thickness (h_m) evolution versus a) liquid Reynolds number for different gas Reynolds numbers; b) gas Reynolds number for several liquid Reynolds numbers; c) liquid Reynolds number comparing both pipe diameters.

As could be intuitively thought-out, there should exist an increasing tendency of liquid film thicknesses with the rise of water flows. While, for the gas flow rate, there should exist a decreasing tendency with the increase of the flow. In Figure 2.8 examples of the evolution of the average thickness of the liquid layer for the $30\ mm$ inner diameter pipe are displayed. Figure 2.9a shows the tendency of this averaged film thickness as function of the liquid flow rate for the different gas Reynolds numbers analyzed. Figure 2.9b presents the evolution of the average thickness of the liquid film as a dependency of the gas flow rate for the different liquid Reynolds numbers. These measurements confirm that the mean film thickness clearly diminishes whit the increase the gas flow. Moreover, there is also a pronounced tendency of the mean film thickness to increase when the liquid flow rises. Figure 2.9c shows this thickness for both 30 and 42 mm facilities. The comparison should be made with caution as the Reynolds numbers represented with the same symbol do not correspond exactly for both diametres. The trend observed is very similar for both installations, with slight discrepancies for the high gas Reynolds number.

Additionally, in order to study the film thickness not only for developed conditions but also for developing flow, several conductance probes have been placed along the facility (Figure 2.1). The study of this evolution can be important because similar conditions of current research take place in different industrial processes under accidental or working conditions. For instance, both free and forced downward cocurrent flows can occur under accidental conditions on the U-tubes of steam generators in PWRs.

Figure 2.9 displays several examples of the average film layer variation as function of the distance to the entrance for the 30 mm of inner diameter pipe. As it is clearly shown in the figure, there is an asymptotical increase with the distance to the entrance towards a maximum value of film thickness, the value of this maximum depends on both fluid flow rates. As shown in this figure and in Figure 2.8, this maximum (developed flow conditions) increases with the increase of the liquid flow and decreases with the increase of the gas flow.

2.4.3. MEASUREMENTS OF THE DISTURBANCE WAVES

Concerning the DWs, two important variables are usually considered when analysing the gas-liquid interface, the wave amplitudes and frequencies. An iterative multi-criteria procedure has been used to predict these two variables of the disturbance wave. In particular, a peak calculation algorithm based on three restrictions was applied during the processing. The principal objective of the procedure is to discard from the disturbance wave counting not only the ripples waves but also multiple close crest peaks.

The first criterion is carried out by establishing a threshold value from which the wave is taken as a disturbance wave (De Jong and Gabriel, 2003; Rodríguez, 2004; Cuadros et al., 2019; Rivera et al., 2021), i.e., peaks that are below the threshold value are removed. This threshold value depends on the flow characteristics, for instance, for this research the average film thickness has been chosen as the cutting value, as displayed in Figure 2.10.

The following consideration is a proximity criterion, implemented to avoid multiple nearby peaks, a situation that mainly occurs in the wave crests vicinity (Cuadros et al., 2019; Rivera et al., 2021). The value applied to consider this closeness criterion depends on the temporal resolution of the measurement system and the characteristics of the waves, then, a minimum distance between successive DW peaks is defined, $d_{min,DW}$, so where the maximum distance between two consecutive DWs is less than this value, only the larger one is taken into account, as also shown in Figure 2.10.

Finally, a prominence criterion has been designed to discard low amplitude peaks, those that are located between DWs (Cuadros et al., 2019; Rivera et al., 2021). Suppose the relative height of a minor peak is less than this prominence cut-off value. In that case, the minor peak is considered a ripple wave overlapped with some part of a DW, and consequently, this second peak is removed, as displayed in Figure 2.10. A gas Reynolds number dependent prominence value has been established. A value ranging from 0.2 for free fall to 0.05 for the maximum gas Reynolds number understudy has been established. For large Reynolds numbers, the relative height of the disturbance waves decreases, so the prominence value has been reduced accordingly.

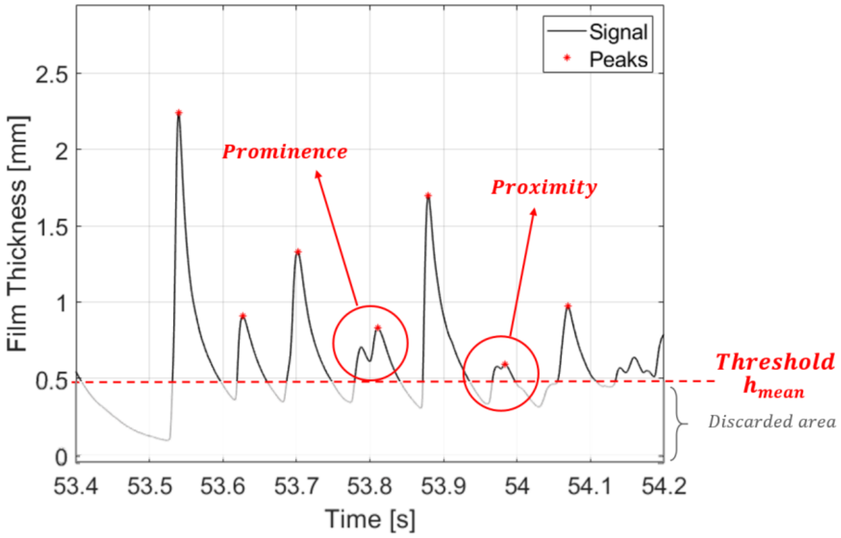

Figure 2.10. Representation of the multi-criteria used to a one-second data.

DISTURBANCE WAVE HEIGHTS

DWs have been identified after applying these three criteria. Figure 2.11 displays examples of the estimations of the DWs' heights as a function of the gas and liquid Reynolds numbers for both pipe diameters.

In the case of the disturbance wave amplitudes, as intuitively could be thought out, an inverse trend of the wave amplitudes with the gas flow rates should exist, as displayed in Figure 2.11a. While, there should exist a direct trend for the liquid flow rate, as displayed in Figure 2.11b. This wave amplitude dependence is much more pronounced with gas velocities, as shown in Figure 2.11, being less dependent on the total inlet water flow. Although, when analysing the experimental data, maximum values of the disturbance wave heights have been measured at approximately 2·104-4·104 gas Reynolds numbers depending on the liquid Reynolds number. Figure 2.11c shows the DW height obtained for each pipe diameter. It can be seen that the measurements follow a similar trend, although, for high Reynolds numbers of the gas, substantial differences can be seen. This comparison would slightly change if only the air surface velocity was considered. However, this study has attempted to maintain the highest degree of generality for potential comparisons with studies under different conditions.

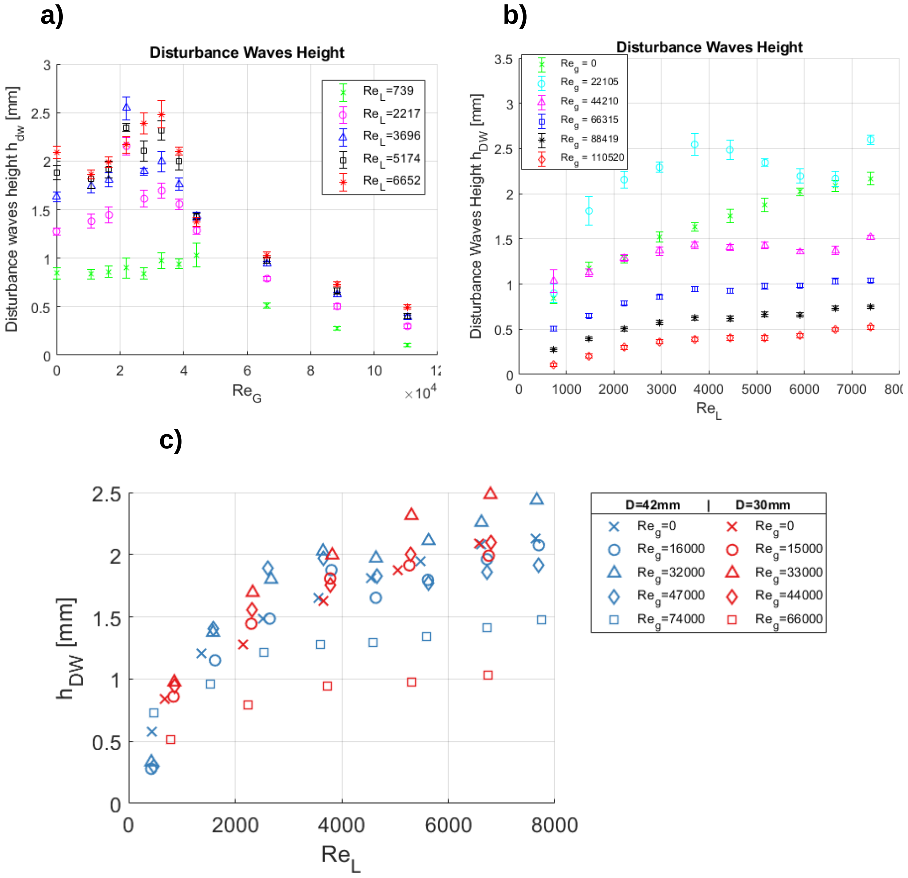

Figure 2.11. Disturbance Wave Height (h_{DW}) evolution: evolution as a function of: a) gas Reynolds number for different liquid Reynolds numbers; b) liquid Reynolds number for different gas Reynolds numbers; c) liquid Reynolds number, comparing both pipe diameters.

As commented above, the changes in the wave amplitude behaviour observed for the liquid film thickness is mainly caused by the gravity effect and the shear stress between the liquid and the gas phases. There is an increase in wave height as the gas velocity increases. This increase stops when the Reynolds values of the gas reach around $Re_{g\_maxhDW} = 2 \cdot 10^4 - 4 \cdot 10^4$. From this point on, the wave height decreases as the interaction between the gas and the liquid increases.

Most classical studies already pointed to a transition between the downward annular flow sub-regimes. The "regular wave" regime (also observed in upward annular flow) appears for gas Reynolds numbers higher than the Re_{g_maxhDW} value described in this paper. The authors Webb and Hewitt (1975) explained that only one type of well-defined disturbance wave is observed in this zone, and the gas-liquid interaction predominates. For lower Re_g values, different sub-regimes can occur, such as the "dual-wave", where two types of DW are distinguished. The first type is observed in free-fall and a second type becomes more and more predominant as the velocity increases until the critical zone. More recent studies, such as Cherdansev et al. (2019), point to bubble trapping in the liquid film. This happens due to the agitation produced by the gas, which becomes particularly significant in the critical zone of regime change.

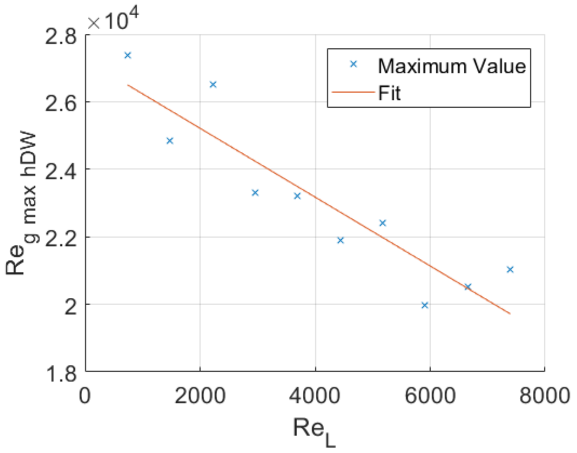

Figure 2.12. Fitting line of gas Reynolds number at which the maximum disturbance wave amplitudes takes place as function of the liquid Reynolds number.

Consequently, in order to capture the variation in the position of this maximum, multiple fits were made for the disturbance waves as a function of the gas Reynolds numbers for each liquid Reynolds number. Then, these maximums of all liquid Reynolds numbers have been correlated using a linear fit (Figure 2.12):

$$Re_{G\_maxhDW} = 27252 - Re_L \tag{2.11}$$

DISTURBANCE WAVE FREQUENCIES

The last issue to be obtained from the experimental measurements is the DWs frequency. The mean frequency value was estimated by calculating the number of peaks per second, counting the number of DW peaks and dividing by the measurement time interval for each experimental condition.

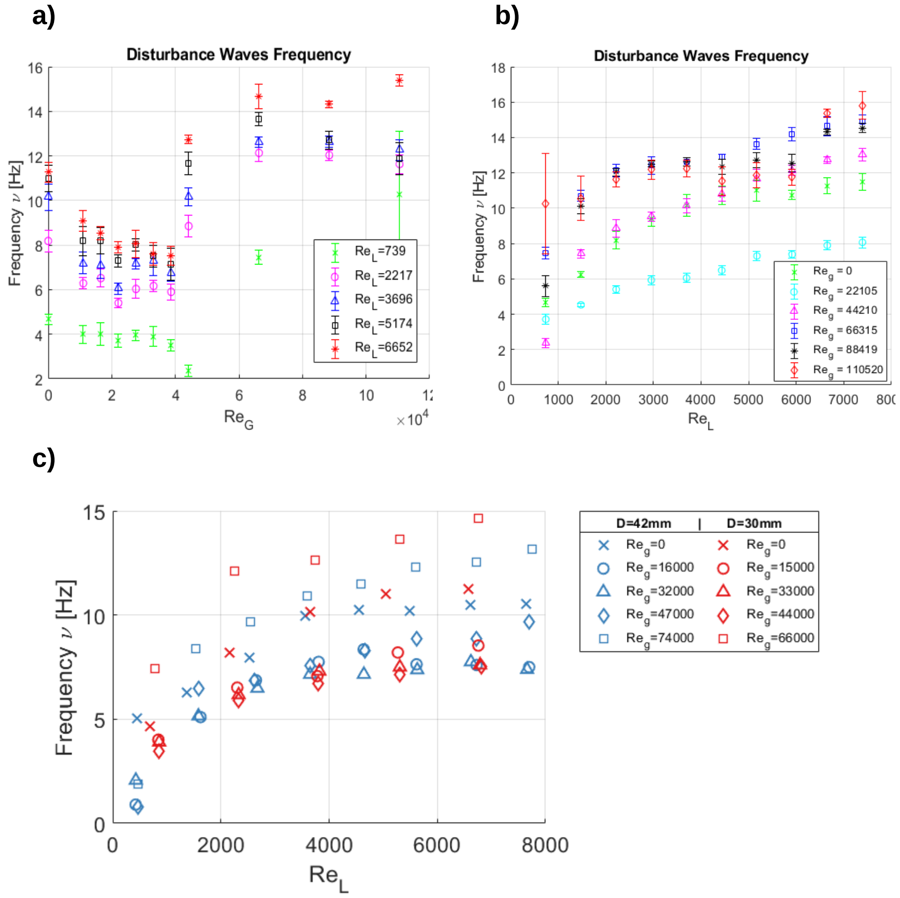

Figure 2.13. Disturbance Wave Frequency (υ_{DW}) evolution as a function of: a) gas Reynolds number for different liquid Reynolds numbers; b) liquid Reynolds number for different gas Reynolds numbers; c) liquid Reynolds number, comparing both pipe diameters.

Figure 2.13 displays the trend dependencies of the DW frequency for the different gas and liquid Reynolds numbers studied. The frequency range covers from 2 to 18 Hz approximately. The lower frequency values are for the lower liquid flow rates and moderately low gas Reynolds numbers.

The frequency evolution with the gas Reynolds number follows a similar behaviour to DW height. Initially, as the gas Reynolds number increases, a downward trend in frequency is observed. However, at about the Re$_{g\_maxhDW}$ described above, there is a sharp increase in frequency. This increase tends to stabilise at a gas Reynolds number of $6{\cdot}10^4$ and above, independently of the liquid flow rate.

Although the explanation is not as simple, the velocity difference between disturbance waves and gas plays an important role. The downward annular flow does not require moving air as gravity generates the movement naturally. The transition from a flow governed by gravity to one influenced by air flow is related to this behaviour of the characteristic variables. Nevertheless, with these reasons alone, it is difficult to explain why a reduction in wave frequency and an increase in height are observed. A more detailed future investigation of this question is probably desirable in order to be able to make a statement on the matter.

When comparing the frequency obtained in the $30\ mm$ and $42\ mm$ diameter test sections (Figure 2.13c), it can be observed that both follow the same pattern. A higher frequency is observed in free fall than during the transition zone. Yet again, the frequency increases in both cases for higher gas Reynolds numbers.

Additionally, it must be commented the huge error bar existent in a point of Figure 2.13. This mistake is caused by the fact that this point is the lowest liquid flow and highest gas flow. Consequently, as the liquid film is so thin and the gas flow is so high, then high variability of the wave frequency between the six experimental series of ten seconds each one has been obtained. However, the averaged values of the wave frequencies are apparently around the expected value.

2.5. DISCUSSION OF RESULTS AND CORRELATIONS

This section focuses on analysing and estimating trends between inlet conditions and other fluid variables with the major film properties, leading to the definition of correlations between them. Several correlations have been developed to determine the water film thicknesses and the interfacial characteristics. The main variables considered in this paper are the mean liquid film thickness (h_{mean}), the DW height (h_{DW}) and the DW frequency (ν_{DW}). When carrying out these types of analyses, dimensionless numbers are strongly recommended. Consequently, dimensionless numbers have been used to characterise all the considered flow magnitudes. All these interfacial characteristics, film thicknesses and wave characteristics result from a dynamic equilibrium between disturbance forces that perturb the flat surface (inertial forces) and the forces opposing the alteration of the surface (related to surface tension and viscosity). Then, as it is inferred in the current study and as it is also widely recognised, the behaviour of interfacial waves inside tubes is very chaotic. Then, in order to characterise film thicknesses and wave behaviours, several dimensionless numbers have been analysed. In particular, their dependence on Reynolds, Froude and Weber numbers have been tested. But, in order to reduce as much as possible the complexity of the correlation, the expressions with the lowest number of dimensionless numbers and the highest determination coefficient (R^2) has been given as a final result, achieving a very good correlation using only gas and liquid Reynolds numbers. In addition, the Strouhal number has been used in the estimation of the wave frequencies.

2.5.1. MEAN LIQUID FILM THICKNESS DISCUSSION

To characterize the liquid film in downward annular flow, the first variable on which the analyses are usually focused is the average film thickness (h_{mean}). This variable corresponds to the average distance between the wall and the air-water interface (Figure 2.7). To study this variable not only the data analysis has been carried out but also a new correlation has been developed. The current experimental data and their correlation curve are displayed against theoretical expressions. In addition, other experimental data found in the literature have been displayed as well as other experimental expressions.

CORRELATION OF THE MEAN LIQUID FILM THICKNESS

This subsection shows the result of relating the h_{mean} to the experimental conditions of the experiments through a correlation. For this purpose, the experimental measurements were approximated by a function using the input properties and boundary conditions. In order to maintain generality and to make the data more accessible, only dimensionless numbers have been used to calculate the mean film thickness.

First, we have correlated the free-falling data for both pipe diameters and for their respective experimental conditions. The new correlation obtained is given by:

$$\frac{h_{mean}}{L_m} = 0.19 \cdot Re_L^{0.54} \tag{2.12}$$

where L_m is the viscous-gravity length, which is defined as

$$L_m = \left(\frac{\upsilon^2}{g \, sin \, \beta}\right)^{1/3} \tag{2.13}$$

in our case, the flow is vertical, $\beta = 90º$ so $\sin(\beta) = 1$.

Eq. (2.12) shows that the film thickness can be calculated using the properties of the liquid and its conditions at the inlet. Figure 2.15 shows the comparison between the data obtained by the new correlation represented as $Fit\ h_{mean}$ and the experimental measurements. As can be seen, the new correlation fits the experimental data very accurately, and all measured points are within the $\pm 10\%$ error band. The R^2 coefficient corresponding to the Pearson product-moment coefficient is 0.985, and the RMS error is 0.0135.

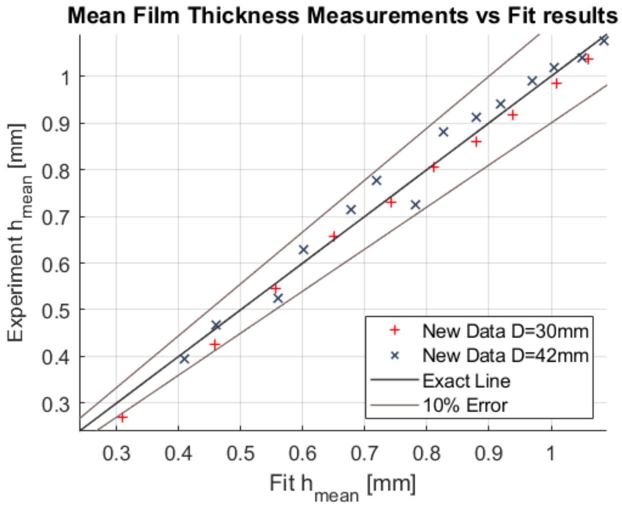

Figure 2.15. Experimental mean film thickness vs. data obtained with the new correlation for free falling conditions.

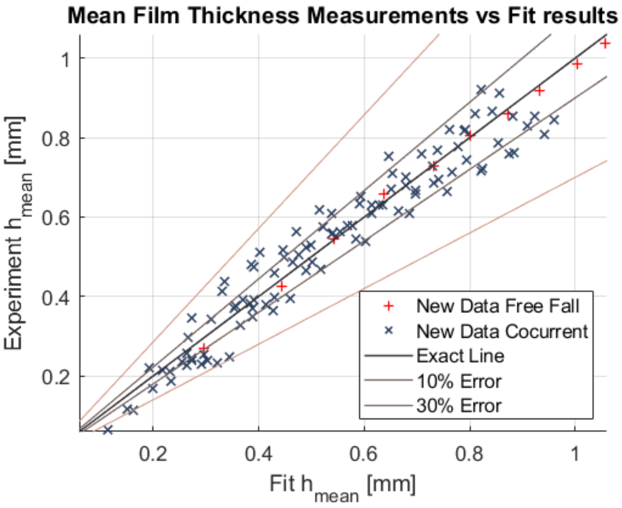

Figure 2.16. Experimental mean film thickness vs. data obtained with the new correlation for co-current downward conditions.

If the cocurrent downward flow data are added to the free falling ones, then only a new term in Eq. (2.14) is needed to capture the influence of these new conditions. As a result, the following correlation is obtained:

$$\frac{h_{mean}}{L_m} = 0.19 \cdot {Re_L}^{0.54} \cdot \left(1 - 1.29 \cdot 10^{-5} \cdot {Re_G}^{0.93}\right) \qquad (2.14)$$

Figure 2.16 compares the data obtained by this new correlation and the experimental measurements. The new correlation fits fairly accurately the experimental data, with all points found within the $\pm 30\%$ error bands. As before, R^2 has been calculated, obtaining a value of 0.939, and the RMS error is 0.055.

As discussed in the previous section, it is important not only to study the film thickness under fully developed flow conditions but also under flow developing conditions. Consequently, the consideration of the development region is of interest, so in order to study the influence of this region, the corresponding data have been added to the previous ones. The result is an additional term in Eq. (2.15) that captures the influence of the developing flow conditions. Finally, the following correlation has been obtained:

$$\frac{h_{mean}}{L_m} = 0.19 \cdot {Re_L}^{0.54} \cdot \left(1 - 1.29 \cdot 10^{-5} \cdot {Re_G}^{0.93}\right) \cdot \left(1 - e^{-0.22 \cdot \left(\frac{z}{D}\right)^{0.52}}\right) \qquad (2.15)$$

Then, following the same procedure as for the free-fall and co-current correlations, the data obtained by applying the correlation and the experimental data have been compared (Figure 2.17). As for the previous cases, the new correlation has a quite good data fitting since most data are inside the 30% error band, with a of $R^2 = 0.895$ and a RMS error of 0.071.

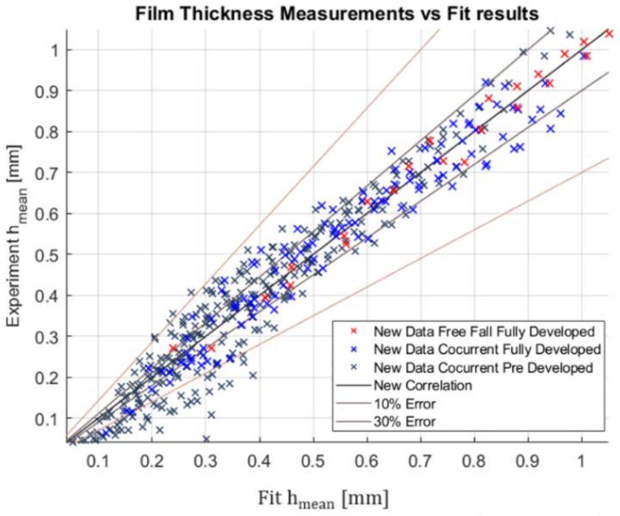

$$\frac{h_{mean}}{L_m} = 0.19 \cdot {Re_L}^{0.54} \cdot \left(1 - 1.29 \cdot 10^{-5} \cdot {Re_G}^{0.93}\right) \cdot \left(1 - e^{-0.22 \cdot \left(\frac{z}{D}\right)^{0.52}}\right)$$

Figure 2.17. Experimental mean film thickness vs. data obtained with the new correlation for co-current conditions considering the developed and developing regions.

PERFORMANCE OF THE NEW CORRELATIONS AGAINST OTHER CORRELATIONS AND EXPERIENTAL DATA

The data and correlations obtained in this research have been compared in detail with studies by other authors. On the one hand, the correlations proposed in this paper have been used to check whether they are able to predict the experimental results of other research groups. On the other hand, the experimental correlations proposed by other authors have been studied to verify their predictive potential for our measurements. Table 2.3 summarises the empirical expressions to calculate the average film thickness and some details related to the conditions to use it.

Theoretical models to estimate the film thickness under free falling conditions have been developed within over a hundred years. Specifically, Nusselt's model provided the first and up to now more widely used estimation of the liquid thickness under laminar conditions (Nusselt, 1916a,b). Nusselt's theory supposes not only laminar but also smooth and two-dimensional flow on an infinite flat plate, the expression is:

$$\frac{h_{mean}}{L_m} = \left(\frac{3}{4}\,Re_L\right)^{1/3} \tag{2.16}$$

Padmanaban, in his PhD (2006), provides a good summary of liquid film expressions. For instance, Bergelin's theoretical expression, valid for the turbulent regime

$$\left(3.0 + 2.5 \cdot ln\,\bar{\delta}^{+}\right)\bar{\delta}^{+} = \frac{Re_L}{4} + 64 \tag{2.17}$$

in which the non-dimensional film thicknesses is defined as,

$$\bar{\delta}^{+} = \frac{\rho \cdot u^{*} \cdot h_{mean}}{\mu_l} \tag{2.18}$$

being the frictional velocity defined from a force balance between wall friction and gravity forces:

$$u^{*} = \sqrt{\frac{\tau_w}{\rho}} = \sqrt{g \cdot h_{mean}} \tag{2.19}$$

The transition laminar-turbulent was also determined by Dukler and Bergelin (Padmanaban, 2006), a liquid Reynolds number of 1080 was proposed. In contrast, other researchers' studies propose higher values, such as Fulford, which gives a value of 2360 to the laminar-turbulent transition to begin. A criterion to estimate the transition from laminar to turbulent flow is also available (Mudawwar and El-Masri, 1986):

$$Re_{crit} = 97\,Ka^{0.3} \tag{2.20}$$

In which the Kapitza number is defined in the usual form,

$$Ka = \frac{\sigma}{\rho\ g^{1/3}\ \nu^{4/3}} \tag{2.21}$$

Kapitza's theoretical expression can be used for smooth wavy laminar flows (Aliyu, 2015), which accounts for the effects of regular periodic waves and surface tension. The proposed equation is a modification of Nusselt's theory to account for the influence of shear stresses and interfacial waves:

$$h_{mean} = \left(\frac{2.4}{4}\frac{\upsilon^2}{g}Re_L\right)^{1/3} \tag{2.22}$$

For the turbulent region, many experimental correlations are available in the literature, in particular, a considerable number of semi-empirical correlations based on the form of Nusselt's theory have been proposed over the last decades, almost all of them having the following form:

$$h_{mean} = A\left(\frac{\upsilon^2}{g}\right)^{1/3} Re_L^B \tag{2.23}$$

in which A and B are regression constants. For instance, Mudawwar and El-Masri (1986) defined a semi-empirical correlation for the mean liquid film thickness estimation:

$$h_{mean} = 0.065\left(\frac{\upsilon^2}{g}\right)^{1/3} Re_L^{0.58} \tag{2.24}$$

If a gas stream is introduced in cocurrent with the free falling water flow, the number of available correlations are much more reduced. Henstock and Hanratty (1976) correlated most of the previous studies carried out for horizontal and vertical flows. The proposed correlation for vertical flows, both downward and upward, is:

$$\frac{h_{mean}}{D} = \frac{6.59\ F}{(1 + 1400\ F)^{1/2}} \tag{2.25}$$

where the parameter F is given by

$$F = \frac{\upsilon_l}{\upsilon_g}\left(\frac{\rho_l}{\rho_g}\right)^{1/2}\frac{\gamma(Re_L)}{Re_g^{0.9}} \tag{2.26}$$

And

$$\gamma(Re_L) = \left[\left(0.707Re_L^{1/2}\right)^{5/2} + \left(0.0379Re_L^{9/10}\right)^{5/2}\right]^{2/5} \tag{2.27}$$

The correlated data, only those of vertical downward flows, covered the following experimental conditions: liquid Reynolds numbers between 20 and $1.51{\cdot}10^4$; gas Reynolds number between 5000 and $2.55{\cdot}10^5$; and inner pipe diameters of 25.4, 50.8 and 63.5 mm.

Kulov et al. (1979) carried out investigations with water-glycerol mixtures ($\upsilon = 10^{-6} - 10^{-5}\ m^2/s$), liquid Reynolds numbers up to $5{\cdot}10^4$ were studied, and gas Reynolds numbers up to 8.5·10^4. The authors proposed the following correlations:

$$h_{mean} = 0.266\left(\frac{\upsilon^2}{g}\right)^{1/3} Re_L^{0.6}\, Re_G^{-0.1}\ ;\ 8000 \le Re_G \le Re_G^* \tag{2.28}$$

$$h_{mean} = 62.6\left(\frac{\upsilon^2}{g}\right)^{1/3} Re_L^{0.52}\, Re_G^{-0.61}\ ;\ Re_G^* \le Re_G \le 85000 \tag{2.29}$$

being Re_G^* a threshold Reynolds number which divides the two flow regions and is given by $Re_G^* = 5.32\cdot 10^4\ \mathrm{Re_L^{-0.19}}$.

Czernek and Witczak (2020) have proposed another correlation, but applicable for very viscous liquids in the range ($\mu = 0.055 - 1.517\ Pa\cdot s$), the correlation is as follows:

$$h_{mean} = h_0\ \frac{1}{1 + 5.68\cdot 10^{-3} Re_L^{0.132}\, Re_G^{0.47}} \tag{2.30}$$

where the reference film height, h_0, is given by:

$$h_0 = 0.852\left(\frac{\upsilon^2}{g}\right)^{1/3} Re_L^{0.516}\ \ ;\ Re_L < 2 \tag{2.31}$$

$$h_0 = 0.9335\left(\frac{\upsilon^2}{g}\right)^{1/3} Re_L^{0.334}\ \ ;\ Re_L > 2 \tag{2.32}$$

The consideration of the development region is of interest, but this region is strongly influenced by the inlet conditions of both gas and liquid phases. In our case, the liquid has been introduced as a thin layer on the pipe wall and the gas phase in the central section of the pipe. This configuration could simulate the conditions of different technological systems, like in heat exchangers. However, no data or expression has been found addressing this issue. Consequently, all three configurations, free falling, forced falling and developing region, have been analysed in this section.

Table 2.3. Summary of Mean Film Thickness expressions.

Reference	**Expression**	**Conditions**
Free Falling Flow		
Nusselt (1916) (Nusselt 2016a,b)	$\frac{h_{\mathrm{mean}}}{\mathrm{L_m}} = \left(\frac{3}{4}\ \mathrm{Re_L}\right)^{1/3}$	Theoretical, laminar regime, smooth flow and infinite flat plate
Duckler (1952)	$\left(3.0 + 2.5\cdot\ln\bar{\delta}^+\right)\bar{\delta}^+ = \frac{\mathrm{Re_L}}{4} + 64;$	Theoretical, turbulent regime

(Takahama, 1980)	$\bar{\delta}^+ = \frac{\rho \cdot u^* \cdot h_{mean}}{\mu_l}$; $u^* = \sqrt{\frac{\tau_w}{\rho}} = \sqrt{g \cdot h_{mean}}$	(Re_L>1080), flat plate, pipe
Brotz (1954)* (Pagmanaban, 2006)	$\frac{h_{\mathrm{mean}}}{\mathrm{L_m}} = 0.641\mathrm{Re}_\mathrm{L}^{2/3}$	Re_L= 2360-17200, pipe inside, $\upsilon = 10^{-6} - 8.48 \cdot 10^{-6}\ m^2/s$
Kapitza, (1955) (Aliyu, 2015)	$\frac{h_{\mathrm{mean}}}{\mathrm{L_m}} = \left(\frac{2.4}{4}\mathrm{Re_L}\right)^{1/3}$	Theoretical, regular periodic waves and surface tension, smooth wavy laminar
Brauer (1956) * (Takahama, 1980)	$\frac{h_{\mathrm{mean}}}{\mathrm{L_m}} = 0.208\ \mathrm{Re}_\mathrm{L}^{8/15}$	Re_L= 1600-7200, pipe outside (o.d. 43 mm), $\upsilon = 0.9 \cdot 10^{-6} - 12.7 \cdot 10^{-5}\ m^2/s$
Fiend (1960)* (Pagmanaban, 2006)	$\frac{h_{\mathrm{mean}}}{\mathrm{L_m}} = 0.266\ \mathrm{Re}_\mathrm{L}^{1/2}$	Turbulent regime, pipe inside (20, 50 mm i.d.), $\upsilon = 10^{-6} - 1.97 \cdot 10^{-5}\ m^2/s$
Zhivaikin (1961)* (Pagmanaban, 2006)	$\frac{h_{\mathrm{mean}}}{\mathrm{L_m}} = 0.141\ \mathrm{Re}_\mathrm{L}^{7/12}$	Re_L= 600-14000, pipe inside (20 mm i.d.)
Takahama *(Takahama, 1980)	$\frac{h_{\mathrm{mean}}}{\mathrm{L_m}} = 0.228\ \mathrm{Re}_\mathrm{L}^{0.526}$	Re_L= 600-8000, pipe inside
Mudawwar *(Mudawwar, 1986)	$\frac{h_{\mathrm{mean}}}{\mathrm{L_m}} = 0.145\ \mathrm{Re}_\mathrm{L}^{0.58}$	Semi-empirical model, turbulent flow
Brauner (1987) *(Brauner, 1987)	$\frac{h_{\mathrm{mean}}}{\mathrm{L_m}} = \left(\frac{3}{8}Re_L\right)^{\frac{1}{3}}$ (Laminar Region) $\frac{h_{\mathrm{mean}}}{\mathrm{L_m}} = 0.104\ \mathrm{Re}_\mathrm{L}^{7/12}$ (Turbulent Region)	Theoretical, harmonic and infinitesimal waves
Karapantsios (1989) *(Pagmanaban, 2006)	$\frac{h_{\mathrm{mean}}}{\mathrm{L_m}} = 0.214\ \mathrm{Re}_\mathrm{L}^{0.538}$	Re_L= 504-13100, pipe inside

Pagmanaban ***** **(**Pagmanaban, 2006)	$\frac{h_{\text{mean}}}{\text{L}_\text{m}} = 0.1855\ \text{Re}_\text{L}^{0.558}$	ReL= 4000-20000, pipe inside
Aliyu (Aliyu, 2015)*	$\frac{h_{\text{mean}}}{\text{L}_\text{m}} = 1.4459\ \text{Re}_\text{L}^{0.3051}$	ReL= 4000-20200, pipe inside, large diameter (101.6 i.d.)
New Correlation, Eq. (2.12)	$\frac{\text{h}_{\text{mean}}}{\text{L}_m} = 0.19\cdot\ \text{Re}_\text{L}^{0.54}$	ReL= 560-11300, pipe inside (30, 42 mm i.d.)
Cocurrent Downward Flow		
Henstock and Hanratty, (Henstock, 1976)	$\frac{\text{h}_{\text{mean}}}{\text{D}} = \frac{6.59\ \text{F}}{(1+1400\ F)^{1/2}}$ $\text{F} = \frac{\upsilon_l}{\upsilon_g}\left(\frac{\rho_l}{\rho_g}\right)^{1/2}\frac{\gamma(Re_L)}{Re_G^{0.9}}$ $\gamma(Re_L) = \left[\left(0.707Re_L^{1/2}\right)^{5/2} + \left(0.0379Re_L^{9/10}\right)^{5/2}\right]^{2/5}$	Vertical upward and downward, ReL = 20-15100, ReG= 5000-255000, pipe inside (25.4, 50.8, 63.5 mm i.d.),
Kulov (1979)*, (Kulov, 1979)	$\frac{h_{\text{mean}}}{\text{L}_\text{m}} = 0.266\ \text{Re}_\text{L}^{0.6}\ \text{Re}_G^{-0.1}\ ;\ 8000 \le Re_G \le Re_G^*$ $\frac{h_{\text{mean}}}{\text{L}_\text{m}} = 62.6\ \text{Re}_\text{L}^{0.52}\ \text{Re}_G^{-0.61}\ ;\ Re_G^* \le Re_G \le 85000$ $Re_G^* = 5.32\cdot 10^4\ \text{Re}_\text{L}^{-0.19}$	ReL ≤ 13000, ReG= 8000-85000,pipe inside (25 mm i.d.), $\upsilon = 10^{-6} - 10^{-5}\ m^2/s$
Czernek (2020)*, (Czernek, 2020)	$\text{h}_{\text{mean}} = \text{h}_0\ \frac{1}{1+5.68\cdot 10^{-3}\text{Re}_\text{L}^{0.132}\ \text{Re}_\text{G}^{0.47}}$ $\text{h}_0 = 0.852\ \text{L}_m\ \text{Re}_\text{L}^{0.516}\ ;\ \text{Re}_\text{L} < 2$ $\text{h}_0 = 0.9335\ \text{L}_m\ \text{Re}_\text{L}^{0.334}\ ;\ \text{Re}_\text{L} > 2$	JL = 0 – 0.254 m/s, JG= 0-29.9 m/s, pipe inside (12.5, 16, 22 and 54 mm i.d.), $\mu = 0.055 - 1.517\ Pa\ s$,
New Correlation, Eq. (2.13)	$\frac{\text{h}_{\text{mean}}}{\text{L}_m} = 0.19\cdot \text{Re}_\text{L}{}^{0.54}\cdot\left(1-1.29\cdot 10^{-5}\cdot \text{Re}_G{}^{0.93}\right)$	ReL= 560-11300, ReG= 0-1.1·10^5, pipe inside (30, 42 mm i.d.)
Cocurrent Downward Flow developing and developed regions		

New Correlation, Eq. (2.14)	$\frac{\mathrm{h_{mean}}}{\mathrm{L}_m} = 0.19 \cdot \mathrm{Re_L}^{0.54} \cdot (1 - 1.29 \cdot 10^{-5} \cdot Re_G^{0.93}) \cdot \left(1 - \mathrm{e}^{-0.22 \cdot \left(\frac{\mathrm{z}}{\mathrm{D}}\right)^{0.52}}\right)$	$\mathrm{Re_L}$= 560-11300, $\mathrm{Re_G}$= 0-1.1·10^5, pipe inside (30, 42 mm i.d.)

*correlations developed for vertical flows which do not use the definition of the viscous-gravity length, $L_m = \left(\frac{\upsilon^2}{\mathrm{g}\, sin\beta}\right)^{1/3}$, but directly $\left(\frac{\upsilon^2}{\mathrm{g}}\right)^{1/3}$.

Figure 2.18 focuses on free falling flows, widely investigated over the last century. The figure shows that all the experimental data closely follow Nusselt's expression for low liquid Reynolds numbers (Nusselt, 1916a,b). However, as the flow gradually becomes turbulent, the expression's estimations underestimate the experimental data. Many expressions to estimate the liquid film thickness in this region are available in the literature (most of them summarised in Table 2.3). Besides, a considerable number of experimental data are available too (Webb and Hewitt, 1975; Takahama and Kato, 1980; Karapantsios et al., 1989 and 1995; Karimi and Kawwaji, 1989; Zadrazil et al., 2014; Cherdansev et al., 2019; Charogiannis et al., 2019). Not only are all data close to each other (Figure 2.18), but all the proposed correlations predict similar values. Consequently, falling films are considered to be fairly well characterised. In fact, only Karimi's data, whose experiments were performed using kerosene instead of water, differ appreciably. Those data suggest the existence of thicker liquid layers for kerosene than for water at the same liquid Reynolds numbers.

Figure 2.19 displays the performance of the new developed expression against the experimental data of several researchers data for downward cocurrent flow conditions. As seen in the figure, there is a much larger scatter between the experimental data and the correlation predictions. However, in general, the values of the different authors are captured adequately. The Zadrazil et al. (2014) and the Cherdanzev et al. (2019) data are quite well captured by the current proposed correlation. The only significant discrepancies are those found in the Vasques et al. data (2018), which are systematically underestimated by the new proposed correlation. This difference is probably due to the significant difference in diameters between installations, which impacts the gas Reynolds number term.

Figure 2.20 shows the predictions for the different expressions proposed by several researchers with those of the currently developed expression for downward cocurrent flows. As shown in the figure, there are significant differences when comparing the different expressions. In particular, the highest discrepancies are with Czernek's correlation. This expression systematically underestimates the thickness of the liquid layer. This result may be justified since this correlation was developed for high surface tension liquids, particularly several types of oils. The currently developed correlation, which gives the best results when compared with the present experimental data, predicts slightly higher values than Henstock's expression for almost all values of the liquid and gas Reynolds numbers covered. Only for small values of both Reynolds numbers does the Henstock expression exceed the values of the new correlation predictions. In contrast, Kulov's correlation provides lower values than Henstock's and the current correlation for almost all gas and liquid Reynolds numbers covered.

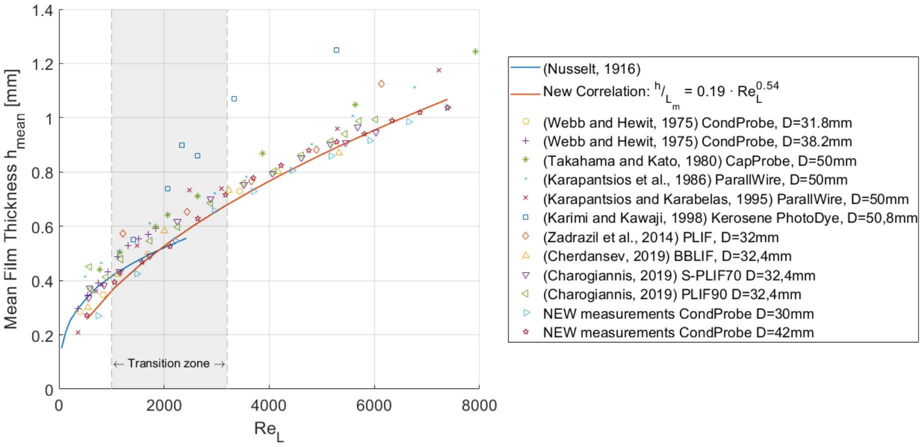

Figure 2.18. Comparison of the mean film thickness obtained by different authors as a function of the Reynolds number of the liquid under Free Falling conditions. The theoretical expression of Nusselt and the empirical correlation proposed in this paper have also been included.

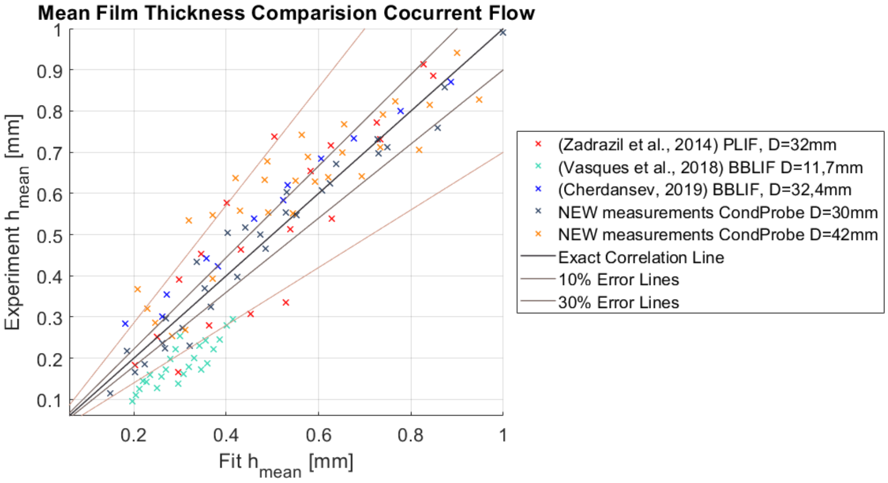

Figure 2.19. Experimental data of the Mean Film Thickness versus the predictions of the new correlation under Cocurrent Downward Flow conditions.

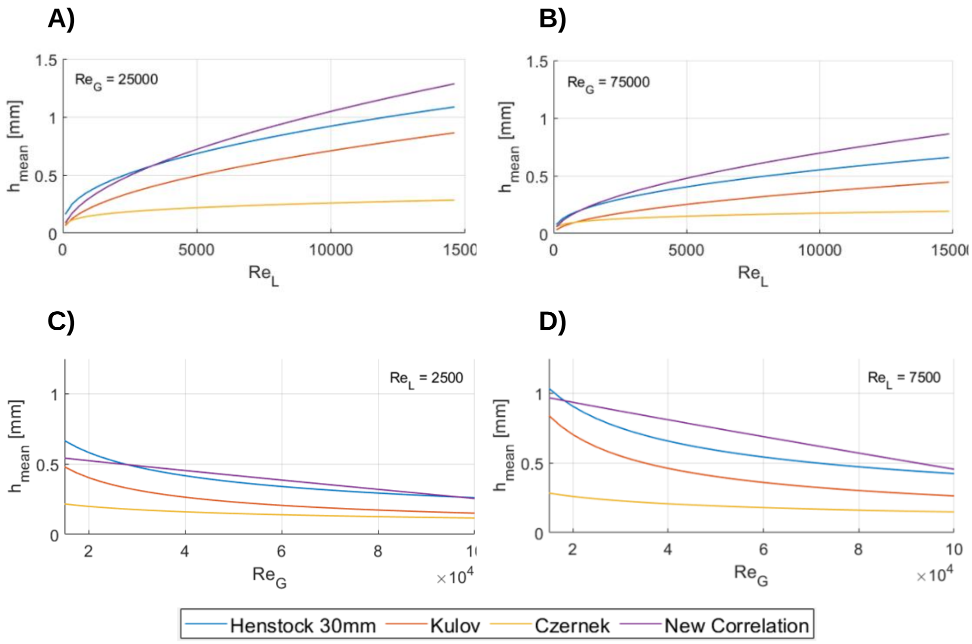

Figure 2.20. Comparison of the Mean Film Thickness obtained according to the empirical correlations proposed by different authors as function of: A-B) Liquid Reynolds number at constant Gas Reynolds number; C-D) Gas Reynolds number at constant Liquid Reynolds number.

2.5.2. DISTURBANCE WAVES DISCUSSION

This section focuses on analysing some of the most important characteristics of DWs. In particular, empirical expressions have been proposed to calculate the average height of the waves as well as the frequency at which they appear. Similar to the procedure in the previous sections, these expressions have been calculated as a function of dimensionless numbers not to lose generality. We have checked the effects of using different dimensional numbers in this adjustment process. However, since the adjustments were very good only using the gas and liquid Reynolds numbers, we have chosen not to increase the complexity of the correlations and present them according to these two dimensionless numbers only.

DISTURBANCE WAVE HEIGHTS

The height of the disturbance waves is defined as the average distance between the wave peaks and the pipe wall. Only the peaks of the DWs have been taken into account, discarding the peaks of the RWs.

Correlation of Disturbance Wave Height Measurements

The empirical correlation proposed that best fits the experimental measurements is:

$$\frac{h_{DW}}{L_m} = 2.6 \cdot {Re_L}^{0.35} \cdot \left(1 - 5.8 \cdot 10^{-5} \cdot abs\left(Re_G - Re_{G\_maxhDW}\right)^{0.845}\right) \tag{2.33}$$

in which the DWs height has been calculated as a function of the liquid and gas Reynolds numbers defined in Eq. (2.5) and Eq. (2.4) respectively, and the Re_{G_maxhDW}. This term corresponds to the gas Reynolds number at which the maximum wave height is reached as a function of the liquid Reynolds number, Eq. (2.11).

The fitting correlation, Eq. (2.33) and the experimental data are displayed in Figure 2.21. As can be seen, the new correlation predicts with fairly good accuracy the experimental measurements, finding a large number of points in the $\pm 10\%$ error bands and most of them within the $\pm 30\%$ error bands. The value of the determination coefficient R^2 is 0.881 and the RMS error is 0.2276.

The tendency observed for the height of the DWs is quite similar to the trend previously explained for the average film thickness. The height of the waves grows as the liquid Reynolds number increases. However, when we observe the behavior of the height as the Reynolds number of the gas varies, the value increases up to a certain number and then decreases rapidly. This behavior has already been explained where the reasoning behind it is detailed.

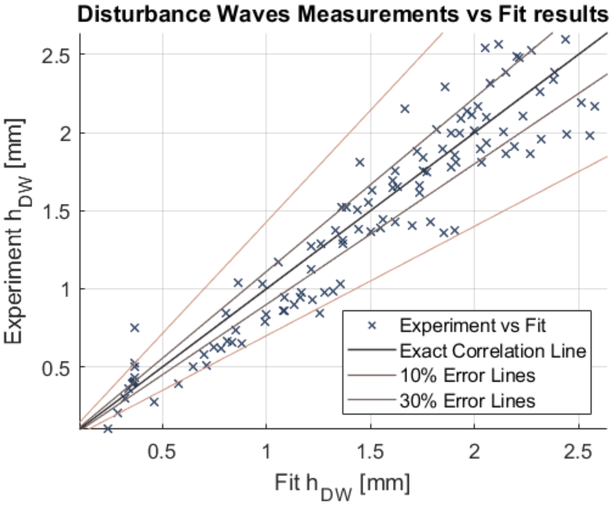

Figure 2.21. Experimental DW heights vs. data obtained with the new correlation.

New Correlation Performance Against Other Correlations and Experimental Data

Very limited expressions to estimate the wave height are available on the literature. Most of them are applicable to free falling films and for low liquid Reynolds numbers. Nosoko et al. (1996) propose the following correlation of the wave peak height for free falling films in a vertical flat plate:

$$h_{DW} = 0.49 \cdot \left(\frac{\upsilon^2}{g}\right)^{1/3} K_F^{\;0.044} \; {N_\lambda}^{0.39} Re_L^{0.46} \tag{2.34}$$

where K_F is the dimensionless group of physical properties and N_λ is the dimensionless wave separation, which are defined as:

$$K_F = \frac{\rho^3 \nu^4 g}{\sigma^3} \tag{2.35}$$

$$N_\lambda = \lambda \left(\frac{g}{\nu^2}\right)^{1/3} \tag{2.36}$$

being λ the separation between neighboring composite waves. The covered range of liquid Reynolds numbers was from $14 - 90$.

Other authors propose analytical expressions, like Chang, Nguyen or Panga among others. Chang used the Nakaya model and proposed an analytical expression (Nguyen and Balakotaiah, 2000), based on a non-linear treatment of longwave approximation. Nguyen and Balakotaiah (2000) proposed a model which is based on a boundary-layer analysis and describes the characteristics of free-falling films, especially for low liquid Reynolds numbers (Re_L =2–20), and low Kapitza numbers (Ka =6–22). Panga et al. (2005) proposed a new scaling method to reduce the Navier-Stokes equations to a single evolution equation for the scaled film thickness, $h(x,t)$. Near the double zero singularity there is the homoclinic bifurcation and using the Melnikov's analysis the authors obtained an expression for the maximum wave amplitude of the solitary waves. All these models have a restricted applicability region, far from the current data, and also have the same form:

$$h_{max} - 1 = A\, We \tag{2.37}$$

being A equal to 7.56, 1.925 and 2.52 respectively, and the Weber number is defined in terms of the mean film thickness of Nusselt's expression:

$$We = \frac{\rho\, u^2 h_{mean,Nusselt}}{\sigma} \tag{2.38}$$

Meza and Balakotaiah (2008) explains that for viscous fluids ($2 < Ka < 200$), there is an increasing tendency of the wave amplitudes with the Weber number, with a saturation value at around $h_{max}/h_{mean,Nusselt} = 3$, having a weak dependency on the Kapitza number. While for less viscous fluids ($200 < Ka < 3890$), the waves are found to be much more dynamic and pronounced, having bigger amplitudes, which saturate at around values of $h_{max}/h_{mean,Nusselt} = 10$.

Holowach et al. (2002) propose a theoretical expression for estimating the wave amplitude. This expression is dependent on fluid properties and the interfacial shear stresses. The methodology was initially proposed by Ishii and Grolmes (1975) and assumes that a shear flow model can express the wave crest motion concerning the liquid film. The model approximates the wave formation process in vertical annular flow, estimating the wave height in the radial direction, neglecting the gravitational forces. The proposed expression is:

$$\Delta h_{DW} = \frac{\sqrt{2}\, C_W\, \mu_l}{(\rho_l\ \tau_i\, f_{li})^{1/2}} \tag{2.39}$$

being τ_i the interfacial shear stress, f_{li} the interfacial liquid friction factor and C_W is a factor that estimates the surface tension on the circulation/dissipation flow in the wave.

The interfacial liquid friction factor is calculated using the correlation originally developed by Hughmark (Berna et al., 2014):

$$\sqrt{f_{li}} = K\, Re_L^m \tag{2.40}$$

where K and m are given by

K = 3.73 , m = -0.47 for 2 < Re_L < 100

K = 1.962, m = -1/3 for 100 < Re_L < 1000

K = 0.735, m = -0.19 for 1000 < Re_L

While the interfacial shear stress is an expression defined by the gas core mixture properties (existence of water droplets carried by the gas phase):

$$\tau_i = \frac{f_{gi}\, \rho_\alpha J_\alpha^2}{(\rho_l\ \tau_i\, f_{li})^{1/2}} \tag{2.41}$$

expression in which all magnitudes are based on the superficial gas core mixture properties. Being ρ_α the weighted mixture density, J_α the weighted mixture superficial velocity ($J_\alpha = G_g/\rho_g + G_e/\rho_l$, where G is the mass fluxes of gas and entrained droplets) and f_{gi} the interfacial gas friction factor. This last variable is given by:

$$f_{gi} = 0.079\, Re_\alpha^{-1/4} \left[1 + 24 \left(\frac{\rho_l}{\rho_g}\right)^{1/3} \frac{h_{mean}}{D}\right] \tag{2.42}$$

being Re_α the mixture Reynolds number defined by

$$Re_\alpha = \frac{(G_g + G_e)D}{\mu_g} \tag{2.43}$$

The factor C_W was defined by Ishii and Grolmes (1975)

$$C_W = \begin{cases} 0.028\, N_\mu & for\ N_\mu \leq {}^{1}\!/_{15} \\ 0.25 & for\ N_\mu > {}^{1}\!/_{15} \end{cases} \tag{2.44}$$

being N_μ the viscosity number, parameter which is the ratio of viscous forces to surface tension forces and is defined as

$$N_\mu = \frac{\mu_l}{\left(\rho_L\ \sigma\ \sqrt{\frac{\sigma}{g\ \Delta\rho}}\right)^{1/2}} \tag{2.45}$$

Han et al. (2006) carried out an experimental work under vertical upward cocurrent conditions, pipe of $9.525\ mm$ I.D., liquid mass fluxes ranging from 126 to 198 kg/m^{2}s and gas mass fluxes ranging from 18 to 47 kg/m^{2}s. The proposed correlation is as follows

$$\Delta h_{DW} = 4 \cdot 10^3\ D\ Re_G^{-1.12} \tag{2.46}$$

Chandrasekhar developed a theoretical expression from the Kelvin-Helmholtz instability in which it is supposed that the waves are caused by the relative motion of the two continuous phases (Kolev, 2007):

$$\Delta h_{DW,K-H} = 3\,\pi \frac{\left(1 + \frac{\rho_g}{\rho_l}\right)\sigma_l}{\rho_g\left(u_g - u_L\right)^2} \tag{2.47}$$

As explained in previous sections, measurements taken at the GEPELON facility have been used to obtain a new empirical correlation, Eq. (2.33). Additionally, the performance of this new correlation has been tested, so several experimental data of other authors have been analysed (Figure 2.22). As in the previous section, we searched for available expressions to estimate DW heights, and a reduced number of expressions have been found. The comparisons of the new correlation against the predictions for the different expressions proposed by several researchers are displayed in Figure 2.23.

Figure 2.22 displays the existent scattering of the reduced experimental data for the DW heights. As shown in the figure, most of the Zadrazil et al. (2014) data are fairly well predicted by the proposed correlation, while Karapantsios et al. (1995) data are systematically under predicted. However, almost all the experimental data series studied are within the 50% error bands.

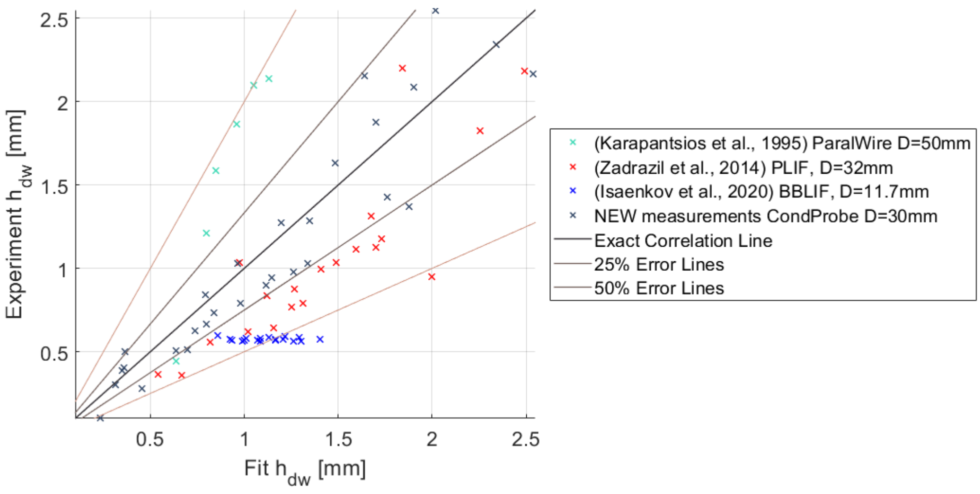

Figure 2.22. Experimental data of the DWs height versus the predictions of the new correlation under Cocurrent Downward Flow conditions.

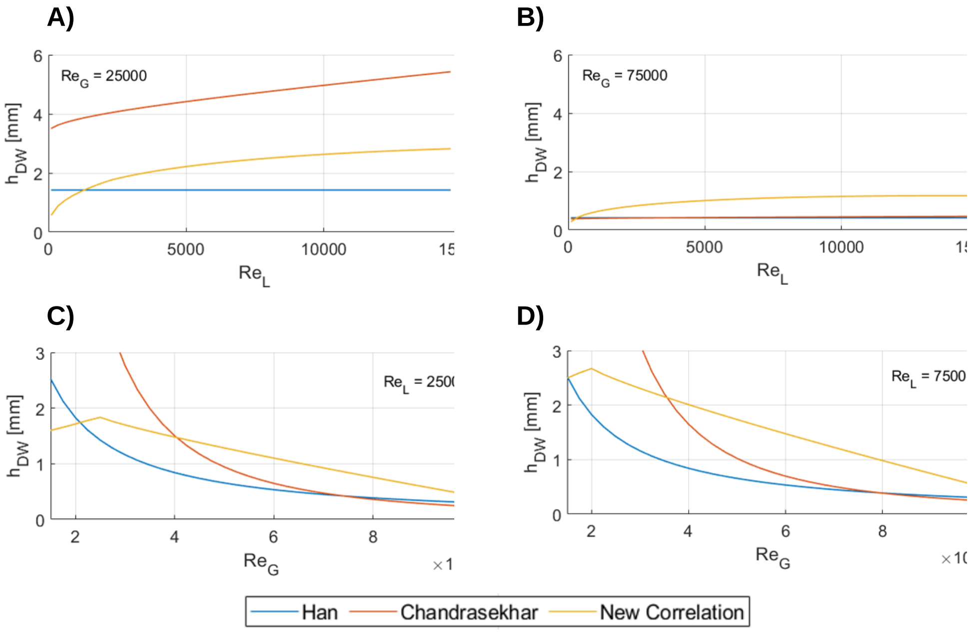

Figure 2.23. Comparison of the DWs height obtained according to the empirical correlations proposed by different authors as function of: A-B) Liquid Reynolds number at constant Gas Reynolds number; C-D) Gas Reynolds number at constant Liquid Reynolds number.

Figure 2.23 shows the comparisons of the DW height predictions for the different expressions proposed by several researchers with those of the new expression under downward cocurrent flow conditions. As shown in the figure, there are significant differences when comparing the different expressions, particularly with Chandrasekar’s expression (Kolev, 2007). This theoretical expression systematically overestimates the DWs heights for low gas Reynolds numbers. In fact, Kelvin-Helmholtz instability arises, for the case of air and water at near-atmospheric conditions, when the velocities of the working fluid differ by at least 7 m/s approximately. Han's correlation only considered the gas Reynolds number and was developed for upward flows (Han, 2006), but despite its simplicity and development for different flow conditions, it provides fairly accurate predictions for the configurations under study. The currently developed correlation, which gives the best results compared to the present experimental data, predicts values slightly higher than Han's expression for almost all gas and liquid Reynolds numbers.

DISTURBANCE WAVE FREQUENCY

The frequency of DWs is the other variable studied in relation to the behavior of gas-liquid interface waves. Note that the frequency shown in the following sections refers only to the DWs thus discarding the small RWs. The DWs frequency is defined as the number of waves per second and is therefore the inverse of the period between successive waves.

DISTURBANCE-WAVE FREQUENCY CORRELATION

The procedure for obtaining the correlation is the same as the process followed for the DWs height. The only difference is that the frequency of the waves is obtained by means of the Strouhal number, which is the dimensionless number used to calculate the frequency. Finally, the following expression has been obtained:

$$St_l = 539 \cdot {Re_L}^{-0.73} \cdot \left(1 + 2.5 \cdot 10^{-3} \cdot abs\left(Re_G - Re_{G\_maxhDW}\right)^{0.56}\right) \qquad (2.48)$$

being St_l is the Strouhal number of the liquid phase, defined as:

$$St_l = \frac{\nu_{DW} D}{J_L} \qquad (2.49)$$

while, the Reynolds numbers of the gas and liquid phases were defined in Eqs. (4) and (5).

Figure 2.24 compares the experimental frequency data and the values obtained using the correlation proposed in Eq. (2.48). Although the scatter is slightly larger than in the previous cases, almost all the points are within the

$\pm 30\%$ error band. Determination coefficient R^2 obtained for this correlation is 0.805 and the RMS error is 1.35.

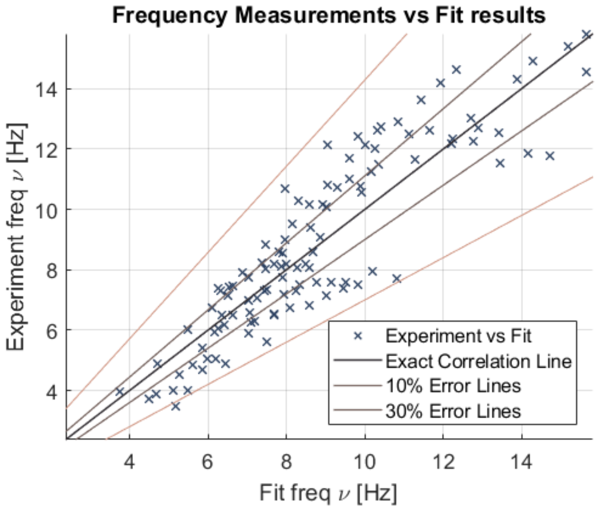

Figure 2.24. Experimental DWs frequency vs. data calculated with the new correlation.

The trend observed for the DW frequency is different from those studied for other variables although it shares with the DW height the particular behavior when increasing Re_G. Generally speaking, the frequency grows as both liquid and gas Reynolds increase. However, as explained in detail in section 4.2.2, there is a slight decrease in frequency until a certain gas Reynolds number is reached, represented as Re_{G_maxhDW}. Note that the liquid Reynolds exponent is negative, which would indicate that the frequency increases as the Reynolds value decreases. However, the Strouhal number contains the liquid velocity, so if we perform a simple balance the exponent would be +0.27 for the superficial liquid velocity.

NEW CORRELATION PERFORMANCE AGAINST EXPERIMENTAL DATA OF OTHER AUTHORS

No expressions have been found for the DWs frequency under downstream co-current flow conditions in the literature. Although a good compendium of the DWs frequency correlations under other conditions, mainly for upward cocurrent flows, can be found in Berna et al. research (2014). For this concerning case, as there are not available expressions for the DW frequency, only the comparison of our data against the limited number of experimental data and the performance of the new developed correlation has been carried out, Figure 2.25.

Comparing measured wave frequencies between different authors represents a challenge and can easily be misinterpreted if not done carefully. Because of the chaotic behavior of the liquid film for different conditions and the limitations of each of the measurement systems, the interfacial waves can be presented in very different ways. Each author uses its own methods to characterize the waves, leading to different frequency measurements. In this paper, the frequency is obtained after counting the DW peaks but other authors such as Isaenkov et al. (2020) measure the frequency as a result of adjacent pairs of peaks and crests. This leads to differences of about an order of magnitude, making the comparison of measurements very complex. Other authors use indirect methods to measure frequency, generally based on the Fast Fourier Transform (FFT), showing a frequency spectrum and in some cases identifying the dominant one. Vasques et al. (2018) compare indirect methods such as FFT and direct counting methods obtaining errors exceeding 30%. Although the comparison may be imprecise, it has been decided to compare the experimental measurements of the authors who have estimated frequency values of large disturbance waves and have avoided counting ripple waves. However, even in this case, a large dispersion can be found caused by the differences in the criteria applied when discerning between DWs and RWs. Then, as shown in Figure 2.25 and quoted above, a great dispersion exists between the experimental data of the different authors. For instance, in Takahama and Kato's research (1980), the experimental data show values of the DW frequencies much higher than those predicted by the current correlation, while Zadrazil et al. data (2014) showed a big dispersion in their measurements.

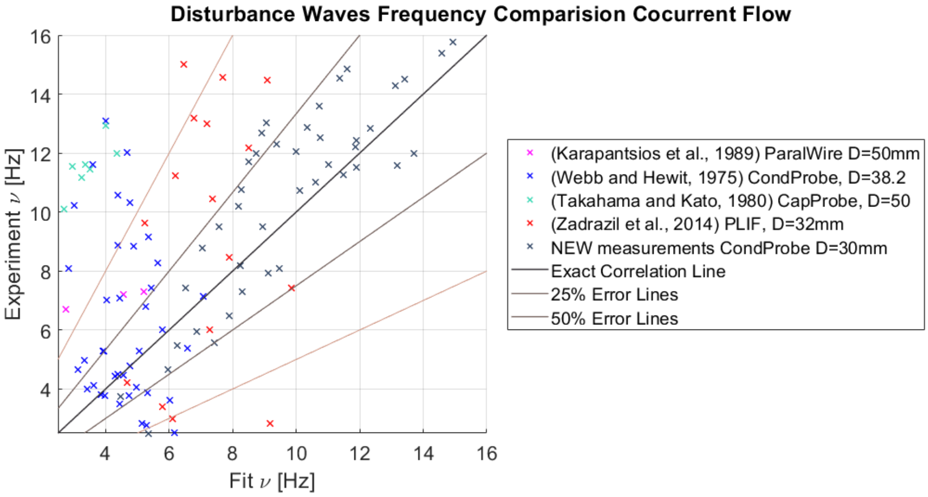

Figure 2.25. Experimental data versus new correlation predictions for the Wave Frequency under Cocurrent Downward Flow conditions.

2.6. CONCLUSIONS

This paper shows the operation of the GEPELON installation, designed to measure the liquid film thickness in a vertical downward co-current gas-liquid flow. For this purpose, three-electrode conductance probes capable of measuring the evolution of the liquid thickness over time have been designed. In addition, for these probes to work properly, it has been necessary to study and manufacture the specific port to reduce flow disturbance and the electronic circuitry to maintain a reliable and clean signal. The signal collected at a sampling rate of $5{\cdot}10^3$ samples per second is converted into distance after a calibration process specifically designed to analyse each probe individually. Six runs have been measured for each experimental condition for ten seconds each in order to analyse the random error. Furthermore, other possible sources of systematic errors, such as the calibration and adjustment process or the data acquisition system, have been studied.

Different variables related to the liquid film can be studied with the information obtained in this facility. In this paper, an in-depth analysis of the average film thickness, disturbance wave height and disturbance wave frequency has been carried out. Correlations have been proposed for each of these variables as a function of the input conditions expressed as dimensionless numbers. In addition, both the experimental measurements and the proposed correlations have been compared with research data from several authors.

It has been observed that the liquid film thickness grows as we increase the liquid Reynolds number; however, it decreases more strongly with the gas Reynolds number. The same tendencies with the gas and liquid flow rates have been observed for the height of the disturbance waves. Nevertheless, a maximum value of this variable has been measured at approximately $2 \cdot 10^4 - 4 \cdot 10^4$ gas Reynolds numbers depending on the liquid Reynolds number. This range corresponds to the change of annular flow sub-regime also observed by other authors. The influence of the gravitational force in this zone becomes less significant, being gas-liquid interaction predominant from here onwards.

For the wave frequency data, a direct proportionality for both gas and liquid flows has been observed, showing similar behaviour to the wave height. In this case, a constant or slow reduction of the wave frequency is also shown up to $2 \cdot 10^4 - 4 \cdot 10^4$ gas Reynolds numbers approximately, depending on the liquid Reynolds number. Three new correlations have been proposed for each of the three studied variables.

Regarding the mean liquid film thickness correlations, highlight that the co-current downward flow correlations are obtained by adding a term to the free falling correlation to consider the effect of the air stream (through the use of the gas Reynolds number). In contrast, the dependency of this variable with the distance to the flow entrance (degree of flow development) has been captured by using an exponential term in the cocurrent correlation (mean film thickness comes to a saturation value downstream depending on the gas and liquid Reynolds numbers).

We must conclude this research by summarising some important insights. It has been presented a notorious contribution of new data to the experimental database and the development of several new correlations for the most important variables of vertical downward cocurrent annular flows. There are many theoretical expressions and empirical correlations to determine the mean film thickness under free falling conditions, most of them based on Nusselt's one. However, this number is drastically reduced when downward cocurrent flows are analysed and, finally, studies and expressions to consider the degree of flow development are extremely scarce. There is also a small number of theoretical and experimental studies concerning the characteristics of the large amplitude waves (DWs), both heights and frequencies. The scarcity accentuates when correlating these two variables with the flow conditions. As an important contribution, correlations for both variables are proposed throughout this paper, and their performance has been tested against the limited experimental data available.

2.7. ACKNOWLEDGEMENTS

This research is supported by the EXMOTRANSIN project ENE2016-79489-C2-1-P included in the I+D Spanish plan.

2.8. REFERENCES

Alekseenko S., Antipin V., Cherdantsev A., Kharlamov S., Markovich D., “Investigation of Waves Interaction in Annular Gas-Liquid Flow Using High-Speed Fluorescent Visualization Technique”. Microgravity Science Technology, Vol. 20 Nº1, pp .271 (2008).

Alekseenko S., Cherdantsev A., Heinz O.M., Kharlamov S.M., Markovich D.M., “Two-Wave Structure of Liquid Film and Wave Interrelation in Annular Gas-Liquid Flow with and without Entrainment”. Physics of Fluids, Vol. 21 Nº1, Ner 061701 (2009).

Alekseenko S.V., Cherdantsev A., Kharlamov S., Markovich D., “Analysis of spatial and temporal evolution of disturbance waves and ripples in annular gas-liquid flow”. International Journal of Multiphase Flow, Vol. 67, pp. 122-134 (2014).

Alekseenko S.V., Cherdantsev A.V., Cherdantsev M.V., Isaenkov S.V., Markovich D.M., “Study of formation and development of disturbance waves in annular gas-liquid flow”. International Journal of Multiphase Flow, Vol. 77, pp. 65-75 (2015).

Aliyu A.M., “Vertical annular gas-liquid two-phase flow in large diameter pipes”. Ph.D. Thesis, Cranfield University, Bedfordshire Shrivenham, Oxfordshire, England (2015).

Belt R.J., Van’t Westende J.M.C., Prasser H.M., Portela L.M., “Time spatially resolved measurements of interfacial waves in vertical annular flow”. International Journal of Multiphase Flow, Vol. 36, pp. 570-587 (2010).

Berna C., Escrivá A., Muñoz-Cobo J.L., Herranz L.E., “Review of droplet entrainment in annular flow: interfacial waves and onset of entrainment”. Progress in Nuclear Energy, Vol. 74, p.p. 14-43 (2014).

Berna C., Escrivá A., Muñoz-Cobo J.L., Herranz L.E., “Review of droplet entrainment in annular flow: characterization of the entrained droplets”. Progress in Nuclear Energy, Vol. 79, p.p. 64-86 (2015).

Bevington P.R., Robinson D.K., “Data Reduction and Error Analysis in the Physical Sciences”. Third Edition, edited by Mac Graw Hill (2003).

Brauner N., “Roll wave celerity and average film thickness in turbulent wavy film flow”. Chemical Engineering Science, Vol. 42, No. 2, pp. 265-273 (1987).

Charogiannis A., An J.S., Voulgaropoulos V., Markides C.N., “Structured planar laser-induced fluorescence (S-PLIF) for the accurate identification of interfaces in mulpiphase flows”. International Journal of Multiphase Flow, Vol. 118, pp. 193-204 (2019).

Cherdansev A.V., Charogiannis A., Markides C.N., “Simultaneous application of two laser-induced fluorescence approaches for film thickness measurements in annular gas-liquid flows”. International Journal of Multiphase Flow, Vol. 119, pp. 237–258. doi: 10.1016/j.ijmultiphaseflow.2019.07.013 (2019).

Chu K.J, Dukler A.E., “Statistical Characteristics of Thin, Wavy Films: Part II. Studies of the Substrate and its Wave Structure”. AIChE, Vol. 20, No 4, pp. 695-706 (1974).

Chu K.J, Dukler A.E., “Structure of the Large Waves and their Resistance to Gas-Flow”. AIChE, Vol. 21, No 3, pp. 583-593 (1975).

Cuadros J.L., Rivera Y., Berna C., Escrivá A., Muñoz-Cobo J.L., Monrós-Andreu G., Chiva S., “Characterization of the gas-liquid interfacial waves in vertical upward co-current annular flows”, Nuclear Engineering and Design, Vol 346, pp 112–130 (2019).

Czernek K., Witczak S., “Precise determination of liquid layer thickness with downward annular two-phase gas-very viscous liquid flow”. Energies, 13, 6529; doi:10.3390/en13246529 (2020).

Dasgupta A., Chandraker D.K., Kshirasagar S., Raghavendra Reddy B., Rajalakshimi R., Nayak A.K., Walker S.P., Vijayan P.K., Hewitt G.F., “Experimental investigation on dominant waves in upward air-water two-phase flow in churn and annular regime”, Experimental Thermal and Fluid Science, Vol. 81, pp. 147-163 (2017).

De Jong P., Gabriel K. S., “A preliminary study of two-phase annular flow at microgravity: experimental data of film thickness”. International Journal of Multiphase Flow, Vol. 23, pp. 1203-1220 (2003).

Fulford G.D., “The Flow of Liquid in Thin Films”. Advances in Chemical Engineering, Vol. 5, pp. 151-236 (1964).

Hall-Taylor N.S., Hewitt G.F., Lacey P.M.C., “The motion and frequency of large disturbance waves in annular two-phase flow of air-water mixtures”. Chem. Eng. Sci. Vol. 18, pp. 537-552 (1963).

Han H., Zhu Z., Gabriel K., “A study on the effect of gas flow rate on the wave characteristics in two-phase gas-liquid annular flow”. Nuclear Engineering and Design, Vol. 236, pp. 2580–2588 (2006).

Hanratty T.J., Hershman, A., “Initiation of roll waves”. Am. Inst. Chem. Eng. Journal, Vol. 7, pp. 488 (1961).

Henstock W.H., Hanratty T.J., “The interfacial drag and the height of the wall layer in annular flows”. AIChE Journal, Vol.22 N.6, pp. 990-1000 (1976).

Hewitt G.F., Hall-Taylor N.S., “Annular Two-phase Flow”. Pergamon Press, Oxford, pp. 136-139 (1970).

Holowach M.J., Hochreiter L.E., Cheung F.B., “A model for droplet entrainment in heated annular flow”. International Journal of Heat and Fluid Flow, Vol. 23, pp. 807-822 (2002).

Isaenkov S.V., Vozhakov I.S., Cherdansev M.V., Arkhipov D.G., Cherdansev A.V., “Effect of liquid viscosity and flow orientation on initial waves in annular gas-liquid flow”. Applied Sciences, 10, 4366; doi:10.3390/app10124366 (2020).

Ishii M., Grolmes M.A., “Inception Criteria for Droplet Entrainment in Two-Phase Concurrent Film Flow”. AIChE Journal, Vol. 21 p. 308-318 (1975).

Karapantsios T.D., Paras S.V., Karabelas A.J., “Statistical characteristics of free falling films at high Reynolds numbers”. International Journal of Multiphase Flow, Vol. 15, No 1, pp. 1-21 (1989).

Karapantsios T.D., Karabelas A.J., “Longitudinal characteristics of wavy falling films”. International Journal of Multiphase Flow, Vol. 21, No 1, pp. 119–127 (1995).

Karimi G., Kawwaji M., “An experimental study of freely falling films in a vertical tube”. Chemical Engineering Science, Vol. 53, No 20, pp. 3501–3512 (1998).

Kolev N.I., “Multiphase Flow Dynamics 2. Nuclear Thermal and Mechanical Interactions”. Springer, ISBN 978-3-540—69834-0 (2007).

Kulov N.N., Maksimov V.V., Maljusov V.A., Zhavoronkov N.M., “Pressure drop, mean film thickness and entrainment in downward two-phase flow”. The Chemical Engineering Journal. Vol. 18, pp 183-188 (1979).

Leven, A., “Filter applications”, Telecommunication Circuits and Technology, pp. 95–160. doi: 10.1016/b978-075065045-8/50016-x (2007).

Liu L., Matar O.K., Hewitt G.F., “Laser-induced fluorescence (LIF) studies of liquid–liquid flows. Part II: Flow pattern transitions at low liquid velocities in downwards flow”. Chemical Engineering Science, Vol. 61 p.p. 4022-4026 (2006).

Meza C.E., Balakotaiah V., “Modeling and experimental studies of large amplitude waves on vertically falling films”. Chemical Engineering Science, Vol. 63, pp. 4704-4743 (2008).

Mudawwar I.A., El-Masri M.A., “Momentum and heat transfer across freely-falling turbulent liquid films”, International Journal of Multiphase Flow, Vol. 12, No 5, pp. 771–790 (1986).

Muñoz-Cobo J.L:, Chiva S., Méndez S., Monrós G., Escrivá A., Cuadros J.L., “Development of Conductivity Sensors for Multi-Phase flow Local Measurements at the Polytechnic University of Valencia (UPV) and University Jaume I of Castellon (UJI)”. Sensors 2017, 17, 1077; doi:10.3390/s17051077 (2017).

Muñoz-Cobo J.L:, Rivera Y., Berna C., Escrivá A., “Analysis of conductance probes for two-phase flow and holdup applications”. Sensors, 20, 7042; doi:10.3390/s20247042 (2020).

Nguyen T., Balakotaiah V., “Modeling and experimental studies of wave evolution on free falling viscous films”. Physics of Fluids, Vol. 12, No. 9, 2236 (2000).

Nosoko T., Yoshimura P.N., Nagata T., Oyakawa K., “Characteristics of two-dimensional waves on a falling liquid film”. Chemical Engineering Science, Vol. 51, No. 5, p.p. 725-732 (1996).

Nusselt W., “Die oberflachenkondensation des wasserdampfes,”. Zeitschrift des Vereines Dtsch. Ingenieure, Vol. 60, No. 27, pp. 541–546 (1916a).

Nusselt W., “Die oberflachenkondensation des wasserdampfes,”. Zeitschrift des Vereines Dtsch. Ingenieure, Vol. 60, No. 28, pp. 569–575 (1916b).

Padmanaban A., “Film thickness measurements in falling annular films”. Ph.D. Thesis, University of Saskatchewan, Saskatoon, Canada (2006).

Panga M.K.R., Mudunuri R.R., Balakotaiah V., “Long-wave equation for vertically falling films”. Physical Review, Vol. 71, 036310, DOI: 10.1103/PhysRevE.71.036310 (2005).

Rivera Y., Muñoz-Cobo J.L., Berna C., Cuadros J.L., Escrivá A., “Experimental study of the interfacial waves produced in upward vertical annular flow when varying the liquid phase surface tension”. Published in the proceedings of the conference: computational and experimental methods in multiphase and complex flow X, WIT Transaction on Engineering Science, Vol 123, pp. 21-31 (2019).

Rivera Y., Muñoz-Cobo J.L., Berna C., Escrivá A., Córdova Y., “Study of liquid film behavior in vertical downward air-water annular flow”. Published in the proceedings of the conference: Advances in Fluid Mechanics, XIII, WIT Transaction on Engineering Science, Vol. 128, pp. 77-88 (2020).

Rivera Y., Muñoz-Cobo J.L., Cuadros J.L., Berna C., Escrivá A., "Experimental study of the effects produced by the changes of the liquid and gas superficial velocities and the surface tension on the interfacial waves and the film thickness in annular concurrent upward vertical flows". Experimental Thermal and Fluid Science, Vol. 120, 110224 (2021).

Schubring, D., Shedd, T.A., "Wave behavior in horizontal annular air-water flow". Int. J. Multiphase Flow 34, pp. 636-646. (2008).

Schubring D., Ashwood A.C., Shedd T.A., Hurlburdt E.T., "Planar laser-induced fluorescence (PLIF) measurements of liquid film thickness in annular flow. Part I: Methods and data". International Journal of Multiphase Flow, Vol. 36, pp. 815-824 (2010).

Setyawan A., Indarto I., Deendarlianto. A., "The effect of the fluid properties on the wave velocity and wave frequency of gas-liquid annular two-phase flow in a horizontal pipe". Experimental Thermal and Fluid Science, Vol. 71, pp. 25-41 (2016).

Takahama H., Kato, S., "Longitudinal flow characteristics of vertically falling liquid films without concurrent gas flow". International Journal of Multiphase Flow, Vol. 6, No 3, pp. 203–215(1980).

Telles A.S., Dukler A.E., "Statistical Characteristics of Thin, Vertical, Wavy, Liquid Films". Ind. Eng. Chem. Fundam., Vol. 9, No 3, pp. 412-421 (1970).

Tiwari R., Damsohn M., Prasser H.M., Wymann D., Gossweiler C., "Multi-range sensors for the measurement of liquid film thickness distributions based on electrical conductance". Flow Meas. Instrum., Vol. 40, pp. 124–132 (2014).

Vasques J., Cherdansev A., Cherdansev M., Isaenkov S., Hann D., "Comparison of disturbance wave parameters with flow orientation in vertical annular gas-liquid flows in a small pipe". Experimental Thermal and Fluid Science, Vol. 97, pp. 484-501 (2018).

Wallis G.B., "One-dimensional Two-phase Flow". McGraw-Hill, Inc, New York, USA. (1969).

Wayne C., "The Interfacial Characteristics of Falling Film Reactors". Ph.D. Thesis, University of Nottingham, Nottingham, UK (2001).

Webb D.R., Hewitt G.F., "Downwards co-current annular flow". International Journal of Multiphase Flow, Vol. 2, pp. 35–49 (1975).

Wolf A., "Film structure of vertical annular flow". PhD. Thesis University of London University and Diploma of Membership of Imperial College (1995).

Wolf A., Jayanti S., Hewitt G.F., "Flow development vertical annular flow", Chemical Engineering Science, Vol. 56, pp. 3221–3225 (2001).

Zadrazil I., Matar O.K., Markides C.N., "An experimental characterization of downwards gas-liquid annular flow by laser-induced fluorescence: Flow regimes and film statistics". International Journal of Multiphase Flow, Vol. 60, pp. 87-102 (2014).

Zhao Y., Markides C.N., Matar O.K., Hewitt G.H., “Disturbance wave development in two-phase gas–liquid upwards vertical annular flow”, International Journal of Multiphase Flow 55, pp. 111–129 (2013).

Chapter 3

SECOND PUBLICATION:

Experimental study of the effects produced by the changes of the liquid and gas superficial velocities and the surface tension on the interfacial waves and the film thickness in annular concurrent upward vertical flows

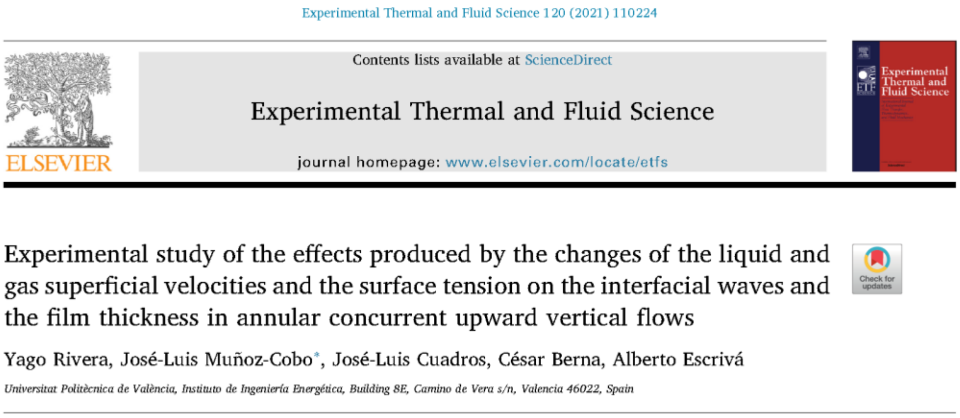

Experimental Thermal and Fluid Science 120 (2021) 110224

Contents lists available at ScienceDirect

Experimental Thermal and Fluid Science

journal homepage: www.elsevier.com/locate/etfs

Experimental study of the effects produced by the changes of the liquid and gas superficial velocities and the surface tension on the interfacial waves and the film thickness in annular concurrent upward vertical flows

Yago Rivera, José-Luis Muñoz-Cobo*, José-Luis Cuadros, César Berna, Alberto Escrivá

Universitat Politècnica de València, Instituto de Ingeniería Energética, Building 8E, Camino de Vera s/n, Valencia 46022, Spain

https://doi.org/10.1016/j.expthermflusci.2020.110224

Experimental Study of the Effects Produced by the Changes of the Liquid and Gas Superficial Velocities and the Surface Tension on the Interfacial Waves and the Film Thickness in Annular Concurrent Upward Vertical Flows

Y. Rivera, J.L. Muñoz-Cobo, J.L. Cuadros, C. Berna, A. Escrivá
Instituto Universitario de Ingeniería Energética
Universitat Politècnica de València (UPV)
Camino de Vera 14, 46022 Valencia (Spain)
Tel: +34 963879245
Emails: yaridu@upv.es; jlcobos@iqn.upv.es; jocuaor@doctor.upv.es;
ceberes@iie.upv.es; aescriva@iqn.upv.es;

Abstract

In this paper, we have performed an experimental study of the effect of changing the surface tension of the water in vertical annular concurrent two-phase flow (air + liquid) by adding small amounts of 1-butanol to the liquid phase. Adding small amounts of this chemical compound diminishes the surface tension of the water, while the dynamic viscosity remains practically unchanged. A set of experiments have been performed in the interval of surface tension values that ranges from $72 \cdot 10^{-3}\ N/m$ to $45 \cdot 10^{-3}\ N/m$, and with different values of the superficial velocities of the gas and liquid flows. In this broad range of surface tensions and boundary condition values the average amplitude and frequency of the disturbance waves have been measured for each boundary condition and surface tension value. In addition, we also measured the mean amplitude of the ripple waves, the mean value of the unperturbed base thickness, and the average film thickness. Also, we obtained a set of correlations expressing all these magnitudes in nondimensional form in terms of the Reynolds number of the gas, the Reynolds number of the liquid and the Kapitza number. Finally, we performed a brief discussion and comparison with the results of other authors.

Keywords: Interfacial waves, disturbance waves, ripple waves, annular flow

3.1. INTRODUCTION

Annular concurrent vertical two-phase flow appears in a big number of nuclear reactor applications as for instance in the vertical channels of Boiling Water Reactors, Advanced Boiling Water Reactors, and in several accidental scenarios of the reactor channels of PWR. In addition, this flow pattern also appears in chemical reactors, and other chemical and energy technologies. When this flow pattern takes place inside a pipe, a liquid film forms close to the pipe walls and moves upward dragged by the shear stress exerted by the gaseous phase, which moves with much higher velocity than this film and is located in the central part of the pipe, forming a gaseous core with small drops. Generally large waves, denoted as disturbance waves (DW), which are coherent over large distances appear at the gas-liquid interface. Additionally, incoherent small waves are observed between these large disturbance waves, which popularly are known as ripples waves (RW). The small drops, which appear in annular flow are separated and does not aggregate forming large droplets as in wispy flow.

These large-scale disturbance waves are separated by a thin film liquid layer known as the base film layer, the small scale RW are travelling over this base film layer surface or over the large scale DW. Some authors, as (Azzopardi, 1997) , and (Alekseenko et al., 2014), consider the presence of these large DW as a necessary condition for the inception of entrainment, because of they assume that the entrained drops are formed in the peaks or crests of these waves by the shear stress forces exerted by the gas on the top of these waves, which are able to overcome the liquid cohesion forces. (Alamu and Azzopardi, 2011) showed experimental evidence of the relationship between periodicity/frequency of the DW with respect to the fluctuation (frequency) of the drop concentration in time.

An important issue is the interaction between the DW and the RW, by high speed fluorescence (Alekseenko et al., 2014) have shown that the RW appear always at the base of the rear front of the large DW. In addition, (Chu and Dukler, 1974) have proved that the RW have a short life in comparison with that of the DW.

Early studies on disturbance waves were performed by (Taylor, Hewitt and Lacey, 1963), they found that the formation of these waves was related with an observed transition in droplet entrainment which is consistent with the recent findings by (Alekseenko et al., 2014). Besides, (Taylor, Hewitt and Lacey, 1963) found that the average wave velocity increased rapidly when the gas flow increased but was less sensitive to the changes in the liquid flow rate. Also, they found that the frequency of these DW increases with the air and liquid flow rates. (Zhao et al., 2013) found that the DW once are formed remain axially and circumferentially coherent. In addition, small ripples and no coherent waves appeared, which were located between the DW and in some cases mounted on the DW.

In addition, a set of authors have performed previous studies on this subject specially we must mention the works by (Belt et al., 2010), and (Azzopardi and Whalley, 1980) which performed a set of measurements in vertical annular flow, of the film thickness, velocity of the DW, and distribution of these waves. In addition, (Sadatomi et al., 2016) performed recently an study on the surface tension effects produced in vertical upward annular flows in small size pipes of 5mm I.D. They measure the pressure drop, the mean film thickness, and the entrainment fraction. Also recently, (Setyawan and Deendarlianto, 2016), studied the effect of the viscosity and surface tension on the wave velocity and wave frequency of gas–liquid annular two-phase flow in a horizontal pipe, they found that the wave frequency decreases with the decrease of surface tension.

The main goal of this paper is to perform a set of experiments adding small amounts of 1-butanol to the water. The effect of this addition is to reduce the surface tension of the water while the viscosity remains practically unchanged. Proceeding in this way, it is possible to study the effect of the changes of the surface tension on the disturbance and ripple wave properties, and to obtain more general correlations for the magnitudes that characterize these waves. The reason is that when one works with the non-dimensional Navier-Stokes equations of thin liquid films appears the following term in these equations $Ka\partial_{xxx}h(x,r,t)$, Being x the distance along the flow direction, $h(x,r,t)$ the film thickness, and Ka the Kapitza number. This term is fundamental for the development of solitary waves or disturbance waves in the annular flow. This term depends on the surface tension and also on the viscosity of the 1-butanol water mixture. Because the viscosity practically does not change when adding small amount of 1-butanol, then the difference between the different experiments performed in this paper with different σ values is that we are changing the Kapitza number, and therefore the important term displayed above is changed. This is the reason why we performed this set of experiments and also this is the reason why we use the Kapitza number in the correlations that will be developed in this paper (Muñoz-Cobo et al., 2016).

The organization of the paper is as follows: section 2 describes the vertical annular flow facility (VAFF), the instrumentation used to perform the measurements of the physical magnitudes, and the calibration methods. In section 3, we describe the conductance probe measurements and methods, the test matrix of the experiments, the main magnitudes being measured as height and frequency of the DW, average thickness of the film, the properties of the ripple waves and so on. In section 4, we correlate the non-dimensionalized physical magnitudes in terms of $\Pi - \text{numbers}$, discussing the results. Finally, in section 5, we give the main conclusions of the paper.

3.2. THE VERTICAL ANNULAR FLOW FACILITY (VAFF), INSTRUMENTATION, DATA ACQUISITION AND CALIBRATION METHODS

3.2.1. LAYOUT, OPERATION, AND CHARACTERISTICS OF THE VAFF FACILITY

In this section, we give a short description of the VAFF facility and its operation. Figure 3.1 displays the main characteristics of the VAFF facility. This facility includes the following interconnected circuits and components:

i. The air injection circuit, which is formed by the following components: i-1) the compressor; i-2) a big air tank, that acts as a reservoir of air to maintain the air flow constant; i-3) a gas filter, that removes any small particle which is being entrained by the gas stream; i-4) a demisting filter to eliminate any small drop or mist contained in the air current; i-5) the flow control valve, that controls that the gas flow is within certain operating limits; i-6) the pressure control valve; i-7) an air flow meter to measure the gas flow entering the test section; i-8) a pressure sensor to measure the pressure near the inlet of the test section.
ii. The water circuit with the following functions: to recover, filter, and store, the water coming from the test section, and then to pump and inject it into the test section through the water injection device (Figure 3.1). This system is formed by the following components and devices: ii-1) the extraction water device, which extracts the water annular film from the test section, this water is removed through a metallic porous material to the water extraction tank, this water is then pumped and after being filtered is send again to the water injection tank; ii-2) The injection water device, which creates the annular flow as shown in Figure 3.1. The water flow between the tank injection system and the test section depends on the pressure difference between both sides of the porous pipe in the injection device.
iii. The test section, which has a height of 5 meters and 44 mm of inner diameter, is made of methacrylate. In its lower part, the test section connects to the injection device, which creates the annular flow, while its upper part connects to the extraction device and the demisting cyclone. Therefore, the test section receives an annular flow that develops through the pipe of the test component. Two differential pressure sensors, located in the upper part of the test section, measure the pressure drop of the annular flow at different points to know if the annular flow is fully developed or not (Cuadros et al., 2019). In the upper part of the test section, it is also located the conductance probe that measures the film thickness evolution with time.

The operation of the facility is performed as follows: filtered and demisted air is injected in the lower part of the injection device that creates the annular flow by means of the air production circuit, which contains a compressor whose maximum working pressure and volumetric flow rate are $8\,bar$ and $3750\ l/min$ respectively. The flow rate of the injected air ranges from 2250 to $3500\ l/min$. At the same time, the injection water device injects the water in the test section, at a lower flow rate ranging from 4 to $10\ l/min$. The water film flow created by this injection device is pushed up by the shear stress acting on the gas-water interface produced by the gas flow moving upward at much higher velocity than that of the water annulus close to the walls. This water-gas flow develops through the test section and disturbance and ripple waves are produced at the interface, which are registered by the conductance probe located in the upper part of the test section. The characteristics of these waves depend on the boundary conditions, mainly gas and liquid superficial velocities (j_l and j_g) and liquid surface tension (σ). This last effect is analyzed adding small quantities of 1-butanol to the water that modifies the surface tension producing small variations on the viscosity.

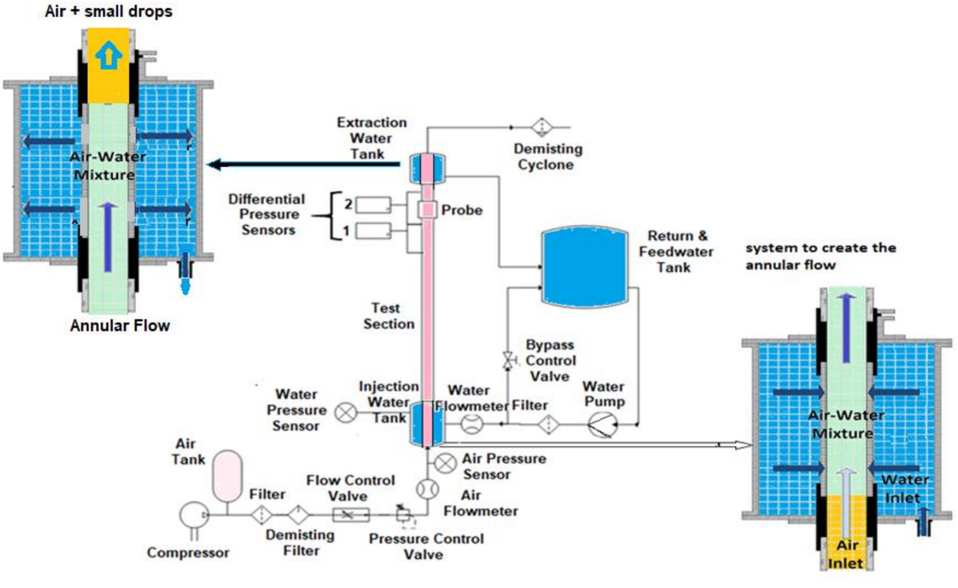

Figure 3.1. Layout of the vertical annular flow facility (VAFF) with a description of the water injection and extraction systems, which create the annular flow and remove the water film respectively.

The gas flow, when its velocity is high enough, can drag small drops from the crest of the disturbance waves that then move with the gas stream. Some of these drops can interact with the water film flow, and others move toward the exit of the test section and enter a centrifugal demisting cyclone, where are separated from the gas stream. The demisted gas stream is then vented to atmosphere. New fresh air is injected into the test section after compression, demisting and filtering, and a new air cycle starts again.

3.2.2. FACILITY INSTRUMENTATION, ELECTRONICS AND DATA ACQUISITION

MAIN FACILITY INSTRUMENTATION

The VAFF facility is equipped with different sensors and probes to check all the state variables and the boundary conditions. All the measurements are performed when the annular flow is completely developed at the measuring point for each experimental condition. To check this issue two differential pressure sensors, denoted as 1 and 2, are located in the upper part of the test section, if both sensors measure the same pressure drop this means that the flow is fully developed. The equipment used to perform these measurements is formed by two SMC PSE 550 low differential pressure transducers. These sensors have a rated pressure range from 0 to $2\ kPa$, with an accuracy $\pm 1.0\%$ at full scale (F.S.) or smaller, a linearity error equal or less than $\pm 0.5\%$ F.S., and a repeatability error of 0.3% F.S. or less.

Because, according to Darcy formula (12), the volumetric flow rate depends on the pressure difference between the inner and outer sides of the porous sintered material with pore size of $19 \mu m$, and coefficient of permeability $\psi_s = 0.8\ 10^{-12} m^2$. Then the local pressure measurements are made at two different points, one in the water injection tank and the other one near the inner side of the porous sintered pipe, see Figure 3.1 for more details. These local measurements are performed with Burkert 8314 relative pressure transducers (difference in pressure between the inner part of the facility and the surrounding atmosphere). These sensors have a pressure range measurement between 0 and 1 bar, with a sum of linearity, hysteresis and repeatability errors less than $\pm 0.3\%$ F.S. and error adjustment accuracy zero point and full scale less than $\pm 0.3\%$.

The temperature of the water was measured during the experiment and an average value was computed for each run with given boundary conditions and 1-butanol concentration which determines a surface tension value (j_l, j_g and σ). Temperature measurements were performed with Type T thermocouples (copper-constantan), which are suitable in the range -200 to $350\ °C$. Their error, for measurements above $0°C$, is the biggest one of the following two values $1.0°C$ or 0.75% of the measured temperature in Celsius degrees.

The water volumetric flow rate measurements were performed with a Krohne Optiflux 4300 C Series electromagnetic flowmeter (EMF) located in the pipe that supplies the water to the injection device. Its volumetric flow rate measurement interval ranges from 0 to $20\ l/min$ and has an accuracy better than $\pm 0.3\%$ of span.

The measurements of the high-speed gas volumetric flow rate were performed with a SMC PF2A706H magnetic flowmeter. Its volumetric flow rate measurement range covers from 300 to $6000\ l/min$, the flowmeter has a linearity accuracy of $\pm 1.5\%$ of full scale (F.S.) or less and a repeatability of $\pm 1.5\%$ F.S. or less.

CONDUCTANCE PROBE CHARACTERISTICS

The estimation of the characteristics of the interfacial waves and the film thickness is performed using a conductance probe. This type of probe, which is displayed in Figure 3.2-b, allows to measure and record the fast-moving wavy film behaviour produced at the gas-liquid interface. This probe consists in three conducting electrodes flush mounted to the wall and aligned with the tube in the direction of the gas and film flows. The first electrode is the transmitter electrode, which emits a signal generated by a signal-generator, the second one is connected to the ground and the third one is the receiver electrode, which collects the current that the water film conduces. The amount of current conducted from the emitter to the receiver and therefore the voltage signal generated depends on the film thickness existing between both electrodes.

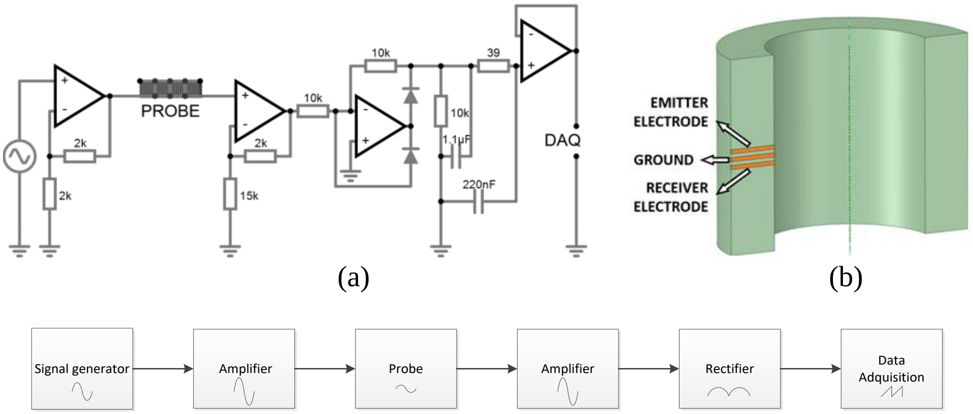

(a) (b)

(c)

Figure 3.2. a) Electronic circuit built for the conductance probe, b) 3D view of the probe with the arrangement of the 3 electrodes, c) flow diagram of the performance of the electronic circuit.

The three electrodes are inserted into the conductance probe port that is made of polypropylene. In addition, the three sensor electrodes are made of stainless steel and are inserted in the port perpendicularly to the port walls as displayed in Figure 3.2-b, the space between the electrodes is $1.5\ mm$, and have a diameter of $2\ mm$. The transmitter electrode is excited, with a $300\ kHz$ sinusoidal signal and $4\ V$ peak to peak. The diameter of the port is the same one that the diameter of the pipe and its length is $170\ mm$. Small slots, not displayed at the Figure 3.2-b, have been created at both sides of the port to connect it to the test pipe without connection discontinuities.

The total amount of current collected by the receiver at any time instant is proportional to the liquid film thickness existing at that time between both electrodes, i.e., the transmitter and the receiver. Also, it is important to notice that the resistance and capacitance between the transmitter and receiver electrodes depends also on the signal frequency. Because of the resistance and the capacitance fall to asymptotic values as the frequency increases, for this reason the frequency of the signal was set to $300\ kHz$, which is beyond the frequency saturation point. The dependence of the signal voltage with the film thickness has been analyzed by several authors for different types of conductance probes (Coney, 2001; Koskie et al., 1989; Lee et al., 2017). All of them have found that the signal in volts increases with the film thickness, being necessary a calibration that depends of the fluid conductivity and the characteristics of the conductance probe. Consequently, the electric signal collected by the receiver changes when an interfacial wave crosses the sensor region for a conducting liquid as water, and this change allows the determination of the liquid film thickness variations with time.

ELECTRONICS AND DATA ACQUISITION SYSTEM

Figure 3.2-a displays the electronic used for the conductance probe, the functions performed are: first the sinusoidal signal produced by the generator is amplified before sending it to the excitation electrode or transmitter (Cuadros et al., 2019). Next, the receiver electrode captures the signal transmitted through the liquid layer. This last signal is amplified again and transformed into a DC current by a rectifier incorporated to the electronics device. Finally, the data acquisition system acquires this DC signal, whose value is related to the liquid film thickness existing between both electrodes. As consequence, the variations with time in the value of this DC signal will indicate the passage of the interfacial waves present in the liquid film. This electronic circuit is made of 4 high frequency amplifiers, several precision resistances (0.1% tolerance), capacitances and diodes 1N4148. All the components used are high precision ones, with low tolerance.

During the test runs all the instrumentation devices, located in the positions given at Figure 3.1 and described in the previous sections, are monitoring in real time all the major experimental conditions, which include air and water volumetric flow rates, temperatures and pressures, in addition to the recording of the experimental data along the test section, i.e. conductance probe signal in volts and pressure test-section values. The data acquisition system has been programmed in LabView. This system distinguishes between two types of measurements: The conductance probe measurements, which suffer fast variation with time and need high sample rates in order to capture the shape of the wave peaks, and the rest of measurements as temperature, pressure and flow rates, which need much smaller sample rates. The acquisition system for the conductance probe records 10^5 samples per second (S/s) (National Instruments PCI 6255 with 80 analogic channels and a maximum rate of $1.25\ MS/s$). For the rest of experimental data, which suffer smaller variations with time, the acquisition system records 120 samples per minute from each sensor of the facility (National Instruments cDAQ-9174 chassis compact-DAQ with a module NI 9207 of 16 analogic channels and a maximum rate of $500\ S/s$).

3.2.3. CALIBRATION OF THE CONDUCTANCE PROBE

To obtain better accuracy (Rivera et al., 2019) than in previous measurements (Cuadros et al., 2019) a new calibration device, displayed at Figure 3.3, was designed and built with higher precision components than the previous one. The goal of the calibration is to relate the voltage signal with the water film thickness. For the measurement performed adding 1-butanol to the water, the sensor calibration must be repeated, because of the water conductivity changes with the 1-butanol concentration and therefore the electric signal is different for each 1-butanol concentration when the rest of conditions are the same. Proceeding is this way; it is possible to relate the information contained in the recorded signals (V) with the amplitude of the waves (mm) and film thicknesses (mm) produced at the fluid interface.

We performed the calibration process with the calibration device displayed at Figure 3.3. This device consists of three major components: one optical precision table; a precision positioning system mounted on this table with an error of 0.002 mm; and several cylinders with known diameters and made with a dielectric material. By setting the dielectric cylinder at the desired position, in the inner part of the conductance probe port, by means of the precision positioning system, we can know the fluid thickness between the dielectric and the probe electrodes inserted in the polypropylene port and connected to the electronics displayed at Figure 3.3. Then, measuring the voltage in the receiver electrode of the probe for each film thickness, we can find by a fitting process the existing relationship between the signal voltage and the fluid thickness.

A total number of 33 calibration measurements were made with the calibration device for each one of the three 1-isobutanol concentrations values, which are denoted by their surface tensions at 25 ºC, $68.5 \cdot 10^{-3}\ N/m$, $55 \cdot 10^{-3}$and $45 \cdot 10^{-3}$. All the calibration measurements saturated beyond a given thickness, i.e., the signal in volts attained a saturation value.

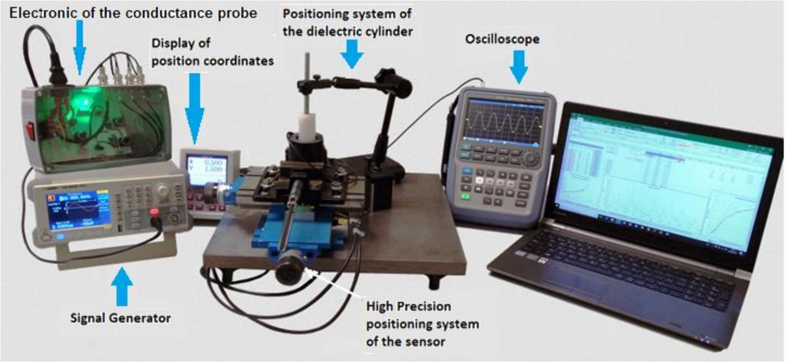

Figure 3.3. Arrangement of elements of the high precision calibration device for the conductance probe.

However, as the experimental data for the boundary conditions used in this paper showed that the signal amplitudes (Volts) were smaller than $0.8\ V$ for all the cases with 1-butanol, then the film thickness and the height of the disturbance waves were always smaller than 1.5 mm for all the experimental condition used. Therefore, the boundary conditions of these experiments were far away to produce disturbance waves and film thicknesses, which attained the saturation conditions. So, we reduced the number of calibration points including only those below $1.5\ mm$, which are inside the shadowed area at Figure 3.4, the number of points inside this area was 16. Another advantage of performing a fitting in this reduced region is that the curve slope has smaller changes in this region, and therefore the fitting can be performed with a polynomial of smaller degree and better determination coefficient (R^2), practically one for the fits performed.

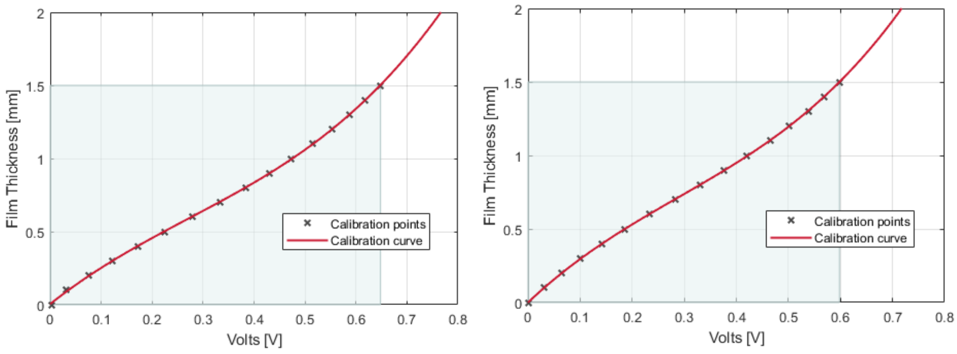

(a) (b)

Figure 3.4. Calibration curve obtained using a third-degree polynomial fit for two of the experiments performed adding (a) 1-butanol to the water to reach $55 \cdot 10^{-3}\ N/m$ and (b) $45 \cdot 10^{-3}\ N/m$. The crosses denote the experimental points and the shadowed area the region where we find all the experimental values of this paper.

The calibration curve used to fit the 1-butanol calibration experiments was a third degree polynomial given by eq. (3.1), with coefficients denoted by the symbols x_0 to x_3, while for pure water the fitting curve was also given by eq. (3.1):

$$\delta(mm) = x_0 + \; x_1 \, V + x_2 V^2 + x_3 V^3 \tag{3.1}$$

The coefficient of determination of the polynomials fits of the calibration curves for all the 1-butanol cases inside the shadowed area was higher than $R^2 = 0.999$.

The expression used to obtain the fitting error $\varepsilon_{fit,cal}$of equation (3.1), with $N = 16$ experimental data points, for the 1-butanol cases, and m degrees of freedom (m=4), can be found in chapter 7 of (Bevington and Robinson, 2003) book and is given by:

$$\varepsilon_{fit,cal} = \sqrt{\tfrac{1}{N-m} \textstyle\sum_{j=1}^{N} \left(\delta_{exp,j} - \sum_{i=0}^{3} x_i V_j^i\right)^2} \tag{3.2}$$

Because of the experimental points display a smooth behavior in the interest region (shadowed area) with small changes of slope as shown in Figure 3.5 Then, a fit was performed using only the calibration points located inside the area of interest and a third degree polynomial, in this way the fitting error was notably reduced in comparison to the result that was obtained using a fifth degree polynomial degree mainly in the region from 0 to $5\,V$ as displayed in Figure 3.4. For instance, we reduced the fitting error from $0.282\,mm$ to $0.0059\,mm$ for the case of 1-butanol with surface tension $68.5 \cdot 10^{-3}\,N/m$. Table 3.1 displays the coefficients obtained for the calibration curves for each one of the 1-butanol concentrations. This table also displays the root mean square errors (RMSE), and the fitting errors calculated with equation (3.2).

Table 3.1. Coefficients of the third-degree polynomial fits obtained for the calibration curves of the different 1-butanol concentrations and the pure water. The last two columns display the coefficient of determination R^2 and the root mean square (RMSE) fitting error.

σ (N/m)	x_3	x_2	x_1	x_0	R^2	RMSE	$\varepsilon_{fit,cal}$ (mm)
72. 10^{-3}	1.605	-2.227	2.413	-0.0095	0.9992	0.0135	0.0191
68.5 10^{-3}	3.793	-2.915	2.659	0.002	0.9999	0.0051	0.0059
55.10^{-3}	4.123	-3.372	2.765	0.005	0.9999	0.0049	0.0057
45.10^{-3}	5.230	-4.538	3.351	0.000	0.9999	0.0026	0.0030

3.3. CONDUCTANCE PROBE MEASUREMENTS: BOUNDARY CONDITIONS, FILTERING RESULTS AND ERRORS.

3.3.1. Test matrix and boundary conditions

The test matrix consisted of four data series; three performed adding 1-butanol to the water plus one additional with only water. Each one of the 1-butanol data series was performed with a constant concentration of 1-butanol. Because of the surface tension of the mixture diminishes when the concentration of 1-butanol increases, then we denote the different runs by their respective surface tensions, which are: $72 \times 10^{-3}\ N/m$ for the water at $25°C$, and $68.5 \cdot 10^{-3}\ N/m$, $55 \cdot 10^{-3}\ N/m$ and $45 \cdot 10^{-3}\ N/m$ for the different mixtures of water-1-butanol with the solute concentrations in increasing order.

For each solution of 1-butanol in water, we performed forty-nine experimental runs, which were obtained by combining seven liquid and seven gas superficial velocities respectively, denoted by $j_l\ (m/s)$ and $j_g(m/s)$. The experimental runs can be also represented by their respective volumetric flow rates, denoted by $Q_l(l/min)$ and $Q_g(l/min)$. The seven liquid flow rates covered the interval from $Q_l = 4$ to $10\ l/min$, with increments of $\Delta Q_l = 1\ l/min$ or from $j_l = 0.044\ m/s$ to $0.11\ m/s$ with increments $\Delta j_l = 0.011\ m/s$. The seven volumetric air flow rates covered from $Q_g = 2000\ l/min$ to $3500\ l/min$, with increments of $\Delta Q_g = 250\ l/min$ from run to run, or from $j_g = 21.9\ m/s$ to $38.4\ m/s$, with increments $\Delta j_g = 2.75\ m/s$.

The main goal of changing the water surface tension is to study the effect produced by this change on the interfacial wave's behavior. The interest of this issue is because we can isolate the effect produced by the surface tension on the disturbance and ripple wave properties. During all the experimental measurements the pressure in the upper part of the facility was kept at atmospheric conditions, and the water and air temperatures were kept approximately constant at about 30 and $25°C$ respectively.

During each experimental test run, we followed the same procedure used by (Cuadros et al., 2019), which consisted in the following four steps:

i. Adjustment of the air and liquid volumetric flow rates to the desired boundary values.
ii. Check that the steady state conditions have been attained for the main variables (air and liquid volumetric flow rates, pressures and differential pressures at the monitored points, and liquid and gas temperatures).
iii. Check that the two-phase annular flow is developed at the measuring point of the conductance probe. This condition is attained when the two differential pressure sensors, located in the upper part of the test section at different positions, provide on average the same value. If the flow is

not developed for the set of stablished boundary conditions, this experimental run is discarded. This is the reason to discard all the runs with $Q_l \leq 3\ l/min$, see the paper by (Cuadros et al., 2019) for more details.

iv. Once the steady state conditions are attained, the facility operator starts the collection and recording of all the data for sixty seconds. The signal from the conductance probe is sampled at a frequency of 10^5 Samples/s, for sixty seconds that yields a total number of 6.10^6 samples for each one of the 49 experimental runs performed for each 1-butanol concentration. The signal coming from the other sensors are sampled at a slower rate of $2\ S/s$, which yield 120 samples for each monitored magnitude during the measuring time.

Table 3.2 displays all the boundary conditions used for the 49 experimental runs of one of the four data series, notice that these boundary conditions are the same ones for the other three remaining data series.

Table 3.2. Boundary conditions of the experiments performed in the VAFF facility for each 1-butanol concentration.

Boundary conditions of the 49 data series for each surface tension value						
$j_g\ (m/s) \times j_l(m/s)$						
21.9 x 0.044	24.6 x 0.044	27.4 x 0.044	30.1 x 0.044	32.9 x 0.044	35.6 x 0.044	38.4 x 0.044
21.9 x 0.055	24.6 x 0.055	27.4 x 0.055	30.1 x 0.055	32.9 x 0.055	35.6 x 0.055	38.4 x 0.055
21.9 x 0.066	24.6 x 0.066	27.4 x 0.066	30.1 x 0.066	32.9 x 0.066	35.6 x 0.066	38.4 x 0.066
21.9 x 0.077	24.6 x 0.077	27.4 x 0.077	30.1 x 0.077	32.9 x 0.077	35.6 x 0.077	38.4 x 0.077
21.9 x 0.088	24.6 x 0.088	27.4 x 0.088	30.1 x 0.088	32.9 x 0.088	35.6 x 0.088	38.4 x 0.088
21.9 x 0.099	24.6 x 0.099	27.4 x 0.099	30.1 x 0.099	32.9 x 0.099	35.6 x 0.099	38.4 x 0.099
21.9 x 0.110	24.6 x 0.110	27.4 x 0.110	30.1 x 0.110	32.9 x 0.110	35.6 x 0.110	38.4 x 0.110

The physical magnitudes monitored, sampled and stored during each experimental data run were: air and water volumetric flow rates, i.e., Q_g and Q_l, liquid and gas temperatures (T_l and T_g respectively), and pressures at the test section entrance and in the water injection tank to the test section. In addition, also the conductance probe voltage signal collected by the receiver electrode and amplified by the electronic system is acquired (Figures 2-a and 2-c).

3.3.2. Conductance probe measurements and errors

From the probe signal in Volts (raw data), we applied first the corresponding calibration functions to each one of the signals for the different experimental data runs of each data series with different 1-butanol concentrations. In this way, we converted the signals in volts versus time, in signals in mm versus time. These signals give the evolution of the film thickness of the water plus 1-butanol mixture versus time. Figure 3.5 displays the evolution of the film thickness versus time for the raw signals for the run case of $2250\ l/min$ x $7\ l/min$ ($Q_g \times Q_l$), and different values of the surface tension in N/m.

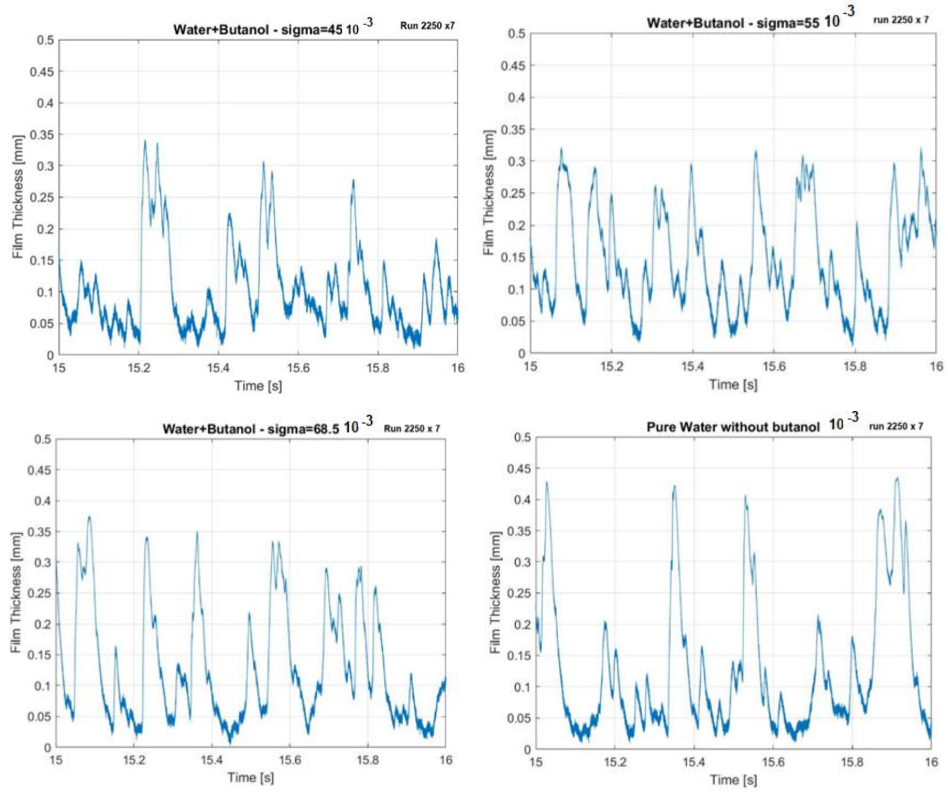

Figure 3.5. Film thickness versus time for $Q_g \times Q_l$ runs 2250 x 7 for different 1-butanol concentrations, with σ values of 45 10-3 N/m, 55 10-3 N/m, 68.5 10-3 N/m, and 72. 10-3 N/m, before applying the Savitzky-Golay moving average filter.

The next step was to apply a Savitzky-Golay moving average filter to the raw data (Savitzky and Golay, 1964). The reason to use this kind of filter is because this type of filters preserves the width and height of the peaks, while standard moving average filters tends to broad the peaks and to reduce their heights as commented by (Press et al., 1992). In addition, the Savitzky-Golay filter produces very little distortion in the signal in comparison to the standard moving average filters (Guiñón et al., 2007). The application of this filter is performed choosing several points or frame length (m), to obtain each component of the filtered signal and a set of coefficients (c_i), which are known as the convolution coefficients. In this filter if we denote by $\{y_k\}$ the sampled signal. Then the Savitzky-Golay filtered signal $\{y_{SG}(j)\}$ is given by the expression:

$$y_{SG}(j) = \sum_{i=-n_p}^{n_p} c_i \ y_{j+i} \tag{3.3}$$

Where $n_p = (m-1)/2$ and the convolution coefficients c_i are obtained by a least square polynomial fit to all the points inside each moving average window.

If the degree of the fitting polynomial is p. Then, the fit is performed selecting the set of coefficients c_i by a least-square fitting to the m signal points contained in the window, which gives the following result:

$$c_i = \sum_{l=0}^{p} \{(A^T A)^{-1}\}_{0l}\, i^l \tag{3.4}$$

Being A^T the transpose of A, which is the matrix with elements given by:

$$A_{il} = i^l \tag{3.5}$$

The elements of $A^T A$ are easy to obtain and are given by:

$$(A^T A)_{il} = \sum_{k=-n_p}^{n_p} A_{ik}^T\, A_{kl} = \sum_{k=-n_p}^{n_p} A_{ki}\, A_{kl} = \sum_{k=-n_p}^{n_p} k^{i+j} \tag{3.6}$$

The calculation of the inverse $(A^T A)^{-1}$ is simple because, according to equation (3.4), we only need the elements of the first row.

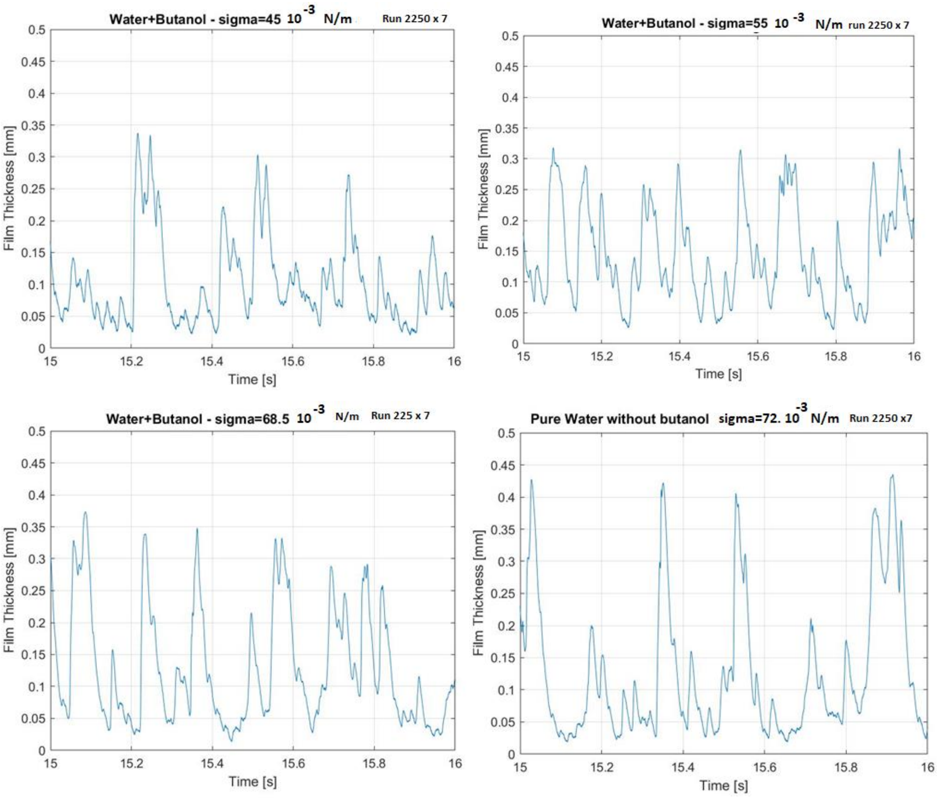

Figure 3.6. Film thickness versus time for $Q_g \times Q_l$ runs 2250 x 7 for different 1-butanol concentrations, with σ values of 45 10-3 N/m, 55 10-3 N/m, 68.5 10-3 N/m, and 72. 10-3 N/m, after application of the Savitzky-Golay moving average filter.

The application of this filter has been performed choosing a polynomial of order $p = 8$ and a frame length $m = 101$. The results obtained by application of the Savitzky-Golay filter to the signals of case $Q_g \times Q_l = 2250 \times 7$, for different 1 butanol concentrations are displayed in Figure 3.7. We observe that the height of the peaks and their widths remain practically unchanged after application of this filter.

We observe from figures 5 and 6 that the height of the disturbance waves increases when the surface tension rises, i.e. when the 1-butanol concentration diminishes. We remind here that the surface tension of the water at saturation temperature and atmospheric pressure is $58.92\ 10^{-3}\ N/m$, so the selected range of interfacial tensions covers a good range of values that can be found in practical applications.

The total error has been obtained from the following expression:

$$\varepsilon_\delta = \sqrt{\left(\frac{\partial f(V)}{\partial V}\right)^2 \varepsilon_V^2 + \varepsilon_{fit,cal}^2 + \varepsilon_{pos}^2 + \varepsilon_{acc}^2} \qquad (3.7)$$

Where $f(V)$ is the polynomial calibration function given by equation (3.1), ε_V is the error of the equipment used to measure the voltage, $\varepsilon_{fit,cal}$ is the fitting error given by expression (3.2), ε_{pos} is the position error during the calibration process, and finally ε_{acc} is the accidental error, calculated by the expression:

$$\varepsilon_{acc}(\delta) = t_{1-\alpha/2} \frac{S(\delta)}{\sqrt{n}}, \qquad (3.8)$$

Where $t_{1-\alpha/2}(df)$ is the $1 - \frac{\alpha}{2}$ quantile of the Student-t with $df = n - 1$ degrees of freedom, being n the number of measurements performed, and S the variance. This quantile depends on the confidence level and on the degrees of freedom, having a value of 2.26 for the usual 95% confidence level ($\alpha = 0.05$) and with 9 degrees of freedom, i.e., when the measurements are repeated ten times. The estimated accidental errors and the relative errors in % for the various magnitudes measured in this work are displayed at Table 3.3.

Table 3.3. Accidental errors obtained from the repeatability analysis for the main physical magnitudes that characterize the interphase.

	$\varepsilon_{acc}(\delta_m)$ (µm)	ε_{acc}(δbun) (µm)	ε_{acc}(ADW) (µm)	ε_{acc}(νDW) (Hz)
ε_{acc}	29.3	5.12	53.4	0.92
$\pm\varepsilon_{rel,acc}$, %	±6.2	±1.76	±7.9	±4.5

The estimated total errors for the average thickness, unperturbed base thickness and amplitude of the DW have been computed from equation (3.7), on account of the calibration curve for each surface tension value and are displayed in Table 3.4.

Table 3.4. Total errors for the main magnitudes obtained for the different surface tension values.

σ (N/m)	$\varepsilon_{tot}(\delta_m)$ (µm)	$\varepsilon_{tot}(\delta_{bun})$ (µm)	$\varepsilon_{tot}(A_{DW})$ (µm)
$72 \cdot 10^{-3}$	35	20	57
$68.5 \cdot 10^{-3}$	30	8	54
$55 \cdot 10^{-3}$	29.9	8	54
$45 \cdot 10^{-3}$	29.5	6	53

3.3.3. Measurement of the magnitudes that characterize the interfacial waves and the film

The magnitudes that have been estimated in the experiments for the different boundary conditions and surface tensions are: the average amplitude A_{DW} of the disturbance waves, the average thickness δ_{bun+RW} of the base film plus the ripples waves, the mean film thickness $\bar{\delta}_m$, the average thickness $\bar{\delta}_{DW}$of the disturbance waves, the average thickness $\bar{\delta}_{bun}$ of the unperturbed base film, the mean amplitude A_{RW} of the ripple waves, and the mean frequency ν_{DW} of the disturbance waves. Figure 3.7 displays a schematic view of the interfacial waves and the previously mentioned magnitudes.

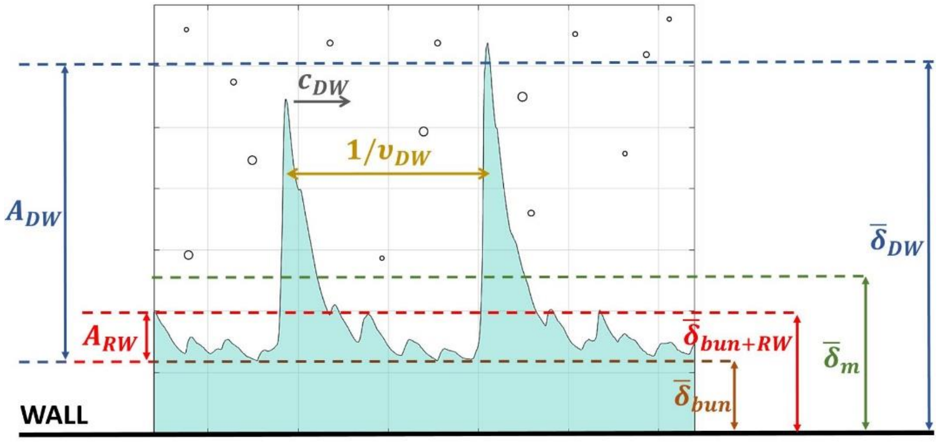

Figure 3.7. Schematic view of the different magnitudes that characterize the interfacial waves.

LIQUID FILM THICKNESS MEASUREMENTS

Four variables related with the liquid film thickness have been estimated, these are the mean film thickness $\bar{\delta}_m$, the unperturbed-base plus RW film thickness $\bar{\delta}_{bun+RW}$, the unperturbed film thickness $\bar{\delta}_{bun}$, and the average thickness of the DW $\bar{\delta}_{DW}$. The average film thickness is the distance from the pipe wall to the mean height of the film, this include computing the average value of the film thickness in all the film regions, i.e. regions with disturbance waves, region with ripple waves and finally regions without any wave. The $\bar{\delta}_{bun+RW}$ is the average film thickness in the inter-space between disturbance waves, including the ripple waves. Finally, the unperturbed film thickness is the average film distance from the pipe wall to the base of all the waves $\bar{\delta}_{bun}$. Based on these definitions, we can define the average amplitudes of the disturbance waves, A_{DW}, and the ripples waves, A_{RW}, as follows:

$$A_{DW} = \bar{\delta}_{DW} - \bar{\delta}_{bun} \tag{3.9}$$

$$A_{RW} = \bar{\delta}_{bun+RW} - \bar{\delta}_{bun} \tag{3.10}$$

Table 3.5 displays A_{RW} in mm in the inter-space between disturbance waves. It is observed that A_{RW} increases with the liquid superficial velocity j_l for all the cases and surface tension values. Also, A_{RW} diminishes when the gas volumetric flow rate Q_g increases. In addition, Figure 3.8 displays the RW amplitude A_{RW} versus j_l for the case with $Q_g = 2500\ l/min$. This amplitude increases with a small slope with j_l. Furthermore, this amplitude shows a small tendency to increase with the increments in the surface tension.

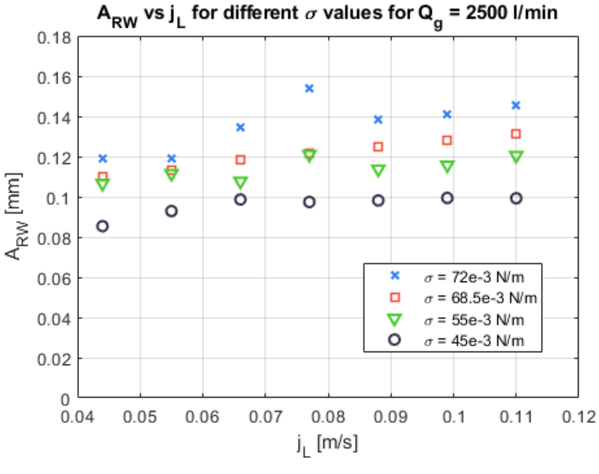

Figure 3.8. Experimental average amplitude A_{RW} versus j_l (m/s) for $Q_g = 2500\ l/min$, and different values of the surface tension ($\sigma = 72\ 10^{-3} N/m$),($\sigma = 68.5\ 10^{-3}$N/m), ($\sigma = 55.10^{-3} N/m$), ($\sigma = 45.10^{-3} N/m$).

Table 3.5. Average amplitude of the ripple waves A_{RW}, for different values of the gas and liquid superficial velocities and surface tensions.

		$A_{RW}\ (mm)$			
$j_g \times j_l$	$Q_g \times Q_l$	72.10^{-3}	$68.5\ 10^{-3}$	55.10^{-3}	$45.\ 10^{-3}$
27.4x0.044	2500x4	0.119	0.111	0.108	0.086
27.4x0.055	2500x5	0.120	0.113	0.113	0.093
27.4x0.066	2500x6	0.135	0.119	0.109	0.099
27.4x0.077	2500x7	0.154	0.121	0.122	0.098
27.4x0.088	2500x8	0.139	0.125	0.115	0.098
27.4x0.099	2500x9	0.141	0.128	0.118	0.099
27.4x0.110	2500x10	0.146	0.132	0.122	0.099
32.88x0.044	3000x4	0.090	0.068	0.057	0.067
32.88x0.055	3000x5	0.105	0.072	0.068	0.076
32.88x0.066	3000x6	0.120	0.077	0.074	0.082
32.88x0.077	3000x7	0.126	0.082	0.077	0.085
32.88x0.088	3000x8	0.120	0.084	0.083	0.089
32.88x0.099	3000x9	0.127	0.090	0.086	0.089
32.88x0.110	3000x10	0.139	0.092	0.091	0.089
38.36x0.044	3500x4	0.086	0.053	0.046	0.058
38.36x0.055	3500x5	0.096	0.058	0.054	0.064
38.36x0.066	3500x6	0.105	0.066	0.061	0.074
38.36x0.077	3500x7	0.117	0.071	0.070	0.084
38.36x0.088	3500x8	0.102	0.074	0.077	0.085
38.36x0.099	3500x9	0.116	0.083	0.079	0.085
38.36x0.110	3500x10	0.121	0.092	0.085	0.093

Concerning the measurements of the unperturbed film thickness, which gives the average film thickness obtained in the regions where the liquid film is not perturbed by the waves and that it is denoted by $\bar{\delta}_{bun}$, it is observed that this base film thickness decreases clearly when increasing the gas flow Q_{gas} for all the surface tension values, as displayed in Table 3.6. However, this parameter is not affected by the surface tension. In addition, there is a small tendency to increase $\bar{\delta}_{bun}$ when the liquid volumetric flow Q_l rises. The value of the unperturbed film thickness is computed by dividing each sensor signal with 60 seconds of recording time, which contains 6.10^6 data points in 100 sub-intervals of $0.6\ s$ containing 6.10^4 data points per sub-interval. Each subinterval contains several

DW and many RW, then at each subinterval the minimum value of the film thickness is computed and finally the average unperturbed film thickness is defined as the mean of all the minimum values obtained in all the subintervals.

Table 3.6. Average value of the unperturbed base film thickness $\bar{\delta}_{bun}(mm)$ for different gas and liquid superficial velocities in m/s and surface tensions in N/m.

		$\bar{\delta}_{bun}$(mm)			
$j_g \times j_l$	$Q_g \times Q_l$	$72\ 10^{-3}$	$68.5\ 10^{-3}$	$55.\ 10^{-3}$	45 x 10^{-3}
27.4x0.044	2500x4	0.031	0.031	0.035	0.028
27.4x0.055	2500x5	0.034	0.035	0.038	0.031
27.4x0.066	2500x6	0.037	0.035	0.041	0.031
27.4x0.077	2500x7	0.041	0.037	0.043	0.033
27.4x0.088	2500x8	0.034	0.041	0.044	0.036
27.4x0.099	2500x9	0.034	0.041	0.046	0.037
27.4x0.110	2500x10	0.034	0.043	0.048	0.038
32.88x0.044	3000x4	0.027	0.021	0.020	0.024
32.88x0.055	3000x5	0.030	0.022	0.021	0.026
32.88x0.066	3000x6	0.033	0.023	0.024	0.028
32.88x0.077	3000x7	0.035	0.024	0.025	0.029
32.88x0.088	3000x8	0.028	0.024	0.026	0.030
32.88x0.000	3000x9	0.030	0.026	0.028	0.032
38.36x0.110	3000x10	0.032	0.027	0.030	0.032
38.36x0.044	3500x4	0.028	0.021	0.019	0.023
38.36x0.055	3500x5	0.030	0.022	0.022	0.025
38.36x0.066	3500x6	0.031	0.023	0.024	0.027
38.36x0.077	3500x7	0.034	0.025	0.025	0.029
38.36x0.088	3500x8	0.024	0.026	0.027	0.031
38.36x0.099	3500x9	0.025	0.027	0.028	0.032
38.36x0.110	3500x10	0.027	0.030	0.029	0.034

Another important measured magnitude is the average mean thickness, which is defined as the distance from the pipe wall to the film surface, obviously this include the surface points located in the DW, in the RW and in regions without waves. This magnitude is denoted as $\bar{\delta}_m$. Table 3.7 displays the mean film thickness for different values of Q_g, Q_l and the liquid surface tensions, σ. From this table, we deduced that the average film thickness diminishes with the increments of the gas superficial velocity while increases with the increments of the surface tension. Also, $\bar{\delta}_m$ increases when the liquid superficial velocity, j_l rises.

Table 3.7. Average film thickness $\bar{\delta}_m(mm)$ for different gas and liquid superficial velocities in units of m/s and different surface tensions σ in N/m.

		$\bar{\delta}_m(mm)$			
$j_g \times j_l$	$Q_g \times Q_l$	72.10^{-3}	$68.5\ 10^{-3}$	$55.\ 10^{-3}$	$45.\ 10^{-3}$
21.92x0.044	2000x4	0.318	0.282	0.241	0.192
21.92x0.055	2000x5	0.383	0.292	0.243	0.199
21.92x0.066	2000x6	0.395	0.302	0.242	0.215
21.92x0.077	2000x7	0.425	0.318	0.243	0.201
21.92x0.088	2000x8	0.451	0.314	0.240	0.203
21.92x0.099	2000x9	0.471	0.311	0.235	0.193
21.92x0.110	2000x10	0.500	0.307	0.230	0.189
27.4x0.044	2500x4	0.194	0.197	0.179	0.137
27.4x0.055	2500x5	0.219	0.211	0.200	0.155
27.4x0.066	2500x6	0.252	0.229	0.219	0.169
27.4x0.077	2500x7	0.275	0.244	0.234	0.178
27.4x0.088	2500x8	0.299	0.255	0.235	0.186
27.4x0.099	2500x9	0.304	0.267	0.244	0.188
27.4x0.110	2500x10	0.330	0.283	0.249	0.190
32.88x0.044	3000x4	0.136	0.113	0.089	0.103
32.88x0.055	3000x5	0.167	0.121	0.111	0.120
32.88x0.066	3000x6	0.190	0.132	0.125	0.134
32.88x0.077	3000x7	0.218	0.145	0.134	0.146
32.88x0.088	3000x8	0.226	0.153	0.146	0.155
32.88x0.099	3000x9	0.249	0.162	0.157	0.163
32.88x0.110	3000x10	0.276	0.172	0.169	0.165
38.36x0.044	3500x4	0.112	0.091	0.077	0.091
38.36x0.055	3500x5	0.136	0.103	0.096	0.104
38.36x0.066	3500x6	0.150	0.114	0.107	0.122
38.36x0.077	3500x7	0,174	0.126	0.122	0.137
38.36x0.088	3500x8	0.177	0.137	0.134	0.146
38.36x0.099	3500x9	0.201	0.149	0.141	0.155
38.36x0.110	3500x10	0.221	0.170	0.152	0.166

In general, for a given fixed value of j_g or Q_g, the mean film thickness $\bar{\delta}_m$increases with the increments of Q_l and the surface tension σ, as displayed in figure 3.9-b, for the case of $Q_g = 2500\ l/min$. However, these increments in $\bar{\delta}_m$

seems to attain a saturation value above $8\ l/min$, for the cases with lower surface tensions. The same behavior is observed for the case with $Q_g = 2250\ l/min$ as displayed in figure 3.9-a.

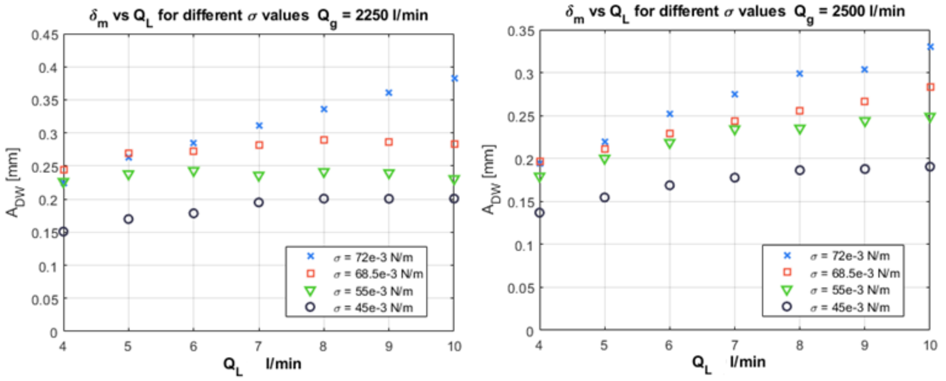

(a) (b)

Figure 3.9. Mean film thickness $\overline{\delta}_m$versus the volumetric liquid flow rate Q_l (l/min), for fixed, $Q_g = 2250\ l/min$ (10-a) and $Q_g = 2500\ l/min$ (10-b) and different values of the surface tension, $(\sigma = 72\ 10^{-3} N/m)$,$(\sigma = 68.5\ 10^{-3}$N/m), $(\sigma = 55.10^{-3} N/m)$, $(\sigma = 45.10^{-3} N/m)$.

MEASUREMENTS OF THE DISTURBANCE WAVE AMPLITUDES AND FREQUENCIES

The amplitude A_{DW} and frequency ν_{DW} of the disturbance waves were measured for different values of the superficial velocities of the gas and the liquid, and also for different values of the surface tension covering a broad range of values. To obtain the amplitude of the disturbance waves, we have followed an iterative multi-criterion. The procedure's major aim is to count only the disturbance waves, eliminating from the counting the ripples waves and to consider as a single peak those cases in which we have a crest with multiple close peaks. The first of these criteria is performed choosing a threshold value, as in the papers by (De Jong and Gabriel, 2003), and (Rodriguez, 2004), so all the peaks which are below this cut value are eliminated in a first round from the peak counting procedure. Specifically, the cut-off value is set at the average value of the film thickness plus one standard deviation. This criterion for many of the experiments with pure water is approximately $0.2\ mm$, but not for all. But for the experiments with 1-butanol is smaller As observed in figure 3.10-a all the peaks below $0.2\ mm$ have been removed from the DW counting.

The second criterion concerns the needs to eliminate the multiple small peaks, which appear in the crest of some disturbance waves as observed in figure 3.10-a for the fifth DW, that contains two peaks. This second criterion, which was also considered by (Cuadros et al., 2019) and denoted as closeness criterion, is applied as follows, first it is stablished a minimum time value $d_{min,DW}$ between successive DW peaks, so that when the time interval between two successive peaks is smaller than this value, then it is considered that we have only one DW. For instance, as shown in Figure 3.10-a, we have considered that this minimum interval is $3.10^{-2}\ s$. Then, because the time interval between the two peaks located in the crest of the fifth DW of Figure 3.10-a is smaller than $3.10^{-2}s$ then the MATLAB program consider them as one peak.

There is a third criterion to eliminate the ripple waves formed on the disturbance waves and those RW reached by the DW. This criterion, called prominence criterion, is based on a prominence cut value defined as a relative value of the DW amplitude, which serve as threshold criterion. Then, if the relative height of these secondary peaks is smaller than this relative amplitude threshold value, these secondary peaks are also produced by ripples waves mounting on some part of a DW. These peaks are more frequently observed in the rear part of the disturbance waves, where the slope of the wave is smaller than in the front part, as displayed at Figures 3.11-a and 3.11-b.

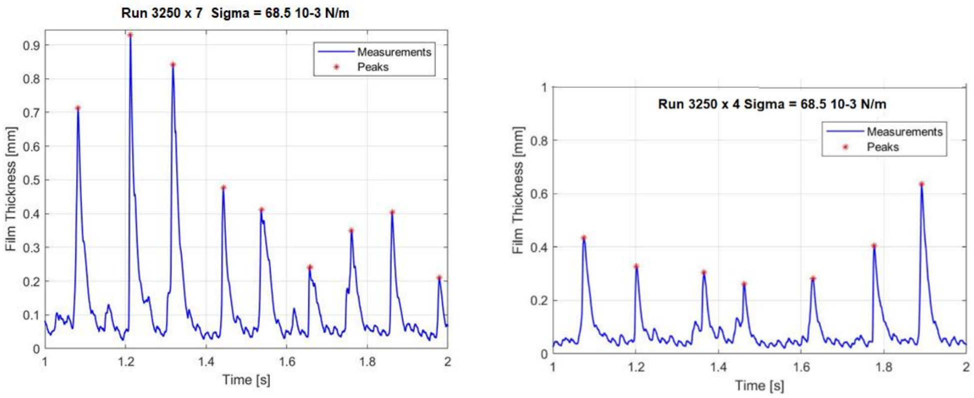

(a) (b)

Figure 3.10. (a) Identification of the disturbance waves peaks, denoted in the figure by an asterisk (*), by the iterative multi-criteria implemented in a MATLAB program for run 3250 x 7 with $\sigma = 68.5\ 10^{-3}N/m$. (b) Identification of DW peaks for run 3250 x 4 with $\sigma = 68.5\ 10^{-3}N/m$.

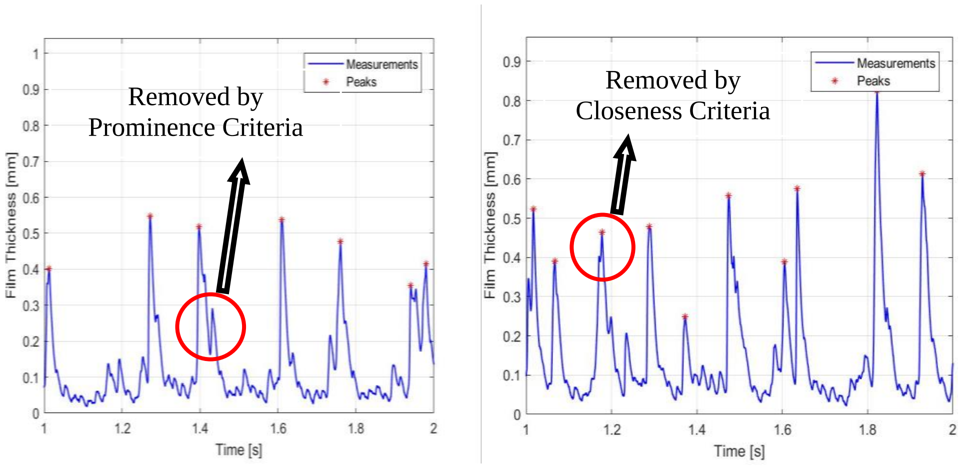

Figure 3.11. Identification of the disturbance waves peaks, denoted in the figure by an asterisk (*), by the iterative multicriteria implemented in a MATLAB program for (a) run 2750 x 5 with $\sigma = 68.5\ 10^{-3} N/m$. (b) Identification of DW peaks for run 2750 x 6 with $\sigma = 68.5\ 10^{-3} N/m$.

After the implementation of this identification multi-criteria of the DW, which removes the waves of small amplitude (RW) and also those RW that are mounted on a DW, we display in Table 3.8, the values of the DW amplitudes, A_{DW}, for different gas and liquid volumetric flow rates and surface tensions. This table shows that, in general, when the gas volumetric flow rate increases then the amplitude of the DW decreases. This decrement in the DW amplitude is produced because rising the gas velocity increases the interfacial shear stress exerted by the gas on the liquid-gas interface. This interfacial force tends to diminish the amplitude of the DW and to drag small drops from the crest of these waves. Another clearly observed effect is that A_{DW} diminishes when the surface tension diminishes; this effect is clearly observed for all the cases of the Table 3.8. This means that when the temperature increases and, consequently, the surface tension diminishes, the DW amplitude will be smaller for the same conditions of the other variables. Concerning the liquid volumetric flow rate, it is observed that the amplitude of the disturbance waves increases for pure water when the liquid flow rate increases. While for the rest of cases, with smaller surface tensions, the effect of the liquid flow rates on the amplitude of the disturbance waves does not show a clear tendency, except for very high gas volumetric flow rates with $Q_g = 3500\ l/min$.

Table 3.8. Amplitude of the disturbance waves in mm for different values of gas and liquid flow rates and different surface tensions in N/m.

		$A_{DW}(mm)$			
$j_g \times j_l$	$Q_g \times Q_l$	σ =72x10-3	68.5x10-3	55x10-3	45x10-3
27.4x0.044	2500x4	0.7502	0.6504	0.4987	0.4384
27.4x0.055	2500x5	0.7687	0.6461	0.5070	0.4537
27.4x0.066	2500x6	0.8200	0.6499	0.4991	0.4459
27.4x0.077	2500x7	0.8642	0.6137	0.4874	0.4287
27.4x0.088	2500x8	0.8770	0.6202	0.4708	0.4143
27.4x0.099	2500x9	0.8649	0.6073	0.4658	0.3906
27.4x0.110	2500x10	0.9180	0.6085	0.4447	0.3777
32.88x0.044	3000x4	0.5922	0.4887	0.3936	0.3985
32.88x0.055	3000x5	0.6588	0.4799	0.4249	0.4083
32.88x0.066	3000x6	0.7035	0.4695	0.4245	0.4054
32.88x0.077	3000x7	0.7433	0.4733	0.4250	0.3857
32.88x0.088	3000x8	0.7817	0.4668	0.4155	0.3755
32.88x0.000	3000x9	0.7911	0.4633	0.4084	0.3633
38.36x0.110	3000x10	0.8379	0.4682	0.4033	0.3556
38.36x0.044	3500x4	0.5158	0.3710	0.3470	0.3723
38.36x0.055	3500x5	0.5628	0.3948	0.3851	0.3817
38.36x0.066	3500x6	0.6114	0.4150	0.3946	0.3945
38.36x0.077	3500x7	0.6271	0.4359	0.4143	0.3972
38.36x0.088	3500x8	0.6613	0.4449	0.4253	0.3795
38.36x0.099	3500x9	0.7032	0.4649	0.3877	0.3621
38.36x0.110	3500x10	0.7419	0.4930	0.4036	0.3616

Figure 3.12 displays the variation of the amplitude A_{DW} of the disturbance waves in mm with the surface tension in Newtons/m for a fixed value of the gas superficial velocity equal to $j_g = 21.92\ m/s$. It is observed that the amplitude increases when the surface tension increases for the three values of j_l represented in this figure, i.e., $0.055\ m/s$ (blue points), $0.077\ m/s$ (orange points) and $0.099\ m/s$ (grey points). Also, we notice that the influence of the liquid superficial velocity on the DW amplitude is small compared with the influence of the surface tension.

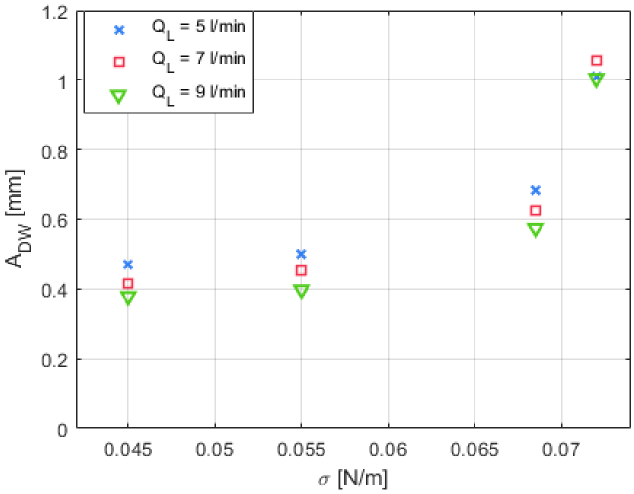

Figure 3.12. Average amplitude $A_{DW}(mm)$of the disturbance waves versus the surface tension (N/m) for $j_g = 21.92\ m/s$, and j_l values of 0.055 m/s ($Q_l = 5\frac{l}{min}$), 0.077 m/s ($Q_l = 7\frac{l}{min}$)and 0.099 m/s ($Q_l = 9\frac{l}{min}$).

The last issue analyzed in this section is the frequency of the disturbance waves. The average value of the DW frequency was computed counting the number of DW peaks and dividing by the measuring time interval in seconds. In this way, we have obtained the average frequency of the DW in Hz for each boundary condition. Table 3.9 shows the frequency of the disturbance waves in Hz for different values of j_g and j_l in m/s and different surface tensions σ in N/m. It is observed that the mean frequency ν_{DW} increases with the liquid superficial velocity j_l for any fixed j_g value, and any fixed surface tension σ value. Also Figure 3.13 confirms this result, where it is clearly observed that the frequency increases with the liquid flow rate Q_l, for all the surface tension values, when Q_g remains fixed at $3000\ l/min$ $(j_g = 27.4\ m/s)$.

Table 3.9. Frequency ν_{DW} of the disturbance waves in Hz for different gas and liquid flow rates and different surface tensions in N/m

		$\nu_{DW}(Hz)$			
$j_g \times j_l$	$Q_g \times Q_l$	72 10^{-3}	68.5 10^{-3}	55 x10^{-3}	45 x 10^{-3}
27.4x0.044	2500x 4	7.53	7.75	7.77	5.82
27.4x0.055	2500x 5	8.42	8.32	8.23	6.60
27.4x0.066	2500x 6	9.22	8.83	8.73	7.13
27.4x0.077	2500x 7	9.30	9.98	9.67	7.42

27.4x0.088	2500x 8	9.92	9.92	9.62	7.62
27.4x0.099	2500x 9	10.32	10.20	9.22	7.60
27.4x0.110	2500x10	10.48	10.88	9.37	7.47
32.88x0.044	3000x4	6.95	6.92	5.45	5.73
32.88x0.055	3000x5	8.03	7.52	6.65	6,57
32.88x0.066	3000x6	8.83	8.02	7.48	7.33
32.88x0.077	3000x7	9.55	8.85	7.98	8.35
32.88x0.088	3000x8	9.70	9.48	8.53	8.53
32.88x0.099	3000x9	10.45	9.67	9.00	9.18
32.88x0.110	3000x10	10.67	10.17	9.72	9.13
38.36x0.044	3500x4	5.48	8.15	6.05	6.20
38.36x0.055	3500x5	7.02	8.93	7.37	7.02
38.36x0.066	3500x6	7.50	9.28	7.87	8.00
38.36x0.077	3500x7	8.70	9.75	8.47	8.75
38.36x0.088	3500x8	9.48	10.38	9.00	9.60
38.36x0.099	3500x9	9.98	10.38	10.07	10.60
38.36x0.110	3500x10	10.47	11.28	10.72	10.75

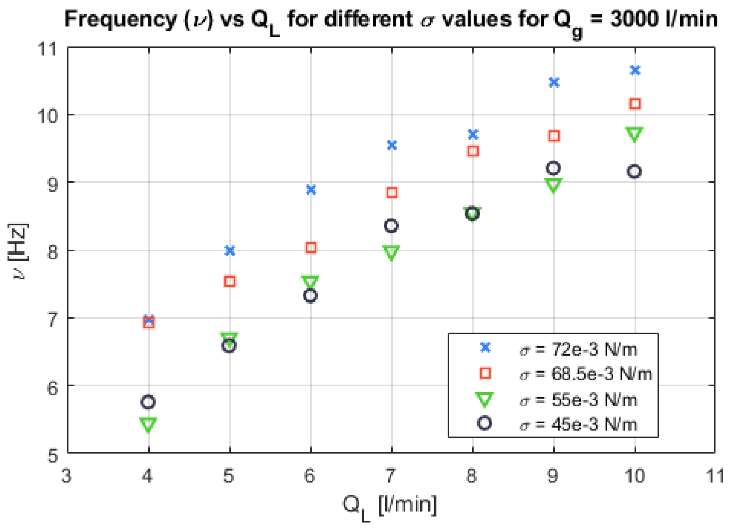

Figure 3.13. DW frequency ν_{DW} (Hz) for different values Q_l in litters/min and $Q_g = 3000\frac{l}{m}$ and different surface tensions in N/m ($72 \cdot 10^{-3}$, $68.5 \cdot 10^{-3}\ N/m$, $55 \cdot 10^{-3}\ N/m$, $45 \cdot 10^{-3}\ N/m$).

3.4. DISCUSSION OF RESULTS AND CORRELATIONS

When performing the analysis of the results and the development of the new correlations for the different magnitudes, it is necessary to consider which non-dimensional numbers must be included in the correlations for the physical variables, which characterizes the annular flow, as mean film thickness, unperturbed film thickness, amplitude and frequency of the disturbance waves. It is well known (Cuadros et al., 2019), that the Reynolds numbers of the gas Re_g and liquid Re_l phases play a fundamental role in the characterization of these magnitudes. However, these Reynolds numbers are normally expressed in experimental applications in terms of the superficial velocities j_g and j_l as follows:

$$Re_g = \frac{\rho_g j_g D}{\mu_g} \tag{3.11}$$

$$Re_l = \frac{\rho_l j_l D}{\mu_l} = \frac{4\Gamma}{\mu_l} \tag{3.12}$$

Where Γ is the liquid mass flow rate of the film flow per unit of circumferential length. However, this last assertion is true when there is not entrainment of the film by the gas flow, which verifies only for low gas superficial velocities, but not for high superficial velocities, condition that usually take place in vertical annular co-current flow. In this case, to characterize properly the flow characteristics of the film, we must consider the entrainment fraction, and to consider a corrected liquid film Reynolds number given by:

$$Re_{film,l} = \frac{\rho_l j_l (1-E) D}{\mu_l} = \frac{4\Gamma(1-\mathrm{E})}{\mu_l} \tag{3.13}$$

Being E the entrainment fraction, which can be measured or obtained from correlations. However, it is common practice to express the correlations in terms of expression (3.12).

In annular two-phase flows with a gaseous core that exerts a shear stress on the gas-liquid interface, as mentioned in the introduction; three types of waves are shown: disturbance, ripples and ephemeral. Obviously, the shear stress depends on the relative velocity of both phases. Because of the liquid velocity is small compared with the gas velocity, then the shear stress depends in a first approximation on the gas velocity, and the friction factor which is a function of the gas Reynolds number. (Oron et al., 1997) studied the Navier-Stokes equations in film flow and the boundary condition which must be satisfied at the gas-liquid interface. The balance of forces at the liquid-gas interface lead to the following equation for the stress force $\vec{t}$ at the interface:

$$\vec{t} = -p\vec{n} + \overleftrightarrow{\tau}_l.\vec{n} = -\sigma\,\kappa\,\vec{n} + \vec{f}_{ex} \tag{3.14}$$

Where κ is the film curvature, $\vec{n}$ is the normal vector to the interface, and $\vec{f}_{ex}$ denotes the interfacial forces due to the gas, p is the pressure, and $\overleftrightarrow{\tau}_l$ is the shear stress tensor of the liquid. The first term of the right-hand side depends on the surface tension and the film curvature. This term, when nondimensionalized, will produce the dependence of the Navier-Stokes equations with the Kapitza number.

The surface wave characteristics depend on the liquid surface tension and the viscosity, and in addition, on the gas and liquid velocities, these last two magnitudes are incorporated into the gas and liquid Reynolds numbers. To consider the effect of the surface tension σ, we can use two non-dimensional numbers the Weber and Kapitza numbers. The Weber number is denoted by We, which is the ratio of the inertial to the surface tension forces. While the Kapitza number, denoted by Ka can be defined in two different ways, the first one defines this non-dimensional number as the square of the ratio of the capillarity length, l_{cap}, and the characteristic length of the fluid, l_ν, which has the advantage to be independent of the flow characteristics, so we have:

$$Ka = \left(\frac{l_{cap}}{l_\nu}\right)^2 = \frac{\sigma}{\rho_l g^{1/3} \nu_l^{4/3}} \tag{3.15}$$

Where the lengths l_{cap} and l_ν are defined by means of the expressions:

$$l_{cap} = \sqrt{\frac{\sigma}{\rho_l g}} \quad , l_\nu = \left(\frac{\nu^2}{g}\right)^{1/3} \tag{3.16}$$

The Kapitza number can also be defined as the ratio of the surface to gravitational forces, choosing the characteristic length as l_ν, it is obtained again equation (3.15):

$$Ka = \frac{(\sigma/l_\nu)}{(\varrho_l g l_\nu)} = \frac{\sigma}{\rho_l g^{1/3} \nu_l^{4/3}} \tag{3.17}$$

Because of the considerations of the previous discussion, we have performed the fitting, to obtain the correlations for the physical magnitudes, in terms of Re_g, Re_l and Ka and also in terms of Re_g, Re_l and We, obtaining slightly better results with Re_g, Re_l and Ka.

3.4.1. Mean film thickness

The experimental data for the non-dimensional mean film thickness, $\bar{\delta}_m/D$, were correlated in terms of Re_g for the gas superficial velocity given by expression (3.11), the Reynolds of the liquid Re_l given by expression (3.12), and the Kapitza number Ka, defined by equation (3.15). A total number of 196 experimental data points were used to obtain this correlation, which is given by the following expression:

$$\frac{\bar{\delta}_m}{D} = 2.35\ Re_l^{0.414}\ Re_g^{-1.415} Ka^{0.781} \tag{3.18}$$

The coefficient of determination obtained for this correlation is $R^2 = 0.98$, and the root mean square error for $\bar{\delta}_m$ is $RMSE\ (\bar{\delta}_m) = 0.0299\ mm$. Figure 3.14 displays the measured values versus the fit results for the average mean film thickness. It is clear, from this correlation, that the mean film thickness diminishes with the gas Reynolds number, and increases with the Kapitza number and Re_l. The advantage of this correlation, equation (3.18), is that provides the mean film thickness for different values of the Kapitza number, i.e., when the surface tension of the liquid changes.

A preliminary analysis of the correlation given by eq (3.18) and the experimental data of Table 3.7 shows that the mean film thickness increases with the liquid Reynolds and the Kapitza number and diminishes with the gas Reynolds number. This reduction with the gas Reynolds number is produced by two effects, the first one is that the shear stress produced by the gas cut the peaks of the disturbance waves and drag drops, while the second one is that the shear stress exerted by the gas on the interface reduces the mean thickness of the film.

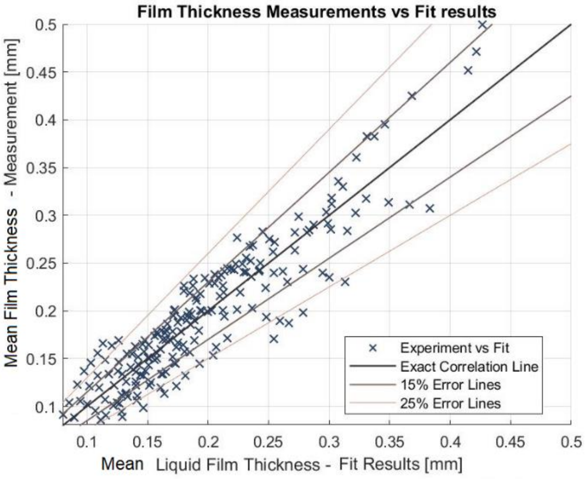

Figure 3.14. Experimental data versus correlation predictions for the mean film thickness.

3.4.2. Height and Amplitude of the disturbance waves

The average height of the DWs, $\bar{\delta}_{DW}$, and their average amplitudes, A_{DW}, see Figure 3.8, are key factors to characterize the DW. Obviously, the gas velocity has a great effect on these two magnitudes because both are affected by the liquid entrainment produced on the crest of the DW. In earlier studies, (Woodmansee and Harrantty, 1969) showed evidences that the production of drops from the film in the channel walls took place at the crests of the DWs. Later, (Azzopardi, 2006) found more evidences of this effect, which obviously affects the height and the amplitude of the DWs. For this reason, it is expected that the height of these waves will reduce when increasing the gas velocity. Also, from physical considerations related to the curvature terms that appears in the Navier-Stokes equations for film flow (Pan et al., 2015), it is expected that the height of these waves will increases with the Kapitza number. Then, from the data of the experiments performed at the VAFF facility with different surface tensions, we have found that the height of the DW can be correlated by the expression:

$$\frac{\bar{\delta}_{DW}}{D} = 0.554\ 10^{-3} Re_l^{0.061} Re_g^{-0.57} Ka^{1.12} \tag{3.19}$$

The coefficient of determination was $R^2 = 0.9757$, and the root mean square error for $\bar{\delta}_{DW}$ was $RMSE\ (\bar{\delta}_{DW}) = 0.0928\ mm$. Figure 3.15-a displays the experimental value versus the obtained from the correlation (3.19) for the average total height of the DW, δ_{DW}.

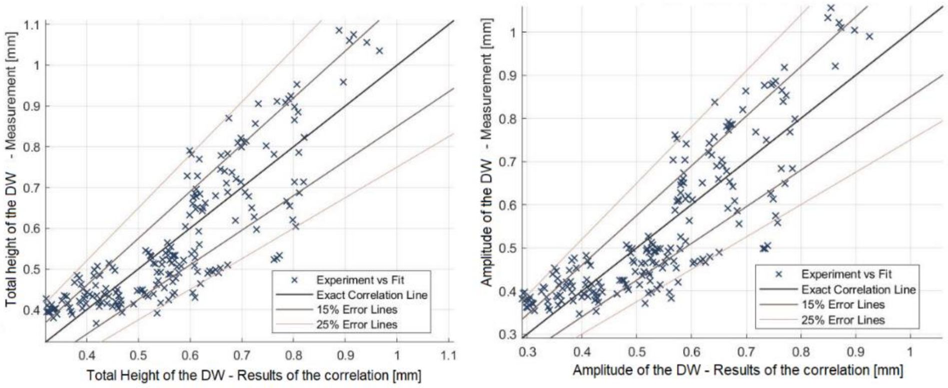

(a) (b)

Figure 3.15. Experimental data versus correlation predictions for the mean height of the DW (a) and the amplitude of the DW (b).

In addition, from the experimental data for the amplitude A_{DW} of the DW, obtained in the VAFF facility for different superficial tensions, we have correlated the non-dimensional amplitude of the DW, i.e., A_{DW}/D, in terms of Re_l, Re_g, and Ka:

$$\frac{A_{DW}}{D} = 0.245\ 10^{-3}\ Re_l^{0.0479} Re_g^{-0.551} Ka^{1.203} \tag{3.20}$$

The coefficient of determination was $R^2 = 0.9737$ and the root mean square error for A_{DW} was $RMSE\ (A_{DW}) = 0.0917\ mm$.

It is observed in both correlations that the height and amplitude of the DWs diminish with the gas Reynolds number, Re_g, and increases with the Kapitza number, Ka, and are practically independent of the liquid Reynolds number, Re_l.

3.4.3. Frequency of the disturbance waves

The DW frequency is defined as the number of large peaks associated to DW per time unit and it is obtained counting the peaks of the disturbance waves in each sampling interval and dividing by the sampling time. To non-dimensionalize the DW frequency, we have used the Strouhal number, which can be expressed in terms of the gas superficial velocity as follows (Cuadros et al., 2019):

$$St_g = \frac{\overline{\nu}_{DW} D}{j_g} \tag{3.21}$$

Performing the fit of the Strouhal number experimental data in terms of Re_l, Re_g and the Ka numbers, the following correlation is obtained:

$$St_g = 0.262\, Re_l^{0.266} Re_g^{-0.79} Ka^{0.46} \tag{3.22}$$

The coefficient of determination of this correlation was $R^2 = 0.9845$, and the root mean square error was $RMSE\ (St_g) = 0.0016$. Figure 3.16 displays the experimental versus the calculated gas Strouhal number using equation (3.22).

In addition, another fit was performed directly with the DW frequency in terms of the same non-dimensional numbers, as carried out in equation (3.20), the correlation obtained in this case was:

$$\nu_{DW}(Hz) = 0.003468\, Re_l^{0.347} Re_g^{0.197} Ka^{0.343} \tag{3.23}$$

The coefficient of determination for this last equation was $R^2 = 0.9863$, and the root mean square error was $1.0\ Hz$.

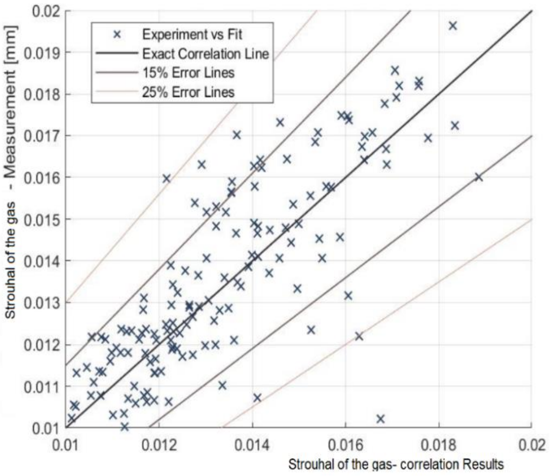

Figure 3.16. Experimental data versus correlation predictions for the gas Strouhal number.

3.4.4. Average thickness of the unperturbed base film plus RW, amplitude of the ripple waves and amplitude of the unperturbed film thickness

The main magnitudes that characterize the small incoherent waves, denoted as RW, are the average thickness of the unperturbed base film plus the amplitude of the RW, denoted by $\bar{\delta}_{bun+RW}$, and the amplitude of the RW, A_{RW}. Table 3.5 displays these amplitude values for several representative cases, and as shown in the table, this amplitude is influenced by the surface tension value. It is observed in Table 3.5 that, in general, the amplitude A_{RW} of the RW diminishes when the surface tension diminishes, for all the gas superficial velocities that are below or equal to $j_g = 27.4\ m/s$ ($Q_g = 2500\ l/min$), while for all the liquid superficial velocity values above this j_g value there is not a clear tendency. Also, it is observed that A_{RW} increase when j_l rises for all the values of j_g and more clearly that A_{RW} diminishes when j_g increases.

To quantify this behavior, we have performed a fit of $\frac{A_{RW}}{D}$ in terms of Re_l, Re_g, and Ka, using the non-linear fitting routine of MATLAB. The correlation obtained for $\frac{A_{RW}}{D}$ using the 196 available experimental points to perform the fit is:

$$\frac{A_{RW}}{D} = 0.084\ Re_l^{0.249} Re_g^{-0.896} Ka^{0.553} \tag{3.24}$$

The coefficient of determination was $R^2 = 0.98$, and the root mean square error $RMSE = 0.015\ mm$. Finally, Figure 3.17 displays the experimental versus the calculated A_{RW} values.

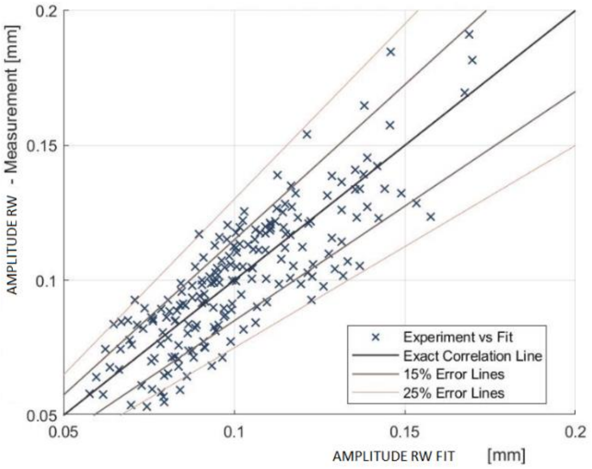

Figure 3.17. Experimental data versus correlation predictions for the amplitude of the RW.

In addition, the correlation obtained for $\bar{\delta}_{bun+RW}$ is given by the expression:

$$\frac{\bar{\delta}_{bun+RW}}{D} = 0.3175\, Re_l^{0.27} Re_g^{-0.895} Ka^{0.4} \tag{3.25}$$

With a coefficient of determination $R^2 = 0.982$, and $RMSE = 0.018\, mm$ for $\bar{\delta}_{bun+RW}$.

Concerning the base film thickness that remains unperturbed by the disturbance waves (DW) or he ripples waves (RW) and that it is denoted by $\bar{\delta}_{bun}$; we have correlated this non-dimensionalized film thickness with Re_l, Re_g and Ka, as previously, obtaining the result:

$$\frac{\bar{\delta}_{bun}}{D} = 1.48\, Re_l^{0.347} Re_g^{-0.889} Ka^{-0.054} \tag{3.26}$$

The coefficient of determination was $R^2 = 0.977$ and RMSE=0.005 mm for $\bar{\delta}_{bun}$. It is observed that the base unperturbed film thickness increases slowly with the liquid Reynolds number and diminishes with the gas Reynolds number almost linearly. This base unperturbed film thickness is not influenced by the Kapitza number, this means that is practically insensitive to the changes in the surface tension.

3.4.5. Comparison with the correlations of other authors

In this subsection, we compare the results of the correlations obtained in the previous sections for the different physical magnitudes with the results of the correlations of other authors and the experimental data obtained in this paper. The first physical magnitude to compare is the mean film thickness $\bar{\delta}_m$, that we compare with the correlations by (Pan et al., 2015) and the (Berna et al., 2014) given respectively by the following expressions:

$$\frac{\bar{\delta}_m}{D} = 2.03\, Re_{lf}^{0.15} Re_g^{-0.6}\ , \tag{3.27}$$

$$\frac{\bar{\delta}_m}{D} = 7.165\, Re_l^{0.48} Re_g^{-1.07} \left(\frac{Fr_g}{Fr_l}\right)^{0.24} \tag{3.28}$$

where the film Reynolds number in equation (3.27) is given by $Re_{lf} = (1-E)Re_l$, being E the entrainment fraction, and Fr_g and Fr_l, are the gas and liquid Froude numbers respectively, defined in terms of the superficial velocities. The entrainment fraction E was obtained from (Berna et al., 2015) correlation. In addition, (Pan et al., 2015) correlation was obtained from a set of experiments, performed with gas superficial velocities 30.0, 23.5, 19.0, 16.0 and $10.5\, m/s$ and liquid superficial velocities 0.03, 0.15 and $0.20\, m/s$, which gives 15 experimental runs. Figure 3.18 gives the results obtained from the mean film thickness versus the gas Reynolds number at different boundary conditions, i.e., different Re_l with $\sigma = 72.10^{-3} N/m$. It is observed that $\bar{\delta}_m$ diminishes when the gas Reynolds number increases.

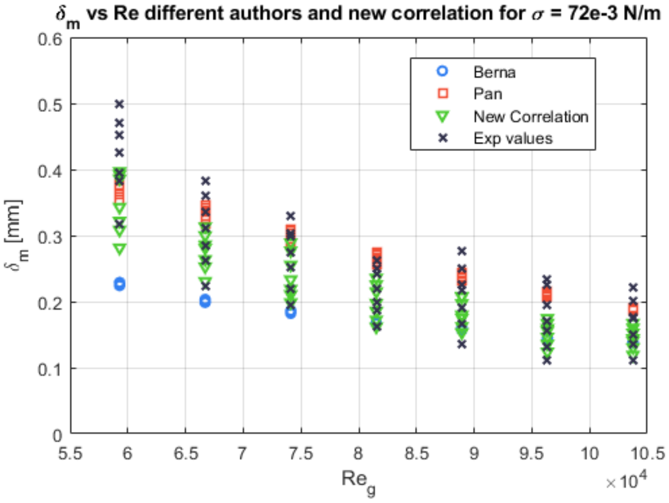

Figure 3.18. Mean film thickness versus Re_g for the different run cases performed at different Re_l, and $\sigma = 72.10^{-3} N/m$. The circles are the results obtained with (Berna et al., 2014) correlation, the squares denote the results obtained with (Pan et al. 2015) correlation, the triangles denote the results obtained with the correlation given by eq. (3.18) of this paper, and the Saint Andrew crosses are the experimental results of this paper.

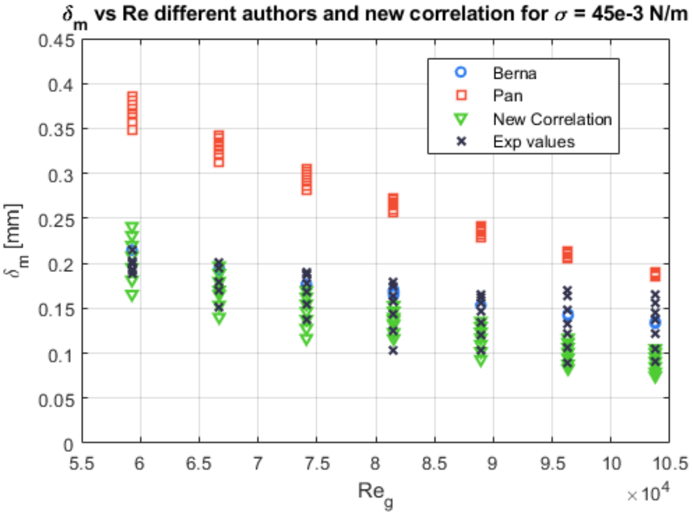

Figure 3.19. Mean film thickness versus Re_g for the different run cases performed at different Re_l, and $\sigma = 45.10^{-3} N/m$. The circles are the results obtained with (Berna et al., 2014) correlation, the squares denote the results obtained with (Pan et al. 2015) correlation, the triangles denote the results obtained with the correlation given by eq. (3.18) of this paper, and the Saint Andrew crosses are the experimental results of this paper.

Also, one notices that Berna et al. correlation is lower than the experimental data for $Re_g < 75000$. When the surface tension decreases to $\sigma = 45.10^{-3} N/m$, the average mean film thickness decreases, as observed in Figure 3.20. However, this behavior is well predicted by the correlation obtained in this paper but Pan et al. correlation is above the experimental results for all the cases (Pan et al., 2015), and (Berna et al., 2014) correlations over predicts a little bit some of the experimental data.

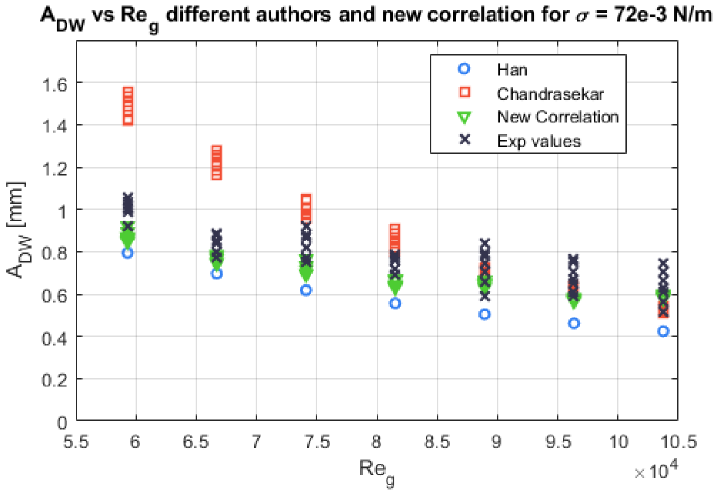

Figure 3.20. Mean amplitude of the DW versus Re_g for the different runs performed at different Re_l, and $\sigma = 72.10^{-3} N/m$. The circles are the results obtained with (Han et al., 2006) correlation, the squares denote the results obtained with (Chandrasekar et al., 1981) correlation, the triangles denote the results obtained with the correlation given by eq. (3.18) of this paper, and the Saint Andrew crosses are the experimental results of this paper.

Another important physical parameter to characterize the film thickness is the amplitude of the disturbance waves, A_{DW}, this amplitude can be affected by two causes. The first one is that the gas velocity entrains droplets from the peaks of the disturbance waves, reducing their height. While the second one is that the amplitude of this waves depends on the surface tension and increases with it as proved by (Chandrasekar et al., 1981), therefore it is expected that A_{DW} will reduce when diminishing σ. The height of the disturbance waves will depend in general of Re_g, Re_l and the Ka. The results for A_{DW} will be projected on the planes (A_{DW}, Re_g) and (A_{DW}, Re_l) for fixed values of σ. In addition, we will compare the results obtained by (Han et al., 2006) for A_{DW} with the results of Chandrasekar formula for the amplitudes of the waves of the Helmholtz- Kelvin instability, which are respectively given by:

$$\frac{A_{DW}}{D} = 4.10^3 / Re_g^{1.12} \tag{3.29}$$

$$A_{DW} = 3\pi \frac{\sigma_l\left(1+(\rho_g/\rho_l)\right)}{\rho_g(u_g-u_l)^2} \tag{3.30}$$

Where u_l is the mean velocity in the film, and σ_l the liquid surface tension.

Figure 3.20 displays the results obtained for A_{DW} with (Han et al., 2006) correlation and (Chandrasekar et al., 1981) formula given by equations (3.29) and (3.30), respectively. Also, this figure displays the experimental results and the results obtained with equation (3.18) of this paper for pure water. Obviously Chandrasekar equation for the amplitude over predict the results because does not consider the effect of the drop entrainment performed by the gas and that reduces the effective height of the DW peaks.

Figure 3.21 displays A_{DW} versus the $\mathrm{Re_g}$ number for the different values of Re_l for $\sigma = 45.10^{-3} N/m$. Obviously, Chandrasekar expression and Han correlation over predict the experimental values except at very high gas Reynolds numbers, where all the expressions give approximately values that are close. The reason for this over prediction is that Han expression was obtained for pure water that has higher Kapitza number and, therefore, the amplitude of the peaks is higher. Furthermore, Chandrasekar expression also over predicts the DW amplitude because does not considers the entrainment of drops from the peaks of the DW. In addition, diminishing the surface tension reduces the cohesion forces in the water and makes easier the entrainment on the DW, reducing more the height of the peaks.

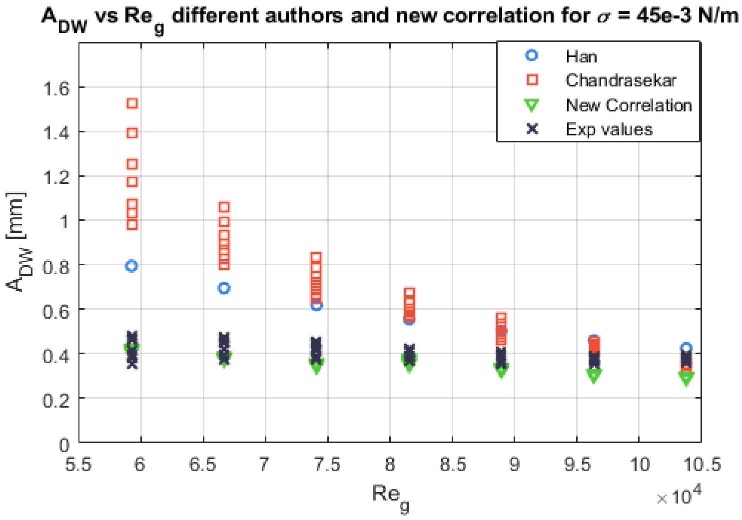

Figure 3.21. Mean amplitude of the DW versus Re_g for the different runs performed at different Re_l, and $\sigma = 45.10^{-3} N/m$. The circles are the results obtained with (Han et al., 2006) correlation, the squares denote the results obtained with (Chandrasekar et al., 1981) equation, the triangles denote the results obtained with the correlation given by eq. (3.18) of this paper, and the Saint Andrew crosses are the experimental results of this paper.

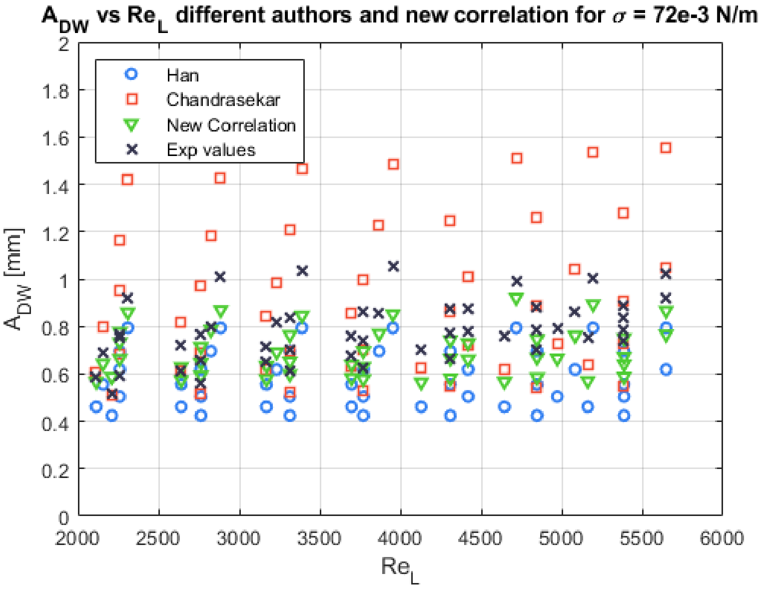

Figure 3.22. Mean amplitude of the DW versus Re_l for the different runs performed at different Re_g, and $\sigma = 72.10^{-3} N/m$. The circles are the results obtained with (Han et al., 2006) correlation, the squares denote the results obtained with (Chandrasekar et al., 1981) equation, the triangles denote the results obtained with the correlation given by eq. (3.18) of this paper, and the Saint Andrew crosses are the experimental results of this paper.

Also, it is interesting to display A_{DW} versus Re_l, to see the influence of liquid Reynolds number on the amplitude of the disturbance waves. Figure 3.22 displays A_{DW} versus Re_l for all the experiments performed with different Re_g, and water with a surface tension $\sigma = 72.10^{-3} N/m$. The variations of A_{DW} with Re_l are very small, the observed variations in A_{DW} , displayed at Figure 3.22, are mainly produced by the changes in Re_g, this fact is confirmed by the exponent of Re_l in equation (3.18) that is equal to 0.0479. Chandrasekar's expression, eq. (3.30), clearly over predicts A_{Dw} as displayed in Figure 3.22, while Han et al.'s correlation predicts a range of amplitudes between $0.4\ mm$ and $0.8\ mm$, which is close to the range predicted by the correlation (3.18) of this paper, which gives values between $0.5\ mm$ and $0.9\ mm$. When the surface tension diminish to $\sigma = 45.10^{-3} N/m$, it is observed in Figure 3.23 that A_{DW} practically does not change with Re_l, and the range of variation for different Re_g reduces to small variations between $0.35\ mm$ and $0.48\ mm$ for the lower $Re_l = 2064$ and even smaller range, between $0.36\ mm$ and $38\ mm$, for $Re_l = 5100$.

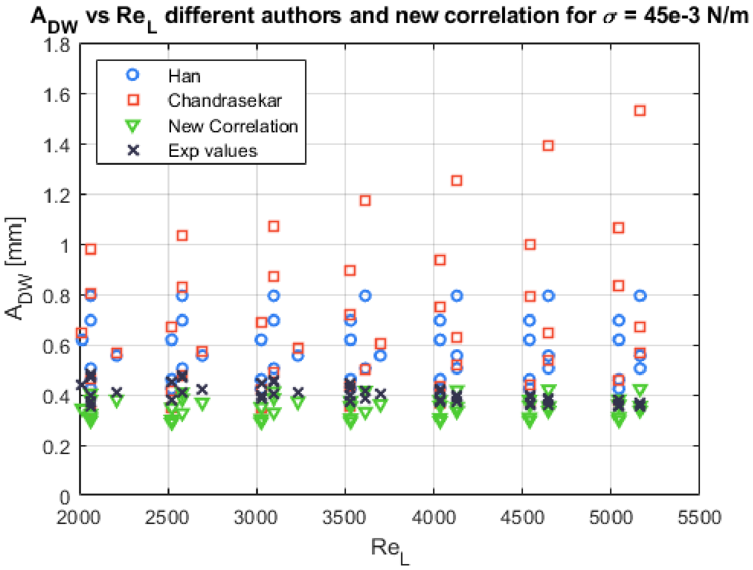

Figure 3.23. Mean amplitude of the DW versus Re_l for the different runs performed at different Re_g, and $\sigma = 45.10^{-3} N/m$. The circles are the results obtained with (Han et al., 2006) correlation, the squares denote the results obtained with (Chandrasekar et al., 1981) expression, the triangles denote the results obtained with the correlation given by eq. (3.18) of this paper, and the Saint Andrew crosses are the experimental results of this paper.

The last comparison performed was among the results obtained by (Alamu and Azzopardi, 2011[3]; Alamu and Azzopardi, 2011[31]), for the Strouhal number St_l of the DW, the experimental results of this paper, and the two correlations obtained in this paper for the Strouhal number and the frequency of the DW. According to Alamu and Azzopardi St_l is given by:

$$St_l = 0.429\, X^{-0.908} \tag{3.31}$$

Being X the Lockhart–Martinelli parameter defined by the expression:

$$X = \sqrt{\frac{\rho_l j_l^2}{\rho_g j_g^2}} \tag{3.32}$$

It is observed that the DW frequencies, ν_{DW}, versus Re_l obtained using the correlations of this paper, given by equations (3.22) and (3.23), are within the limits of the frequencies obtained with Alamu and Azzopardi correlation, for the lower Re_l and in the upper part for the higher Re_l values, when considering the different Re_g values for the different boundary condition runs, as displayed in Figure 3.24 for the water. In addition, ν_{DW} increases with the Re_l.

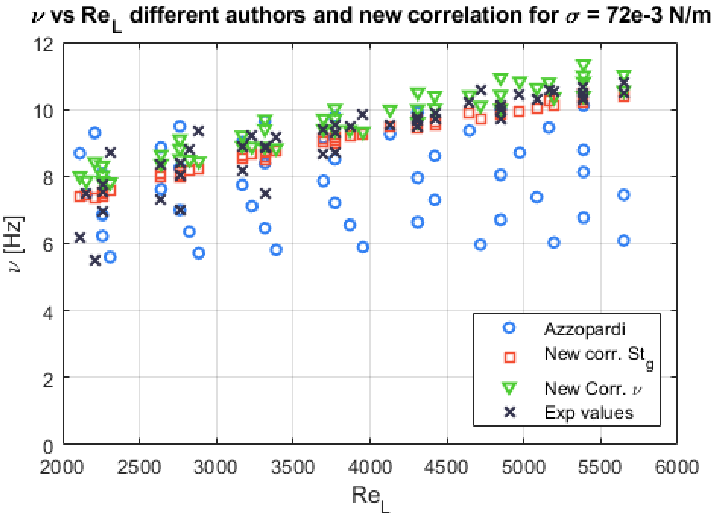

Figure 3.24. DW frequency values versus Re_l for $\sigma = 72.10^{-3} N/m$ and different Re_g, obtained with (Alamu and Azzopardi, 2011) correlation (circles), the correlation of this paper, equation (3.22) (squares), the second correlation of this paper for the frequency, equation (3.23) (triangles) and the experimental data (Saint Andrew crosses).

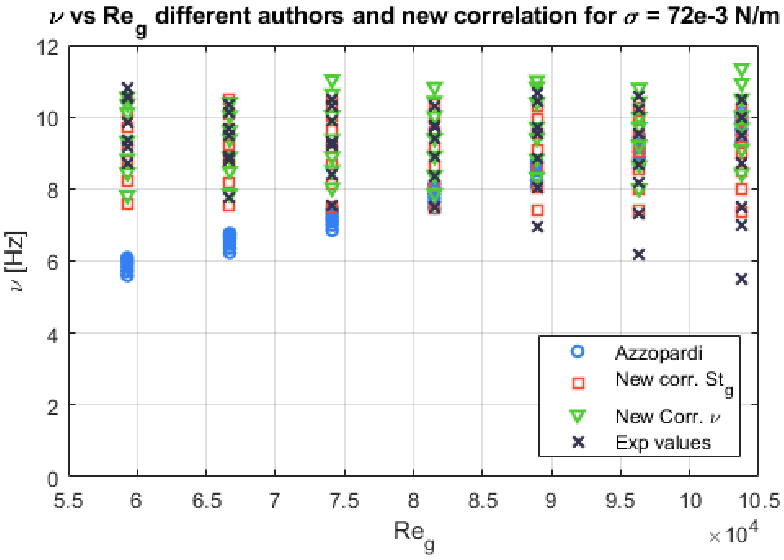

Figure 3.25. DW frequency values versus Re_g for $\sigma = 72.0\ 10^{-3} N/m$ and different Re_l values obtained with (Alamu and Azzopardi, 2011) correlation (circles), the correlation of this paper, equation (3.22) (squares), the second correlation of this paper for the frequency, equation (3.23) (triangles) and the experimental data (Saint Andrew crosses).

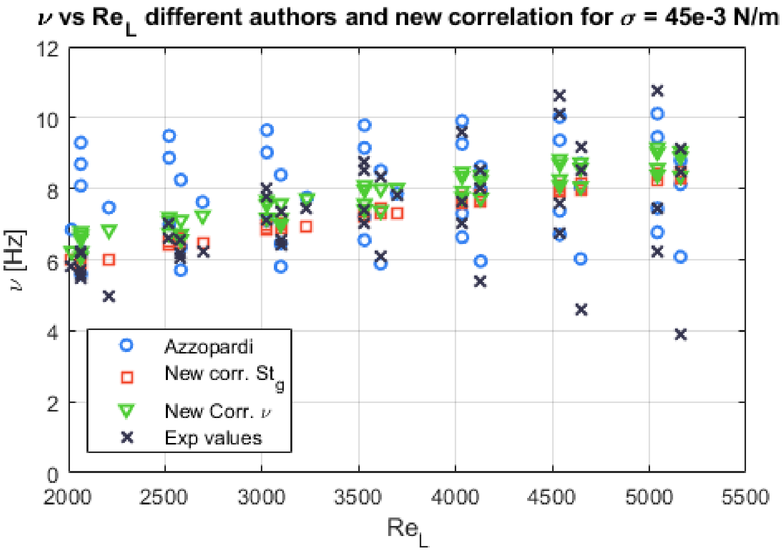

Figure 3.26. DW frequency versus Re_l for $\sigma = 45.10^{-3} N/m$ and different Re_g values obtained with (Alamu and Azzopardi, 2011) correlation (circles), the correlation of this paper, equation (3.22) (squares), second correlation of this paper, equation (3.23) (triangles) and the experimental data (Saint Andrew crosses).

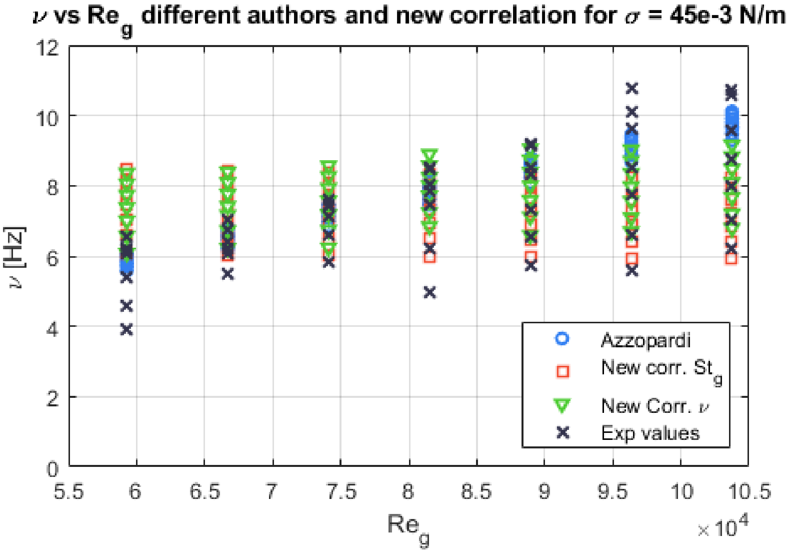

Figure 3.27. DW frequency versus Re_g for $\sigma = 45.10^{-3}\ N/m$ and different Re_l values obtained with (Alamu and Azzopardi, 2011) correlation (circles), the correlation of this paper, equation (3.22) (squares), second correlation of this paper, equation (3.23) (triangles) and the experimental data (Saint Andrew crosses).

Besides, when the surface tension diminishes from $72.10^{-3}\ N/m$ to $45.10^{-3}\ N/m$, by adding small quantities of 1-butanol, the overall behavior is that the DW frequency, ν_{DW}, versus Re_l still increases, as displayed in Figure 3.26, but the values are smaller. Both correlations, (3.22) and (3.23), show that the frequency and the Strouhal number increase with the Kapitza number, so that for the same gas and liquid Reynolds numbers ν_{DW} increases with the surface tension because the density and the kinematic viscosity are very little affected by the small amounts of 1-butanol added. Concerning the change of ν_{DW} with Re_g, it is observed that ν_{DW} increases with Re_g, for Alamu and Azzopardi correlation, as displayed in Figure 3.27. An increment of ν_{DW} with Re_g, it is also observed in correlations (3.22) and (3.23), but these increments are smaller than the obtained by Alamu and Azzopardi. The frequency changes are proportional to $j_g^{0.2}$, as deduced from equations (3.22) and (3.23), this small exponent is probably due to the surface tension effects.

3.5. CONCLUSIONS

The study of the variations produced in the physical magnitudes that characterize the gas-liquid interface when changing the surface tension, and the gas and liquid superficial velocities in annular vertical concurrent two-phase flow has been the main goal of this paper. Many experiments were performed in the past (Alamu and Azzopardi, 2011[3]; Alamu and Azzopardi, 2011[31]), (Belt et al. 2010), (Alekseenko et al., 2014) mainly with water and liquids with different viscosities, but very few changing the surface tension of the water and maintaining the value of the viscosity. This has been possible adding small amounts of 1-butanol to the water, which has the property of changing the surface tension of the water, σ, while maintaining practically constant the dynamic viscosity, μ. The range of surface tensions selected was from $0.072\ N/m$ equal to the surface tension of the water at 25 ºC and $p = 1$ atm to $0.045\ N/m$ that is below the surface tension at boiling conditions and $p = 1\ atm$. We performed experiments at water surface tension of $\sigma = 0.072\ N/m$, $0.0685\ N/m$, $0.055\ N/m$ and $0.045\ N/m$ with a broad range of superficial velocities of the gas and liquid phases, as displayed at Table 3.2, which covers a broad range of applications for the correlations developed in this paper.

In general, it is observed that the amplitude of the DW and the RW diminishes when increasing the superficial velocity of the gas for all the surface tension values as showed in Tables (3.8) and (3.5). This effect is caused by two mechanisms, the first one is that increasing the gas velocity increases the shear stress exerted by the gas on the peaks of the DW and this effect drags small drops from the crest of the DW when the inception velocity for velocity is sur-passed (Berna et al., 2014), while the ripple waves are not affected by the entrainment but the shear stress can modify the height and shape of the DW and RW. The second one is that reducing the surface tension by adding 1-butanol to the water, it reduces the intermolecular cohesion forces and makes easier that the gas drags small drops from the peaks of the waves reducing the DW amplitude when the surface tension diminishes as observed in Table 3.8. This same effect is also observed in the dependence of $A_{DW,}$ found in this paper with the Kapitza number that is given by equation (3.20), and which is proportional to $Ka^{1.12}$. In addition, it is noticed that the dependence of A_{DW} with Re_g becomes smaller at lower surface tension values, as observed comparing Figures 3.20 and 3.21.

The unperturbed base film thickness, δ_{bun}, diminishes when Re_g increases, probably due to the shear stress exerted on the interphase by the gas moving at higher velocity, being this effect observed for all the surface tension values, as displayed in Table 3.6. Also, the amplitude of the ripple waves diminishes with Re_g. In addition, A_{RW} diminishes when the surface tension becomes smaller.

The DW frequency, ν_{DW}, increases with Re_l for all the surface tension values, as it is observed comparing Figures 3.24 and 3.26, and in the correlation given by equation (3.23). However the dependence of ν_{DW} with Re_g, given by expression 3.23, is smaller than the one found by other authors, as (Alamu and Azzopardi, 2011[3]; Alamu and Azzopardi, 2011[31]) for water, which depends on $Re_g^{0.902}$, while for the expression found in this paper $\nu_{DW} \propto Re_g^{0.2}$. The explanation of this fact could be that increasing the gas velocity increases the shear stress acting on the interphase and this perturbation increases the number of DW per second. But, at the same time, when the surface tension diminishes maintaining the viscosity practically constant the height of the peaks diminishes, because the Kapitza number that governs the term that depends on the interphase curvature decreases. In addition, the cohesion forces in the water diminish, so drops are easily dragged from the crest of the peaks and, in general, the height of all the peaks becomes smaller when reducing the surface tension. So, it is expected a reduction of the exponent of the dependence of the DW frequency with Re_g at lower Ka numbers, as happens according to the experimental results, Figures 3.24 and 3.26 and equation (3.23).

Also, it is interesting to compare the overall results obtained in this paper varying the surface tension, with the results obtained by (Matsuyama et al. 2017), in these experiments the flow was annular co-current in a vertical pipe of $19.2\ mm$ i.d. and $5.4\ m$ long. In the experiment, air was the test gas, while water and/or a dilute water solution of Polyoxyethylene-Lauryl-Ether (PLE)was the test liquid. The data of Matsuyama et al. showed that the liquid film behavior strongly depends on the surface tension. The passing frequency of the DW for PLE decreased remarkably, this is the same effect observed in this paper were the frequency of the DW decreases when the surface tension decreased. Also the height of the DW observed by Matsuyama et becomes smaller when reducing the surface tension, as also observed in this paper.

In addition , we cannot forget the fact that 1-butanol is a weakly surfactant, if we remind that surfactants are molecules that have an affinity for the interfaces and common examples include soap and oil. Owing to their molecular structure (often a hydrophilic head and hydrophobic tail), they find it energetically favourable to reside at the free surface. Their presence reduces the surface tension; consequently, gradients in surfactant concentration result in surface tension gradients. Surfactants thus generate a special class of Marangoni flows. This issue of Marangoni flows is actually under study as mentioned in (Kitahata and Yoshinaga, 2018).

3.6. ACKNOWLEDGEMENTS

This work was supported by the project EXMOTRANSIN ENE2016-79489-C2-1-P of the Spain National Research I+D Plan.

3.7. REFERENCES

[1] Azzopardi, B.J., 1997. Drops in Annular two-phase flow, Int. J. Multiphase Flow Vol. 23, Issue 7, pp. 1-53.

[2] Alekseenko, S.V., Cherdantsev, A.V., Heinz, O.M, Kharlamov, S.M., Markovich, D.M., Analysis of spatial and temporal evolution of disturbance waves and ripples in annular gas–liquid flow, International Journal of Multiphase Flow Vol 67 (2014) pp 122–134.

[3] Alamu, M.B., Azzopardi, B.J., 2011. Wave and drop periodicity in transient annular flow, Nuclear Engineering and Design 241 (2011) 5079–5092.

[4] Chu, K.J., Dukler, A.E., 1974. Statistical characteristics of thin, wavy films: Part II. Studies of the substrate and its wave structure. AIChE J. 20, 695–706.

[5] Hall-Taylor, N., Hewitt, G., Lacey, P., 1963. The motion and frequency of large DW in annular two-phase flow of air-water mixtures. Chem. Eng. Sci. 18, 537–552.

[6] Zhao, Y., Markides, C., Hewitt, G., 2013. Disturbance wave development in two-phase gas–liquid upwards vertical annular flow. Int. J. Multiphase Flow Vol 55, pp 111–129.

[7] Belt, R.J., Van't Westende, Prasser, H.M., Portela, L.M., Time and spatially resolved measurements of interfacial waves in annular flow, International Journal of Multiphase Flow, vol 36, pp 570-587 (2010).

[8] Azzopardi, B. J. and Whalley, P. B., 1980. Artificial waves in annular two-phase flow. ASME Winter Annual Meeting, Chicago, Published in Basic Mechanisms in Two-Phase Flow and Heat-Transfer, pp. 1-8.

[9] Sadatomi, M., Kawahara, A., Suzuki ,A., Surface tension effects on vertical upward annular flows in a small diameter pipe, Nuclear Engineering and Design 310 (2016) 612–619

[10] Setyawan, A., and Deendarlianto, I., The effect of the fluid properties on the wave velocity and wave frequency of gas–liquid annular two-phase flow in a horizontal pipe. Experimental Thermal and Fluid Science 71 (2016) 25–41.

[11] Muñoz-Cobo, J.L., Miquel, A., Berna, C., Escrivá, A. " Spatial and time evolution of non-linear waves in falling liquid films by the harmonic expansion method with predictor-corrector integration", 12 -th International Conference on Heat Transfer Fluid Dynamics and Thermodynamics, Marbella, Málaga 11-15 July (2016).

[12] Cuadros, J.L., Rivera, Y., Berna, C., Escrivá, A., Muñoz-Cobo, J.L., Monrós-Andreu, G., Chiva, S., 2019, Characterization of the gas-liquid interfacial waves in vertical upward co-current annular flows, Nuclear Engineering and Design, Vol 346, pp 112–130.

[13] Coney, M.E., 2001, The theory and application of conductance probes for the measurement of liquid film thickness in two-phase flow, 1973 J. Phys. E: Sci. Instruments. 6 pp 903-910.

[14] Koskie, J. E., I. Mudawar, and W. G. Tiederman. 1989. "Parallel-Wire Probes for Measurement of Thick Liquid Films." *International Journal of Multiphase Flow* 15 (4). Pergamon: 521–30. doi:10.1016/0301-9322(89)90051-7.

[15] Lee, Kyu-Byung, Kim, Jong-Rok, Park, Goon-Cherl and Cho, Hyoung-Kyu, 2017, Feasibility Test of a Liquid Film Thickness Sensor on a Flexible Printed Circuit Board Using a Three-Electrode Conductance Method, Sensors, 17, 42; doi:10.3390/s17010042.

[16] Rivera, Y., Muñoz-Cobo, J.L., Berna, C., Cuadros, J.L., Escrivá, A., 2019. Experimental study of the interfacial waves produced in upward vertical annular flow when varying the liquid phase surface tension. Published in the proceedings of the conference: computational and experimental methods in multiphase and complex flow X, WIT Transaction on Engineering Science, Vol 123, pp 21-31.

[17] Bevington, P.R., Robinson, D.K., Data Reduction and Error Analysis in the Physical Sciences, Third Edition, edited by Mac Graw Hill (2003).

[18] Savitzky, A., Golay, M.J.E. “Smoothing and differentiation of data by simplified least squares procedures” Analytical Chemistry, 36(2), p.1627, (1964).

[19] Press, W.H., Teukolsky, S.A., Vetterling, W.T., Flannery, B.P., Numerical Recipes in Fortran, the Art of Scientific Computing, Second Edition, Cambridge University Press (1992).

[20] Guiñón, J.L., Ortega, E., García-Antón, J., Pérez-Herranz, V., Moving Average and Savitzki-Golay Smoothing Filters Using Mathcad, Proceedings of the InternationalConference on Engineering Education, ICEE 2007, Coimbra 3-7 September (2007).

[21] De Jong, P., Gabriel, K.S., 2003. A preliminary study of two-phase annular flow at microgravity: experimental data of film thickness. Int. J. Multiphase Flow 23, pp 1203–1220.

[22] Rodriguez, D.J., 2004. “Characterization of bubble entrainment, interfacial roughness and the sliding bubble mechanism in horizontal annular flow.” PhD. Thesis. University of Wisconsin-Madison.

[23] Oron, A., Davis, S.H., Bankoff, S.G., Long-Scale Evolution of Thin Liquid Films, Reviews of Modern Physics Vol 69, Number 3, 1997.

[24] Woodmansee, D.E., Hanratty, T.J., Mechanism for the removal of droplets from a liquid surface by a parallel air flow. Chem. Eng. Sci. 24, 299-307 (1969).

[25] Azzopardi, B.J., Gas-Liquid Flows. Begell House Inc., New York (2006).

[26] Pan, L.M., He, H., Hibiki, T., Ishii, M., 2015. Experimental study and modeling of disturbance wave height of vertical annular flow. Int. J. Heat Mass Transf. Vol 89, pp 165–175.

[27] Berna, C., Escriva, A., Munoz-Cobo, J.L., Herranz, L.E., Review of droplet entrainment in annular flow: interfacial waves and onset of entrainment. Prog. Nucl. Energy 74, 14-43 (2014).

[28] Berna, C., Escriva, A., Munoz-Cobo, J.L., Herranz, L.E., Review of droplet entrainment in annular flow: Characterization of the entrained droplets”, Progress in Nuclear Energy 79, 64-86 (2015)

[29] Chandrasekhar, S., 1981. Hydrodynamic and Hydromagnetic Stability. Oxford University Press.

[30] Han, H., Zhu, Z., Gabriel, K., 2006. A study on the effect of gas flow rate on the wave characteristics in two-phase gas-liquid annular flow. Nucl. Eng. Des. Vol 236, pp 2580-2588.

[31] Alamu, M.B., Azzopardi, B.J., 2011. Simultaneous investigation of entrained liquid fraction, liquid film thickness and pressure drop in vertical annular flow. J. Energy Resource. Technol. Trans. ASME 133 (023103), 1–10, doi:10.1115/1.4004265.

[32] Matsuyama, F., Kawahara, A., Sadatomi, M., Nakashima, K., Johno, Y., Effects of Surface Tension on Liquid Film Behavior and Interfacial Shear Stress of Two-Phase Annular Flow in a Vertical Pipe, Journal of Mechanical Engineering and Automation 2017, 7(5): pp 164-171.

[33] Kitahata, H., and Yoshinaga, N., Effective diffusion coefficient including the Marangoni effect, J. Chem. Phys. 148, 134906 (2018)

Chapter 4

THIRD PUBLICATION:

CFD simulation plus Uncertainty Quantification of the mixing of two fluid with different density for the Cold-Leg mixing benchmark

Nuclear Engineering and Design 383 (2021) 111449

Contents lists available at ScienceDirect

Nuclear Engineering and Design

journal homepage: www.elsevier.com/locate/nucengdes

CFD simulation plus uncertainty quantification of the mixing of two fluid with different density for the Cold-Leg mixing benchmark

Y. Rivera [a,*], J.L. Muñoz-Cobo [a], C. Berna [a], A. Escrivá [a], E. Vela [b]

[a] *Universitat Politècnica de València, Institute for Energy Engineering, Camino de Vera s/n, 46022 Valencia, Spain*
[b] *Consejo de Seguridad Nuclear, Subdirección de Ingeniería, C/ Pedro Justo dorado Dellmans, 11, 28040 Madrid, Spain*

https://doi.org/10.1016/j.nucengdes.2021.111449

CFD simulation plus uncertainty quantification of the mixing of two fluid with different density for the Cold-Leg Mixing Benchmark

Y. Rivera[1], J.L. Muñoz-Cobo[1], C. Berna[1], A. Escrivá[1], E. Vela[2]

[1]Instituto Universitario de Ingeniería Energética
Universitat Politècnica de València (UPV)
Camino de Vera 14, 46022 Valencia (Spain)
Tel: +34 963879245

[2]Consejo de Seguridad Nuclear
Subdirección de Ingeniería, Spain
C/ Pedro Justo dorado Dellmans, 11, 28040 Madrid (Spain)

Emails: *yaridu@upv.es*; ceberes@iie.upv.es; jlcobos@iqn.upv.es;
aescriva@iqn.upv.es; evb@csn.es

Abstract

This document describes the details of the simulations and uncertainty quantification of the Cold-Leg Mixing benchmark performed at the Institute for Energy Engineering (Polytechnic University of Valencia, Spain). The experiment, carried out by Texas A&M University, consists of the mixing of two water flows with different densities inside two tanks joined by a pipeline or cold leg. The tank that accumulates the low-density water and its connection to the cold leg are designed to create a downcomer like the one found in a PWR reactor vessel. On the other hand, the high-density water reservoir represents the cold-water injection accumulator. The method of Polynomial Chaos Expansion (PCE) based on Gaussian Quadrature is applied to calculate the uncertainty of the results, and a model created in Ansys CFX is developed to carry out the simulations. A 5th order Polynomial Chaos Expansion by Gaussian-Hermite Quadrature has been applied using as uncertain parameter the density difference between the mixing fluids. Therefore, five simulations have been done for both the open and the blind test. This methodology aims to provide an efficient solution since PCE solved by Gaussian Quadrature allows to obtain uncertainty quantification through a low number of simulations when the amount of uncertain input variables is low. It has been observed that the turbulence model significantly affects the results obtained, being the LES model the only one able to reproduce the real behavior consistently. Simulation results show a good agreement with experimental data for the cold-leg measurement zone while, in the downcomer a slightly different velocity profile than the one measured experimentally is obtained. The concentration profile of each fluid shows a gap in the transition zone that does not seem to agree with the velocity results. That behavior remains for higher time averages when comparing simulation results with experimental measurements.

Keywords: Computational fluid dynamics, uncertainty quantification, polynomial chaos expansion, cold-leg mixing, benchmark.

4.1. Introduction

Computational Fluid Dynamic (CFD) codes are a very useful tool in the nuclear field but there are still scenarios in which their application is complex or requires high computational power. To validate the results obtained with these codes it is necessary, among other things, to carry out studies based on experimental measurements (ASME V&V 20, 2009). A very good way to advance in the validation of CFD codes is to carry out benchmarks in which different organizations or companies at an international level participate by simulating a concrete experiment using different CFD codes and different modeling approaches. This practice serves to share the different methodologies and codes used by the different participants, as well as to increase the know-how about the different CFD models, as for instance averaged Navier Stokes Equations with k-epsilon model or Large Eddy Simulation model (LES), when we apply this kind of codes to different types of experiments.

CFD codes are a widely used tool in the nuclear field because of the multiple applications, which they have both in design and licensing of nuclear power plants and in addition in nuclear reactor safety (Mahaffy et al., 2014). This type of methods is especially useful when we focus on studying the specific operation of a reactor component, being able to observe the behavior of the fluids moving inside of it. Despite being available for several years, CFD codes still require a lot of research to ensure that the results are correct; especially in scenarios where safety is the most relevant factor. However, best practice guidelines for the nuclear codes in nuclear safety applications developed in the last few years have increased the confidence of the regulatory bodies in this type of codes (Mahaffy et al., 2014). Nevertheless, CFD codes are becoming more and more established as they offer great advantages such as the possibility of simulating complex 3D geometries, optimized numerical codes, etc (Smith et al., 2008).

To continue making progress in the use and knowledge of CFD codes, the Institute of Energy Engineering of the Polytechnical University of Valencia (UPV) has participated with many organizations of different countries as PSI, CEA, NRC, JAERI, KAERI, among others. In the six latest benchmarks organized by the OECD/NEA WGAMA group, including:

- OECD/NEA-Vattenfall CFD Benchmark Exercise 2008-2010. Simulation of an experiment in one of the facilities of the Älvkarleby laboratory, Vattenfall Research and Development about mixing fluids at different temperatures in a T-junction. Details could be found in Smith et al. (2013) and the official OECD/NEA report (OECD/NEA/ CSNI et al., 2011).
- OECD/NEA-KAERI CFD Benchmark Exercise 2010-2012 Simulation of the MATiS-H experiment that studies the cross flow in a subchannel with several measurements downstream of a spacer grid. All the information can be found in the document presented by Chang et al. (2014) and in the OECD/NEA/CSNI report (B.L. Smith et al., 2013).
- OECD/NEA-PSI CFD Benchmark Exercise 2012-2014. Simulation of an experiment in the PANDA installation of the PSI about helium concentration in different parts of a vessel. A synthesis of the benchmark exercise is described in Andreani's et al. (2016) paper and a more detailed report can be found in OECD/NEA/CSNI (2016).
- OECD/NEA-PSI CFD Benchmark Exercise 2014-2016. Simulation of an experiment in the PSI GEMIX installation about the mixing of two fluids with different temperature. In this benchmark, in addition to the modeling, the participants were required to calculate the uncertainty of the simulations. The most important information and all the data can be found in the report Fokken et al. (2019) and the paper Badillo et al. (2013).
- OECD/NEA-Texas A&M University Benchmark Exercise 2017-2019 Simulation of an experiment in the COLD-LEG MIXING installation of Texas A&M University about the mixing of two fluids with different density ($\Delta\rho$ between $100 - 200\ kg/m^3$). Authors have already published a paper (Orea et al., 2020) explaining the experimental approach, measurement techniques, test conditions and results. Some of the more active members of the benchmark group are already writing the official OECD/NEA report and it is expected to be available soon.

In the field of nuclear reactor safety, it is mandatory to know the uncertainty of the predictions obtained from computational codes. These statistical techniques are known as Best Estimate plus Uncertainty (BEPU) methodologies because these codes use the best physical and numerical methods available (state of the art) and at the same time these methodologies include an estimation of the uncertainty in the results (D 'Auria et al., 2012). Therefore, different techniques are being adapted for their use in CFD simulations considering both intrusive and non-intrusive methodologies. For the last two benchmark exercises, GEMIX (Fokken et al., 2019) and Cold-leg mixing, the study has been extended to consider not only the development of the model but also the uncertainty quantification of the results.

This research together with that of the other participants will show the capabilities of CFD codes to predict fluid mixing by turbulence and buoyancy effects. The results obtained by the Institute for Energy Engineering and the different international organizations that are involved in these benchmarks will be used to develop a set of best practices guidelines (also known as BPG) for the use of CFD codes for Nuclear Reactor Safety issues. As a reference, the document (Mahaffy et al., 2014) collect a lot of information regarding this aspect, but more documentation can be added to a new version for both new and experienced users.

Throughout this paper, the application of CFD methods to the scenario selected for the Cold Leg Mixing benchmark exercise is shown. As usual in these activities, the exercise consists of two assessment, first an open test from which the experimental measurements are known, and secondly a blind test from which only the initial conditions are given to the participants. For each of those tests two different parts have been addressed throughout the document. Firstly, the development of the experimental facility model which includes the activities of geometry generation, mesh development and optimization, preparation of the setup and the different simulation models, and post-processing. The second step is the development of an efficient methodology of uncertainty quantification for the predictions of the model of the experimental facility. For this purpose, the different alternatives already known by other authors must be studied and the most convenient one selected. For this benchmark it has been decided to use the Polynomial Chaos Expansion (PCE) based on Gaussian Quadrature because of its efficiency when the number of uncertain variables is small.

The theoretical aspects of PCE were first developed by Wiener (1938), and later generalized by Xiu and Karniadakis (2003a), based on previous studies by Askey and Wilson (1985). Since the early stages of its development, PCE has been successfully applied to numerous CFD simulations, and more recently to system thermal-hydraulic codes by Muñoz-Cobo et al. (2018). A complete review of the different PCE techniques, along with some CFD applications, is presented by Knio and Le Maître (2006) and Najm (2009).

Special mention should be made of the study carried out in Badillo's et al. (2013) research where the PCE method is applied to quantify the uncertainty in the GEMIX Benchmark results. The authors used a methodology similar to the one presented in this paper although they chose Collocation Points instead of Gaussian Quadrature as the technique for the resolution of the system derived from the Polynomial Chaos Expansion.

Many investigations have emerged from GEMIX benchmark, proposing different uncertainty quantification methodologies. For example in Rakhimov's et al. (2018) research the Latin Hypercube Sampling (LHS) technique is applied following the ASME standard for verification and validation in CFD and Heat

Transfer (ASME V&V 20, 2009) obtaining a good agreement between experiment and simulation. Moreover, the authors present in Rakhimov et al. (2019) the application of the Deterministic Sampling (DS) technique based on the research done by Hessling (2013) to increase the efficiency by reducing the number of simulations required while maintaining a high level of reliability. In addition, they carry out comparisons between DS-standard ensemble and DS-simplex ensemble, obtaining the highest degree of accuracy-efficiency with the second one.

A different approach is investigated in the paper presented by Prošek et al. (2017), where the authors use the Optimal Statistical Estimator (OSE) method as response surface generator to apply in Monte Carlo analysis. This method, as the one presented in this paper, is optimal when the number of uncertain variables is small. Consequently, they need a total of 30 simulations when two input parameters are considered as uncertain variables.

Many other authors have presented interesting results on the GEMIX benchmark although some of them without uncertainty calculation as Krpan and Končar (2018) or Kim (2019). This paper aims to bring the Polynomial Chaos Expansion by Gaussian Quadrature methodology for the calculation of uncertainty in CFD simulations to all, allowing its application in an efficient way. Therefore, it is possible to overcome the high computational cost barrier derived from the use of CFD in simulations where the uncertainty calculation is needed.

In order to achieve the objectives mentioned in this introduction, the document is structured as follows. Section 2 contains the information related to the experimental installation. The section 3 covers the details of the model and the simulation conditions, and the section 4 the quantification of the uncertainty. Finally, section 5 contains the results obtained and their discussion, followed by the conclusions of the research.

4.2. EXPERIMENTAL FACILITY COLD-LEG MIXING

The Cold-Leg Mixing Texas A&M University experiment (Orea et al., 2020) adds some complexity to the previous GEMIX benchmark (Badillo et al., 2013) performed at PSI. The geometry becomes more realistic in relation to the design of a light water PWR and the phenomena involved are transient. Following the guidelines of the previous benchmark, participants should carry out an uncertainty calculation (UQ) under conditions, which are closer to the existing ones in real reactors.

The experiment consists of two streams of water of different densities that are mixed after the opening of a valve located approximately in the center of a pipeline that links two liquid tanks (Figure 4.1a). The left tank contains the high-density fluid, and the right tank contains the lighter fluid as happens inside the downcomer of the reactor vessel. The two fluids are initially at rest and when the valve is opened, a temporary mixing process of several minutes begins, because of the heavier fluid tends to move below the lighter one towards the downcomer.

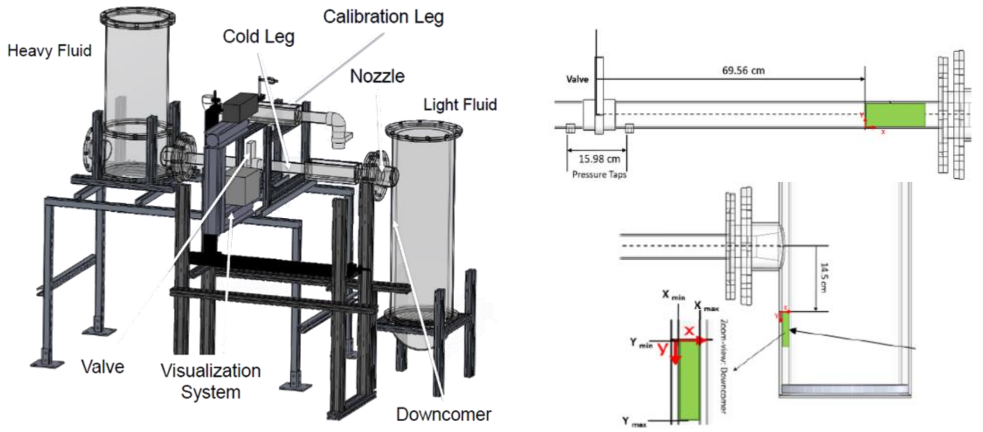

(a) (b)

Figure 4.1: Experimental facility Cold-Leg Mixing (Orea et al., 2020) (a) 3D design and (b) Measurement zones of the experiment: Cold-Leg on the upper side (PIV+LIF) and below the downcomer zone (PIV).

Texas A&M University carried out velocity measurements in two study areas (Figure 4.1b) using a PIV (Particle Image Velocimetry) system. The first zone is located near the end of the cold-leg, and the second one in the entrance zone to the downcomer. In the first zone, in addition to the PIV system, the density has been measured using a LIF system (Laser-induced fluorescence). Detailed information about the experiment can be found in (Orea et al., 2020).

The characteristics of the fluids for the open test are shown in Table 4.1. Additionally, the standard deviations of the measurements of the properties of the two fluids denoted as σ_H and $\sigma_L$are 6.505 and 7.311 kg/m^3 respectively and the viscosity $\pm 1.5\%$ for both fluids. The Atwood number is defined as the ratio of the difference of the densities divided by their sum.

Table 4.1. Fluid characteristics for the open and blind test.

Case	Fluid	Density $[kg/m^3]$	Density difference $[kg/m^3]$	Atwood Number	Viscosity $[Pa \cdot s]$
OPEN TEST	High density	1064.7	108.16	0.054	$1.09 \cdot 10^{-3}$
	Low density	956.54			$2.45 \cdot 10^{-3}$

BLIND TEST	High density	1107.07	195.73	0.097	$1.377 \cdot 10^{-3}$
	Low density	911.34			$2.847 \cdot 10^{-3}$

Three Reynolds numbers have been obtained for near-developed conditions, two in the cold-leg and one in the downcomer. Since in the cold-leg the two fluids move in different directions, an approximate hydraulic diameter has been obtained taking into account the position of the interface between both fluids. In the downcomer, the downward movement of the mixture predominates, so only one Reynolds number has been calculated. Table 4.2 shows their values for both the Open Test and the Blind Test. Fluids moving along the cold-leg have a Reynolds number much lower than that of the downcomer mixture. This is directly related to the flow regime and turbulence of each of these zones. In the cold-leg, buoyancy and gravity forces predominate although eddies can be seen at the front of the moving fluid. With time, slight oscillations also appear at the interface. On the other hand, in the downcomer, turbulence predominates over other forces

Table 4.2. Characteristic velocities, lengths and Reynolds Numbers for the Open and Blind Test.

OPEN TEST				
Zone	Fluid	Characteristic velocity [m/s]	Characteristic length [m]	Reynolds Number
Cold-Leg	Low-density fluid	0.054	0.038	2060
	High-density fluid	0.075	0.026	1964
Downcomer	Mixture	0.194	0.078	15137
BLIND TEST				
Zone	Fluid	Characteristic velocity [m/s]	Characteristic length [m]	Reynolds Number
Cold-Leg	Low-density fluid	0.067	0.038	2527
	High-density fluid	0.116	0.027	3114
Downcomer	Mixture	0.212	0.078	16497

To focus the experiment only on the phenomenology derived from the density difference between the fluids, the heights of the low-density water and high-density water tanks were balanced so that the pressure difference on both sides of the valve located in the pipe center was equal to zero. Thus, for the open test, the high-density liquid tank reached the height of $25.06\ cm$ while for the blind test only $22.97\ cm$ were needed. This must be considered since it is needed to vary the geometry and the mesh depending on the test that we want to perform.

The experiment starts with the opening of the valve. At this moment, the two fluids, which had remained separated, begin to mix. The high-density fluid starts to flow through the bottom of the pipe entering the region where there was only low-density fluid (first measurement area). At some point, the high-density fluid reaches the low-density liquid tank and descends through the downcomer, thus reaching the second measurement zone. The opening of the valve has been simplified, so the start of the simulation is the opening of the "invisible wall" that separates the high and low density fluid instead of the physical opening of a valve. The total measurement time is 42 seconds.

Benchmark participants must simulate this behavior of the fluid by means of CFD codes. In addition, they need to carry out an uncertainty study of the most important output variables. Table 4.3 shows the required averages in 2 lines located in the cold-leg and another 2 in the downcomer. Note that the prefix “d” refers to the uncertainty or error, e.g. U-dU would correspond to the mean value of U minus the lower error band.

Table 4.3. Averaged variables required for the Cold-Leg Mixing benchmark and its averaged upper and lower uncertainty band.

Name	Variables	Equation
Mean velocity components	U, U-dU, U+dU, V, V-dV, V+dV [cm/s]	$U_{mean} = U = \frac{1}{N}\sum_{i=1}^{N} u_i$
Standard deviation of the velocity components	U_{sd}, U_{sd}-dU_{sd}, U_{sd}+dU_{sd}, V_{sd}, V_{sd}-dV_{sd}, V_{sd}+dV_{sd} [cm/s]	$U_{sd} = \sqrt{\frac{1}{N-1}\sum_{i=1}^{N}(u_i - U_{mean})^2}$
Reynolds stresses	Re_{stress}, Re_{stress}-dRe_{stress}, Re_{stress}+dRe_{stress} [cm^2/s^2]	$Re_{stress} = \frac{1}{N-1}\sum_{i=1}^{N}(u_i - U_{mean})(v_i - V_{mean})$
Concentration (only in the cold-leg)	C, C-dC, C+dC [%]	$C_{mean} = C = \frac{1}{N}\sum_{i=1}^{N} c_i$

The averaged times intervals of the velocity are 0-5s, 5-10s, 10-15s, 15-22.5s, 0-10s y 10-22.5s in the cold-leg. In the downcomer the averages are 10.5-15.5s, 15.5-20.5s, 20.5-25.5s, 25.5-30.5s, 30.5-35.5s, 35.5-41.538s, 10.5-20.5s, 20.5-30.5s, and 30.5-41.538s. Therefore, each participant must provide all the averages defined in Table 4.3 for each variable.

In addition, to this set of averaged measures, it is also necessary to present measures of instantaneous variables, see Table 4.4. The timestep used is a decision of each participant. As for the averaged variables, its two error bands should be send along with each instantaneous result.

Table 4.4. Instantaneous variables required for the Cold-Leg Mixing benchmark.

Name	Variables	Details
Instantaneous velocity	u_i, u_i-du_i, $u_{i+}du_i$ v_i, v_i-dv_i, $v_{i+}dv_i$	Speed u_i and v_i in 6 determined points of the cold leg from the second 0 to 22.24 and other 6 points of the downcomer between the seconds 10.5 and 41.538.
Instantaneous concentration (only in the cold leg)	c_i, c_i-dc_i, $c_{i+}dc_i$	Instantaneous concentration in the 6 points of the cold leg from the second 0 to 22.24 and their corresponding error bands.

4.3. CFD MODEL

The CFD code Ansys CFX has been used to make the model. The geometry of the experimental setup provided by Texas A&M University is shown in Figure 4.2. The part of the domain where the low-density fluid is stored is represented by the blue color. On the other side, the orange color corresponds to the high-density fluid. In the middle of the pipe is located the valve, which starts the experiment after opening allowing the motion and the mixing of both fluids. Adjustments has been implemented in the geometry provided by TAMU to decrease the incompatibility problems with the Ansys geometry manager. For this purpose, a debugging and reduction of sharp edges has been carried out.

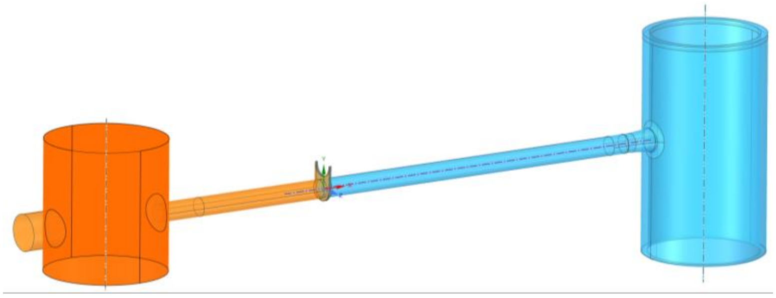

Figure 4.2: Domain geometry provided by (Orea et al., 2020).

ICEM CFD software has been selected to create the unstructured, conformal hexa mesh. Figure 4.3 shows the details of some important parts of the mesh. The total number of nodes of the mesh is 4 million.

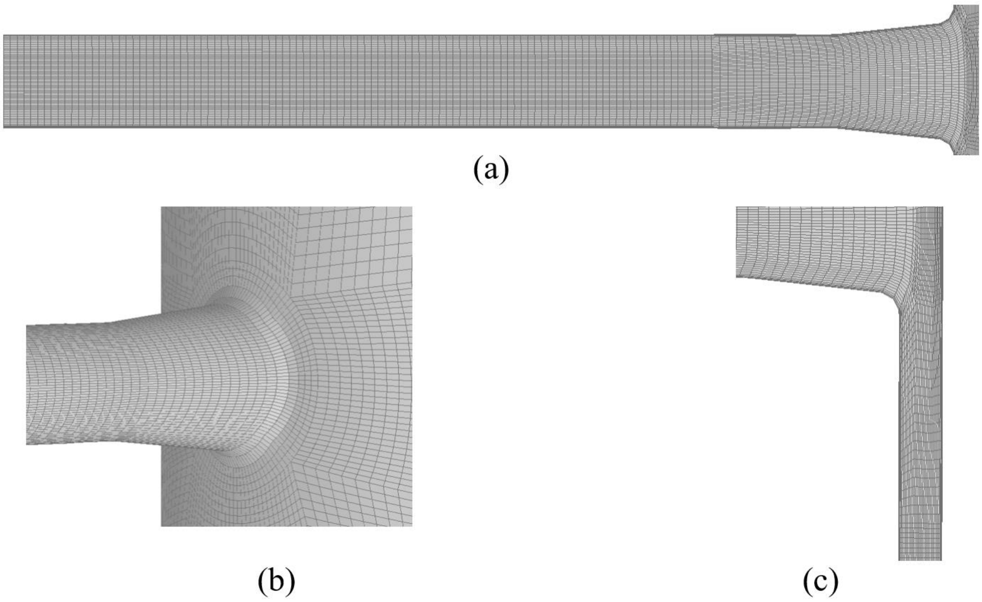

Figure 4.3: Mesh details, (a) longitudinal cut of the cold leg, (b) connection between the cold leg and the downcomer and (c) longitudinal cut of the cold leg and downcomer connection

In order to facilitate the replicability of the simulations Table 4.5 has been included, showing the most important parameters and models used in the simulations. The column corresponding to the LES model represents the final configuration used for the benchmark simulations, as well as for the simulations performed for uncertainty quantification.

Table 4.5. Most important model and parameters applied for the different simulations.

	LES SIMULATION	**DES**	**SST**	**LAMINAR**
Code	CFX	CFX	CFX	CFX
Fluid modelling approach	LES	Hybrid	URANS	LAMINAR
Specific turbulence (URANS) or SGS (LES) model	Smagorinsky	Detached eddy simulation	SST	-

Variable density treatment	Density difference			
Advection Scheme	Central Difference Scheme	CFX High resolution scheme	CFX High resolution scheme	CFX High resolution scheme
Time discretization scheme	Second order backward Euler			
Time step size (dt)	0.005s			
Total time	42s	20s	60s	60s
Maximum and average CFL	13 (max)	8 (max)	7 (max)	10 (max)
	0.4 (average)	0.23 (average)	0.2 (average)	0.34 (average)
Meshing features	4 million nodes, unstructured, conformal, hexa mesh	2 million nodes, unstructured, conformal, hexa mesh	1.5 million nodes, unstructured, conformal, hexa+tetra	1.3 million nodes, unstructured, conformal, hexa
Wall treatment - type possibly including details on near wall damping	Automatic CFX near-wall treatment	Automatic CFX near-wall treatment	Automatic CFX near-wall treatment	-
Wall treatment - maximum y+ value	30 (max)	25 (max)	23 (max)	-
	1.3 (ave)	1.7 (average)	0.7 (average)	-
Boundary condition for the free surface	No-slip wall			
Modelling/assumptions for the valve opening	Opening not modelled. Fluid domain initialized at heavy fluid mass fraction equal 1 and 0 on the heavy and light side, respectively.			

Following the parameters included in CFD best practice guidelines (Mahaffy et al., 2014) and Ansys Meshing User Manual (Canonsburg, 2011), almost all of the mesh elements are within the high quality rating. There are certain regions of the mesh that are outside the best quality parameters. These zones are very complicated to mesh keeping the different parameters of quality of mesh at a high value. Each one of the most compromised elements has been analyzed and it has been observed that its impact in the solution is very small.

Figure 4.4 shows the elements that remains outside the high-quality standards. As can be seen, these elements are mainly found in the high-density water tank and do not pose a problem for the motion of the fluid in this experiment. Most of the volumes could be eliminated by increasing the refining of the mesh, but the computational cost is too high to justify it (Salvetti et al., 2018).

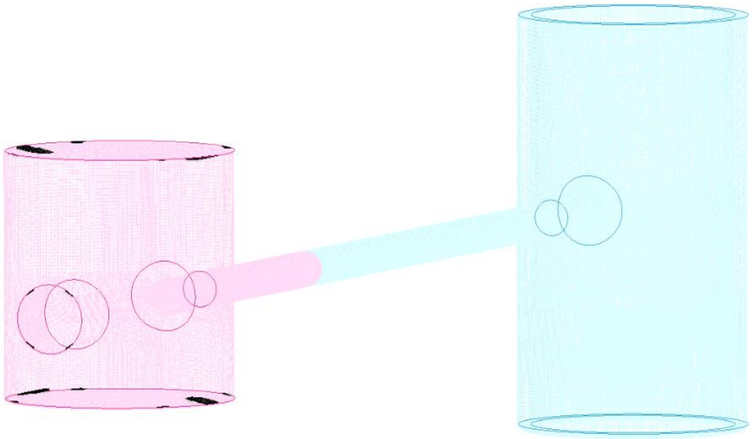

Figure 4.4: Lower quality elements of the mesh located entirely in the upper and lower area of the high-density water tank

The total simulation time was 42 seconds in order to measure the high-density fluid flowing down the downcomer. The timestep was set to 5 milliseconds in order to obtain acceptable Courant numbers during the transient simulation. The time scheme used in all cases is Second Order Backward Euler, which is an implicit time-stepping scheme with a second order accuracy in the time derivative. All the boundaries correspond to walls so there are no inlets or outlets and the velocity was fixed at 0 using the No Slip Wall model. Table 4.5 also shows the maximum and average y+ value for each of the simulations. It is important to mention that CFX includes a special wall treatment that automatically switches between wall functions and low-Re approach depending on the spacing in the wall zone. A homogeneous model has been adjusted for both phases and for the temperature transfer (at 22.5 ºC).

In many scenarios the Large Eddy Simulation (LES) turbulence model is the most realistic and most reliable model for simulating turbulence (Simoneau et al., 2010). However, the high cost in terms of computational time limits the application capabilities of many uncertainty quantification techniques that require performing many simulations. For this reason, before selecting the turbulence model to be used, several tests were performed with different models including: Laminar, Shear Stress Transport (SST), Detached Eddy Simulation (DES) and Large Eddy Simulation (LES) among others. It should be mentioned that the model that best reproduced the behavior of the experiment was the LES model in its three variations of sub-grid eddy models Smagorinsky, WALE and Dynamic Model. Further information about the results of each turbulence model is shown in section 5.

Between the two options of buoyancy model that CFX has implemented, density difference and Boussinesq, the first one usually offers slightly better results than the second one. The savings in computational time are practically negligible in this second option so Density Difference model was used for most of the simulations. Central difference scheme was used for the LES simulations.

Table 4.6. Mesh sensibility study parameters.

Parameter	Coarse	Medium	Fine
Total number of nodes	1 million	4 million	8 million
Turbulence model	LES Smagorinsky		
Max/mean y+	35 (max)	30 (max)	28 (max)
	3.3 (average)	1.3 (average)	1.1 (average)
Max/mean Courant Number	3 (max)	14 (max)	10 (max)
	0.1 (average)	0.34 (average)	0.1 (average)
Max Mesh Expansion Factor and percentage of elements from 20 to max	53	30	26
	0.5% from 20 to 53	0.2% from 20 to 30	0.07% from 20 to 26
Max Aspect Ratio and percentage of elements from 30 to max	64	50	55
	4.7% from 30 to 64	4.4% from 30-50	0.1% from 30 to 55
Min equiangle skewness and percentaje from min to 0.5	0.17	0.2	0.25
	3.9% from 0.17 to 0.5	3.5% from 0.2 to 0.5	4.2% from 0.25 to 0.5
Timestep	5 ms		
Type of mesh	Unstruc. hexa		

The final mesh size decision was made according to a sensitivity study and the available computational capacity. Table 4.6 shows some of the most important parameters of the meshes used in the sensitivity analysis. The study was performed with the LES Smagorinsky turbulence model during 20s and the only parameter that was modified was the number of nodes. Thus, three grids were defined (coarse, medium and fine) with approximately 1, 4 and 8 million nodes respectively.

Table 4.7. Sensibility study results for coarse, medium and fine meshes.

		Coarse	Medium	Fine	Percentage of difference	
					From Coarse to Medium	From Medium to Fine
Cold-Leg	Max velocity	0.039	0.105	0.099	63%	6%
	Mean Velocity	0.0051	0.0106	0.0091	52%	16%
	Max density	1008	1048	1047	4%	1%
Downcomer	Max velocity	0.19	0.256	0.33	26%	22%
	Mean Velocity	0.182	0.235	0.278	23%	15%
	Max density	981	988	993	1%	1%

The difference between the meshes was evaluated in two areas (cold-leg and downcomer), following the measurement zones of the experiment. Table 4.7 shows the values of maximum velocity, average velocity and maximum density obtained for these reference zones. Additionally, two columns are included with the percentage variation of these variables between grids. It can be seen that in the case of velocities and densities in the cold leg, the values are much tighter. However, in the downcomer the difference is much more appreciable. Although the behavior of these variables was analyzed for the different meshes, the high computational cost greatly limited the possibilities of performing the simulations with a fine mesh. Since the main objective was to develop and test the uncertainty quantification methodology using polynomial chaos, it was necessary not only to carry out the different initial studies but also the different simulations for the calculation of the error bands. Consequently, the 4 million mesh was selected. The mesh behaved quite well in the cold-leg although larger discrepancies were expected in the downcomer.

4.4. UNCERTAINTY QUANTIFICATION

Two models of uncertainty quantification have been considered for this benchmark. Firstly, Wilks method is reliable and easy to implement but has the important drawback of requiring almost 100 simulations to meet the usual safety requirements of coverage and confidence. This methodology can become very expensive in terms of computational cost if the simulations are time-consuming. On the other hand, Polynomial Chaos Expansion method (also known as PCE) is a more efficient alternative when the number of uncertain variables is small. For this reason, Polynomial Chaos Expansion method has been selected for the uncertainty quantification. In this benchmark there is a variable whose uncertainty is very relevant in the simulation results: the density. To avoid a very pronounced increase in simulations, the less relevant uncertain variables have been discarded because of their low impact on the results, for example, viscosity. Future analyses will also take into account subscale constants as they may affect the results depending on the importance of small scales in this type of simulations (Lucor et al., 2007).

$$\Delta\rho = \rho_H - \rho_L \tag{4.1}$$

$$\sigma_{\Delta\rho} = \sqrt{{\sigma_H}^2 + {\sigma_l}^2} \tag{4.2}$$

Being $\Delta\rho$ the density difference between heavy (ρ_H) and light (ρ_L) fluids and $\sigma_{\Delta\rho}$ its standard deviation. The uncertainty of the density difference between fluids follows a Gaussian probability distribution so Hermite polynomials were used (Wiener, 1938).

In PCE the response of a system $R(x)$, which depends on a set of uncertain parameters x, is expressed as a linear combination of a certain orthogonal basis of orthogonal polynomials $\{\phi_i\}_{i=0}^{\infty}$ known as Askey polynomials. The type of these polynomials depends on the probability distribution functions (PDF) of the uncertain parameters (Xiu and Karniadakis, 2003a):

$$R(x) = \sum_{n=0}^{\infty} \alpha_n \phi_n(x) \tag{4.3}$$

The parameters x $(x_1, x_2, \dots, x_{n_u})$ are usually assumed to be statistically independent, and therefore the PDF is written as $p(x) = \Pi_{i=0}^{n_u} p_i(x_i)$. Then, based on the orthogonal property of these polynomials the expansion coefficients α_i in eq. (4.3) are given by:

$$\alpha_n = \frac{1}{\langle {\phi_n}^2 \rangle} \int_X p(x)\, R(x) \phi_n(x)\, dx \tag{4.4}$$

Being

$$\langle {\phi_n}^2 \rangle = \int_X p(x)\, {\phi_n}^2(x) dx \tag{4.5}$$

The mean μ_R and the variance σ_R^2 of the system response $R(x)$, can be obtained easily from (4.3) using the orthogonality condition of the base functions and choosing without loss of generality $\phi_0 = 1$. Then, the mean is obtained computing the expected value of eq. (4.3), which yields:

$$\mu = \langle R(x) \rangle = \alpha_0 \tag{4.6}$$

While the variance is obtained from the variance definition on account of eq. (4.6), and the orthogonality condition of the base functions:

$$\sigma_R^2 = \langle R(x) - \mu^2 \rangle = \sum_{n=1}^{\infty} {\alpha_n}^2 \langle {\phi_n}^2 \rangle \cong \sum_{n=1}^{N} {\alpha_n}^2 \langle {\phi_n}^2 \rangle \tag{4.7}$$

The first simplification used to compute the variance was to reduce the number of terms in the expansion to a finite number N as displayed in equation (4.7), the value chosen for N is discussed later. It is important to highlight that the number of terms in the PCE of the system response is $N + 1$, because there is a term that contains α_0. First, we notice that because of the PDFs of the uncertain parameter is the fluid density and this density follows according to the test specifications a Gaussian distribution function, then it follows that the orthogonal polynomials must be the Hermite ones denoted by $H_n(x)$, being n the order of the polynomial. Then, the Gauss-Hermite quadrature method with 5-th order Hermite polynomials is applied, which is valid for any function $f(x)$, to compute the integrals of equations (4.4) and (4.5):

$$\int_{-\infty}^{\infty} e^{-x^2} f(x)\, dx = \sum_{j=1}^{m=5} w_j\, f(x_j) \tag{4.8}$$

Being w_j the quadrature weights and x_j the zeros of the Hermite polynomials used in defining the quadrature order $n_q$in this case 5. We remind that the Gauss-Hermite quadrature method of integration it is exact when $f(x)$ is a polynomial of degree $2n_q - 1 = 9$.

Because of the PDF of the input uncertain variable of this benchmark (density difference between fluids) x^{in} follows a Gaussian distribution with mean μ

and standard deviation σ, then the integrals that are necessary to compute the coefficients α_n of the expansion can be written as follows. Note that eq. 4.9 and 4.10 are calculated in Appendix A, where we show the reasoning followed to obtain the integrals whose polynomials are orthogonal after the variable change (to fit the mean and variance of our uncertain variable).

$$\begin{aligned}\langle R\phi_n\rangle &= \int_{-\infty}^{\infty} \frac{1}{\sqrt{2\pi\sigma}} e^{-\left(\frac{x^{in}-\mu}{\sqrt{2}\,\sigma}\right)^2} R\left(x^{in}\right) He_n^{(\sigma^2,\mu)}\left(x^{in}\right) dx \\ &= \frac{\sigma^n}{\sqrt{\pi}\, 2^{n/2}} \sum_{j=1}^{5} w_j\, R\left(\mu + \sqrt{2}\,\sigma\, x_j\right) H_n\left(x_j\right)\end{aligned} \tag{4.9}$$

And

$$\begin{aligned}\langle {\phi_n}^2\rangle = \langle \left(He_n^{(\sigma^2,\mu)}\right)^2 \rangle &= \int_{-\infty}^{\infty} \frac{1}{\sqrt{2\pi\sigma}} e^{-\left(\frac{x-\mu}{\sqrt{2}\,\sigma}\right)^2} \left(He_n^{(\sigma^2,\mu)}(x)\right)^2 dx \\ &= \sigma^{2n}\, n!\end{aligned} \tag{4.10}$$

Being $He_n^{(\sigma^2,\mu)}\left(x^{in}\right)$ the Hermite polynomial, which are orthogonal with the weight function $N(\mu,\sigma). T$he variable change of equation (4.11) was performed in the input uncertain variable, in order to use the standard Hermite quadrature method (Abramovitz and Stegun, 1972). Notice that to perform the calculations with the CFD code we must input to the code the set of input values$\left\{x_j^{in}\right\}_{j=1}^{5}$, given by the expression:

$$x_j^{in} = \mu + \sqrt{2} \cdot \sigma \cdot x_j \tag{4.11}$$

Being x_j the roots of the Hermite polynomials of 5-th order and x_j^{in}, the input values of the uncertain parameter that must be supplied to the CFD code in order to obtain the code response.

A polynomial expansion of order 4 has been selected to quantify the uncertainty by means of Polynomial Chaos in the Cold-Leg Mixing benchmark, although other authors claim that using polynomials of order 2 achieves a fairly good precision (Safta *et al.*, 2017). The number of terms of the expansion $N+1$ and the minimum number of simulations points n_{sim} needed to achieve a good accuracy when we have n_u uncertain input parameters, and we perform the Hermite-Gauss quadrature integration with n_q weights and the PCE up to order q, is given by equation (4.12) and (4.13) as reported in (Xiu and Karniadakis, 2003b), (Richard. Askey and Wilson, 1985) and (Crestaux et al., 2009).

$$N + 1 = \frac{(n_u + q)!}{n_u!\,q!} \tag{4.12}$$

$$n_{sim} = n_q^{n_u} \tag{4.13}$$

Therefore, for this benchmark we have performed the integrals in (9) by means of Gauss-Hermite quadrature of 5th order (five zeros and weights per dimension). In this case, the number of uncertain parameters is only one, so the number of simulations needed is five and the number of terms of the Polynomial chaos expansion is also five. Table 4.8 displays the weights and the roots when using Gauss-Hermite quadrature.

Table 4.8. Roots of the 5th order Hermite Polynomials and its correspondent density value.

Roots x_j	-2.0202	-0.9586	0	0.9586	2.0202
Weights w_j	0.001993	0.393619	0.945308	0.393619	0.001993
OPEN TEST $\Delta\rho\ x_j^{in}$	80.2	94.9	108.2	121.4	136.1
BLIND TEST $\Delta\rho\ x_j^{in}$	167.7	182.4	195.7	208.9	223.6

To achieve a better understanding on the procedure performed to calculate the uncertainty of the results, the steps carried out are shown below:

1. The Matlab® script first loads all the vectors R, obtained for each output variable. This R vector corresponds to each variable for which we wish to know the uncertainty. Therefore, the number of components of each vector R is n_{sim}, being $n_{sim} = q^{n_u}$ and n_u the number of uncertain variables.

$$R = \begin{pmatrix} R_1 \\ R_2 \\ \vdots \\ R_{n_{sim}} \end{pmatrix} \tag{4.14}$$

2. Then it loads the data vectors of the uncertain variable values that are input to the code, which in this case is only one V_1 containing n_q values. In general, we will have n_u × n_q data. For this case it simplifies to:

$$V_1 = \begin{pmatrix} V_{1_1} \\ V_{1_2} \\ \vdots \\ V_{1_{n_{sim}}} \end{pmatrix} \tag{4.15}$$

3. Because there is only one uncertain variable, then the calculation of the polynomial base is very simple and reduces when the PCE is truncated at order 4 to:

$$Base = \begin{pmatrix} H_0 = 1 \\ H_1 = 2x \\ H_2 = 4x^2 - 2 \\ H_3 = 8x^3 - 12x \\ H_4 = 16x^4 - 48x^2 + 12 \end{pmatrix} \tag{4.16}$$

4. There are five weights w_j and five roots x_j because we use Gaussian-Hermite quadrature of order 5 that make the calculation of the integrals of the quadrature by Gauss-Hermite procedure exact for integrations of polynomials up to order 9. The weights are:

$$w = \begin{pmatrix} w_1 = 0.019932 \\ w_2 = 0.393619 \\ w_3 = 0.945308 \\ w_4 = 0.393619 \\ w_5 = 0.019932 \end{pmatrix} \tag{4.17}$$

5. Calculation of the alpha coefficients α_n of the Polynomial Chaos Expansion.
    a. The objective is to calculate the alpha coefficients in the following way:

$$\alpha_n = \frac{\langle R\phi_n \rangle}{\langle {\phi_n}^2 \rangle} \tag{4.18}$$

    b. The first step is to calculate the denominator $\langle {\phi_n}^2 \rangle$. This result is direct and does not require values obtained from the simulations because ϕ_n are the Hermite polynomials.

$$\langle {\phi_n}^2 \rangle = \sigma^{2n}\, n! \tag{4.19}$$

    c. Next, we will calculate the numerator $\langle R\phi_n \rangle$. This is done by solving the integral using Gaussian-Hermite quadrature obtaining the equation explained in Appendix A.

$$\langle R\phi_n \rangle = \frac{\sigma^n}{\sqrt{\pi}\, 2^{n/2}} \sum_{j=1}^{5} w_j\, R\big(\mu + \sqrt{2}\,\sigma\, x_j\big)\, H_n\big(x_j\big) \tag{4.20}$$

6. Using the alpha coefficients α_n it is possible to obtain the mean and standard deviation values of each of the variables resulting from the R arrays.

$$\mu = \alpha_0 \tag{4.21}$$

$$\sigma^2 = \sum_{n=1}^{5} {\alpha_n}^2 \cdot \langle {\phi_n}^2 \rangle \tag{4.22}$$

4.5. RESULTS AND DISCUSSION

The first thing that was observed was the great dependence of the results on the turbulence model. Simulations of the open test showed that models based on the RANS equations tended to attenuate the velocities at the interface while those carried out using the LES turbulence model offered much higher accuracy (Figure 4.5). In addition, the results obtained for the GEMIX experiment revealed the possibility of using high-cost computational models (such as LES) for the CFD simulations if the uncertainty quantification is supported by an efficient method, such as the Polynomial Chaos by means of Gaussian quadrature.

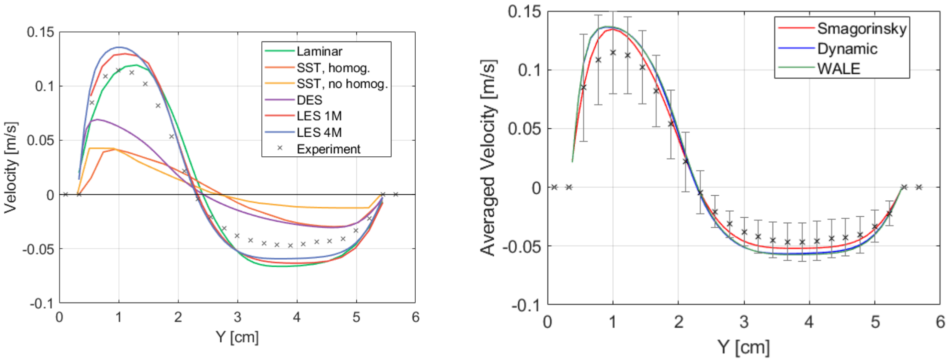

(a) (b)

Figure 4.5: Cold-leg velocity comparison of the open test for different turbulence models (a) Laminar, SST, LES vs experiment, and (b) LES Smagorinsky, Dynamic and WALE vs experiment.

Different models were tested removing transfer characteristics at the interface, modifying the surface tension, refining the mesh at the interface, etc. However, none of these modifications managed to avoid the disparity between results and experimental measurements of RANS-based models. Despite not having ample computational power, the LES turbulence model was essential for a correct performance of the simulation under these conditions (Figure 4.5a). The case of the DES turbulence model is decisive since it is located between the RANS and LES models. A clear improvement can be observed with respect to RANS, but the medium and small scales of turbulence are overestimated. This leads to the appearance of a much more diffuse interface in which the phases are mixed more than expected. In the research carried out by Hassan et al. (2021) a similar behavior is observed when $k - \omega$ SST (RANS model) is used in the simulations. However, the authors obtain much better results when using the RKE (Realizable $k - \epsilon$) or SKE (Standard $k - \epsilon$) turbulence models. The laminar model gives good results for the cold-leg. However, in the downcomer the motion is influenced by the turbulent mixing of both fluids so the use of a laminar model was discarded.

The resolution capability of the three LES models implemented in Ansys (Smagorinsky, WALE and Dynamic LES) was evaluated in the cold leg test section (see Section 2 for more information about the measurement zones). The results, as shown in the Figure 4.5b, are very close to each other, so it could be said that all three are valid for this simulation. The Euclidean distance (O’Neill, 2006) and the Mahalanobis distance (Mahalanobis, 1936) between experiment and each simulation were used as a method to estimate how close the results to the experimental measurements are. The model which results are closer for the velocities at the cold leg measurement zone was the Smagorinsky.

Finally, tests of the open test ended after the successful realization of the Polynomial Chaos by means of Gaussian quadrature for the quantification of the uncertainty. Figure 4.6 shows the comparison between the velocity obtained in the simulation and the experimental measurement for the cold leg and the downcomer. The shaded areas depicted in Figures 6 and 7 represent the uncertainty band of the simulation results. Predicted velocities are quite close to the experimental measurements, although the simulation does not capture all the points. As mentioned previously, the LES turbulence model is very effective in this type of situation, but it requires a very fine mesh and a very small timestep. There are no data for the concentration in the open test, so this variable is studied only in the blind test.

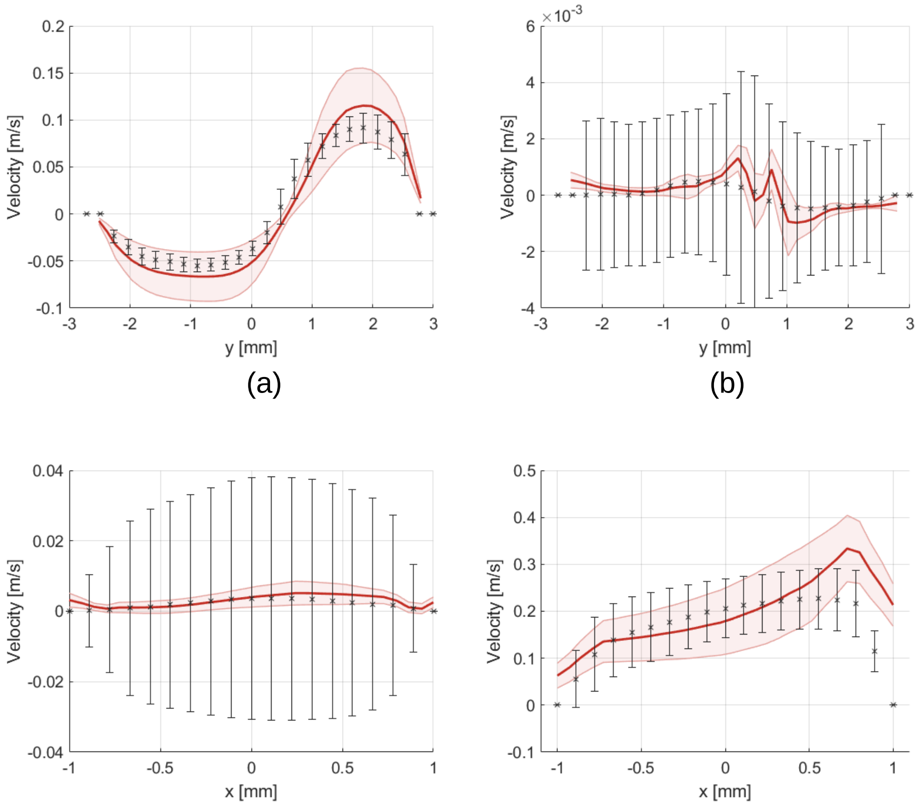

(a) (b)

(c) (d)

Figure 4.6: Velocities of the open test obtained after the application of Polynomial Chaos Expansion by Gauss-Hermite quadrature. Experiment represented in black and the simulations in red. a) longitudinal velocity in the cold-leg, b) transversal velocity in the cold-leg, c) downward velocity in the downcomer and d) transversal velocity in the downcomer.

As summary for the open test, the experimental measurements obtained by PIV in the TAMU installation are predicted quite well by Ansys CFX code. The domain of the fluid must be generated in such a way that the meshing does not have problems of cell quality. All those conflicting areas must either be treated carefully during the discretization or eliminated. The selected turbulence model has a great influence on the result obtained. RANS models are not capable of simulating the wavy interface of the cold-leg. The deviation between the simulations using these turbulence models and the experiment is amplified over time and tend to overestimate the mixing and turbulence between the two fluids. Turbulence models based on Large Eddy Simulation can reproduce the behavior more accurately in exchange for a considerably higher computational cost.

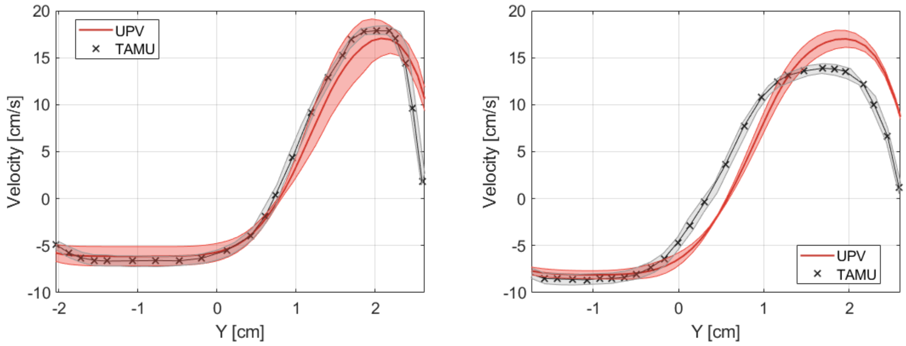

(a) Velocity CL 5-10s average (b) Velocity CL 10-15s average

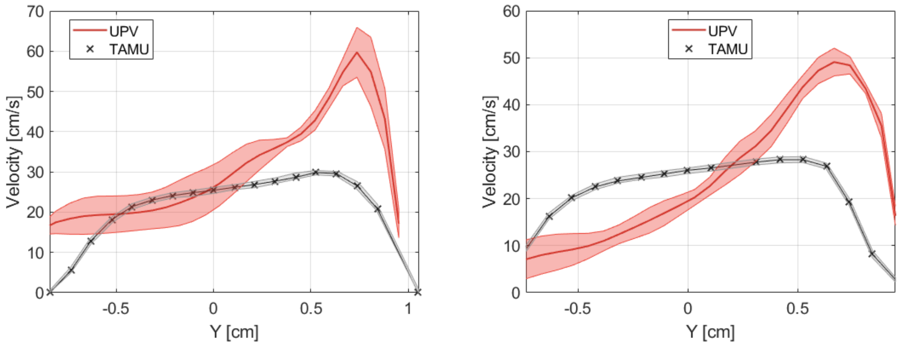

(c) Velocity DC 10.5-15.5s average (d) Velocity DC 25.5-30.5s average

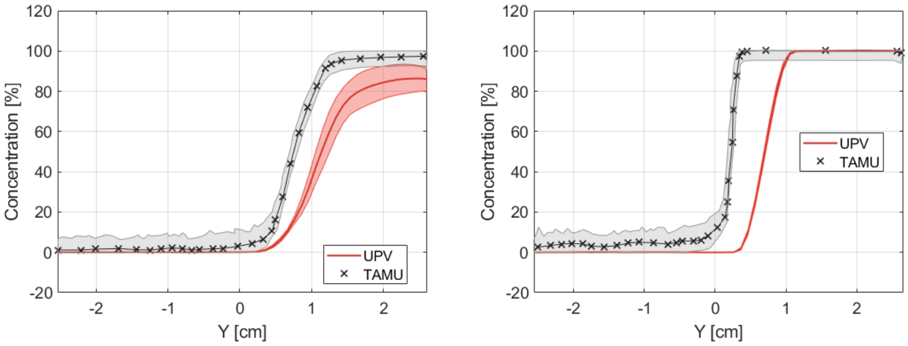

(e) Concentration CL 5-10s average (f) Concentration CL 25.5-30.5s average

Figure 4.7: Velocities of the blind test obtained after the application of Polynomial Chaos Expansion by Gauss Square. (a) longitudinal velocity in the cold-leg (CL) for the time average 5-10s, (b) longitudinal velocity in the cold-leg (CL) for the time average 10-15s, (c) downward velocity in the downcomer (DC) for the time average 10.5-15.5s, (d) downward velocity in the downcomer. (DC) for the time average 25.5-30.5s, (e) concentration in the cold-leg (CL) for the time average 5-10s and (f) concentration in the cold-leg (CL) for the time average 15-22.24s.

In the case of the UPV the cold-leg zone is predicted quite accurately as the motion is produced by gravity and buoyancy forces. For the downcomer, the turbulent mixing between the high-density current and the low-density current mainly influence the flow. This phenomenon is predicted with less accuracy, although the orders of magnitude are correctly maintained. The cell size therefore plays an important role in this zone improving the results as its value is reduced. At the WGAMA group, meeting in Paris in 2019 several organizations recognized the enormous difficulties they had encountered in predicting the vertical downward velocity of the mixture in the downcomer. The uncertainty analysis has been carried out by Polynomial Chaos Expansion and the results are satisfactory despite considering only the difference in density as an input uncertain variable.

For the blind test, a change in geometry and meshing was carried out to adjust the new liquid level of the high-density tank. To carry out the new uncertainty quantification, five new simulations by means of a 4 million cells mesh have been run.

The shape of the velocity profile is correct as shown in Figure 4.7 (a) and (b). However, the inflexion point, which is correctly predicted in the first time average (5-10s) is slightly shifted downwards for the following time intervals (10-15s) and (15-22s). The velocity of the low-density fluid is predicted accurately, but the high-density fluid is above the experimental measurements for the latest time averages. Similar behavior is observed by Lai et al. (2020) and Hassan et al. (2021) where the velocities difference between experiment and simulation increases over time.

There is an important scattering in the shape of the velocity profile in the downcomer, Figure 4.7 (c) and (d). In general, the jet of our simulations seems to be concentrated on the right side of the downcomer where its velocity is higher than on the left side. This behavior seems to be recurrent for those participants that have used RANS, URANS or LES with a low number of cells in the grid.

Figure 4.7 (e) and (f) shows that the vertical position of the stratification of concentrations (where concentrations change from low-density fluid to high-density fluid) is displaced downwards. This gap remains for the following intervals. For the initial time average (5-10s) the concentration values of the high-density fluid are below the experimental values, but they hit the experiment ones in the following intervals. This is probably due to the diffusion that appears at the interface or the possible offset of the high-density flow front in the measurement zone.

It should be noted that it is strange that fairly good inflexion points are obtained for the velocity profile (v = 0 m/s) but the concentration profile does not match in any of the cases. In general, for our case, it is observed that the deviations that occur in the concentration of the high-density fluid are recovered over time. This is indicative that our results are slightly shifted presumably due to the mesh resolution requirements of the LES model. Further research is needed to identify the problem. Looking at the velocities, the accuracy for the low-density fluid is very good, but for the high-density fluid the values are above the experimental one. This situation seems to be recurrent in most of the participants and it should be studied in detail.

4.6. CONCLUSIONS

The Institute for Energy Engineering of the Polytechnic University of Valencia has participated in the OECD Cold-Leg Mixing Benchmark by providing data from both the simulations and the uncertainty quantification. Our work is included within a project with the Spanish Nuclear Safety Council, aimed at seeking a set of good practices in the use of CFD codes to increase know-how in this field of knowledge.

Firstly, the most important characteristics of the experimental facility developed by Texas A&M University have been described. The properties of the fluids, the boundary conditions of the experiments and the measurements have been detailed. From the geometry provided by the developers of the experiment, a 4 million node mesh has been created using ICEM CFD and imported to Ansys CFX to generate the model. The turbulence model has been decisive for the accuracy of the results, so it was decided to use Large Eddy Simulations that filters the small scales of the turbulence and substitute them by an average effect. Other RANS based models tended to increase the mixing of the fluids resulting in a reduction of the velocities.

The steps followed to apply the Polynomial Chaos Expansion as a method of uncertainty quantification are explained and an appendix has been included with the procedure to ensure the orthogonality of the polynomials. The Gauss-Hermite Quadrature PCE is more efficient when the number of uncertain variables is small, so density was selected as the most relevant uncertain input variable. Therefore, selecting four as the order of the polynomial chaos expansion and five the quadrature order, the resulting number of simulations required was five. The uncertainty in the density difference between fluids follows a normal probability distribution thus Hermite polynomials were used.

For both the open and the blind test, the velocities obtained in the cold-leg are quite accurate, slightly overestimating the maximum value. However, in the downcomer the shape of the velocity profile is not correctly predicted, although, the order of magnitude is correct. In this area, simulation results show an increase in velocity on the inside of the downcomer which reduces its value as it approaches the outside. The profile of the concentrations is correct but there is a gap in the transition zone that is maintained for different time intervals. This difference leaves room for doubt because in the velocity profile this gap is not observed so further investigation is needed.

4.7. ACKNOWLEDGEMENTS

This work was supported by the project THAIS co-financed by the CSN (Nuclear Safety Council of Spain) and the UPV (Polytechnical University of Valencia). The authors would also like to acknowledge the Texas A&M University for the experimental measurements, the OECD/NEA for organizing the benchmark and all the participants who make it possible.

4.8. REFERENCES

Abramovitz, M., Stegun, I.A., 1972. Handbook of Mathematical Functions with Formulas, Graphs and Mathematical Tables., National Bureau of Standards Applied Mathematics Series.

Andreani, M., Badillo, A., Kapulla, R., 2016. Synthesis of the OECD/NEA-PSI CFD benchmark exercise. Nucl. Eng. Des. 299, 59–80. https://doi.org/10.1016/j.nucengdes.2015.12.029

Askey, Richard., Wilson, J., 1985. Some basic hypergeometric orthogonal polynomials that generalize Jacobi polynomials. Mem. Am. Math. Soc. 54, 0–0. https://doi.org/10.1090/memo/0319

Askey, R., Wilson, J.A., 1985. Some basic hypergeometric orthogonal polynomials that generalize Jacobi polynomials. Am. Math. Soc. 319.

ASME V&V 20, 2009. Standard for Verification and Validation in Computational Fluid Dynamics and Heat Transfer ASME V & V 20-2009. Am. Soc. Mech. Eng. 102.

Badillo, A., Kapulla, R., Niceno, B., 2013. Uncertainty Quantification in CFD Simulations of Isokinetic Turbulent Mixing Layers, in: The 15th International Topical Meeting on Nuclear Reactor Thermal-Hydraulics, NURETH-15.

Canonsburg, T.D., 2011. ANSYS Meshing User ’ s Guide. Knowl. Creat. Diffus. Util. 15317, 724–746.

Chang, S.K., Kim, S., Song, C.H., 2014. Turbulent mixing in a rod bundle with vaned spacer grids: OECD/NEA-KAERI CFD benchmark exercise test. Nucl. Eng. Des. 279, 19–36. https://doi.org/10.1016/j.nucengdes.2014.05.013

Crestaux, T., Le Maître, O., Martinez, J.M., 2009. Polynomial chaos expansion for sensitivity analysis. Reliab. Eng. Syst. Saf. 94, 1161–1172. https://doi.org/10.1016/j.ress.2008.10.008

D ’auria, F., Camargo, C., Mazzantini, O., 2012. The Best Estimate Plus Uncertainty (BEPU) approach in licensing of current nuclear reactors. Nucl. Eng. Des. 248, 317–328. https://doi.org/10.1016/j.nucengdes.2012.04.002

Fokken, J., Krohn, B., Kapulla, R., Niceno, B., Prasser, H.-M., Badillo, A., 2019. NEA Benchmark Exercise : Computational Fluid Dynamic Prediction and

Uncertainty Quantification of a GEMIX Mixing Layer Test, NEA/CSNI/R(2017)19.

Hassan, M., Xiong, J., Cheng, X., 2021. Unsteady RANS simulation of OECD-TAMU cold-leg mixing benchmark. Nucl. Eng. Des. 372, 110978. https://doi.org/10.1016/j.nucengdes.2020.110978

Hessling, J.P., 2013. Deterministic Sampling for Propagating Model Covariance. Soc. Ind. Appl. Math. Am. Stat. Assoc. 1, 297–318. https://doi.org/https://doi.org/10.1137/120899133

Kim, J., 2019. Evaluation of RANS k – ε calculations for turbulent stably stratified layers based on GEMIX experiments using the CUPID code. Int. Commun. Heat Mass Transf. 108, 104341. https://doi.org/10.1016/j.icheatmasstransfer.2019.104341

Knio, O.M., Le Maître, O.P., 2006. Uncertainty propagation in CFD using polynomial chaos decomposition, Fluid Dynamics Research. https://doi.org/10.1016/j.fluiddyn.2005.12.003

Krpan, R., Končar, B., 2018. Simulation of Turbulent Wake at Mixing of Two Confined Horizontal Flows. Sci. Technol. Nucl. Install. 2018. https://doi.org/10.1155/2018/5240361

Lai, J.K., Merzari, E., Hassan, Y.A., Fischer, P., Marin, O., 2020. Verification and validation of large eddy simulation with Nek5000 for cold leg mixing benchmark. Nucl. Eng. Des. 358, 110427. https://doi.org/10.1016/j.nucengdes.2019.110427

Lucor, D., Meyers, J., Sagaut, P., 2007. Sensitivity analysis of large-eddy simulations to subgrid-scale-model parametric uncertainty using polynomial chaos. J. Fluid Mech. 585, 255–279. https://doi.org/10.1017/S0022112007006751

Mahaffy, J., Chung, B., Dubois, F., Ducros, F., Graffard, E., Heitsch, M., Henriksson, M., Komen, E., Moretti, F., Morii, T., Mühlbauer, P., Rohde, U., Scheuerer, M., Smith, B.L., Song, C., Watanabe, T., Zigh, G., 2014. Best Practice Guidelines for the Use of CFD in Nuclear Reactor Safety Applications, Nea/Csni/R(2014)11.

Mahalanobis, P.C., 1936. On The Generalized Distance in Statistics, Proceedings of the National Institute of Sciences of India.

Muñoz-Cobo, J.L., Miquel, A., Escrivá, A., Berna, C., Rivera, Y., 2018. Efficient uncertainty quantification in nuclear thermal-hydraulic simulations by means of polynomial chaos expansion., in: ANS Best Estimate Plus Uncertainty International Conference (BEPU 2018) Real Collegio, Lucca, Italy, May 13-19, 2018. p. 11.

Najm, H.N., 2009. Uncertainty Quantification and Polynomial Chaos Techniques in Computational Fluid Dynamics. Annu. Rev. Fluid Mech. 41, 35–52.

https://doi.org/https://doi.org/10.1146/annurev.fluid.010908.165248

O'Neill, B., 2006. Calculus on Euclidean Space, in: Elementary Differential Geometry. Elsevier, pp. 3–42. https://doi.org/10.1016/b978-0-12-088735-4.50005-5

OECD/NEA/CSNI, 2016. The Nuclear Energy Agency–Paul Scherrer Institut Computation Fluid Dynamics Benchmark Exercise, Nea/Csni/R(2016)2.

OECD/NEA/CSNI, Smith, B.L., Mahaffy, J.H., Angele, K., Westin, J., 2011. Report of the OECD/NEA-Vattenfall T-Junction Benchmark exercise.

Orea, D., Vaghetto, R., Nguyen, T., Hassan, Y., 2020. Experimental measurements of flow mixing in cold leg of a pressurized water reactor. Ann. Nucl. Energy 140, 107137. https://doi.org/10.1016/j.anucene.2019.107137

Prošek, A., Končar, B., Leskovar, M., 2017. Uncertainty analysis of CFD benchmark case using optimal statistical estimator. Nucl. Eng. Des. 321, 132–143. https://doi.org/10.1016/j.nucengdes.2016.12.008

Rakhimov, A.C., Visser, D.C., Komen, E.M.J., 2019. Uncertainty Quantification method for CFD applied to the turbulent mixing of two water layers – II: Deterministic Sampling for input uncertainty. Nucl. Eng. Des. 348, 146–158. https://doi.org/10.1016/j.nucengdes.2019.04.016

Rakhimov, A.C., Visser, D.C., Komen, E.M.J., 2018. Uncertainty Quantification method for CFD applied to the turbulent mixing of two water layers. Nucl. Eng. Des. 333, 1–15. https://doi.org/10.1016/j.nucengdes.2018.04.004

Salvetti, M. V., Meldi, M., Bruno, L., Sagaut, P., 2018. Reliability of large-eddy simulations: Benchmarking and uncertainty quantification. ERCOFTAC Ser. 24, 15–23. https://doi.org/10.1007/978-3-319-63212-4_2

Simoneau, J.-P., Champigny, J., Gelineau, O., 2010. Applications of large eddy simulations in nuclear field. Nucl. Eng. Des. 240, 429–439. https://doi.org/10.1016/j.nucengdes.2008.08.018

Smith, B.L. (PSI), Bieder, U. (CEA), Grafard, E. (IRSN), Heitsch, M. (GRS), Henriksson, M. (Vattenfall), Höhne, T. (FZD), Komen, E. (NRG), Mahaffy, J. (PSU), Moretti, F. (UPisa), Morii, T. (JNES), Mühlbauer, P. (NRI), Rohde, U. (FZD), Scheuerer, M. (GRS), Song, C.-H. (KAERI), Zigh, G. (USNRC), 2008. Assessment of Computational Fluid Dynamics (CFD) for Nuclear Reactor Safety Problems, NEA/CSNI/R(2007)13.

Smith, B. L., Mahaffy, J.H., Angele, K., 2013. A CFD benchmarking exercise based on flow mixing in a T-junction. Nucl. Eng. Des. 264, 80–88. https://doi.org/10.1016/j.nucengdes.2013.02.030

Smith, B.L., Song, C.H., Chang, S.K., Lee, J.R., Kim, J.W., 2013. Report of the OECD/NEA KAERI Rod Bundle CFD Benchmark Exercise.

Wiener, N., 1938. The homogeneous chaos. Am. J. Math. 60(4), 897–936.

Xiu, D., Karniadakis, G.E., 2003a. Modeling uncertainty in flow simulations via generalized polynomial chaos. J. Comput. Phys. 187, 137–167. https://doi.org/10.1016/S0021-9991(03)00092-5

Xiu, D., Karniadakis, G.E., 2003b. Modeling uncertainty in flow simulations via generalized polynomial chaos. J. Comput. Phys. 187, 137–167. https://doi.org/10.1016/S0021-9991(03)00092-5

APPENDIX A. ORTHOGONALITY OF HERMITE POLYNOMIALS TO APPLY POLYNOMIAL CHAOS EXPANSION WITH AN UNCERTAIN VARIABLE OF ANY MEAN AND VARIANCE

This appendix addresses the issue of Hermite polynomials orthogonality when it is necessary to perform a variable change. To apply the Polynomial Chaos Expansion in the case of an uncertain variable with Gaussian distribution function it is necessary to use Hermite polynomials. However, it is most likely that our uncertain variable will have a mean and variance different from 0 and 1. Therefore, it is necessary to obtain Hermite polynomials that are orthogonal to the new variable characteristics.

It is easy to find in the literature the Hermite polynomials that satisfy the following relation:

$$\langle H_n^2 \rangle = \int_{-\infty}^{\infty} e^{-x^2}\, H_n^2(x)\, dx = h_n = \sqrt{\pi}\, 2^n\, n! \tag{A1}$$

Note that the polynomials H_n are orthogonal on $(-\infty, \infty)$ for the weight function $w(x) = e^{-x^2}$. Hermite polynomials can also be found as He_n, but the relationship is similar as shown in eq. A2.

$$\langle He_n^2 \rangle = \int_{-\infty}^{\infty} e^{-\frac{x^2}{2}}\, He_n^2(x)\, dx = \sqrt{2\pi}\, n! \tag{A2}$$

Some authors move the constant $\sqrt{2\pi}$ into the integral so the expression can be arranged according to the eq. A2.

$$\langle He_n^2 \rangle = \int_{-\infty}^{\infty} p(x)\, He_n^2(x)\, dx = \int_{-\infty}^{\infty} \frac{1}{\sqrt{2\pi}} e^{-\frac{x^2}{2}}\, He_n^2(x)\, dx = n! \tag{A3}$$

Being $p(x)$ the probability density function for a normal distribution with $\mu = 0$ and $\sigma = 1$. The relation between both H_n and He_n correspond to the equations A4 and A5.

$$H_n(x) = 2^{n/2}\, He_n\left(\sqrt{2}x\right) \tag{A4}$$

$$He_n(x) = 2^{-(n/2)}\, H_n\left(\frac{x}{\sqrt{2}}\right) \tag{A5}$$

Then, the same reasoning is followed, but starting from the probability density function shown in eq. A6 and then calculating the orthogonal Hermite polynomials.

$$p(x) = \frac{1}{\sqrt{2\pi}\sigma} e^{-\frac{x^2}{2\sigma^2}} \tag{A6}$$

$$\begin{aligned}\langle \left(He_n^{\sigma^2}\right)^2 \rangle &= \int_{-\infty}^{\infty} p(x)\ \left(He_n^{\sigma^2}(x)\right)^2\ dx \\ &= \int_{-\infty}^{\infty} \frac{1}{\sqrt{2\pi}\sigma} e^{-\frac{x^2}{2\sigma^2}}\ \left(He_n^{\sigma^2}(x)\right)^2\ dx\end{aligned} \tag{A7}$$

For this scenario the new polynomials are denoted as $He_n^{\sigma^2}$ and the relation with H_n and He_n is the next one.

$$He_n^{\sigma^2}(x) = \sigma^n\ He_n\left(\frac{x}{\sigma}\right) = \frac{\sigma^n}{2^{n/2}} H_n\left(\frac{x}{\sqrt{2}\sigma}\right) \tag{A8}$$

Then, it is possible to follow the reasoning started in eq. A7:

$$\begin{aligned}\langle \left(He_n^{\sigma^2}\right)^2 \rangle &= \int_{-\infty}^{\infty} \frac{1}{\sqrt{2\pi}\sigma} e^{-\frac{x^2}{2\sigma^2}}\ \left(He_n^{\sigma^2}(x)\right)^2\ dx \\ &= \left(\frac{\sigma^2}{2}\right)^n \int_{-\infty}^{\infty} \frac{1}{\sqrt{2\pi}\sigma} e^{-\frac{x^2}{2\sigma^2}}\ \left(H_n\left(\frac{x}{\sqrt{2}\sigma}\right)\right)^2\ dx\end{aligned} \tag{A9}$$

Finally, applying the variable change $t = \frac{x}{\sqrt{2}\sigma}$ and $dt = \frac{dx}{\sqrt{2}\sigma}$.

$$\langle \left(He_n^{\sigma^2}\right)^2 \rangle = \left(\frac{\sigma^2}{2}\right)^n \frac{1}{\sqrt{\pi}} \int_{-\infty}^{\infty} e^{-t^2}\ {H_n}^2(t)\ dt \tag{A10}$$

The result for $\frac{1}{\sqrt{\pi}} \int_{-\infty}^{\infty} e^{-t^2}\ {H_n}^2(t)\ dt$ is given by eq. A1, so the result for the new Hermite polynomials $\langle \left(He_n^{\sigma^2}\right)^2 \rangle$ is also known.

$$\langle \left(He_n^{\sigma^2}\right)^2 \rangle = \left(\frac{\sigma^2}{2}\right)^n \frac{1}{\sqrt{\pi}} \sqrt{\pi}\ 2^n\ n! = \sigma^{2n}\ n! \tag{A11}$$

There is one more step needed before obtaining the last expression for the calculation of the Polynomial Chaos Expansion. As a quick reminder, our simulations will be performed after changing the variable. Following the relation $x^{in} = \mu + \sqrt{2}\ \sigma\ t$ it is possible to obtain the input values that we will have to introduce in our code. Then, it is necessary to repeat the process for the probability density function of eq. A12.

$$p(x) = \frac{1}{\sqrt{2\pi}\sigma} e^{-\left(\frac{x-\mu}{\sqrt{2}\ \sigma}\right)^2} \tag{A12}$$

After performing an intermediate variable change $x = t - \mu$ and $dt = dx$ and starting from the eq. A8

$$He_n^{\sigma^2}(t-\mu) = \frac{\sigma^n}{2^{n/2}} H_n\left(\frac{t-\mu}{\sqrt{2}\,\sigma}\right) \tag{A13}$$

Therefore the new orthogonal polynomials are defined as follows:

$$He_n^{(\sigma^2,\mu)}(x) = \frac{\sigma^n}{2^{n/2}} H_n\left(\frac{x-\mu}{\sqrt{2}\,\sigma}\right) \tag{A14}$$

Then,

$$\begin{aligned}\left\langle\left(He_n^{(\sigma^2,\mu)}\right)^2\right\rangle = \langle{\phi_n}^2\rangle &= \int_{-\infty}^{\infty} \frac{1}{\sqrt{2\pi\sigma}} e^{-\left(\frac{x-\mu}{\sqrt{2}\,\sigma}\right)^2} \left(He_n^{(\sigma^2,\mu)}(x)\right)^2 dx \\ &= \sigma^{2n}\, n!\end{aligned} \tag{A15}$$

The definition of $He_n^{(\sigma^2,\mu)}$ is shown in eq. A14, his module $\left\langle\left(He_n^{(\sigma^2,\mu)}\right)^2\right\rangle$ in eq. A15 so the only missing term to calculate the alpha coefficients $\alpha = \frac{\langle R\phi_n\rangle}{{\phi_n}^2}$ of the Polynomial Chaos Expansion by Gauss-Quadrature is displayed in eq. A16.

$$\langle R\phi_n\rangle = \int_{-\infty}^{\infty} \frac{1}{\sqrt{2\pi\sigma}} e^{-\left(\frac{x-\mu}{\sqrt{2}\,\sigma}\right)^2} R(x)\, He_n^{(\sigma^2,\mu)}(x)\, dx \tag{A16}$$

The last variable change is $x^{in} = \mu + \sqrt{2}\,\sigma\, t$ and $dx^{in} = dt\,\sqrt{2}\,\sigma$. Note that we have included the superscript in referring to the fact that this variable x corresponds to the uncertain variable of our simulation input.

$$\langle R\phi_n\rangle = \frac{1}{\sqrt{\pi}} \int_{-\infty}^{\infty} e^{-t^2} R\left(\mu + \sqrt{2}\,\sigma\, t\right) He_n^{(\sigma^2,\mu)}\left(\mu + \sqrt{2}\,\sigma\, t\right) dt \tag{A17}$$

Substituting orthogonal polynomials $He_n^{\sigma^2\mu}$ by eq. A14.

$$\begin{aligned}\langle R\phi_n\rangle &= \frac{1}{\sqrt{\pi}} \int_{-\infty}^{\infty} e^{-t^2}\, R\left(\mu + \sqrt{2}\,\sigma\, t\right) \frac{\sigma^n}{2^{n/2}}\, H_n\left(\frac{\mu + \sqrt{2}\,\sigma\, t - \mu}{\sqrt{2}\,\sigma}\right) dt \\ &= \frac{\sigma^n}{\sqrt{\pi}\, 2^{n/2}} \int_{-\infty}^{\infty} e^{-t^2}\, R\left(\mu + \sqrt{2}\,\sigma\, t\right)\, H_n(t)\, dt\end{aligned} \tag{A18}$$

Finally, as it has been exposed in this article, the integral has been solved by means of Gauss quadrature following the eq. A19.

$$\langle R\phi_n\rangle = \frac{\sigma^n}{\sqrt{\pi}\, 2^{n/2}} \sum_{j=1}^{5} w_j\, R\left(\mu + \sqrt{2}\,\sigma\, t_j\right) H_n\left(t_j\right) \tag{A19}$$

Chapter 5

COMPUTATIONAL FLUID DYNAMICS APPLIED TO ANNULAR FLOW

5.1. INTRODUCTION

Computational dynamics codes are a very powerful tool for simulating fluid behavior, including multiphase flows. However, their use in nuclear reactor safety applications is highly complex due to the rigorous confidence requirements demanded by the industry (Smith et al., 2008). Researchers around the world are focusing many resources and efforts to boost the use of CFD codes in all types of applications.

Multiphase simulations are much more computationally demanding than single-phase simulations, especially if heat and mass exchange phenomena are included. In addition, annular flow is characterized by relatively high liquid and gas velocities. This makes the simulations unstable and it requires a very demanding time scheme.

There are multiple CFD codes available with multiphase calculation capabilities. Both open access and commercial CFD have those tools although there are different calculation methodologies. Annular flow falls into the category of multiphase flow known as free surface flow since both fluids are immiscible with each other. In the case study of air-water, this phenomenon is even more evident by eliminating the heat transfer process. The simplest method to capture free-surface interfaces is the Volume-of-fluid or VOF method. This method has already been discussed in chapter 1.5.2. CFD Simulations and Annular Flow and is characterized by not allowing phase mixing using the void fraction in a single set of equations. The VOF method has been employed multiple times for annular flow simulation (Dai et al., 2013; Ghosh et al., 2010; Liu et al., 2011) showing the phenomenal capabilities of this methodology.

To carry out the simulations of the GEPELON experimental facility, the commercial CFD code ANSYS CFX was used. This software, along with most current CFD software, is based on the finite volume technique for the discretization of the equations in the domain. The complete flow characterization is thus obtained as an approximation of each variable in small control volumes. In relation to multiphase flow modeling, ANSYS CFX has available Euler-Euler and Euler-Lagrangian models (which Ansys refer to the latest as Lagrangian Particle Tracking). The Euler-Euler model is the one used to carry out the simulations for this thesis. ANSYS CFX treats this model in two different ways: inhomogeneous or homogeneous.

The inhomogeneous model uses two velocity fields (among other variables) to calculate the equations for each fluid. The pressure field however is shared by both. There are different interfacial transfer terms that are responsible for producing the interaction between fluids. For example, the velocities will tend to equalize due to the interfacial drag interaction, although they will not necessarily do so.

On the other hand, the homogeneous model uses a single velocity field for both fluids as well as sharing the field of other variables such as temperature or turbulence. The pressure field, as in the inhomogeneous case, is also shared. Although this model represents a specific multiphase case by using a single field for all variables and fluids, it has several advantages such as reducing the number of equations and optimizing the calculation time. Therefore, it is generally recommended for cases such as free surface. In annular flow, where the dominant force is the drag force, it is common that both fluids tend to equalize in the interfacial zone. However, this model does not allow the slip of velocities between phases, which limits its applications to transient simulations. For the modeling of the GEPELON installation, the inhomogeneous model has been used but with the shared turbulence field (option available in ANSYS CFX).

The section 5.3 is based on the paper *Experimental Measurements and CFD Results of Liquid Film Thickness in Vertical Downward Air - Water Annular Flow* that has been published in the *International Journal of Computational Methods and Experimental Measurements*. This journal gathers the best papers selected at the *International Conference on Advances in Fluid Dynamics with emphasis on Multiphase and Complex Flow* (AFM-MPF 2021). However, it has been decided not to include the paper as a complete chapter since this section required additional parts. Therefore, this chapter first shows a compendium with the best practice guidelines that have been elaborated for the appropriate simulation of annular flow. Next, the three-dimensional CFD model is shown with the results that were published in the aforementioned paper. Finally, the results of the application of the uncertainty quantification method of Polynomial Chaos Expansion to the experimental facility simulations are shown.

5.2. BEST PRACTICE GUIDELINES FOR ANNULAR FLOW SIMULATION

The Best Practice Guidelines (BPG) for free-surface annular flow scenarios have been studied in depth prior to the decision to use this methodology. Below, a comprehensive BPG summary that have been extracted based on the experience generated during the elaboration of this thesis as well as on the different ANSYS documentation, especially ANSYS Solver Modelling Guide (Canonsburg, 2009) is described.

- It is highly recommended to run a steady-state simulation first to generate the proper initial conditions along the domain. It might be necessary to estimate a proper physical timescale different from the one approximated automatically by the code.
- For air-water multiphase model where the velocity difference is high it is recommended to use inhomogeneous Euler-Euler model as they don’t travel at the same velocity and there can be a slip between the two continuous phases.
- Gravity should be enabled to account for the buoyancy effects.
- For air-water adiabatic simulation with no heat transfer is recommended to accelerate the simulation if not needed.
- Selection of the turbulence model:
  - Homogeneous turbulence model recommended if the multiphase model is inhomogeneous according to ANSYS documentation.
  - Shear Stress Transport omega based model is a good starting point as it employs the k-ω turbulence model with a special wall treatment.
  - If using URANS models, best target would be Reynolds Stress Models (RSM) as it naturally includes the effects of streamline curvature, sudden changes in the strain rate, secondary flows or buoyancy compared to turbulence models using the eddy-viscosity approximation). Best ones: SSL RSM or SMC-BSL RSM (LLR-IQ and LLR-IP obsolete) or the EARSM model. The main counterpart is that they add complexity as there are 6 equations to resolve instead of 2 and they have around 12 parameters to tune if needed.

    - Best option if possible would be LES. Nevertheless. The use of this model would require many resources (at least 15 points in boundary layers, specific meshing, Courant Number below 1, etc.). Best initial recommendations are LES WALE or a zonal model like SAS or DES.
- The wall-treatment is mainly dependent on the turbulence model selected. Next, different examples are exhibit to better understand how ANSYS CFX calculate the boundary layer near the wall:
    - ε-based does not resolve viscous and logarithmic layer. CFX add the scalable wall functions to allow it to avoid the problem but it adds complex damping functions. For this reason, this turbulence model is not recommended.
    - ω-based models avoid this difficulties as CFX uses an automatic near-wall treatment, which allows for a smooth shift between low-Re approaches to wall functions. A resolution of about 10 nodes in the boundary layer is recommended so the wall functions are not used. By means of this model it is not necessary to define a y+ greater than 20 for standard wall functions or smaller than 2 for low-Re approach. However, 15 nodes would be necessary for a low-Re treatment.
    - LES uses an automatic near-wall treatment also, but a good mesh resolution of approximately 15 nodes in the boundary layer.
    - Wall functions won't resolve properly the front of the water film as there could be eddies near the wall.
    - In order to calculate near wall spacing different methods can be found. The estimation that has been used for this thesis is:
        - Reynolds number of de liquid: $Re_L = \rho\, u_0\, L/\mu$, being $L = plate\ length$ and $u_0 = characteristic\ velocity$.
        - Near wall spacing: $\Delta\mathrm{y} = \mathrm{L} \cdot \Delta y^{+}\sqrt{74}\, Re_L^{-13/14}$, being $\Delta y^{+} = target\ y^{+}$.
        - Number of nodes: 15 for a low-Re approach.
        - Boundary layer thickness: $\delta_{BL} = 0.035\, L\, Re_L^{-1/7}$.
- Free surface model enabled. The characteristics of this model are:
    - ANSYS CFX model for immiscible phases to properly predict the interface. CFX relies on an interface capturing approach for VOF.
    - Interface is tracked in the grid, which is fixed, not adaptive. It is therefore very mesh dependent.

  - Transport equation is solved for the volume fraction of each phase.
  - Compressive discretization scheme is used to keep interface sharp (2 or 3 elements less diffusive).
  - Finally, a Rhie-Chow treatment is applied for pressure-velocity coupling (4th order).
  - Free surface method is therefore kind of sharpening method for the interface, which should be pretty clear between both fluids.
  - Important additional recommendations:
    - Necessary to keep Courant Number around 1 near the interphase.
    - Fine mesh at interface required for the model.
    - If smearing appears, it usually will not go away but persist.
    - By default, the sharpening is aggressive with a two-step compressive scheme. Reduce the order or deactivate the compression if needed for convergence although it is not recommended.
- By default, the volume fraction is segregated from the other variables. For this reason, Coupled Volume Fraction (CVF) option is recommended for free surface models. Nevertheless, it might introduce instabilities so it could be deactivate if robustness issues appear. This option couples velocity, pressure and volume fraction implicitly.
- Prior to any calculation, the length scale should be estimated for flow characterization:
  - Integral Length Scale l_0 is the size of the largest eddies in our simulation. It also corresponds to the size of an eddy with mean turbulent kinetic energy. A mesh spacing of around $1/5$ of the l_0 would be the ideal final target for LES simulations $l_0 = {k^{3/2}}/{\varepsilon}$. ó $l_0 = {k^{1/2}}/{C_\mu \omega}$. A integral Length Scale Reynolds number can be defined as $Re_{l_0} = \frac{ul_0}{\nu}$.
  - Taylor Microscale is also a good option for Length scale. It gives information of the variation of the velocity fluctuation. It is a reference about where viscosity starts to influence the eddy behaviour. It is located between large and small eddies. Can be approximated using $\lambda \approx \sqrt{10\nu\frac{k}{\varepsilon}}$. The value obtained can be directly used to calculate the mesh spacing.

  - Kolmogorov Microscale: It is the smallest hydrodynamic scale in turbulent flows where the turbulent kinetic energy is dissipated into heat. At this scale, the flow is dominated by viscosity. It's value can be estimated as $\eta = \sqrt[4]{\frac{\nu^3}{\varepsilon}}$.
- The velocity scale should be estimated as the characteristic velocity of the flow:
  - Characteristic velocity may also depend on the length scale selected, as it should be the maximum of a representative velocity specific of our flow. A good estimate for our simulation could be the maximum velocity of the water velocity profile.
  - Velocity scale could be calculated also as $\sqrt{k}$
- Finally, both length and velocity scale can be used to calculate the timescale. Time scale will correspond to the timestep of the transient simulations or the physical timestep of a steady state simulation:
  - Time scale is defined as the length scale divided by the velocity scale.
    - For URANS time scale can be calculated using the Integral Length Scale l_o
    - For LES simulations, at least the Taylor Microscale should be used. It is recommended to resolve around 80% of the turbulent kinetic energy, being only the 20% modelled. This can be estimated applying a length scale $1/5$ of the l_0 scale approximately.
  - It is often helpful to reduce the timestep for the volume fraction equations by an order of magnitude than the other equations.
- Meshing basic recommendations:
  - Hexa meshing recommended to generate cell faces perpendicular to the flow direction.
  - If using Ansys Meshing it is recommended to generate the mesh using the Multizone method.
  - Spacing between adjacent cells estimated depending on Length Scale selected.
  - Inflation in the wall designed for the turbulence model and wall-treatment approach desired, which can be estimated as 10 to 15 elements.

Finally, some additional remarks can be added to facilitate the user's model convergence. Sometimes, it is better to run simple simulations by making certain assumptions before including all the phenomenology. For example, the model can be converged by turning off gravity and then turning it on in a second simulation. As previously mentioned, a refined mesh is not always the best idea, especially at the beginning. However, sensitivity analysis will always be necessary before showing definitive results. It is also important to properly consider the spatial, velocity and time scale as it will save time in the long run. Finally, implicit solvers such as ANSYS CFX and most current codes can work with Courant numbers greater than 1. For stationary simulations this may be appropriate and therefore larger timesteps could be used. For transient simulations, it is highly recommended to keep this value around 1. Nevertheless, it is to be expected that simulations for high gas velocities will not always meet this criterion. In that case it is necessary to be aware that the code will not be able to correctly predict the nonlinear behavior in cells where this value is higher.

5.3. THREE-DIMENSIONAL CFD MODEL FOR COCURRENT DOWNWARD ANNULAR FLOW

5.3.1. CFD MODEL CONFIGURATION

The design of a CFD model generally has a similar workflow. First, the geometry, usually referred to as the *domain*, is designed as the place where the two phases can move. Next, the domain is discretized into finite volumes in a process known as meshing. This step is very important as the quality requirements of the mesh are very high. The next step consists of generating an input that collects the conditions to be imposed on the simulation such as the type of fluids, the models to be used, the boundary conditions, the results to be obtained or the convergence characteristics. The solver is then run to calculate the result in each of the cells of the domain. Finally, different results can be visualized and extracted in the post-processing and visualization software.

The domain of the GEPELON facility consists of a $30\,mm$ diameter vertical pipe (Figure 5.1a). The pipe length has been simplified to $500\,mm$, down from $4000\,mm$ because the initial objective is the prediction of the mean liquid film thickness. For this reason, the simulations were performed in steady-state. After initial tests, it was found that, from $300\,mm$ onwards, the void fraction of the two phases did not vary as it moved down the pipe. Figure 5.1b shows the air volume fraction as a function of distance from the wall. Each line represents the positions with respect to the inlet at 100, 300 and $500\,mm$. To be conservative, since this study did not extend to all flow rates, it was decided to maintain a domain length of 500 mm.

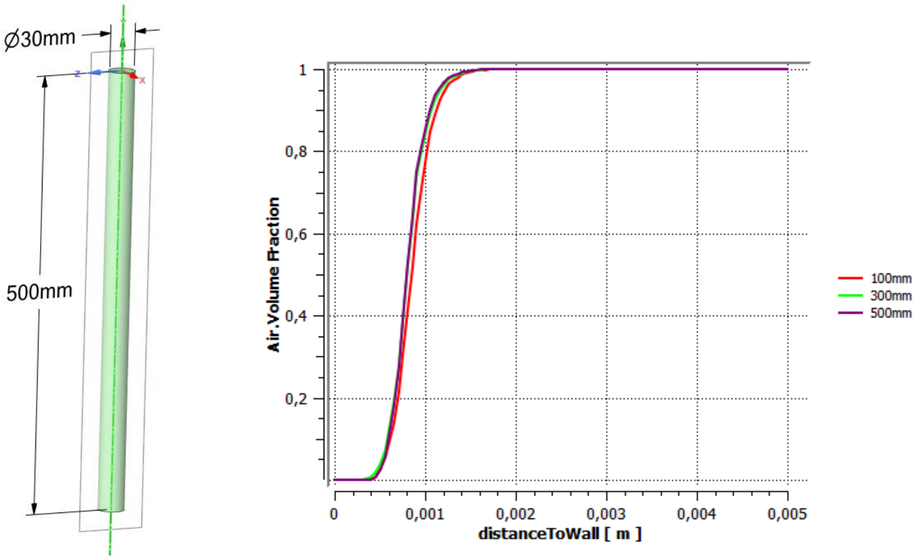

a) b)

Source: Author's design

Figure 5.1. a) Geometry implemented in the CFD code, b) Air volume fraction obtained at 100, 300 and 500mm from the inlet.

The mesh was generated using the ICEM CFD tool with a total of $4\ million$ hexa cells. Figure 5.2Figure 5. shows some details of the geometry and meshing used. The details of the figures on the far right represent in blue the space occupied by the liquid film for an intermediate flow simulation ($Re_L = 4000$).

The mesh has been adjusted so the y+ does not exceed 1, being the first layer wall spacing 0.01mm. The film consists of more than 15 cells for this intermediate flow rate. However, due to the y+ requirement and the high velocity of liquid movement with values above $1\ m/s$ the aspect ratio of the cells closest to the wall is considerably high. If we increase the number of longitudinal cells, it is easy to improve this parameter. However, the Courant number would increase considerably and could only be compensated by reducing the time step. In order to maintain a compromise between mesh quality and computational cost, a mesh of 4 million nodes and a time scale of 1ms has been kept.

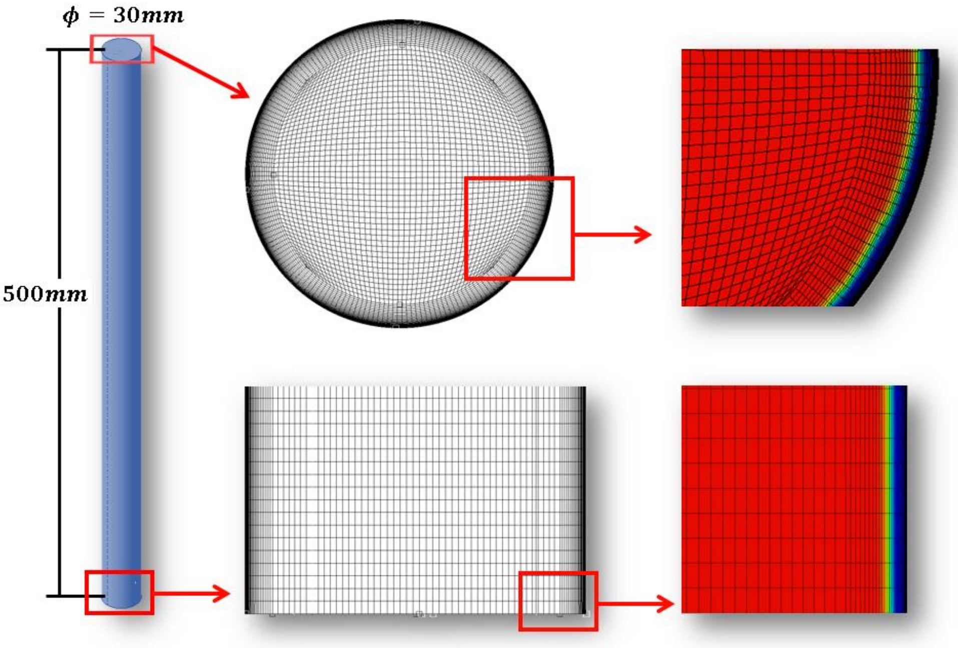

Source: Author's design

Figure 5.2. Detailed information about the mesh. Colored images at the right side show the location of the water phase in the mesh

Most important requirements for a mesh for annular flow simulations are the number of elements near the interphase and the small near wall spacing. In addition, it is important that the mesh follow an O-grid approach for circular pipes. The number of nodes plays important role as the more nodes added, the more accuracy you will have at the interphase. Nevertheless, at the same time, the more nodes, the more unstable is going to be the simulation as there is less diffusion (Figure 5.3). For this thesis, it has been estimated that a good initial guess is 1 million cells every 200mm of a 30mm-diameter pipe.

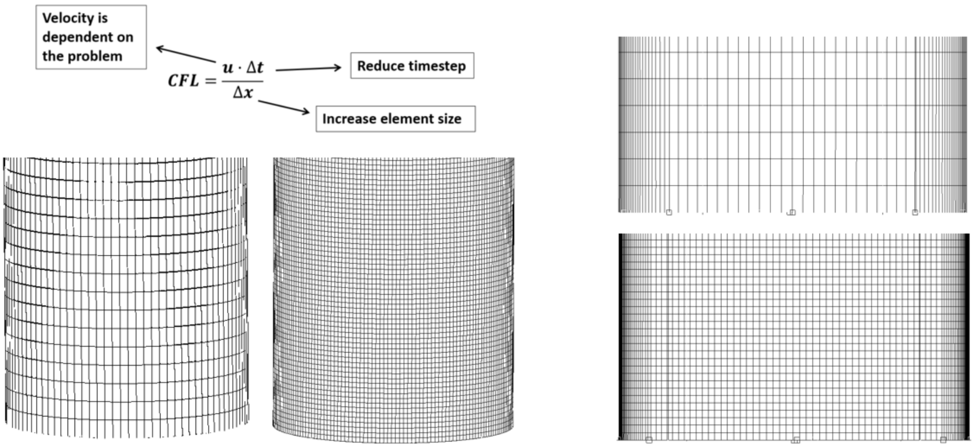

Source: Author's design

Figure 5.3. Comparison between coarse and fine mesh relating the timestep and element size requirements with the Courant Number (CFL).

The turbulence model applied was Shear Stress Transport (SST), since this model was designed to predict turbulence near the wall vicinity using an k-ω approach, which is where the thin liquid film is located. In addition, this 2-equation model is able to achieve a good compromise between computational speed and accuracy. When the value of y+ is below 1, the automatic CFX wall model calculates the velocity near the wall using a Low-Re approach. Large Eddy simulation Model (LES) would be the best option if a transient statistic approach is taken. Due to the high computational cost of this model, this option was discarded for this stage.

The boundary conditions consist of an inlet situated in the upper part of the domain, a wall and an opening at the bottom. The water volume fraction at the inlet has been defined in such a way that the liquid enters through an annulus located $1\ mm$ from the pipe's inner wall. A user expression has been introduced to define the water volume fraction (VF_{water}) as follows.

$$VF_{water} = \begin{cases} 1 & if \quad \sqrt{x^2 + z^2} \geq r_{int} \\ 0 & if \quad \sqrt{x^2 + z^2} < r_{int} \end{cases} \tag{5.1}$$

being x^2 and z^2 the radial coordinates with the origin at the center of the pipe, and r_{int} an arbitrary value of internal radius. This value can be estimated as h_0, the Nusselt's laminar film thickness (Nusselt, 1916). In the inner part of the inlet, the air phase is initialized as the opposite of the void fraction of the liquid. The opening has been configured to allow air re-entry with a relative pressure of $0\ Pa$. The domain wall is configured as no-slip walls with smooth roughness.

In general, a good domain initialization is very important to properly start to converge the simulation solution. Therefore, to initialize the domain, the same conditions that has been imposed for the inlet can be directly implemented along the whole domain. The liquid phase is located near the wall initially with an estimated speed depending on the mass flow rate while the air is moving in the pipe core. Initial pressure inside the tank can be initialized using the following expression.

$$P_{ini} = (l - y)\rho g \cdot VF_{water} \tag{5.2}$$

being l the pipe length and y the longitudinal coordinate with origin in the bottom part of the pipe.

The most important features that have been defined in the ANSYS CFX setup are summarized below.

- Euler-Euler inhomogeneous multiphase flow model.
- Gravity enabled.
- Free Surface 2nd order sharpening model or the model .
- Turbulence model: SST.
- Heat transfer disabled.
- Surface tension coefficient = $0{,}072\ N/m$ (at $25°C$).
- Advection scheme: High resolution (blend between 1st and 2nd order based on local solution gradients) for RANS based turbulence models.
- Transient scheme: Second Order Backward Euler.
- Timestep: Between $0{,}5 - 0{,}1\ ms$ for downward annular flow.
- Iterations per timestep: $4 - 10\ iterations/\Delta t$.
- Volume Fraction Coupled (CFV).

5.3.2. RESULTS AND DISCUSSION

To model the GEPELON facility with a cocurrent downward annular flow configuration a total of 27 simulations have been carried out. The Reynolds numbers ranges are 800 to 6600 for the liquid and 0 to 4400 for the gas. In order to understand more visually the behavior of the code, the void fraction and the air velocity in a longitudinal plane passing through the center of the pipe (Figure 5.4) in a free-falling annular flow scenario have been extracted. In Figure 5.4a the water is shown in blue color and it can be observed how the film thickness becomes thin until a constant value is reached and maintained. In relation to the velocity in Figure 5.4b, the liquid accelerates as a consequence of the acceleration of gravity and consequently its thickness is reduced until it reaches an equilibrium.

The mean film thickness(h_{mean}) is the variable that has been used as a reference to compare the experiment and the simulation. However, it should be noted that the ANSYS CFX code will always represent a diffuse zone at the interface during the gap fraction transition from 1 to 0. This means that there are a certain amount of cells where the void fraction does not determine whether we would find water or air in that zone. There are different methodologies to calculate the exact position of the interface while maintaining the mass of each fluid (S. Dominguez et al., 2019). Nevertheless, as the cells have a low aspect ratio in the diffuse zone, we can estimate the interface at its intermediate point (Figure 5.5).

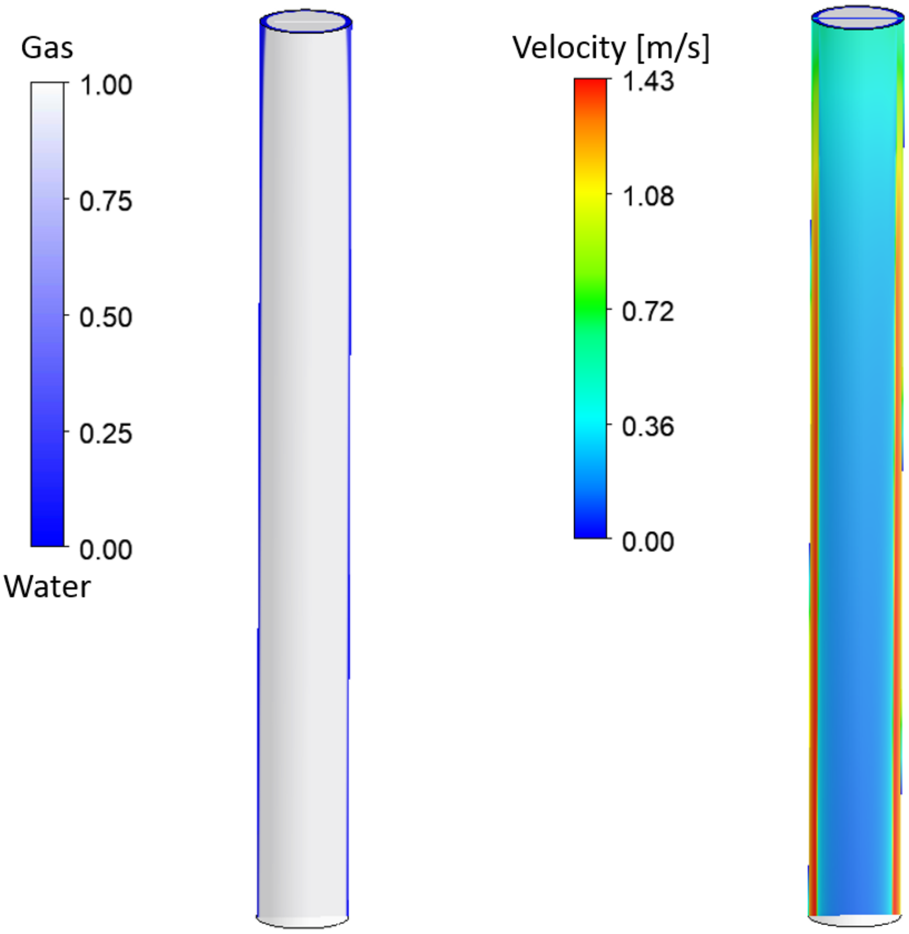

Source: Author's design

Figure 5.4. Example of the volume fraction and velocity represented in a longitudinal plane that crossing through the center of the pipe.

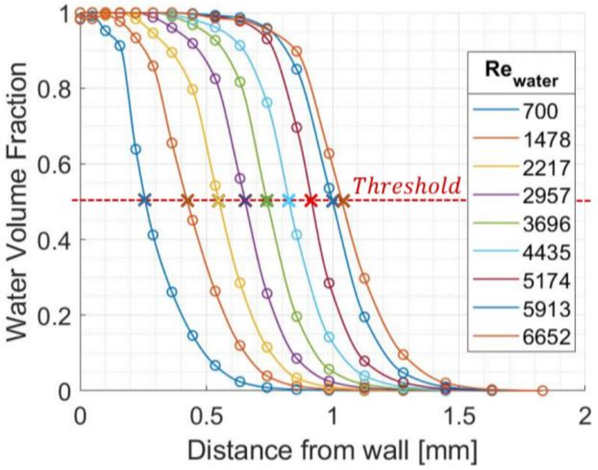

Source: (Rivera et al., 2021)

Figure 5.5. Water volume fraction for different Re_L depending on the distance from the wall.

The free-fall liquid film thickness has been studied by numerous authors over the years. Figure 5. compares the results obtained by the code with those studied by these authors. The two correlations used by Nusselt and Mudawar (Mudawwar & El-Masri, 1986; Nusselt, 1916) represent the most accepted expressions by the community for the laminar and turbulent ranges respectively. On the other hand, the symbols represent experimental measurements studied by different methodologies. All these techniques have been thoroughly analyzed in Chapter 1 showing the advantages and disadvantages associated with each of them. In relation to the measurements by electrical methods we find first of all the conductance probes used by (Webb & Hewitt, 1975) as well as the experimental installation GEPELON (Rivera et al., 2022). Using capacitance probes, the results of (Takahama & Kato, 1980) are shown. Finally, we find the work of (Karapantsions et al., 1989; Karapantsios & Karabelas, 1995) using parallel-wires probes. In contrast, the rest of the works use optical methods such as (Karimi and Kawaji, 1998) using the photo-chromic dye tracer technique, (Charogiannis et al., 2019; Cherdantsev et al., 2019; Zadrazil et al., 2012) using different subtypes of the laser induces fluorescence methodology (LIF).

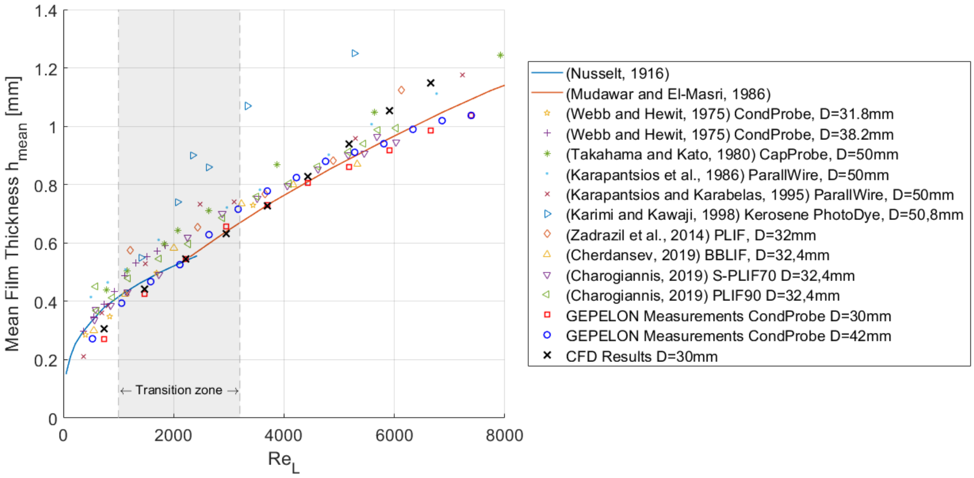

Source: (Rivera et al., 2021)

Figure 5.6. Comparison between experimental measurements from different authors, correlations and CFD results. Red squares and blue cycles represent the experimental measurements while the black crosses correspond to the CFD predictions.

CFD predictions obtained for free fall are within the expected range with little noticeable differences with the rest of the experimental measurements. However, a much more linear trend than expected is observed and the differences with the experimental measurements tend to increase as we approach the larger liquid Reynolds numbers.

In addition to free-fall simulations, cocurrent annular flow calculations have also been carried out. Experimental measurements cover a wider range of air flow rates than the one explored by means of CFD simulations. The CFD results have been compared with the experimental measurements obtained in the GEPELON facility (Figura 5.7). Code predictions are good for the free-fall scenario previously analyzed. However, as the air flow rate increases, the behavior of the code does not correctly reflect the experimental measurements. The liquid film drop obtained in the code predictions is lower than that obtained in the installation. Better results are expected to be obtained if the simulations are performed in transient by extracting the average parameters through film statistics. Part of the diffusion obtained at the interface is probably attributed to interfacial waves that would be observed in a transient. Therefore, future work will be aligned with performing transient simulations applying advanced turbulence models such as LES, DES or SAS.

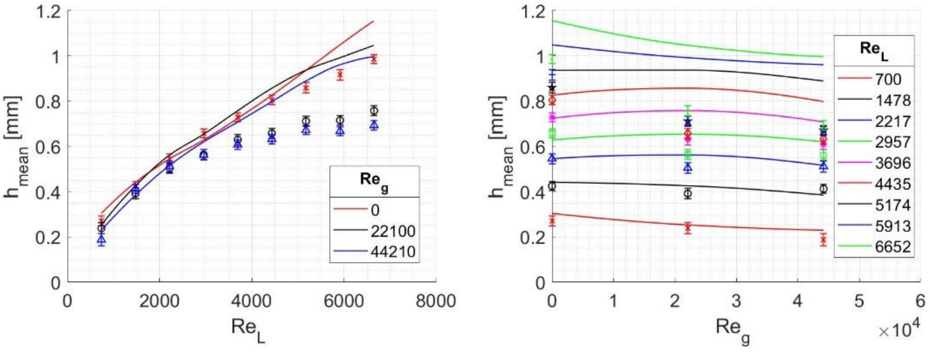

(a) (b)

Source: (Rivera et al., 2021)

Figure 5.7. Comparison between experimental measurements and CFD results for downward co-current annular flow. (a) Mean film thickness vs Re_L; (b) Mean film thickness vs Re_g.

5.4. UNCERTAINTY QUANTIFICATION APPLIED TO ANNULAR FLOW SIMULATIONS

The uncertainty quantification in CFD codes is very important to determine the results sensitivity to the uncertain parameters of our model. In Chapter 1 of this thesis an extensive explanation of the different sources of uncertainty affecting simulation results is given. Likewise, the different methods of uncertainty quantification are identified, among which is the subrogated method of Polynomial Chaos Expansion propagation.

The advances made in the development of this method for its use in CFD codes for uncertainty analysis in nuclear reactor safety simulations have been described in Chapter 4. The main objective of this section is therefore to apply this methodology to CFD simulations of the annular flow. This research is in progress during the writing of the thesis so the last results obtained are shown below.

The Polynomial Chaos Expansion method is optimal for obtaining the uncertainty when there is a predominant source of uncertainty. This is because the number of simulations required is very low initially and grows exponentially with the number of uncertain variables. As discussed previously, there are multiple sources of uncertainty in annular flow CFD calculations. However, to get the most out of the PCE methodology, it is important to select the most relevant ones. For this research, the inlet velocity has been selected as the most impactful uncertain parameter. The inlet velocity depends directly on the flow rate, so several samples have been taken in the laboratory to determine its probability distribution.

The process was carried out by obtaining the water flow rate by collecting and weighing the water flow through the installation for 1 minute. This procedure has been repeated by restarting the installation from standstill each time and waiting 3 minutes at each interval to let it reach the stationary operating point. The probability function of the inflow follows a normal with an average standard deviation of $0.14\ l/min$.

For the estimation of the uncertainty in the cases of annular flow in vertical free fall by Polynomial Chaos Expansion the 5th order Hermite polynomials have been used. Therefore, for each liquid flow rate, 5 different simulations are performed. Due to the high computational cost of the simulations, five liquid flow rates were selected covering the same range as the experiment from 1 to $9\ l/min$. The corresponding Reynolds numbers are 700, 2220, 3700, 5200 and 6600. The total number of simulations performed to obtain the uncertainty in this range was 25. Table 5.1 shows a summary of the values included in each simulation based on the roots of the 5th order Hermite polynomials.

Table 5.1. Summary list of the 5th order Hermite polynomials roots and weights as well as its corresponding water flow rate.

5th-order Hermite polynomial roots and weights					
Roots	-2,0202	-0,9586	0	0,9586	2,0202
Weights	0,001993	0,393619	0,945308	0,393619	0,001993
Water flow rates [l/min]					
1 l/min	0,60	0,81	1,00	1,19	1,40
3 l/min	2,60	2,81	3,00	3,19	3,40
5 l/min	4,60	4,81	5,00	5,19	5,40
7 l/min	6,60	6,81	7,00	7,19	7,40
9 l/min	8,60	8,81	9,00	9,19	9,40

The procedure followed has been described in detail in Chapter 4 and the post-processing was performed using the Matlab® algorithm developed for the simulations in that publication. First, the 25 simulations were carried out for the inlet flow rates in the table above. The three-dimensional model used is the same as the one described in the previous section, as well as the processing of the data to obtain the liquid film thickness. As a result of this simulation phase, the following result matrix (R) is obtained, where the columns correspond to each flow rate.

$$R = \begin{pmatrix} 0.251 & 0.521 & 0.722 & 0.907 & 1.067 \\ 0.304 & 0.543 & 0.743 & 0.925 & 1.083 \\ 0.306 & 0.559 & 0.760 & 0.933 & 1.100 \\ 0.333 & 0.579 & 0.776 & 0.950 & 1.121 \\ 0.367 & 0.604 & 0.795 & 0.970 & 1.142 \end{pmatrix} \tag{5.3}$$

From these results we can obtain the uncertainty by applying the Polynomial Chaos Expansion and solving the integral by Gaussian-Hermite quadrature. This method allows us to obtain the alpha coefficients α_n of the subrogate model polynomials. Then, using α_n, it is possible to calculate the mean and standard deviation of the results. For this case, the mean obtained is as follows.

$$\mu = \begin{pmatrix} 0.312 & 0.560 & 0.760 & 0.935 & 1.101 \end{pmatrix} \tag{5.4}$$

Figure 5.8 shows the comparison between code predictions and experimental measurements for mean free-fall film thickness. The experimental error is represented by bars at each measurement point and was obtained as shown in Chapter 2. This error has been calculated taking into account the sources of accidental error as well as the systematic error. The uncertainty of the code as a consequence of the uncertain input variable considered is shown by red shading, being the central line the mean obtained.

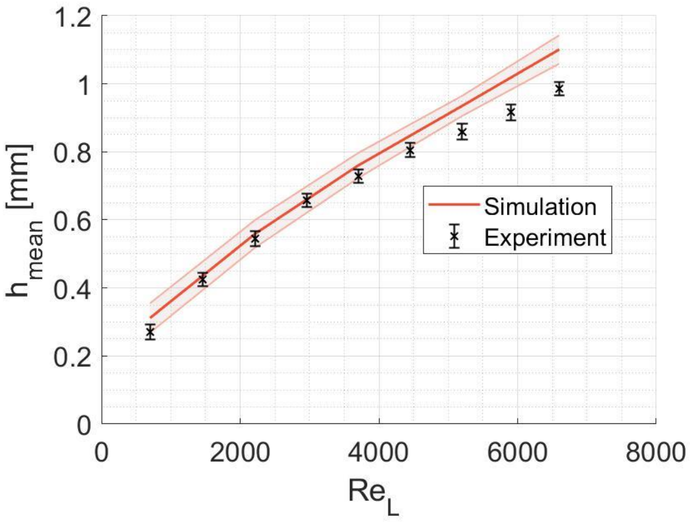

Source: Author's design

Figure 5.8. Average film thickness obtained experimentally and in CFD simulations. The shaded area corresponds to the uncertainty of the predictions and the bars to the experimental error.

It can be seen that the band covers a thickness of approximately $0.1\ mm$ which remains relatively constant over the entire range. The great importance of uncertainty quantification in simulations lies precisely in this, it is important to consider the margins of variability of the code prediction. Generally speaking, it is considered that the simulation predicts the real phenomenon when both regions (uncertainty for the simulation and error for the measurement) overlap. In this case it can be observed that this happens for values lower than $Re_L < 5000$. However, above this value the simulation overpredicts the thickness value. As mentioned in the previous section, it would be advisable to perform the simulations in transient regime and obtain the average value of the liquid film. Transient simulations ensure less diffusion of the interface by tracking possible interfacial waves. Instead, steady-state simulations capture this behavior as a probability of finding a region where waves could be found in that zone. This results in a wider and more inaccurate gap fraction band between 0 and 1.

The biggest problem with transient simulations is that the simulation time increases in ranges of an order of magnitude. Even using highly optimized uncertainty quantization methods, such as Polynomial Chaos Expansion by Gaussian Quadrature, the computational time is very large. To obtain the uncertainty of the film thickness for 5 input values with a single uncertain variable alone requires 25 simulations. Depending on the simulation requirements, this can result in very long or unaffordable computational times. However, the breakthrough in the development of new and more powerful processors as well as access to supercomputing centers is favoring the development of the uncertainty quantification field.

5.5. REFERENCES

Canonsburg, T. D. (2009). *ANSYS CFX-Solver Modeling Guide*. *15317*(April), 724–746.

Charogiannis, A., Sik An, J., Voulgaropoulos, V., & Markides, C. N. (2019). Structured planar laser-induced fluorescence (S-PLIF) for the accurate identification of interfaces in multiphase flows. *International Journal of Multiphase Flow*, *118*, 193–204. https://doi.org/10.1016/j.ijmultiphaseflow.2019.06.002

Cherdantsev, A. V., An, J. S., Charogiannis, A., & Markides, C. N. (2019). Simultaneous application of two laser-induced fluorescence approaches for film thickness measurements in annular gas-liquid flows. *International Journal of Multiphase Flow*, *119*, 237–258. https://doi.org/10.1016/j.ijmultiphaseflow.2019.07.013

Dai, Y., Dakshinammorthy, D., & Agrawal, M. (2013). *CFD Modeling of Bubbly, Slug and Annular Flow Regimes in Vertical Pipelines*. https://doi.org/10.4043/24245-ms

Ghosh, S., Das, G., & Das, P. K. (2010). Simulation of core annular downflow through CFD-A comprehensive study. *Chemical Engineering and Processing: Process Intensification*, *49*(11), 1222–1228. https://doi.org/10.1016/j.cep.2010.09.007

Karapantsions, T. D., Paras, S. V., & Karabelas, A. J. (1989). Statistical Characteristics of Free Falling Films at High Reynolds Numbers. *International Journal of Multiphase Flow*, *15*(1), 1–21.

Karapantsios, T. D., & Karabelas, A. J. (1995). Longitudinal Characteristics of Wavy Falling Films. *International Journal of Multiphase Flow*, *21*(1), 119–127.

Liu, Y., Li, W. Z., & Quan, S. L. (2011). A self-standing two-fluid CFD model for vertical upward two-phase annular flow. *Nuclear Engineering and Design*, *241*(5), 1636–1642. https://doi.org/10.1016/J.NUCENGDES.2011.01.037

Mudawwar, I. A., & El-Masri, M. A. (1986). Momentum and heat transfer across freely-falling turbulent liquid films. *International Journal of Multiphase Flow*, *12*(5), 771–790. https://doi.org/10.1016/0301-9322(86)90051-0

Nusselt, W. (1916). Die oberflächenkondensation des wasserdampfes. *Zeitschrift Des Vereines Dtsch. Ingenieure*, *60*, 541-546 (n^{o}27) and 569-575 (n^o 28).

Rivera, Y., Berna, C., Muñoz-Cobo, J. L., Escrivá, A., & Córdova, Y. (2022). Experiments in Free Falling and Downward Cocurrent Annular Flows – Characterization of Liquid Films and Interfacial Waves. *Nuclear Engineering and Design*, *382*, 111769. https://doi.org/doi.org/10.1016/j.nucengdes.2022.111769

Rivera, Y., Muñoz-Cobo, J. L., Escrivá, A., Berna, C., & Córdova, Y. (2021). Experimental Measurements and CFD Results of Liquid Film Thickness in Vertical Downward Air – Water Annular Flow. *International Journal of Computational Methods and Experimental Measurements*, *10*(2), 93–103. https://doi.org/10.2495/CMEM-V0-N0-1-11

S. Dominguez, D., M. Iglesias, S., Muñoz-cobo, J. L., Escrivá, A., Berna, C., & Rivera, Y. (2019). Modelo Analítico Aplicado al Problema de Onda Solitaria en Películas de Agua Gobernadas por Gravedad en Tuberías Verticales. *45 Reunión Anual de La Sociedad Nuclear Española*, 25–27.

Smith, B. L. (PSI), Bieder, U. (CEA), Grafard, E. (IRSN), Heitsch, M. (GRS), Henriksson, M. (Vattenfall), Höhne, T. (FZD), Komen, E. (NRG), Mahaffy, J. (PSU), Moretti, F. (UPisa), Morii, T. (JNES), Mühlbauer, P. (NRI), Rohde, U. (FZD), Scheuerer, M. (GRS), Song, C.-H. (KAERI), & Zigh, G. (USNRC). (2008). Assessment of Computational Fluid Dynamics (CFD) for Nuclear Reactor Safety Problems. In *NEA/CSNI/R(2007)13* (Vol. 33, Issue January).

Takahama, H., & Kato, S. (1980). Longitudinal Flow Characteristics of Vertically Falling Liquid Films Without Concurrent Gas Flow. *Int. J. Multiphase Flow*, *6*, 203–215.

Webb, D. R., & Hewitt, G. F. (1975). Downwards co-current annular flow. *International Journal of Multiphase Flow*, *2*(1), 35–49. https://doi.org/10.1016/0301-9322(75)90027-0

Zadrazil, I., Markides, C. N., Matar, O. K., Náraigh, L., & Hewitt, G. F. (2012). Characterisation of downwards co-current gas-liquid annular flows. *Proceedings of the International Symposium on Turbulence, Heat and Mass*

Transfer, *2012-Septe*, 753–764. https://doi.org/10.1615/ICHMT.2012.ProcSevIntSympTurbHeatTransfPal.820

Chapter 6

GENERAL DISCUSSION, CONCLUSIONS AND FUTURE WORK

6.1. INTRODUCTION

This chapter presents the general discussion of the results obtained in this PhD thesis. A particular discussion is carried out in each of the publications, however the aim of this chapter is to group all of them together to give an overview of the results obtained.

This thesis is framed within the project Experimentación y Modelación de Procesos de Transferencia de Energía y Cambio de Fase y Ondas Superficiales en Sistemas Energéticos Convencionales y Nucleares (Experimental and Modeling of Energy Transfer and Phase Change Processes and Surface Waves in Conventional and Nuclear Energy Systems). This project was approved and funded by the Spanish Ministry of Economy, Industry and Competitiveness with the objective of studying liquid film systems through Experimental and modelling. These types of systems are found in multiple industrial applications including the nuclear energy industry. A good knowledge of the liquid film promotes the good performance of heat transfer processes under these conditions especially due to the surface waves found at the interface. Furthermore, in systems where gravity represents the driving force of the liquid film it is of great interest to know the passive character of the system for plant safety situations.

To develop the project it was proposed to perform a series of separate effects experiments dedicated to understand the nature of these systems and the physical phenomenology. To achieve these goals, it was decided to design and build a versatile experimental facility capable of generating different air-water annular flow conditions. Additionally, the design of computational tools based on CFD methods for the study of thin liquid films was proposed. This thesis shows the main findings and results obtained, although further studies derived from this research are expected.

In addition, the need to develop CFD models for this project and the increasing requirements in terms of their uncertainty, promoted parallel studies for the development of the methodology. Therefore, simultaneously to the research of the experimental part of the project, several institutions around the world including us collaborated in the development of benchmarks in CFD simulations for nuclear reactor safety. This collaboration allowed the development of the Polynomial Chaos Expansion uncertainty quantification method, which was later applied in simulations of the experimental facility.

The organization of the international benchmarks was done by the OECD/NEA as part of the working group WGAMA (Working Group on Analysis and Management of Accidents). It is very important to mention that as a consequence of the participation in these benchmarks a valuable bidirectional exchange of information was promoted regarding the proper use of CFD codes as well as the development of uncertainty quantification tools. The main pillars of this collaboration focused on the development of best practice guidelines (BPGs) in the use of CFD, the development of methods for uncertainty analysis of their predictions, the enhancement of CFD-grade experimental material and the promotion of the use of multiphase CFD modeling.

The PhD thesis has been structured in six chapters in which this research is discussed in detail. The whole document is presented as a journey from the most basic concepts of annular flow and liquid film, through the experimental findings and ending with the simulation tools predictions.

Chapter 1 corresponds to the introduction of the thesis. This section represents one of the most important parts since it contains the main motivation of the work as well as an extensive compilation of the state of the art. It is designed to introduce from the most basic concepts and ideas related to annular flow to the most advanced methods for experimental measuring and simulation. The importance of the annular flow regime is described in detail and its significance in terms of nuclear reactor safety is discussed.

Prior to the literature review, the most important features of annular flow are introduced. In particular, the behavior of the liquid film is analyzed explaining why it is so important in industrial facilities. Its wave nature is described and the most important properties that have interested researchers worldwide over the last decades are justified.

To measure this liquid film behavior, different techniques are available. Therefore, the introductory chapter also includes an extensive literature review of these techniques. The different methodologies have different advantages and disadvantages which are discussed throughout this section. In order to facilitate the understanding of each technique, especially the more complex ones, 3D diagrams of each technique have been generated including graphically the measurement principle of each technique. The techniques have been categorized mainly according to their spatial and temporal resolution as well as the principle of operation. In general, the importance of electrical and optical methods is emphasized, although other types of methodologies such as acoustics or X-ray absorption have been considered.

Most experimental annular flow research facilities have some common features. In order to develop a facility of this characteristics it is very important to know all the peculiarities and problems that have concerned the scientific community in similar studies. For this reason, the different experimental facilities related to annular flow have been analyzed in depth. Each of them has been characterized by the type of flow regime on which they have been focused, the measurement range and the technique employed to measure the liquid film. In order to dimension the GEPELON experimental installation, a large number of characteristics have been taken into account, such as the operating range, the knowledge gaps, or the requirements to make the installation versatile with minimum adjustments.

As previously mentioned, the ability to simulate this type of flow using CFD codes was another of the initial objectives of this project. Therefore, the introduction also includes a chapter dedicated to the use of CFD. Initially, the fundamental Navier-Stokes equations governing fluid motion are described. A summary has been made that aims not only to present the equations but also to explain how to proceed with them to obtain the format used by the simulation codes.

One of the most important pillars in the use of these equations is the turbulence model. Therefore, an explanation of each of the categories into which these models are grouped is also presented in this section. The most important equations of the RANS (Reynolds-Average Navier-Stokes) and LES (Large Eddy Simulations) turbulence models have been included because of their importance when planning a CFD simulation.

Next, it is analyzed how to simulate a multiphase phenomenon like the annular flow. As it includes two different phases it is necessary to know the techniques used by the codes to deal with this problem so the euler-euler and lagrangian-euler methods have been briefly described. Multiple mentions of how other authors have proceeded to successfully simulate annular flow are also included.

The last section of the introduction is completely dedicated to the treatment of uncertainty in CFD codes. This section is especially important when considering simulations in the field of nuclear safety where the margins are very tight. Although CFD codes are still a developing tool in this field, it is important to make an effort by the whole scientific community to obtain more and more robust tools.

This section first discusses the sources of uncertainty in CFD codes and shows a summary of the most important ones to be taken into account in annular flow simulations. Finally, the different uncertainty quantification methods available and the characteristics of each of them are presented.

6.2. GENERAL DISCUSSION OF THE RESULTS

Second and third chapter correspond to the publications directly related to the GEPELON experimental setup. This facility was designed to study the different annular flow sub-regimes. All the details related to the characteristics of the facility are shown in both papers as well as the peculiarities of each configuration. Of particular interest is the injection approach of the different phases in the test section. The methodology is shown in detail in section 1.4 Experimental Facilities and consists of using a sintered porous pipe to recreate the liquid film inlet. The porous pipe acts as a material that allows water to pass through when exposed to a pressure gradient. In this way, water enters the main pipe of the facility close to the wall in the position where it is expected to be found in developed flow conditions. This allows first of all a reduction of the dimensions of the test section by initially favoring the position of the water. Secondly, it allows a very good control of the liquid flow by not altering the initial velocity as it happens with other injection methodologies.

In addition, both studies use conductance probes as the main measurement system. These conductance probes have been developed from scratch in the laboratory including manufacturing, electronics, calibration system and testing. This process was presented before journal publications in different conferences obtaining in the Annual Meeting of the Spanish Nuclear Society of 2017 the award for best paper-poster.

Chapter 2, in particular, studies the liquid film under free-fall and downward cocurrent flow conditions. The use of conductance probes to measure the time evolution of the liquid film allows to analyze variables of the liquid film such as the mean thickness, the height of the disturbance waves or the frequency of the disturbance waves. These variables have been studied in detail as a function of liquid and gas Reynolds numbers in the range of $800 - 8500$ and $0 - 110000$ respectively. The liquid film thickness increases with liquid flow rate while it decreases with air flow rate. However, for the wave properties of the film a transition point is observed around $2 \cdot 10^4 - 4 \cdot 10^4$ gas Reynolds numbers. At this point a maximum in wave height and a minimum in wave frequency are observed.

There are four fundamental aspects that make this paper particularly relevant. Firstly, all the measurements are post-processed to obtain empirical correlations that allow predicting the value that these variables will take from the input data. This means that any researcher in the world can obtain an estimate of what the film characteristics would be for the type of facility they wish to build within the range. Secondly, the study includes a comparison between different pipelines allowing to identify the relationship between duct diameter and film characteristics.

Thirdly, measurements have been made at different lengths of the inlet in the so-called "undeveloped" zone. This zone is not normally explored by researchers as its conditions are not maintained over time. However, this region allows a better understanding of how the film thickness evolves and how surface waves are formed and developed. Finally, there is an important finding related to the transition between low air velocities and high velocities. This causes a behavioral change in wave height and frequency that is reflected in a change of downward annular flow subregime. The confirmation of this behavior establishes a future line of research related to the analysis by this or other methodologies of the phenomenology occurring in this Reynolds number region of the gas.

Chapter 3 focuses on upward cocurrent annular flow measurements. This flow is one of the most important in the nuclear sector since it is the one observed during the normal operation of boiling water reactors (BWR). Therefore, it is also one of the most studied by the scientific community. For that reason, in this research it was decided to consider a very important variable in the interfacial behavior, the surface tension. Its effect is decisive since surface tension represents the "interface resistance" to superficial variations, which directly affects the ability of the waves to alter their size. In addition, the high gas velocities required for annular upward flow to occur cause liquid to be released from the film to travel as droplets with the gas. This effect, known as entrainment, is enhanced when the surface tension decreases.

Furthermore, the surface tension of water in contact with air decreases with temperature. Therefore, changes in surface tension will have an effect that can be related to increasing its temperature. It should be noted that temperature also affects viscosity and density although its impact on is much weaker. To produce the surface tension variation, small amounts of 1-butanol were added to the water. This product is a surfactant that has an affinity to be located close to free surfaces. The reason for this behavior is the molecular structure of 1-butanol which is hydrophobic and causes it to be located in the interfacial position. This is why small amounts of it significantly alter the surface tension which is an interfacial property.

In this paper we therefore analyzed the effect of surface tension on the behavior of the film in the range of $72 \cdot 10^{-3}\ N/m$ to $45 \cdot 10^{-3}\ N/m$, being the first value the equivalent to that of water at room temperature. In addition, the experimental range covered a wide number of liquid and gas flow rates. However, for the gas drag force to be large enough to produce upward movement of the film, the gas velocity is required to be correspondingly high. For that reason, the range of surface air velocities starts at around $22\ m/$s, which is equivalent to approximately 60000 Reynolds number for this facility. The maximum Reynolds number of the gas analyzed in this investigation was 103000, corresponding to a surface velocity of almost $39\ m/s$. The range of liquid flow rates also had to be reduced since for very small flow rates it was detected that the film was not adequately developed in the measurement zone. For this purpose, the pressure drop in the area of interest was analyzed so that only flow rates where the pressure drop remained constant along the measuring section were taken into account. The range of liquid Reynolds numbers was from 2000 to 6000 or, in terms of surface velocity, from 0.044 to $0.11\ m/s$. A series of 49 cases were analyzed for each surface tension, resulting in a total of almost 200 cases.

The variables analyzed were the mean film thickness, the height and frequency of the disturbance waves as well as the height of the unperturbed film and the height of the ripple waves. Following the same procedure as in the publication of chapter 2, data of the temporal evolution of the film thickness were obtained using a conductance probe.

The main results obtained show that almost all the film variables decrease when the surface tension decreases. This supports the initial hypothesis that the reduction of this interfacial variable enhanced the entrainment of liquid from the film to the air stream in the form of small drag droplets. However, not all film characteristics are altered in the same way. The Kapitza number relates surface forces to gravitational forces so it was the dimensionless number used to include surface tension in the correlations. In general terms, the exponent which Kapitza's number takes gives insights into how much the surface tension affects each variable. For example, in the case of the height of the disturbance waves the exponent is 1.12 which translates into a strong dependence on surface tension. However, for the mean film thickness or the disturbance wave frequency the exponent is much lower at 0.78 and 0.46 respectively. In relation to the effect of water and air velocity the behavior is similar to the one observed in the downward cocurrent flow, where the main variables increase with liquid velocity and decrease with gas velocity.

This research has been very valuable and the paper has been very well received by the scientific community. The detailed study of the analyzed properties of the liquid film as well as the addition of the surface tension as an experimental condition have been of great relevance. In addition, this research includes a detailed analysis of the sources of systematic and random errors that give an added value to the results.

The following chapters focus on fluid simulation using CFD codes. **Chapter 4** describes the Polynomial Chaos Expansion methodology for uncertainty quantification. To demonstrate its application, we participated in an OECD/NEA benchmark where multiple organizations from all over the world presented their ideas of uncertainty quantification applied to a case study. The CFD simulations were done based on an experimental CFD-grade facility on mixing of two water flow streams with different density. The experiment was carried out by Texas

A&M University and represented in a simplified format the injection of cold-water from the accumulators through a cold leg into the downcomer.

The commercial software ANSYS CFX was used to carry out the simulations and ICEM CFD was used to generate the mesh. In order to follow a rigorous simulation process, multiple analyses were carried out, such as the mesh sensitivity study or the impact comparison of the different turbulence models. The turbulence model finally used was LES Smagorinsky after analyzing its application together with the LES WALE and LES Dynamic models.

The central part of this research was the Polynomial Chaos Expansion uncertainty quantification method. This technique is based on the relationship between the system response and a linear combination of a defined orthogonal polynomial basis. These polynomials depend on the probability distribution function of the uncertain variables that affects the system response. The relationship between the polynomials and the system response is accompanied by a series of $\propto_i$ coefficients or expansion coefficients. The main target of the methodology is to solve the PCE to obtain these $\propto_i$ values that will allow to know the mean and variance of the system response, and subsequently the uncertainty.

An uncertain variable, the difference in densities between the fluids in the experiment, was used for the benchmark. The researchers at the experimental facility provided the input uncertainty in the measurement of the densities using a normal distribution of known mean and variance. Hermite polynomials are used for this type of distribution probability functions. After developing the methodology, part of the process involves solving a specific integral. This integral can be solved by Gauss quadrature. The Gauss quadrature consists of a weighted sum of the corresponding function at certain points determined by the polynomial basis. These points correspond to the roots of the polynomials of degree n. For this case the Hermite polynomials of degree 5 where selected, whose values are known. The degree of the polynomials is chosen by the user, although the higher the degree, the more simulations will be necessary.

The results obtained in the cold leg section of the benchmark case, for both the open and blind tests, were very satisfactory. In some occasions the maximum velocities reached by the higher density fluid were overpredicted. Larger discrepancies were obtained in the downcomer zone, where the profile shape was not obtained correctly. The simulation predicted an increase in velocity in the inner part of the downcomer that did not correspond to the experimental result. This unexpected behavior most probably happened due to an underprediction of the turbulence along the long cold leg until reaching the downcomer.

In summary, the paper presented in this chapter was a relevant contribution to the development of uncertainty quantification methods in CFD simulation. The ability to estimate the uncertainty of the system response to uncertain parameters is one of the main objectives of researchers in the field of nuclear reactor safety. It is expected that upcoming OECD/NEA benchmarks will continue to promote the further development of these methodologies.

The following section corresponds to **Chapter 5** where the CFD simulations performed on annular flow are described. Throughout this section, the best practices to simulate this type of systems are described in detail, the three-dimensional modeling of the GEPELON experimental facility is shown and finally the application of the Polynomial Chaos Expansion uncertainty quantification method is described. The best practice guidelines included in this chapter are the result of an extensive study carried out during the preparation of the thesis. Many of the statements are postulated based on the ANSYS modeling guidelines, although they have been complemented with our own experience during the development of the simulations.

Section 5.3 is based on the paper Experimental Measurements and CFD Results of Liquid Film Thickness in Vertical Downward Air-Water Annular Flow, although it has focused solely on CFD modeling. The information regarding the development of the model setup has been greatly expanded to include all the necessary details to ensure the replicability of the simulation. The results obtained for downward annular flow in free fall have been compared with a large database of other researchers. The simulation predictions are really good for free-fall, although they show a more linear behavior than expected. The steady-state simulation is not able to correctly predict the behavior of the mean film thickness when introducing higher air flow rates,. Although a decrease of the film thickness with the air Reynolds number is generally observed, this reduction is much smaller than the one obtained experimentally.

The final part of the chapter focuses on the application of the PCE method to simulations of downward annular flow in free fall conditions. Following the procedure described in Chapter 4, the inlet liquid flow rate was used as an uncertain variable. Five simulations were performed for each experimental condition studied. The total number of simulations was 25 since five Reynolds numbers of the liquid were studied, covering a range from 700 to 6600. After applying the PCE methodology it is observed that a standard deviation of $0.14\ l/min$ in the inlet flow rate causes an uncertainty in the average film thickness of approximately $100\ \mu m$.

6.3. GENERAL CONCLUSIONS OF THE THESIS

This section presents the most important conclusions of the doctoral thesis. However, first of all, it is necessary to explain the fulfillment degree of the proposed objectives.

6.3.1. GOALS FULFILLMENT

The first objective that was proposed and that represents the central part of this PhD thesis was *The study of surface waves in air-water annular flow regime experimentally and by means of CFD simulation. Generation of a film thickness database for the following types of annular flow: downward free-fall, cocurrent with vertical drag and downward cocurrent*. This objective has been successfully completed and three articles derived from this part of the thesis have been published. In addition, the initial scope was slightly widened since during the research related to the upward annular flow it was decided to include surface tension as an experimental condition. The CFD simulation part of this objective has been analyzed in detail and the results have been compared with experimental laboratory measurements.

The second objective that was defined was *Development of conductivity sensors for precise measurement of liquid film thicknesses. Study of the size and separation of the electrodes to obtain an optimum sensitivity between 1 and 3 mm thickness. Design and construction of the electronic circuit to amplify and rectify the sensor signal in the range 1-10V. Calibration of the probes to work with the conductivity of the treated water in the laboratory*. This goal had to be completed during the first stage of the thesis as it was a "sine qua non" condition. In other words, in order to carry out the liquid film study it was necessary to have an accurate measuring system specifically designed for the experimental facility. The design process of this system had to include multiple stages such as the manufacture of the probes, the design of the electronic circuit, the calibration methodology and instrumentation or its commissioning. Although there is multiple documentation related to the operation of conductance probes, it was proposed to design a specific system for this facility with calibration capability for each particular sensor and without dependence on specific external partners. Information about all the details of this system has been included in the different publications that compose this thesis as well as multiple participations in conferences allowing to detect both the strong points of this system and its limitations.

The third and last objective proposed was *Uncertainty quantification and new development methods for the determination of uncertainties in calculations with CFD codes. Study of the Polynomial Chaos Expansion method by means of different techniques such as Gauss Quadrature or Collocation Points*. Initially this section was proposed without a clear methodology of study but after an in-depth analysis of the literature it was decided to focus the analysis on the Polynomial Chaos Expansion (PCE). This methodology is included within the category known as propagation methods by means of subrogated models. Its application for uncertainty quantification in CFD codes is underdeveloped. To enrich the study of the PCE, I actively participated in the OECD/NEA international benchmarks where it was possible to share different perspectives of each methodology for uncertainty quantification. This objective was concluded with the publication of the paper that forms chapter 4, which allows the transfer of knowledge in terms of both CFD modeling and PCE methodology. In addition, although it was not initially planned, to finalize the dissertation the same PCE methodology was applied to the annular flow CFD simulations.

6.3.2. GLOBAL CONCLUSIONS

To summarize the most important conclusions, it is convenient to divide the research carried out in two groups. The first one corresponds to the experimental part while the second one would be focused on the simulation by means of CFD codes. In addition, this dissertation consists of a compendium of different articles with their own identity, so it is necessary to draw general conclusions in order to give the thesis a global perspective.

In relation to the experimental part, an experimental facility has been designed and built in the Thermohydraulic Laboratory of the Institute for Energy Engineering at the Universitat Politècnica de València. This experimental facility was developed with the aim of researching the behavior of the liquid film in an annular flow system for multiple experimental conditions.

- The experimental setup consists of two main circuits, one for water and one for air, which feed the main pipe or test section, where the measurements were performed. The intended design of the facility allowed the generation of different annular flow regimes including free-fall, downward cocurrent flow and upward cocurrent flow. Countercurrent annular flow was left out of the scope of the measurements due to limitations in the space required to develop both fluids in the test section.
- During the development phase of the mock-up, the system for measuring the time evolution of the liquid film thickness by means of conductance probes was designed. It was observed that to obtain an acceptable measurement range to capture the wave behavior of the liquid film, electrodes of 1.5mm internal diameter with a separation of 1.5mm were necessary. The electronic circuit includes four parts consisting of two amplifiers, a rectifier and a signal filter. The variable current flowing between the electrodes depending on the liquid thickness needed to be correlated by a calibration system. For this purpose, dielectric cylinders of different diameters were used to generate a water ring of known thickness. Finally, a signal acquisition system with a sampling frequency of $5000 Hz$ was designed.
- Conductivity is essential to ensure the correct operation of the designed probes, so a system was implemented to detect possible changes in conductivity. By means of an algorithm it was possible to adjust the calibration curves depending on the changes in the saturation voltage of the probes.

- The range of different experimental conditions was planned to cover a wide range of possibilities. Therefore, for downward annular flow this range was $800 - 8500$ and $0 - 110000$ for liquid and gas Reynolds numbers respectively. In the case of upward annular flow, it should be noted that the velocities must meet certain requirements to ensure film drag. Hence, the final measurement range was $2000 - 6000$ for the liquid Reynolds number and $60000 - 103000$ for the gas Reynolds number. For the upward annular flow configuration, surface tension was also studied as an experimental condition. This was accomplished by adding small amounts of 1-butanol, a substance that varies the surface tension of water with minimal impact on its viscosity and density due to its hydrophobic properties. The experimental range of this variable was from $0.045 - 0.072\ N/m$.
- The most important liquid film variables that can be studied using this measurement system are the average film thickness, the height and frequency of disturbance waves, the height of ripple waves and the unperturbed base film thickness. Other variables such as wave velocity cannot be measured with this system since it consists of a single set of electrodes.
- A detailed study of the sources of systematic and random error affecting the measurements was carried out. The systematic error was obtained by propagating the errors in the measurement system of the acquisition card, the calibration curve fitting error and the positioning error of the calibration dielectric cylinders. The accidental error was analyzed by repeating the experiments in 6 sets. The total average errors obtained were about $30\ \mu m$ um for the average thickness, $60\ \mu m$ for the height of the disturbance waves, $0.5\ Hz$ for their frequency, $20\ \mu m$ for the unperturbed base film thickness.
- Overall conclusions can be drawn common to the three configurations studied (free fall, downward cocurrent flow and upward cocurrent flow). The most straightforward conclusion is that the liquid film thickness increases with water flow. In contrast, for all scenarios, increasing air velocity causes the mean liquid film thickness to decrease as more interfacial drag occurs.
- In relation to the wave behavior of the film, a distinction is made between disturbance waves and ripple waves. The former correspond to coherent waves that grow and travel along the entire flow while the latter are small non-coherent waves of low amplitude that appear and disappear continuously. These ripple waves are much more noticeable in the upward annular flow since the liquid-gas interaction is much more important and the gravity force opposes the movement of the liquid.
- For all configurations, the height of the disturbance waves and their frequency increases with the liquid flow rate. However, with gas flow it is

necessary to distinguish between downward and upward flow behavior. For upward flow, the frequency tends to increase or remain almost constant. However, for downward flow, an inflexion point is observed around $20000 - 40000$ Reynolds number of the gas. Up to this zone, the wave height increases and then decreases. The opposite effect is observed for the frequency which decreases and then increases substantially. For the upward annular flow study, the ripple wave height was also analyzed observing small variations with liquid flow rate and a slight decrease with gas flow rate.

- The surface tension affects the liquid film since a decrease in its value enhances the detachment of droplets on the surface, increases entrainment and affects the thickness of both the film and its waves. It has been experimentally observed that the decrease in surface tension produces a generalized decrease in all variables including the frequency of the waves. The variable most affected by the surface tension was the height of the disturbance waves since it is the parameter most exposed to the drag produced by the gas.
- Multiple correlations have been formulated for each of the variables described in terms of dimensionless numbers. For the mean film thickness and average wave heights, the Reynolds numbers of the liquid and gas have been used. For the frequency, in addition to these, the Strouhal number was considered. Finally, for the variables studied as a function of surface tension, the dimensionless Kapitza number was used. All correlations were compared with experimental values of other authors and other correlations were analyzed together, if available.
- The correlations of mean film height and disturbance wave height show good prediction when compared to experimental values of other authors. However, the variable that presents more scattering is the frequency of the waves where much more diverse values are observed. This may be due to the wave detection algorithm or to the fact that some authors do not distinguish between different types of waves.
- Finally, it should be mentioned that this research is the only one in which all the correlations generated for downward annular flow have been obtained with test section measurements of different diameters. In addition, this study includes measurements of the liquid film in the development zone where it is possible to observe how the different variables of the liquid film evolve. The degree of development has also been included as an additional term in the correlation of the mean film thickness.

Focusing on the CFD part, a methodology for uncertainty quantification by propagation has been developed and applied to two case studies. The first one is related to the mixing of fluids of different density included in an international benchmark organized by the OECD/NEA and related to nuclear reactor safety.

The second one corresponds to the GEPELON experimental facility, where the measurements of this thesis have been carried out.

- The sources of uncertainty are multiple and diverse, such as possible measurement errors of experimental conditions, model simplifications, or discretization errors. Although most of these affect the predictions of the codes, in many cases they cannot be easily estimated.
- There are multiple methodologies for the uncertainty quantification in CFD simulations. They are generally divided into propagation methods and extrapolation methods. Although some of these techniques have been studied for other situations, in the case of CFD codes they are still in an early state of maturity. The uncertainty quantification in CFD simulations is complex as they are very demanding in computational terms.
- Polynomial Chaos Expansion (PCE) method belongs to the group of propagation methodologies using a subrogated model. It is based on the projection of the system response on an orthogonal basis of polynomials and, if resolved using Gauss quadrature, it is characterized by being very efficient when the number of uncertain variables is reduced. Therefore, if the main uncertainty source is determined, it is possible to estimate the uncertainty of the result in an optimized way.
- The orthogonal polynomials used to obtain the system response in PCE depend on the probability distribution function of the uncertain input variables. Therefore, a variable following a normal distribution requires Hermite polynomials and one following a uniform distribution will use Legendre polynomials.
- The objective of the PCE methodology is to obtain the polynomial expansion coefficients to calculate the mean and standard deviation of the system results. The integral from which they are obtained by this method can be solved by Gauss quadrature if the simulations are selected according to the roots of the corresponding polynomials.
- For both cases of study a normal uncertain variable has been used, which requires the use of Hermite polynomials. The PCE development has been solved by means of 5th order Gauss quadrature so it was necessary to perform 5 simulations for each experimental condition.
- It is necessary to establish a change of variable to fit our uncertain variable of a given mean and variance. Therefore, it was necessary to add a term to the integral to make the polynomials orthogonal in the new range (Appendix A in Chapter 4).
- The results obtained for the CLM benchmark show that the PCE methodology performs well even when running a small number of simulations. With only 5 simulations it was possible to identify the output uncertainty depending on the uncertainty in the experimental measurements of the fluid density of the experiment.

- The code predictions for the CLM case were good for the cold leg zone although in the downcomer larger deviations were observed, probably due to an underprediction of the turbulence along the entire pipeline until reaching the downcomer. Comparing the different turbulence models, it was observed that the RANS models did not correctly predict the behavior, and a substantial reduction in the velocity magnitude was observed.
- In relation to the case of the GEPELON experimental facility, the PCE method allowed obtaining the uncertainty for a wide range of free-fall annular flow inlet flows with only 25 stationary simulations taking into account as uncertain variable the inlet flow. This is acceptable for steady-state simulations, but for transient statistics the times are considerable longer.
- The code predictions for the GEPELON facility are very good for the free-fall regime. For downward co-current flow, larger discrepancies are observed and the code is not able to correctly predict the decrease in mean film thickness for high air flow rates.

6.3.3. FUTURE RESEARCH LINES

The main lines of future research arising from this thesis are described below. They have been structured in two main sections in relation to the experimental part and to the simulation part, following the same approach adopted for the conclusions.

- Firstly, the versatility of the GEPELON experimental setup design allows to continue investigating the annular flow in different ways. As previously mentioned, countercurrent flow can be investigated although it can only be done for certain developed conditions in the 30mm pipe (the smallest one).
- For all annular flow configurations, it is possible to perform experiments from other points of view. An example of this is Chapter 3 where small amounts of 1-butanol were introduced to analyze the effect of surface tension on the liquid film. This study could be extended to the other configurations, especially for downward cocurrent flow where a particular wave behavior was detected for different gas velocities.
- Additionally, without major changes in the installation it is possible to study the effect of water temperature and even establish possible relationships with the change in surface tension. Producing film heating along the test section would be very interesting but this study would require major changes. However, it is possible to increase the water temperature beforehand entering the test section.
- During the explanation of the methods of measuring the liquid film in Chapter 1 it was shown that it is possible to study this regime in different

ways. Although conductance probes have many advantages, their measurements are localized on a point and other essential aspects of the film such as wave velocity or azimuthal coherence cannot be analyzed. Therefore, it would be very interesting to compare and complement the measurements by an alternative method such as an optical method. It is important to mention that next to the GEPELON facility, a smaller CAPELON twin (approx. 1:2) was designed where the PLIF technique is currently being implemented to perform the measurements. This mock-up incorporates a PFA (polyfluoroalkyl) pipe whose refractive index is very close to that of water, thus minimizing possible refraction problems when measuring using high-speed cameras.

- Finally, if more elaborate changes are made to the facility it would be possible to shift to the research line of water-steam annular flow measurements where mass and energy exchange play an important role. Likewise, the facility could be designed to incorporate other materials closer to the water at different conditions. For example, a chloroform facility would allow assimilation to conditions more similar to those observed in LWR.

Simulation using CFD codes and quantification of prediction uncertainty presents multiple lines of future research. In most cases, these lines are limited by access to high performance computing (HPC) services. However, there are also lines that can be addressed in a more straightforward manner.

- The first line of future research currently being addressed is the implementation of Polynomial Chaos Expansion for multiple uncertain variables and with different probability distribution function (normal, uniform, exponential, etc.). Whereas the most efficient way to use PCE is by means of a small number of uncertain variables, it is important to study the combination of bases necessary to use several uncertain variables. In addition, sparse grid techniques can be implemented, for example, to substantially reduce the number of simulations required for cases with multiple uncertain variables.
- Also related to the Polynomial Chaos Expansion it would be very interesting to compare the results obtained by other methodologies. This includes other PCE solving techniques, such as collocation points, and other propagation or extrapolation methods. In addition, if sufficient computational resources are available, the Wilks methodology could be used, which has traditionally been one of the most reliable and reliable but also one of the most demanding.
- In relation to the simulation of the GEPELON facility, there are multiple lines of future research. The most direct one is the performance of transient simulations to obtain average statistics. Transient simulations offer

solutions with a higher degree of convergence and more information specially related to the interfacial waves, although they also take much more simulation time. Again, access to higher computational resources would significantly facilitate progress along these research lines.

- Another option available is the comparison between different codes. Currently the ANSYS CFX license also allows the use of ANSYS FLUENT, so it would be the most immediate candidate. However, this study can be extended to other codes, either open access codes such as OpenFOAM or commercial ones like STAR-CCM+. In addition, a collaboration is currently underway to use the ALYA code that is focused on exploiting massive parallelization for use on supercomputers.

Chapter 7

BIBLIOGRAPHY AND SCIENTIFIC PRODUCTION

BIBLIOGRAPHY

Adaze, E., Badr, H. M., & Al-Sarkhi, A. (2019). CFD modeling of two-phase annular flow toward the onset of liquid film reversal in a vertical pipe. Journal of Petroleum Science and Engineering, 175(October 2018), 755–774. https://doi.org/10.1016/j.petrol.2019.01.026

Åkesjö, A., Gourdon, M., Vamling, L., Innings, F., & Sasic, S. (2017). Hydrodynamics of vertical falling films in a large-scale pilot unit – a combined experimental and numerical study. International Journal of Multiphase Flow, 95, 188–198. https://doi.org/10.1016/j.ijmultiphaseflow.2017.06.003

Åkesjö, A., Gourdon, M., Vamling, L., Innings, F., & Sasic, S. (2018). Experimental and numerical study of heat transfer in a large-scale vertical falling film pilot unit. International Journal of Heat and Mass Transfer, 125, 53–65. https://doi.org/10.1016/j.ijheatmasstransfer.2018.04.052

Åkesjö, A., Olausson, L., Vamling, L., & Gourdon, M. (2015). New Measurement Approaches for Film Thickness and Wall Temperature in Falling Film Heat Exchangers. 11th International Conference on Heat Transfer, Fluid Mechanics and Thermodynamics, 3(3), 613–619.

Alekseenko, S. V., Nakoryakov, V. E., & Pokusaev, B. G. (1985). Wave formation on vertical falling liquid films. International Journal of Multiphase Flow, 11(5), 607–627.

Alekseenko, S. V., Antipin, V. A., Cherdantsev, A. V., Kharlamov, S. M., & Markovich, D. M. (2008). Investigation of waves interaction in annular gas-liquid flow using high-speed fluorescent visualization technique. Microgravity Science and Technology, 20(3–4), 271–275. https://doi.org/10.1007/s12217-008-9028-1

Alekseenko, S. V., Cherdantsev, A. V., Cherdantsev, M., Isaenkov, S., Kharlamov, S., & Markovich, D. (2012). Application of a high-speed laser-induced fluorescence technique for studying the three-dimensional structure of annular gas-liquid flow. Experiments in Fluids, 53(1), 77–89. https://doi.org/10.1007/s00348-011-1200-5

Alekseenko, S. V., Cherdantsev, A. V., Markovich, D. M., & Rabusov, A. V. (2014). INVESTIGATION OF DROPLETS ENTRAINMENT AND DEPOSITION IN ANNULAR FLOW USING LIF TECHNIQUE. Atomization and Sprays, 24(3), 193–222. https://doi.org/10.1615/AtomizSpr.2013008168

Almabrok, A. A., Aliyu, A. M., Lao, L., & Yeung, H. (2016). Gas/liquid flow behaviours in a downward section of large diameter vertical serpentine pipes. International Journal of Multiphase Flow, 78, 25–43. https://doi.org/10.1016/j.ijmultiphaseflow.2015.09.012

Ambrosini, W., Anhom, L., Forgione, N., Oriolo, F., & Vigni, P. (1998). Surface characteristics of a water film falling clown a flat plate in the laminar-wavy regime. Third International Conference on Multiphase Flow, ICMF'98, Lyon, France.

Ambrosini, W., Forgione, N., & Oriolo, F. (2002). Statistical characteristics of a water film falling down a flat plate at different inclinations and temperatures. International Journal of Multiphase Flow, 28(9), 1521–1540. https://doi.org/10.1016/S0301-9322(02)00039-3

An, J. S., Cherdantsev, A. V., Zadrazil, I., & Markides, C. N. (2020). Study of disturbance wave development in downwards annular flows with a moving frame-of-reference brightness-based laser-induced fluorescence method. Experiments in Fluids, 61(7). https://doi.org/10.1007/s00348-020-03001-w

Andreani, M., Bestion, D., Ducros, F., Houkema, M., Lucas, D., Menter, F., & Watanabe, T. (2008). Assessment of Computational Fluid Dynamics (CFD) For Nuclear Reactor Safety Problems. NEA / CSNI / R (2007) 13 Unclassified, January.

Aragaki, T., Nakayama, S., Suzuki, M., & Toyama, S. (1987). Characteristics of a falling liquid on a vertical tube. International Chemical Engineering, 27(2), 326– 333.

Asali, J. C., Hanratty, T. J., & Andreussi, P. (1985). Interfacial drag and film height for vertical annular flow. American Institutefar Chemical Engineers Journal, 31(6), 895–902.

ASME V&V 20. (2009). Standard for Verification and Validation in Computational Fluid Dynamics and Heat Transfer ASME V & V 20-2009. The American Society of Mechanical Engineers, 102.

Azzopardi, B. J. (1978). Consideration of the fluorescence film thickness technique. Oxford University Engineering Laboratory, Report 1229/78.

Azzopardi, B. J. (1997). Drops in annular two-phase flow. International Journal of Multiphase Flow, 23(7), 1–53. https://doi.org/10.1016/S0301-9322(97)90087-2

Babakhani Dehkordi, P., Colombo, L. P. M., Guilizzoni, M., & Sotgia, G. (2017). CFD simulation with experimental validation of oil-water core-annular flows through Venturi and Nozzle flow meters. Journal of Petroleum Science and Engineering, 149(September 2016), 540–552. https://doi.org/10.1016/j.petrol.2016.10.058

Baldwin, B. S., & Barth, T. J. (1990). A One-Equation Turbulence Transport Model for High Reynolds Number Wall-Bounded Flows. NASA TM 102847.

Baldwin, B. S., & Lomax, H. (1978). Thin Layer Approximation and Algebraic Model for Separated Turbulent Flows. AOAA Paper, 78–257.

Boussinesq, J. (1877). Essai sur la théorie des eaux courantes. Mémoires Présentés Par Divers Savants à l'Académie Des Sciences, 23(1), 1–680.

Brennen, C. E. (2013). Fundamentals of Multiphase Flows. California Institute of Technology, Pasadena, California, 9780521848, 1–345. https://doi.org/10.1017/CBO9780511807169

Budka, M., & Gabrys, B. (2013). Density-preserving sampling: Robust and efficient alternative to cross-validation for error estimation. IEEE Transactions on Neural Networks and Learning Systems, 24(1), 22–34. https://doi.org/10.1109/TNNLS.2012.2222925

Camassa, R., Forest, M. G., Lee, L., Ogrosky, H. R., & Olander, J. (2012). Ring waves as a mass transport mechanism in air-driven core-annular flows. Physical Review E - Statistical, Nonlinear, and Soft Matter Physics, 86(6), 1–11. https://doi.org/10.1103/PhysRevE.86.066305

Charogiannis, A., An, J. S., & Markides, C. N. (2017). A Novel Optical Technique for Accurate Planar Measurements of Film-Thickness and Velocity in Annular Flows. 13th International Conference on Heat Transfer, Fluid Mechanics and Thermodynamics, 4–6.

Charogiannis, Alexandros, Sik An, J., Voulgaropoulos, V., & Markides, C. N. (2019). Structured planar laser-induced fluorescence (S-PLIF) for the accurate identification of interfaces in multiphase flows. International Journal of Multiphase Flow, 118, 193–204. https://doi.org/10.1016/j.ijmultiphaseflow.2019.06.002

Cherdantsev, A. V., An, J. S., Charogiannis, A., & Markides, C. N. (2019). Simultaneous application of two laser-induced fluorescence approaches for film thickness measurements in annular gas-liquid flows. International Journal of Multiphase Flow, 119, 237–258. https://doi.org/10.1016/j.ijmultiphaseflow.2019.07.013

Chu, K. J., & Dukler, A. E. (1974). Statistical characteristics of thin, wavy films. Part II: Studies on the substrate and its wave structure. American Institute of Chemical Engineering]Ournal, 20(4), 695–706.

Chu, K. J., & Dukler, A. E. (1975). Statistical characteristics of thin, wavy films. Part III: Structure of the large waves and their resistances to gas flow,"American. Institute of Chemica/ Engjneering]Ournal, 20(4), 695–706.

Chun, M. H., Park, J. R., & Lee, S. (1984). Parametric effects on the liquid-film thickness measurement by an ultrasonic method. Transactions of the American Nuclear Society, 46, 849–850.

Collier, J. G., & Hewitt, G. . (1961). Data on the vertical flow of air-water mixtures in the annular and dispersed flow regions, Part II: Film thickness and entrainment data and analysis of pressure drop measurements. Trans. Inst. Chem. Eng., 37, 127–136.

Collier, J. G., & Hewitt, G. F. (1964). Film thickness measurements. UKAEA, Report No.

Coney, J. E. R., El-Shafei, E. A. M., & Sheppard, C. G. W. (1989). A dual laser beam method for wavy thickness measurement. Optics and Lasers in Engineering, 11, 1– 14.

Craft, T. J., Launder, B. E., & Suga, K. (1996). Development and application of a cubic eddy-viscosity model of turbulence. International Journal of Heat and Fluid Flow, 17(2), 108–115. https://doi.org/10.1016/0142-727X(95)00079-6

Cravarolo, L., Hassid, A., & Villani, S. (1961). A beta-ray attenuation method for density measurements of liquid-gas mixtures in adiabatic flow. Energy Nuclear, 8(12), 751–757.

Cuadros, J. L., Rivera, Y., Berna, C., Escrivá, A., Muñoz-Cobo, J. L., Monrós-Andreu, G., & Chiva, S. (2019). Characterization of the gas-liquid interfacial waves in vertical upward co-current annular flows. Nuclear Engineering and Design, 346(March), 112–130. https://doi.org/10.1016/j.nucengdes.2019.03.008

Cutrono Rakhimov, A., Visser, D. C., & Komen, E. M. J. (2019). Uncertainty Quantification method for CFD applied to the turbulent mixing of two water layers – II: Deterministic Sampling for input uncertainty. Nuclear Engineering and Design, 348(July 2018), 146–158. https://doi.org/10.1016/j.nucengdes.2019.04.016

Czernek, K., & Witczak, S. (2020). Precise determination of liquid layer thickness with downward annular two-phase gas-very viscous liquid flow. Energies, 13(24), 1–17.

https://doi.org/10.3390/en13246529

D'Auria, F., Galassi, G. M., & Debrecin, N. (1995). Outline of the uncertainty methodology based on accuracy extrapolation. Nuclear Technology, 109(1), 21–38.

Dai, Y., Dakshinammorthy, D., & Agrawal, M. (2013). CFD Modeling of Bubbly, Slug and Annular Flow Regimes in Vertical Pipelines. https://doi.org/10.4043/24245-ms

Damsohn, M., & Prasser, H. M. (2009). High-speed liquid film sensor for two-phase flows with high spatial resolution based on electrical conductance. Flow Measurement and Instrumentation, 20(1), 1–14. https://doi.org/10.1016/j.flowmeasinst.2008.06.006

Dasgupta, A., Chandraker, D. K., Kshirasagar, S., Reddy, B. R., Rajalakshmi, R., Nayak, A. K., Walker, S. P., Vijayan, P. K., & Hewitt, G. F. (2017). Experimental investigation on dominant waves in upward air-water two-phase flow in churn and annular regime. Experimental Thermal and Fluid Science, 81, 147–163. https://doi.org/10.1016/j.expthermflusci.2016.10.012

David C. Wilcox. (1993). Turbulence-Modeling-for-CFD.

De Jong, P., & Gabriel, K. S. (2003). A preliminary study of two-phase annular flow at microgravity: Experimental data of film thickness. International Journal of Multiphase Flow, 29(8), 1203–1220. https://doi.org/10.1016/S0301-9322(03)00085-5

El-Sayed, E.-A., L., D., & Stepanek, J. B. (1983). Use of microwaves in the measurements of frequencies and amplitudes in liquid hold-up fluctuations. International Journal of Multiphase Flow, 9(1), 49–72.

Fan, W., Cherdantsev, A. V., & Anglart, H. (2020). Experimental and numerical study of formation and development of disturbance waves in annular gas-liquid flow. Energy, 207, 118309. https://doi.org/10.1016/j.energy.2020.118309

Farias, P. S. C., Martins, F. J. W. A., Sampaio, L. E. B., Serfaty, R., & Azevedo, L. F. A. (2012). Liquid film characterization in horizontal, annular, two-phase, gas-liquid flow using time-resolved laser-induced fluorescence. Experiments in Fluids, 52(3), 633–645. https://doi.org/10.1007/s00348-011-1084-4

Fedon, C., Cervantes, E. Y. G., Salamon, L., & Erasmus, B. (2021). Application of deterministic sampling methods for uncertainty quantification in manufacturing tolerances in neutron physics. Nuclear Engineering and Design, 373(October 2020), 111023. https://doi.org/10.1016/j.nucengdes.2020.111023

Fokken, J., Krohn, B., Kapulla, R., Niceno, B., Prasser, H.-M., & Badillo, A. (2019a). NEA Benchmark Exercise : Computational Fluid Dynamic Prediction and Uncertainty Quantification of a GEMIX Mixing Layer Test. In NEA/CSNI/R(2017)19 (Issue February).

Fokken, J., Krohn, B., Kapulla, R., Niceno, B., Prasser, H.-M., & Badillo, A. (2019b). NEA Benchmark Exercise : Computational Fluid Dynamic Prediction and Uncertainty Quantification of a GEMIX Mixing Layer Test. OECD/NEA/CSNI, February.

Fujita, H., Katoh, K., & Takahama, H. (1986). Falling water films on a vertical cylinder with a downward step. Internationa/ Journal of Enginming Science, 24(8), 1405–1418.

Fukano, T. (1998). Measurement of time varying thickness of liquid film flowing with high speed gas flow by a constant electric current method (CECM). Nuclear Engineering and Design, 184(2–3), 363–377. https://doi.org/10.1016/S0029-5493(98)00209-X

Germano, M., Piomelli, U., Moin, P., & Cabot, W. H. (1991). A Dynamic Subgrid-Scale Eddy Viscosity Model. Physics of Fluids A, 3(7), 1760–1765.

Ghosh, S, Pratihar, D. K., Maiti, B., & Das, P. K. (2013). Automatic classification of vertical counter-current two-phase flow by capturing hydrodynamic characteristics through objective descriptions. International Journal of Multiphase Flow, 52, 102–120. https://doi.org/10.1016/j.ijmultiphaseflow.2012.12.007

Ghosh, Sumana, Das, G., & Das, P. K. (2010). Simulation of core annular downflow through CFD-A comprehensive study. Chemical Engineering and Processing: Process Intensification, 49(11), 1222–1228. https://doi.org/10.1016/j.cep.2010.09.007

Grimley, S. S. (1945). Liquid Flow conditions in packed towers. Trans. Inst. Chem. Engrs., 23, 228–235.

Gross, U., Storch, T., Philipp, C., & Doeg, A. (2009). Wave frequency of falling liquid films and the effect on reflux condensation in vertical tubes. International Journal of Multiphase Flow, 35(4), 398–409. https://doi.org/10.1016/j.ijmultiphaseflow.2009.01.001

Gu, F., Liu, C. J., Yuan, X. G., & Yu, G. C. (2004). CFD simulation of liquid film flow on inclined plates. Chemical Engineering and Technology, 27(10), 1099–1104. https://doi.org/10.1002/ceat.200402018

Guzanov, V. V., Bobylev, A. V., Heinz, O. M., Kharlamov, S. M., Kvon, A. Z., & Markovich, D. M. (2017). Characterization of 3-D wave flow regimes on falling liquid films. International Journal of Multiphase Flow, 99, 474–484. https://doi.org/10.1016/j.ijmultiphaseflow.2017.11.013

Hagiwara, Y., Miwada, T., Suzuki, K., & Sato, T. (1984). A study on liquid film flow characteristics in annular two-phase flow. Proceedings of Multi-Phase Flow and Heat Transftr 3, April 18-20, 249–263.

Hessling, J. P. (2013). Deterministic Sampling for Quantification of Modeling Uncertainty of Signals. Digital Filters and Signal Processing. https://doi.org/10.5772/52193

Ibarra, R., Matar, O. K., & Markides, C. N. (2021). Experimental investigations of upward-inclined stratified oil-water flows using simultaneous two-line planar laser-induced fluorescence and particle velocimetry. International Journal of Multiphase Flow, 135, 103502. https://doi.org/10.1016/j.ijmultiphaseflow.2020.103502

Ibarra, R., Zadrazil, I., Matar, O. K., & Markides, C. N. (2018). Dynamics of liquid–liquid flows in horizontal pipes using simultaneous two–line planar laser–induced fluorescence and particle velocimetry. International Journal of Multiphase Flow, 101, 47–63. https://doi.org/10.1016/j.ijmultiphaseflow.2017.12.018

Isaenkov, S., Cherdantsev, A., Cherdantsev, M., & Markovich, D. (2017). Quantitative analysis of transverse non-uniformity of liquid film at the initial stage of annular-dispersed flow. Journal of Physics: Conference Series. https://doi.org/10.1088/1742-6596/894/1/012105

Ishii, M., & Grolmes, M. A. (1975). Inception criteria for droplet entrainment in two-phase concurrent film flow. AIChE Journal, 21(2), 308–318. https://doi.org/10.1002/aic.690210212

Ishii, M., & Hibiki, T. (2006). Thermo-Fluid Dynamics of Two-Phase Flow. Springer.

Jackson, M. L. (1955). Liquid films in viscous flow. American Institute of Chemical Engineering]Ournal, 1(2), 231–240.

Jeong, H. Y., Kim, B. N., & Lee, K. (1998). Thermal-hydraulic phenomena during reflux condensation cooling in steam generator tubes. Annals of Nuclear Energy, 25(17), 1419–1428. https://doi.org/10.1016/s0306-4549(98)00041-3

Jones, W. P., & Launder, B. E. (1972). The prediction of laminarization with a two-equation model of turbulence. International Journal of Heat and Mass Transfer, 15, 301–314.

Ju, P., Yang, X., Schlegel, J. P., Liu, Y., Hibiki, T., & Ishii, M. (2018). Average liquid film thickness of annular air-water two-phase flow in 8 × 8 rod bundle. International Journal of Heat and Fluid Flow, 73, 63–73. https://doi.org/10.1016/j.ijheatfluidflow.2018.06.015

Kabir, H. M. D., Khosravi, A., Hosen, M. A., & Nahavandi, S. (2018). Neural Network-Based Uncertainty Quantification: A Survey of Methodologies and Applications. IEEE Access, 6, 36218–36234. https://doi.org/10.1109/ACCESS.2018.2836917

Karapantsios, T. D., & Karabelas, A. J. (1995). Longitudinal Characteristics of Wavy Falling Films. International Journal of Multiphase Flow, 21(1), 119–127.

Karimi, G., & Kawaji, M. (1998). An experimental study of freely falling films in a vertical tube. Chemical Engineering Science, 53(20), 3501–3512. https://doi.org/10.1016/S0009-2509(98)00159-6

Karimi, G., & Kawaji, M. (1996). A study of hydrodynamic characteristics of non-conductive falling films in counter-current annular flow. 31 National Heat Transfer Conference, 326, 205–221.

Kolev, N. I. (2015). Multiphase Flow Dynamics 5 (Nuclear Th). Springer.

Konakli, K., & Sudret, B. (2016). Polynomial meta-models with canonical low-rank approximations: Numerical insights and comparison to sparse polynomial chaos expansions. Journal of Computational Physics, 321, 1144–1169. https://doi.org/10.1016/j.jcp.2016.06.005

Koskie, J. E., Mudawar, I., & Tiederman, W. G. (1989). Parallel-wire probes for measurement of thick liquid films. International Journal of Multiphase Flow, 15(4), 521–530. https://doi.org/10.1016/0301-9322(89)90051-7

Kulov, N. N., Maksimov, V. V., Maljusov, V. A., & Zhavoronkov, N. M. (1979). Pressure drop, mean film thickness and entrainment in downward two-phase flow. The Chemical Engineering Journal. https://doi.org/10.1016/0300-9467(79)80038-6

Launder, B. E., Reece, G. J., & Rodi, W. (1975). Progress in the Development of a Reynolds-Stress Turbulent Closure. Journal of Fluid Mechanics, 68(3), 537–566.

Lee, K., Kim, J., Park, G., & Cho, H. (2016). Feasibility Test of a Liquid Film Thickness Sensor on a Flexible Printed Circuit Board Using a Three-Electrode Conductance Method. Sensors, 17(1), 42. https://doi.org/10.3390/s17010042

Li, C., Song, Y., Xu, L., Zhao, N., Wang, F., Fang, L., & Li, X. (2021). Prediction of the interfacial disturbance wave velocity in vertical upward gas-liquid annular flow via ensemble learning. Energy, 242, 122990. https://doi.org/10.1016/j.energy.2021.122990

Li, H., & Anglart, H. (2015). CFD model of diabatic annular two-phase flow using the Eulerian-Lagrangian approach. Annals of Nuclear Energy, 77, 415–424. https://doi.org/10.1016/j.anucene.2014.12.002

Li, H., & Anglart, H. (2017). CFD prediction of droplet deposition in steam-water annular flow with flow obstacle effects. Nuclear Engineering and Design, 321, 173–179. https://doi.org/10.1016/j.nucengdes.2016.11.021

Li, H., & Anglart, H. (2019). Dryout prediction with CFD model of annular two-phase flow. Nuclear Engineering and Design, 349(April), 20–26. https://doi.org/10.1016/j.nucengdes.2019.04.020

Liang, F., Hang, Y., Yu, H., & Jifeng Gao. (2021). Identification of gas-liquid two-phase flow patterns in a horizontal pipe based on ultrasonic echoes and RBF neural network. Flow Measurement and Instrumentation, 79(January 2020), 101960. https://doi.org/10.1016/j.flowmeasinst.2021.101960

Lilleleht, L. U., & Hanratty, T. J. (1961). Measurement of interfacial structure for co- current air-water flow. Fluid Mechanics, 11(1), 65–81.

Liu, A., Yan, C., Zhu, F., Gu, H., & Gong, S. (2021). Liquid film thickness of vertical upward annular flow in narrow rectangular channel. Chemical Engineering Research and Design, 175, 10–24. https://doi.org/10.1016/j.cherd.2021.08.011

Liu, Y., Li, W. Z., & Quan, S. L. (2011). A self-standing two-fluid CFD model for vertical upward two-phase annular flow. Nuclear Engineering and Design, 241(5), 1636–1642. https://doi.org/10.1016/J.NUCENGDES.2011.01.037

Liu, Yang, Hu, R., Wang, D., Liu, Y., Sun, X., & Dinh, N. (2021). Uncertainty quantification for Multiphase-CFD simulations of bubbly flows: a machine learning-based Bayesian approach supported by high-resolution experiments. Reliability Engineering and System Safety, 212(March), 107636. https://doi.org/10.1016/j.ress.2021.107636

Mascarenhas, N., & Mudawar, I. (2013). Study of the influence of interfacial waves on heat transfer in turbulent falling films. International Journal of Heat and Mass Transfer, 67, 1106–1121. https://doi.org/10.1016/j.ijheatmasstransfer.2013.08.100

Mastrippolito, F., Aubert, S., & Ducros, F. (2021). Kriging metamodels-based multi-objective shape optimization applied to a multi-scale heat exchanger. Computers and Fluids, 221, 104899. https://doi.org/10.1016/j.compfluid.2021.104899

Mendez, M. A., Scheid, B., & Buchlin, J. M. (2017). Low Kapitza falling liquid films. Chemical Engineering Science, 170, 122–138. https://doi.org/10.1016/j.ces.2016.12.050

Menter, F. R. (1993). Zonal Two Equation k-ω Turbulence Models for Aerodynamic Flows. AIAA Paper 93-2906.

Menter, F. R. (1994). Two-Equation Eddy-Viscosity Turbulence Models for Engineering Applications. AIAA Journal, 32(8), 1598–1605. https://doi.org/https://doi.org/10.2514/3.12149

Metropolis, N., & Ulam, S. (1949). The Monte Carlo Method. Journal of the American Statistical Association, 44(247), 335–341.

Mudawar, I, & Houpt, R. A. (1993a). Mass and momentum transport in smooth falling liquid films laminarized at relatively high Reynolds numbers. International Journal of Heat and Mass Transfer, 36(14), 3437–3448.

Mudawar, I, & Houpt, R. A. (1993b). Measurement of mass and momentum transport in wavy-laminar falling liquid films. International Journal of Real and Mass Transfer, 36(17), 4151–4162.

Muñoz-Cobo, J. L., Rivera, Y., Berna, C., & Escrivá, A. (2020). Analysis of conductance probes for two-phase flow and holdup applications. Sensors (Switzerland), 20(24), 1–29. https://doi.org/10.3390/s20247042

Musa Aliyu, A. (2015). Vertical Annular gas-liquid two-phase flow in large diameter pipes. In CRANFIELD UNIVERSITY, OIL AND GAS ENGINEERING CENTRE PhD (Vol. 151). https://doi.org/10.1145/3132847.3132886

Nencini, F., & Andreussi, P. (1982). Studies of the behaviour of disturbance waves in annular two-phase flow. The Canadian Journal of Chemical Engineering, 60, 459– 465.

Nicoud, F., & Ducros, F. (1999). Subgrid-scale stress modelling based on the square of the velocity. Flow Measurement and Instrumentation, 62, 183–200.

OECD/NEA. (2016). Review of Uncertainty Methods for Computational Fluid Dynamics Application to Nuclear Reactor Thermal Hydraulics. February, 1–132. www.oecd-nea.org

Ohba, K., Naimi, F., Morimoto, T., & Nakamura, K. (1996). Dynamic interaction between ripple, ring and disturbance waves in vertically upward air-water annular flow. Proceedings of the Japan - U.S. Seminar on Two-Phase Flow Dynamics, July 15-20, Fukuoka, Japan.

Orszag, S. A. (1970). Analytical Theories of Turbulence. Journal of Fluid Mechanics, 41, 363–386.

Pan, L., He, H., Ju, P., Hibiki, T., & Ishii, M. (2015). Experimental study and modeling of disturbance wave height of vertical annular flow. Heat and Mass Transfer, 89(2015), 165–175. https://doi.org/10.1016/j.ijheatmasstransfer.2015.05.073

Pham, S. H., Kawara, Z., Yokomine, T., & Kunugi, T. (2015). Measurements of liquid film and droplets of annular two-phase flow on a rod-bundle geometry with spacer. International Journal of Multiphase Flow, 70, 35–57. https://doi.org/10.1016/j.ijmultiphaseflow.2014.11.010

Qiao, S., Mena, D., & Kim, S. (2017). Inlet effects on vertical-downward air–water two-phase flow. Nuclear Engineering and Design, 312, 375–388. https://doi.org/10.1016/j.nucengdes.2016.04.033

Rahman, M. M., Siikonen, T., & Agarwal, R. K. (2011). Improved Low Re-Number One-Equation Turbulence Model. AIAA, 49(4).

Rakhimov, A. C., Visser, D. C., & Komen, E. M. J. (2018). Uncertainty Quantification method for CFD applied to the turbulent mixing of two water layers. Nuclear Engineering and Design, 333(April), 1–15. https://doi.org/10.1016/j.nucengdes.2018.04.004

Rivera, Y., Berna, C., Muñoz-Cobo, J. L., Escrivá, A., & Córdova, Y. (2022). Experiments in Free Falling and Downward Cocurrent Annular Flows – Characterization of Liquid Films and Interfacial Waves. Nuclear Engineering and Design, 382, 111769.

Rivera, Y., Muñoz-Cobo, J.-L., Berna, C., Cuadros, J.-L., & Escrivá, A. (2019). Experimental study of the interfacial waves produced in upward vertical annular flows when varying the liquid-phase surface tension. WIT Transactions on Engineering Sciences, 123. https://doi.org/10.2495/MPF190031

Rivera, Y., Muñoz-Cobo, J. L., Berna, C., Escrivá, A., & Cordova, Y. (2020). STUDY OF LIQUID FILM BEHAVIOUR IN VERTICAL DOWNWARD AIR–WATER ANNULAR FLOW. Proceedings of Advances in Fluid Mechanics XIII, 128, 77–88. https://doi.org/10.1115/1.3138339

Rivera, Y., Muñoz-Cobo, J. L., Berna, C., Escrivá, A., & Vela, E. (2021). CFD simulation plus uncertainty quantification of the mixing of two fluid with different density for the Cold-Leg mixing benchmark. Nuclear Engineering and Design, 383(September). https://doi.org/10.1016/j.nucengdes.2021.111449

Rivera, Y., Muñoz-Cobo, J. L., Cuadros, J. L., Berna, C., & Escrivá, A. (2021). Experimental study of the effects produced by the changes of the liquid and gas superficial velocities and the surface tension on the interfacial waves and the film thickness in annular concurrent upward vertical flows. Experimental Thermal and Fluid Science, 120. https://doi.org/10.1016/j.expthermflusci.2020.110224

Rivera, Y., Muñoz-Cobo, J. L., Escrivá, A., Berna, C., & Córdova, Y. (2021). Experimental Measurements and CFD Results of Liquid Film Thickness in Vertical Downward Air – Water Annular Flow. International Journal of Computational Methods and Experimental Measurements, 10(2), 93–103. https://doi.org/10.2495/CMEM-V0-N0-1-11

Roy, R. P., Ku, J., Kaufman, L., & Shukla, J. (1986). Microwave method for measurement of liquid film thickness in gas-liquid flow. Review of Scientific Instruments, 57(5), 952–956.

Sawant, P., Ishii, M., & Mori, M. (2009). Prediction of amount of entrained droplets in vertical annular two-phase flow. International Journal of Heat and Fluid Flow, 30(4), 715–728. https://doi.org/10.1016/j.ijheatfluidflow.2009.03.003

Schmitt, R. L., Stevenson, W. H., & Simmons, H. C. (1982). Optical measurement of liquid film thickness. In Laser Institute of America (LIA) (Vol. 33, pp. 31–35).

Schubring, D., Ashwood, A. C., Shedd, T. A., & Hurlburt, E. T. (2010). Planar laser-induced fluorescence (PLIF) measurements of liquid film thickness in annular flow. Part I: Methods and data. International Journal of Multiphase Flow, 36(10), 815–824. https://doi.org/10.1016/j.ijmultiphaseflow.2010.05.007

Schubring, D., Shedd, T. A., & Hurlburt, E. T. (2010). Studying disturbance waves in vertical annular flow with high-speed video. International Journal of Multiphase Flow, 36(5), 385–396. https://doi.org/10.1016/j.ijmultiphaseflow.2010.01.003

Serizawa, A., Kamei, T., Nagane, K., Takahashi, T., & Kawara, Z. (1994). Non-intrusive measurement of dynamic behaviour of a liquid film. Proceedings of the German-Japanese Symposium on Multiphase Flow, Karlsruhe, Germany, 63–73.

Setyawan, A., Indarto, & Deendarlianto. (2016). The effect of the fluid properties on the wave velocity and wave frequency of gas-liquid annular two-phase flow in a horizontal pipe. Experimental Thermal and Fluid Science, 71, 25–41. https://doi.org/10.1016/j.expthermflusci.2015.10.008

Shih, T. H., Liou, W. W., Shabbir, A., Z.Yang, Z., & Zhu, J. (1995). A New k-ε Eddy-Viscosity Model for High Reynolds Number Turbulent Flows - Model Development and Validation. Computers Fluids, 24(3), 227–238.

Shuai, S., & Agarwal, R. K. (2020). A New Improved One-Equation Turbulence Model Based on k-kL Closure. AIAA Paper 2020-1075.

Smagorinsky, J. (1963). General Circulation Experiments with the Primitive Equations. Monthly Weather Review, 91(3), 99–164. https://doi.org/10.1126/science.12.306.731-a

Smith, A. M. O., & Cebeci, T. (1967). Numerical solution of the turbulent boundary layer equations. Douglas Aircraft Division Report DAC 33735.

Solesio, J. N. (1978). Measurement of liquid film thickness by X-ray absorption. Houille Blanche, 5, 341–343.

Spalart, P. R., & Allmaras, S. R. (1992). A One-Equation Turbulence Model for Aerodynamic Flows. AIAA Paper 92-0439.

Speziale, C. G., Sarkar, S., & Gatski, T. B. (1991). Modeling the Pressure-Strain Correlation of Turbulence: an Invariant Dynamical Systems Approach. Journal of Fluid Mechanics, 227, 245–272.

Strazza, D., Demori, M., Ferrari, V., & Poesio, P. (2011). Capacitance sensor for hold-up measurement in high-viscous-oil/conductive-water core-annular flows. Flow Measurement and Instrumentation, 22(5), 360–369. https://doi.org/10.1016/j.flowmeasinst.2011.04.008

Takahama, H, Okada, O., Fujita, H., & Mizuno, A. (1983). Study on annular mist flow in pipe (2nd report, Behaviour of water film in the non-equilibrium region of downward annular mist flow with low water flow rate. Bulletin of the Japanese Society of Mechanical Engineers, 26(222), 2091–2099.

Takahama, Heishichiro, & Kato, S. (1980). Longitudinal Flow Characteristics of Vertically Falling Liquid Films Without Concurrent Gas Flow. Int. J. Multiphase Flow, 6, 203–215.

Ueda, T., & Tanaka, T. (1974). Studies of liquid film flow in two-phase annular and annular-mist flow regions (Part 1, downflow in a vertical tube). Boletin of the JSME, 17(107), 603–613.

Van Nimwegen, A. T., Portela, L. M., & Henkes, R. A. W. M. (2017). The effect of the diameter on air-water annular and churn flow in vertical pipes with and without surfactants. International Journal of Multiphase Flow, 88, 179–190. https://doi.org/10.1016/j.ijmultiphaseflow.2016.09.013

Vasques, J., Cherdantsev, A., Cherdantsev, M., Isaenkov, S., & Hann, D. (2018). Comparison of disturbance wave parameters with flow orientation in vertical annular gas-liquid flows in a small pipe. Experimental Thermal and Fluid Science, 97, 484–501. https://doi.org/10.1016/j.expthermflusci.2018.03.020

Vijayan, M., Jayanti, S., & Balakrishnan, A. R. (2002). Experimental study of air-water countercurrent annular flow under post-flooding conditions. International Journal of Multiphase Flow, 28(1), 51–67. https://doi.org/10.1016/S0301-9322(01)00066-0

Voulgaropoulos, V., Patapas, A., Lecompte, S., Charogiannis, A., Matar, O. K., De Paepe, M., & Markides, C. N. (2021). Simultaneous laser-induced fluorescence and capacitance probe measurement of downwards annular gas-liquid flows. International Journal of Multiphase Flow, 142, 103665. https://doi.org/10.1016/j.ijmultiphaseflow.2021.103665

Wallin, S., & Johansson, A. V. (2000). An explicit algebraic Reynolds stress model for incompressible and compressible turbulent flows. Journal of Fluid Mechanics, 403, 89–132. https://doi.org/10.1017/S0022112099007004

Wang, C., Zhao, N., Chen, C., & Sun, H. (2018). A method for direct thickness measurement of wavy liquid film in gas-liquid two-phase annular flow using conductance probes. Flow Measurement and Instrumentation, 62, 66–75. https://doi.org/10.1016/j.flowmeasinst.2018.05.002

Wang, G., Dang, Z., & Ishii, M. (2021). Wave structure and velocity in vertical upward annular two-phase flow. Experimental Thermal and Fluid Science, 120(June 2020), 110205. https://doi.org/10.1016/j.expthermflusci.2020.110205

Wang, G., Dang, Z., Ju, P., Yang, X., Ishii, M., Ireland, A., Bajorek, S., & Bernard, M. (2017). Experimental study on interfacial structure and interfacial area transport in downward two-phase flow. International Journal of Heat and Mass Transfer, 106, 1303–1317. https://doi.org/10.1016/j.ijheatmasstransfer.2016.10.112

Wang, L. song, Liu, S., Hou, L. tong, Yang, M., Zhang, J., & Xu, J. yu. (2022). Prediction of the liquid film reversal of annular flow in vertical and inclined pipes. International Journal of Multiphase Flow, 146(June 2021), 103853. https://doi.org/10.1016/j.ijmultiphaseflow.2021.103853

Wang, M., Zheng, D., & Wu, Y. (2019). Experimental and modeling study on interfacial disturbance wave velocity in horizontal gas-liquid flow by ultrasonic method. Experimental Thermal and Fluid Science, 109(January), 109908. https://doi.org/10.1016/j.expthermflusci.2019.109908

Wang, M., Zheng, D., & Xu, Y. (2019). A new method for liquid film thickness measurement based on ultrasonic echo resonance technique in gas-liquid flow. Measurement: Journal of the International Measurement Confederation, 146, 447–457. https://doi.org/10.1016/j.measurement.2019.06.027

Webb, D. R., & Hewitt, G. F. (1975). Downwards co-current annular flow. International Journal of Multiphase Flow, 2(1), 35–49. https://doi.org/10.1016/0301-9322(75)90027-0

Wikle, C. K. (2017). Hierarchical models for uncertainty quantification: An overview. Handbook of Uncertainty Quantification, 193–218. https://doi.org/10.1007/978-3-319-12385-1_4

Wilcox, D. C. (1988). Re-assessment of the scale-determining equation for advanced turbulence models. AIAA Journal, 26(11), 1299–1310.

Wilcox, D. C. (2006). Turbulence Modeling for CFD (3rd ed.). DCW Industries, Inc., La Canada CA.

Wolf, A. (1995). Film Structure of Vertical Annular Flow (Issue January 1995). Imperial College of Science, Technology and Medicine. London University.

Wolf, A., Jayanti, S., & Hewitt, G. F. (2001). Flow development in vertical annular flow. Chemical Engineering Science, 56(10), 3221–3235. https://doi.org/10.1016/S0009-2509(00)00546-7

Woods, B. G., Groome, J., & Collins, B. (2009). An assessment of PWR steam generator condensation at the Oregon State University APEX facility. Nuclear Engineering and Design, 239(1), 96–105. https://doi.org/10.1016/j.nucengdes.2008.08.004

X. Han, T. J. W., & Agarwal, R. K. (2017). Application of a New DES Model Based on Wray-Agarwal Turbulence Model for Simulation of Wall-Bounded Flows with Separation. AIAA Paper 2017-3996.

Xue, T., & Zhang, S. (2018). Investigation on heat transfer characteristics of falling liquid film by planar laser-induced fluorescence. International Journal of Heat and Mass Transfer, 126, 715–724. https://doi.org/10.1016/j.ijheatmasstransfer.2018.05.039

Yakhot, V., Orszag, S. A., Thangam, S., Gatski, T. B., & Speziale, C. G. (1992). Development of turbulence models for shear flows by a double expansion technique. Physics of Fluids A Fluid Dynamics, 4(7), 1510–1520. https://doi.org/10.1063/1.858424

Yeoh, G. H., & Tu, J. (2010). Computational Techniques for Multi-phase Flows. IChemE. Elsevier.

Yih, S., & Hsu, T. (1985). Gas absorption into wavy and turbulent non-newtonian falling liquid films in a wetted-wall column. Chemical Engj,Neering Communications, 34(1–6), 65–76.

Yu, S. C. M., & Tso, C. P. (1995). Simulation of fiber optic sensors in determination of thin liquid film thicknesses,"Advances. Advances in Engineering Software, 22, 55–62.

Zadrazil, I., Markides, C. N., Matar, O. K., Náraigh, L., & Hewitt, G. F. (2012). Characterisation of downwards co-current gas-liquid annular flows. Proceedings of the International Symposium on Turbulence, Heat and Mass Transfer, 2012-Septe, 753–764. https://doi.org/10.1615/ICHMT.2012.ProcSevIntSympTurbHeatTransfPal.820

Zadrazil, I., Matar, O. K., & Markides, C. N. (2014). An experimental characterization of downwards gas-liquid annular flow by laser-induced fluorescence: Flow regimes and film statistics. International Journal of Multiphase Flow, 60, 87–102. https://doi.org/10.1016/j.ijmultiphaseflow.2013.11.008

Zadrazil, Ivan, & Markides, C. N. (2014). An experimental characterization of liquid films in downwards co-current gas-liquid annular flow by particle image and tracking velocimetry. International Journal of Multiphase Flow, 67(S), 42–53. https://doi.org/10.1016/j.ijmultiphaseflow.2014.08.007

Zahedi, P., Zhang, J., Arabnejad, H., McLaury, B. S., & Shirazi, S. A. (2017). CFD simulation of multiphase flows and erosion predictions under annular flow and low liquid loading conditions. Wear, 376–377, 1260–1270. https://doi.org/10.1016/j.wear.2017.01.111

Zhao, Y., Markides, C. N., Matar, O. K., & Hewitt, G. F. (2013a). Disturbance wave development in two-phase gas – liquid upwards vertical annular flow. International Journal of Multiphase Flow, 55, 111–129. https://doi.org/10.1016/j.ijmultiphaseflow.2013.04.001

Zhao, Y., Markides, C. N., Matar, O. K., & Hewitt, G. F. (2013b). Disturbance wave development in two-phase gas–liquid upwards vertical annular flow. International Journal of Multiphase Flow, 55, 111–129. https://doi.org/10.1016/J.IJMULTIPHASEFLOW.2013.04.001

SCIENTIFIC PRODUCTION

JOURNAL CONTRIBUTION

Y. Rivera, C. Berna, J.L. Muñoz-Cobo, A. Escrivá, Y. Córdova (2022). *Experiments in Free Falling and Downward Cocurrent Annular Flows – Characterization of Liquid Films and Interfacial Waves*. Nuclear Engineering and Design, 382, 111769. Open Access. https://doi.org/10.1016/j.nucengdes.2022.111769

Y. Rivera, C. Berna, J.L. Muñoz-Cobo, A. Escrivá, Y. Córdova (2022). Experimental Measurements and CFD Results of Liquid Film Thickness in Vertical Downward Air–Water Annular Flow. International Journal of Computational Methods and Experimental Measurements, 10(2) pp. 93-103. Open Access. https://doi.org/10.2495/CMEM-V10-N2-93-103

Y. Rivera, J.L. Muñoz-Cobo, C. Berna, A. Escrivá, E. Vela (2021). *CFD simulation plus uncertainty quantification of the mixing of two fluid with different density for the Cold-Leg mixing benchmark*. Nuclear Engineering and Design, 383 (September). https://doi.org/10.1016/j.nucengdes.2021.111449

Y. Rivera, J.L. Muñoz-Cobo, J.L. Cuadros, C. Berna, A. Escrivá (2021). *Experimental study of the effects produced by the changes of the liquid and gas superficial velocities and the surface tension on the interfacial waves and the film thickness in annular concurrent upward vertical flows*. Experimental Thermal and Fluid Science, 120. https://doi.org/10.1016/j.expthermflusci.2020.110224

J.L. Muñoz-Cobo, Y. Rivera, C. Berna, A. Escrivá (2020). *Analysis of conductance probes for two-phase flow and holdup applications*. Sensors (Switzerland), 20(24), 1–29. Open Access. https://doi.org/10.3390/s20247042

J.L. Cuadros, Y. Rivera, C. Berna, A. Escrivá, J.L. Muñoz-Cobo, G. Monrós-Andreu, S. Chiva (2019). *Characterization of the gas-liquid interfacial waves in vertical upward co-current annular flows*. Nuclear Engineering and Design, 346(March), 112–130. https://doi.org/10.1016/j.nucengdes.2019.03.008

NATIONAL AND INTERNATIONAL CONFERENCE CONTRIBUTION

J.L. Muñoz-Cobo, Y. Rivera, J.L. Cuadros, C. Berna, A. Escrivá. *Desarrollo y calibración de sondas de medida del espesor de película de agua en flujo anular aire-agua*. 43 Reunión Anual Sociedad Nuclear Española, October 2017.

J.L.Muñoz-Cobo, A.Miquel, A.Escrivá, C.Berna, Y.Rivera. *Efficient uncertainty quantification in nuclear thermal-hydraulic simulations by means of polynomial chaos expansion*. ANS Best Estimate Plus Uncertainty International Conference (BEPU 2018), May 2018.

D.S. Domínguez, S.M. Iglesias, A.Escrivá, J.L.Muñoz-Cobo, C.Berna, Y.Rivera, J.L. Cuadros. *Modelación de regímenes con película ondulatoria aire-agua en tuberías verticales usando técnicas de fluido dinámica computacional*. 44 Reunión Anual Sociedad Nuclear Española, September 2018.

J.L. Muñoz-Cobo, Y. Rivera, J.L. Cuadros, C. Berna, A. Escrivá, Susana M. Iglesias, Dany S. Domínguez. *Desarrollo y calibración de sondas de medida del espesor de película de agua en flujo anular aire-agua.* 44 Reunión Anual Sociedad Nuclear Española, September 2018.

J.L. Muñoz-Cobo, Y. Rivera, J.L. Cuadros, C. Berna, A. Escrivá, Susana M. Iglesias, Dany S. Domínguez. *Cuantificación de incertidumbre en simulaciones CFD mediante Expansión en Caos Polinómico*. 44 Reunión Anual Sociedad Nuclear Española, September 2018.

S.M. Iglesias, D.S. Domínguez, A.Escrivá, J.L.Muñoz-Cobo, C.Berna, Y.Rivera, J.L. Cuadros. *Computational fluid dynamics applied to the study of air-water regime in vertical pipes*. 16th Multiphase Flow Conference & Short Course HZDR Dresden, November 2018.

Y. Rivera, J.L. Muñoz-Cobo, C. Berna, J.L. Cuadros, A. Escrivá. *Experimental Study of the Interfacial Waves Produced in Upward Vertical Annular Flows when Varying the Liquid-Phase Surface Tension*. 10th International Conference on Computational & Experimental Methods in Multiphase & Complex Flow – Wessex Institute. May 2019.

D.S. Domínguez, S.M. Iglesias, J.L. Muñoz-Cobo, A. Escrivá, C. Berna, Y. Rivera. *Modelo Analítico Aplicado al Problema de Onda Solitaria en Películas de Agua Gobernadas por Gravedad en Tuberías Verticales*. 45 Reunión Anual Sociedad Nuclear Española. September 2019.

Y. Rivera, J.L. Muñoz-Cobo, C. Berna, A. Escrivá. *Expansión en Caos Polinómico como método de Cuantificación de la Incertidumbre en simulaciones CFD. Aplicación al benchmark Cold-Leg Mixing de la OECD/NEA*. 45 Reunión Anual Sociedad Nuclear Española. September 2019.

Y. Rivera, J.L. Muñoz-Cobo, C. Berna, A. Escrivá, Susana M. Iglesias, Dany S. Domínguez. *Estudio del comportamiento de la película de líquido en flujo anular aire-agua en caída libre vertical*. 45 Reunión Anual Sociedad Nuclear Española. September 2019.

Y. Rivera, J.L. Muñoz-Cobo, J.L. Cuadros, C. Berna, A. Escrivá, Susana M. Iglesias, Dany S. Domínguez. *Estudio del comportamiento de la película de*

líquido en flujo anular aire-agua vertical ascendente al variar la tensión superficial mediante mezclas agua-1-butanol. 45 Reunión Anual Sociedad Nuclear Española. September 2019.

Y. Rivera, J. L. Muñoz-Cobo, C. Berna, A. Escrivá, Y. Córdova. *Study of liquid film behaviour in vertical downward air–water annular flow*. 13th International Conference on Advances in Fluid Mechanics. September 2020. Proceedings of Advances in Fluid Mechanics XIII, 128, 77–88. https://doi.org/10.1115/1.3138339

Y. Rivera, J. L. Muñoz-Cobo, C. Berna, A. Escrivá, Y. Córdova. *Análisis de las características más importantes de la película de líquido en flujo anular aire-agua en caída libre vertical*. Reunión Virtual Sociedad Nuclear Española, November 2020.

Y. Rivera, J.L. Muñoz-Cobo, C. Berna, A. Escrivá. *Simulación mediante CFD y cuantificación de la incertidumbre del benchmark internacional de la OECD/NEA Cold Leg mixing donde se produce una mezcla de fluidos de diferente densidad*. Reunión Virtual Sociedad Nuclear Española, November 2020.

Y. Rivera, J. L. Muñoz-Cobo, C. Berna, A. Escrivá, Y. Córdova. *Experimental measurements and CFD results of liquid film thickness in vertical downward air-water annular flow*. 11th International Conference on Advances in Fluid Dynamics with emphasis on Multiphase and Complex Flow (AFM/MPF 2021), July 2021.

J. L. Muñoz-Cobo, Y. Rivera, C. Berna, A. Escrivá. *Design of optimal conductance probes for two-phase flow tomography and liquid holdup: application to the determination of the average void fraction in a region*. 11th International Conference on Advances in Fluid Dynamics with emphasis on Multiphase and Complex Flow (AFM/MPF 2021) , July 2021.

Y. Rivera, J.L. Muñoz-Cobo, A. Escrivá C. Berna, Y. Córdova. *Estudio experimental del efecto de la temperatura en las ondas interfaciales en flujo anular descendente aire-agua*. 47ª Reunión Anual de la Sociedad Nuclear Española, September 2022.